“Development of a Numerical Model for the Heat and Mass Transport in an Electric Arc Furnace Freeboard”

From the Faculty of Georesources and Materials Engineering of the
RWTH Aachen University

Submitted by

Dipl- Ing. Jacqueline Christina Gruber

from Johannesburg, South Africa

in respect of the academic degree of

Doctor of Engineering

approved thesis

Advisors: **Univ.-Prof. Dr.-Ing. Herbert Pfeifer**
Prof. Dr.-Ing. Klaus Krüger
PD Dr. rer. nat. M. Kirschen

Date of the oral examination: 09.12.2015

This thesis is available in electronic format on the university library’s website

Jaqueline Christina Gruber
Development of a Numerical Model for the Heat and Mass Transport in an Electric Arc Furnace Freeboard

ISBN: 978-3-95886-087-2
1. Auflage 2016

Bibliografische Information der Deutschen Bibliothek
Die Deutsche Bibliothek verzeichnet diese Publikation in der Deutschen Nationalbibliografie; detaillierte bibliografische Daten sind im Internet über http://dnb.ddb.de abrufbar.

Vertrieb:

1. Auflage 2016
© Verlagshaus Mainz GmbH Aachen
Süsterfeldstr. 83, 52072 Aachen
Tel. 0241/87 34 34
Fax 0241/87 55 77
www.Verlag-Mainz.de

Herstellung:

Druck und Verlagshaus Mainz GmbH Aachen
Süsterfeldstraße 83
52072 Aachen
Tel. 0241/87 34 34
Fax 0241/87 55 77
www.DruckereiMainz.de

Satz: nach Druckvorlage des Autors
Umschlaggestaltung: Druckerei Mainz

printed in Germany
D 82 (Diss. RWTH Aachen University, 2015)

Acknowledgements

This thesis was created during my time as a research associate at the Department of Industrial Furnaces and Heat Engineering (IOB) of the RWTH Aachen University in Germany.

I would especially like to thank University Professor Dr.-Ing. Herbert Pfeifer and Dr.-Ing. Thomas Echterhof for giving me the opportunity to carry out the work concerning this dissertation and for their patience, guidance, encouragement and advice. I greatly appreciate the invaluable input, especially of Professor Pfeifer, during the phase when the results of the work done had to be consolidated, explained and clearly presented, resulting in this thesis.

In addition, the constructive advice and correction suggestions made by both Prof. Dr.-Ing. Klaus Krüger and PD Dr. rer. nat. Markus Kirschen should be mentioned. I would like to thank both my advisors for their time and for their valuable input, giving me the benefit of advice based on many years of in-depth experience concerning the topic of steel production in an EAF.

I would also like to thank all my colleagues at the IOB for their support. My special thanks goes to those who have become good friends and whose inspiration, advice, good cheer and company make working at the IOB a pleasure.

Last, but not least, I would like to thank my family, my children and especially my husband, for their support and patience.

Content

Nomenclature

Latin characters

Symbol	Description	Unit
a	Absorption coeff. of a fluid for thermal radiation	1/m
$A_{arc,inlet}$	Area of arc inlet	m^2
A_r	Pre-exp. factor for Arrhenius reaction rate	1/s
$C_{j,r}$	Molar concentration of species j	$kmol/m^3$
c_p	Specific heat	J/(kg·K)
C_S	Roughness constant	-
d	Diameter	m
$d_{electrode}$	Electrode diameter	m
$d_{upper\ vessel}$	Diameter of upper vessel of EAF	m
e	Electron charge	C
E	Internal energy	J/kg
$\dot{E}_{air}$	Energy inflow of air	W
$\dot{E}_{arc,inflow}$	Energy outflow due to inflow into arc columns	W
$\dot{E}_{arc,outflow}$	Energy input due to outflow of arc columns	W
$\dot{E}_{conv}$	Energy flow due to convection	W
$\Delta\dot{E}_{chem.reac.}$	Sum of heat of reaction	W
$\dot{E}_{cyl.surface}$	Net energy input due to thermal radiation exchange and convection at the cylindrical surface	W
$\dot{E}_{off\text{-}gas}$	Energy outflow of off-gas	W
E_r	Activation energy for Arrhenius reaction rate	J/kmol
$\dot{E}_{sources}$	Net energy input due to CO sources and O2 sink	W
$\dot{E}_{steam}$	Energy inflow of steam	W
f	Frequency	1/s
$\vec{F}$	External body force vector	N/m^3
g	Gravitational acceleration	m/s^2
G_b	Generation of k due to buoyancy	W/m^3
G_k	Generation of k due to mean velocity gradients	W/m^3
h	Specific enthalpy	J/kg
h_{arc}	Arc specific enthalpy	J/kg
h_F	Surrounding fluid specific enthalpy	J/kg
h_{slag}	Height of foaming slag layer	m
$I_{arc,elec}$	Electric arc current	A
I_{elec}	Electric current	A
$I_{electrode}$	Electric current flowing through the electrodes	A
I_{rad}	Thermal radiation intensity	W/m^2
j	Electric current density	A/m^2
$j_{arc,CAM}$	Mean electric arc current density (CAM)	kA/cm^2

$\vec{J}_j$	Diffusion flux of species j	kg/(s·m^2)
$j_{cathode}$	Average electric current density at the cathode	A/m^2
J_{max}	Maximum electric current density	A/m^2
k	Turbulent kinetic energy	m^2/s^2
k_B	Boltzmann's constant	J/K
k_{eff}	Effective conductivity	W/(m·K)
$k_{f,r}$	Arrhenius forward rate constant for reaction r	1/s
K_S	Surface roughness height	m
$\ell_{arc,CAM}$	Arc length from electrode tip to bath (CAM)	m
ℓ_{ch}	Characteristic length	m
$\ell_{electrode}$	Electrode length	m
$\dot{m}$	Mass flow rate	kg/s
$\dot{m}_{arc,CAM}$	Mass flow rate in arc channel (CAM)	kg/s
$\dot{m}_{arc,inflow}$	Defined mass flow rate into arc channel	kg/s
m_{tap}	EAF capacity	tons
$\dot{m}_{ingress\_air}$	Mass flow rate of ingress air into EAF	kg/s
$\dot{m}_{post\_combustion\_air}$	Mass flow rate of air at post-combustion gap	kg/s
$\dot{m}_{total,off-gas}$	Total mass flow rate of off-gas	kg/s
$M_{w,i}$	Molecular weight of species i	kg/mol
n	Coordinate normal to a wall	m
n	Refractive index	-
O_{an}	Work function for the anode	V
P	Operating power	W
p	Pressure	Pa
$P_{arc,Joule}$	Electric arc power due to Joule heating	W
$P_{conv,CAM}$	Energy dissipation at the electric arcs due to convection	W
$P_{e,CAM}$	Energy dissipation at the electric arcs due to electron flow	W
$P_{in,electric}$	Electrical power input	W
p_{op}	Operating pressure	Pa
$P_{r,CAM}$	Energy dissipation at the electric arcs due to radiation	W
p_s	Static pressure of surroundings	Pa
$\dot{Q}_{arc\,region}$	Energy input from arc region	W
$\dot{Q}_{arc\,/\,electrode}$	Energy input at plasma/electrode interface	W
$\dot{Q}_{arc\,/\,melt}$	Energy input at plasma/melt interface	W
$\dot{Q}_{cooling}$	Energy outflow due to cooling by water cooled panels	W
$\dot{Q}_{bath}$	Net energy outflow at bottom surface	W
$\dot{Q}_{conduc.electr.}$	Energy outflow by conduction at top surface of electrodes	W
$\dot{Q}_{electrode}$	Heat source in the electrodes due to Joule heating	W
$\dot{q}'''_{electrode}$	Volumetric electrode heat source due to Joule heating	W/m^3

$\dot{Q}_{heat\,loss}$	Energy outflow due to heat losses at the uncooled walls made of refractory material	W
$\dot{Q}_{Joule\,heating}$	Joule heating of the electrodes	W
$\dot{Q}_{rad.,gaps}$	Energy loss due to thermal radiation out of all gaps and the slag door	W
$\dot{Q}_{thermal\,radiation}$	Energy flow due to thermal radiation	W
$\dot{Q}_{total,anode}$	Total heat transferred at the anode surface	W
R	Universal gas constant	J/(K·mol)
r	Radius	m
$\vec{r}$	Point position	m
$r_{arc,CAM}$	Radius of electric arc (CAM)	m
R_{arc}	Electrical resistance	V/A = Ω
$r_{cathode}$	Cathode spot radius	m
$R_{electrode}$	Electric resistance	Ω
$\hat{R}_{i,r}$	Molar rate of creation or destruction of species i during reaction r	kmol/(m^3·s)
$R_{i,r}$	Net rate of production of species i due to reaction r	kg/(m^3·s)
$\vec{s}$	Vector direction	m
S_ε	User defined source term	W/m^3·s
S_h	Energy sources	W/m^3
S_k	User defined source term	W/m^3
S_m	Mass sources	kg/(s·m^3)
T	Temperature	K
t	Time	s
T_{arc}	Arc temperature (CAM)	K
T_S	Temperature of surroundings	Pa
u*	Dimensionless velocity	-
U_1, U_2, U_3	AC phase voltages	V
U_{12}, U_{23}, U_{31}	Phase to phase voltages	V
U_{an}	Anode drop voltage	V
U_{arc}	Electric potential of the electric arc	V
u_i, u_j	Velocity components in i- or j- direction	m/s
u_P	Mean velocity of the fluid at the near-wall node P	m/s
$u_{rad,arc}$	Arc radiation density	W/m^3
V	Volume	m^3
$\dot{V}$	Volumetric flow rate	m^3/s
V_1, V_2, V_3	AC phase voltages without transformer voltage drop	V
$V_{electrode}$	Electrode volume	m^3
V_m	Neutral point potential	V
$\overline{v}_{arc,CAM}$	Average gas velocity of arc (CAM)	m/s
$v_{arc,inflow}$	Velocity defined at arc inlets	m/s
$\vec{v}$	Velocity vector	m/s
v_t	Tangential velocity component at a wall	m/s
v_x,v_y,v_z	Velocity components in x-, y-, z-direction	m/s

$x_{n,i}$	Mole fraction of species i	-
Y_m	Contribution of fluctuating dilation in compr. turbulence to the overall dissipation rate	W/m^3
x, y, z	Cylindrical coordinates	m
y_P	Distance of near-wall node P from the wall	m
Z_{tr}	Transformer and reactor impedance	Ω
Z_{line}	Line impedance	Ω
Z_{arc}	Arc impedance	Ω
Z_{media}	Media impedance	Ω

Greek characters

Symbol	Description	Unit
β_r	Temperature exponent for Arrhenius reaction rate	-
$\delta_{i,j}$	Kronecker delta ($\delta_{ij} = 0$ if $i \neq j$ and $\delta_{ij} = 1$ if $i = j$)	-
$d\Omega$	Solid angle	m^2/m^2
ε	Emissivity	-
ε	Turbulent dissipation rate	m^2/s^3
ϕ_{elec}	Electric potential	V
ϕ	Scalar (e.g. velocity, pressure, shear stress,…)	-
κ	Isentropic exponent	-
λ	Thermal conductivity	W/(m·K)
λ	Air-fuel equivalence ratio	-
μ_0	Magnetic field constant	H/m
μ	Dynamic viscosity	kg/(s·m)
μ_t	Turbulent viscosity	kg/(s·m)
$\eta'_{j,r}$	Reactant rate exp. of species j for reaction r	-
$\eta''_{j,r}$	Product rate exp. of species j for reaction r	-
$\nu'_{j,r}$	Reactant stoichiometric coeff. of species j for reaction r	-
$\nu''_{j,r}$	Product stoichiometric coeff. of species j for reaction r	-
ρ	Density	kg/m^3
ρ_{DC}	Density of a DC arc	kg/m^3
$\rho_{elec,arc}$	Specific electrical resistance	Ω·m
σ	Stefan-Boltzmann constant	J/K
σ_{elec}	Electrical conductivity	A/(V·m)
$\sigma_k, \sigma_\varepsilon$	Turbulent Prandtl numbers	-
σ_s	Scattering coefficient	1/m
τ	Shear stress	N/m^2
τ	Space-time	s
ω	Pulsation of the power supply voltage	1/s
ξ_i	Mass fraction of species i	kg/kg
Y_i	Mass fraction of species i	kg/kg

Abbreviations

Abbreviation	Meaning
AC	Alternating current

atm	One atmosphere (101.325 kPa)
BOF	Basic Oxygen Furnaces
BOS	Basic Oxygen Steelmaking
CAM	Channel Arc model
CFD	Computational fluid dynamics
DC	Direct current
DO model	Discrete Ordinates Model for radiation
DR	Direct Reduction
DRI	Direct Reduced Iron
EAF	Electric arc furnace
HBI	Hot Briquetted Iron (compacted DRI)
IF	Induction furnace
ISP	Integrated steel plant
KMS	Klöckner Maxhütte Steelmaking
K-OBM-S	Klöckner Oxygen Blowing Maxhütte Steelmaking
LD	Linz-Donawitz
LTE	Local thermodynamic equilibrium
MSP	Mini steel plant
RTD	Residence time distribution
S	Surroundings

Chemical formula

Formula	Term
Al_2O_3	Aluminium oxide
CaO	Calcium oxide
CH_4	Methane
CO	Carbon monoxide
CO_2	Carbon dioxide
Cr	Chromium
Cr_2O_3	Chromium (III) oxide
Fe	Elemental iron
Fe_2O_3	Hematite
Fe_2O_3	Iron(III) oxide
$Fe_2O_3H_2O$	Goethite (hydrous ferrous oxide)
Fe_3O_4	Magnetite
$FeCO_3$	Siderite
FeS_2	Pyrite
H_2	Hydrogen
H_2O	Water vapour
MgO	Magnesium oxide
Mn	Manganese
MnO	Manganese(II) oxide
Mo	Molybdenum
N_2	Nitrogen
Ni	Nickel
O_2	Oxygen
P	Phosphorus
SiO, SiO_2	Silicon monoxide, Silica (silicon dioxide)
TiO_2	Titanium dioxide

Abstract

The topic of this thesis is the development of a numerical model to investigate the heat and mass transport in an EAF freeboard. Some of the challenges presently faced by European steelmakers are increasing costs for raw materials and energy, as well as strict environmental policies. These can be addressed by improving the energy efficiency of the EAF steelmaking process by reducing off-gas and cooling losses. This can be achieved by increasing the degree of combustion of CO and H_2 in the furnace freeboard. A better understanding of the mechanisms that cause unwanted emissions during the steelmaking process can also help to develop new methods to reduce pollutants. The long term motivation behind the topic of this thesis is therefore to create a numerical EAF model with which the influence of process innovations on the fluid flow field, energy transport and chemical reactions within the freeboard of an electric arc furnace can be analysed. At this stage, the main objective is to qualitatively investigate the influence of the arc region on the amount of post-combustion within the freeboard. The effect of a change in the foamy slag height on the resulting amount of post-combustion is also investigated.

The numerical EAF model represents the power-on/flat-bath stage of the steelmaking process in an exemplary AC electric arc furnace for quasi-steady state heat loss conditions. The AC EAF has a capacity of 100 tons of steel, a transformer rating of 90 MVA and and an inner vessel diameter of 6.1 m.

A simplified time-averaged arc model based on the channel arc model was developed in order to include the influence of the arc region on the conditions within the freeboard. The plasma arcs are not part of the solution domain, but are represented as segmented cylindrical surfaces extending from each electrode tip to the bath surface. In contrast to previous models, this simplified arc model includes not only the energy input due to the intense thermal radiation, but also the kinetic energy input due to the arc in- and outflow as well as the energy input due to the heating of the entrained furnace atmosphere in the arcs. The graphite electrodes are part of the solution domain, whereby the Joule heating due to the AC current flowing through the electrodes is taken into account. For the energy balance of the solution domain the energy input from the arc region plus the Joule heating in the electrodes represents the electric power input from the secondary circuit. This energy contribution is much smaller than the true electric power input, as it equates the amount needed, in addition to the other energy inflows, to cover the stationary power losses. The discrete ordinates thermal radiation model available in the CFD code ANSYS FLUENT (Version 14.5) was chosen to model the thermal radiation exchange, whereby the thermal radiation absorption coefficient of the furnace atmosphere is calculated with the weighted-sum-of-grey-gases-model. Species transport with volumetric reactions and the finite-rate/eddy dissipation turbulence chemistry interaction is used to calculate the mass transfer and chemical reactions within the freeboard. The furnace atmosphere is defined to be a mixture of CO, CO_2, H_2O, N_2 and O_2. The post combustion of CO to CO_2 is simulated according to the gas-shift reaction available for the oxidation of CO in FLUENT. The realizable k-ε

model with standard wall functions for the near wall treatment was selected to simulate the turbulent viscous flow.

The geometry of the EAF model extends from the uppermost layer of the metal bath to the beginning of the off-gas extraction downstream of the post-combustion gap. The foamy slag is modelled as a solid layer and the top layer of the bath, also considered as a solid, is included. These two layers allow the simulation of downward absorption and redistribution of energy from the arc region, which is reflected by the resulting temperature distribution at the foamy slag layer surface. Burners, lances or injectors are not included at present. The decarburization of the molten metal bath is taken into account by the definition of a homogenous source of CO at the surface of the foamy slag layer. An average value for the graphite electrode consumption is modelled by a corresponding CO source and O_2 sink at the electrode surfaces. Ingress air is defined to enter the freeboard through the slag door, roof gap and electrode gaps and air flows in at the post-combustion gap. It is assumed that a small amount of steam enters the vessel through the electrode gaps due to electrode cooling. The upper vessel, roof, exhaust elbow and exhaust extraction are cooled by water cooled panels. The walls of the lower vessel, balcony and roof delta zone are defined to consist of refractory material and are cooled by natural convection and thermal radiation to the ambient on the outside of the vessel.

The results obtained with the numerical EAF model are used to evaluate the influence of the inclusion of the energy input due to the heating and increase in momentum of the furnace atmosphere drawn into and flowing out of the arc region on the conditions within the freeboard. Furthermore, the impact of the arc region flow on the post-combustion of CO to CO_2 in the freeboard for a free-burning arc length of 230 mm is compared to that for a free-burning arc length of only 50 mm.

The modelling of the arc region has a large influence on the flow field, temperature distribution and post-combustion. The results show that due to the inclusion of the arc in- and outflow a total increase in the simulated energy input within the vessel of 4.42 MW results. This is due to the correspondingly higher temperatures and circulation leading to an increase in the post-combustion of CO to CO_2 within the freeboard. The inclusion of the arc in- and outflow should therefore not be neglected in future EAF models. An increased slag height not only protects the cooling panels from the thermal radiation of the arcs. It also leads to a reduction in the interaction between the flow in the arc region and in the freeboard. This in turn reduces the amount of mixing of CO from the slag layer with the ingress air and therefore also the amount of post-combustion in the freeboard. As a result a decrease in the free-burning arc length from 230 mm to 50 mm leads to a reduction in the total energy input within the solution domain of 3.22 MW.

The numerical EAF simulation model developed during this thesis delivers valuable information which helps one to understand the heat and mass transfer processes taking place within the EAF freeboard. Furthermore, several important insights were gained concerning necessary future developments of the model.

Kurzfassung

Das Thema dieser Dissertation ist die Entwicklung eines numerischen Modells zur Untersuchung des Wärme- und Stofftransports in einem Lichtbogenofen oberhalb der Schmelze. Europäische Stahlhersteller müssen mit steigenden Kosten und strengen umweltrechtlichen Regelungen zurechtkommen. Eine Steigerung der Energieeffizienz im LBO durch eine Reduzierung der Kühlungs- und Abgasverluste kann helfen den Herausforderungen gerecht zu werden. Dieses kann erreicht werden, indem die Verbrennung des im Ofengefäß vorhandenen CO und H_2 verbessert wird. Ein vertieftes Verständnis der Mechanismen, die zu unerwünschten Abgasen führen, kann die Entwicklung neuer Methoden zur Vermeidung dieser Abgase erleichtern. Das langfristige Ziel ist daher die Erzeugung eines numerischen LBO Modells, mit dem der Einfluss von Prozessänderungen auf das Strömungsfeld, den Energietransport und die chemischen Reaktionen oberhalb der Schmelze untersucht werden kann. Das aktuelle Ziel ist eine qualitative Untersuchung des Einflusses des Lichtbogenbereiches auf die Nachverbrennung innerhalb des Ofens. Zusätzlich dazu wird die Auswirkung einer Veränderung der Dicke der geschäumten Schlackenschicht auf die Nachverbrennung im Ofengefäß untersucht.

Das LBO Modell stellt die Flachbadphase des Stahlprozesses in einem Lichtbogenofen während des Betriebs der AC Lichtbögen für quasi-stationäre Wärmeverlustbedingungen dar. Der LBO hat eine Transformatorleistung von 90 MVA, ein Abstichgewicht von 100 Tonnen und einen Ofendurchmesser von 6,1 m.

Ein vereinfachtes zeitgemitteltes Lichtbogen-Modell auf Basis des Kanalmodells ist zur Einbringung des Einflusses dieses Bereiches auf die Zustände im Ofen entwickelt worden. Die Plasmabögen sind nicht im Lösungsbereich enthalten. Sie werden stattdessen von unterteilten zylindrischen Oberflächen modelliert, die von den Elektrodenspitzen bis zur Badoberfläche reichen. Dieses Modell beinhaltet nicht nur den Energieeinsatz wegen der intensiven Wärmestrahlung, sondern auch den kinetischen Energieeinsatz wegen der Ein- und Ausströmung aus den Lichtbögen und die Erwärmung des in die Lichtbögen eingezogenen Gases. Die Graphit-elektroden sind Teil des Lösungsbereiches, wobei die joulesche Erwärmung der Elektroden berücksichtigt wird. Für die Energiebilanz der Simulation repräsentiert die Summe des Energiebeitrags durch den Lichtbogenbereich und die joulesche Erwärmung der Elektroden den Energieeinsatz des elektrischen Sekundär-kreislaufes. Diese Summe ist kleiner als der reale Wert, da es zusammen mit den anderen Energiequellen im Ofengefäß die quasistationären Energieverluste ausgleicht. Das DO- thermische Wärmestrahlungs-modell, welches in ANSYS FLUENT (Version 14.5) zur Verfügung steht, wird angewendet. Dabei wird der Absorptionskoeffizient der Ofenatmosphäre anhand des „weighted-sum-of-grey-gases“ Modell berechnet. Zur Simulation des Stofftransports und der chemischen Reaktionen wird die Option Spezies Transport mit volumetrischen Reaktionen und die Modellierungsmethode Finite-rate/Eddy-dissipation für die Interaktion der kinetischen Reaktionsgeschwindigkeit und der turbulenten Durchmischung verwendet. Die Ofenatmosphäre besteht aus CO, CO_2, H_2O, N_2 und O_2. Die

Nachverbrennung wird anhand der vereinfachten Wassergas-reaktion, welches in FLUENT verfügbar ist, modelliert. Die turbulente Strömung wird mit dem Realizable k-ε Modell und der wandnahe Bereich mit den Standard Wandfunktionen modelliert.

Die Geometrie umfasst die oberste Schicht des Bades, bis zum ersten Abschnitt des Abgastraktes nach dem Nachverbrennungsspalt. Die oberste Schicht des Bades und die geschäumte Schlackenschicht werden als Feststoffe modelliert. Diese erlauben es, die Umverteilung der absorbierten Wärme von den Lichtbögen nach unten hin näherungsweise abzubilden, welches zu einer entsprechenden Temperaturverteilung auf der Oberfläche der geschäumten Schlackenschicht führt. Brenner, Lanzen und Injektoren sind zurzeit nicht im Modell enthalten. Die Entkohlung des Bades wird durch eine homogene CO Quelle an der Oberfläche der Schlackenschicht berücksichtigt. Ein durchschnittlicher Elektrodenverbrauch wird mithilfe einer CO Quelle und entsprechenden O_2 Senke an den Elektrodenoberflächen modelliert. Eine Lufteinströmung durch die Schlackentür, den Dachspalt, die Elektrodenspalten und durch den Nachverbrennungsspalt nach dem Krümmer wird berücksichtigt. Es wird angenommen, dass wegen der Elektrodenkühlung an den Elektrodenspalten Dampf in das Ofengefäß eindringt. Das Obergefäß, der Deckel, der Krümmer und der Abgasentzug werden durch wasserdurchflossene Wandpaneele gekühlt. Die Wände des Untergefäßes, der Abstich-Erker und mittlere Bereich des Daches bestehen aus Feuerfestmaterial und verlieren an Ihren äußeren Oberflächen durch natürliche Konvektion und Wärmestrahlung Wärme an die Umgebung.

Die Simulationsergebnisse werden zur Untersuchung des Einflusses der Lichtbogenmodellierung auf die Bedingungen im Ofen verwendet. Darüber hinaus wird untersucht, inwiefern der Einfluss des Lichtbogenbereichs auf die Nachverbrennung von CO zu CO_2 im Ofengefäß sich verändert, wenn die frei-brennende Lichtbogenlänge von 230 mm auf 50 mm verringert wird. Die Ergebnisse zeigen, dass die Mitberücksichtigung der Ein- und Ausströmung in die Lichtbögen einen sehr großen Einfluss auf das Strömungsfeld, die Temperaturverteilung und die Nachverbrennung hat. Die zusätzliche kinetische Energie und die erhöhten Temperaturen wegen der Erhitzung des in die Lichtbögen eingezogenen Gases führen zu einer erhöhten Zirkulation im Ofengefäß und zu einer Erhöhung der Umsetzung von CO zu CO_2. Dieses entspricht insgesamt einer Erhöhung des simulierten Energieeintrages in den Lösungsbereich von 4.42 MW. Eine dickere Schlackenschicht beschützt die Wandpaneele vor der intensiven Wärmestrahlung der Lichtbögen und führt zu einer reduzierten Interaktion zwischen der Strömung im Lichtbogenbereich und im Ofengefäß. Dieses beeinflusst die Vermischung von CO mit der Einströmenden Falschluft, sodass eine Verringerung der Nachverbrennung erfolgt. Eine Veränderung der frei-brennenden Lichtbogenlänge von 230 mm auf 50 mm führt somit insgesamt zu einer Reduzierung der eingebrachten Energie von 3.22 MW. Das entwickelte LBO Modell liefert wertvolle Erkenntnisse, die zum Verständnis der Wärme- und Stofftransportphänomene im Ofengefäß beitragen. Die Ergebnisse haben zu wichtigen Schlussfolgerungen hinsichtlich der langfristigen Weiterentwicklung des Modells geführt.

1 Introduction

1.1 EAF-Steelmaking

The topic of this thesis is the development of a numerical model to be able to simulate the heat and mass transport in an electric arc furnace freeboard. The motivation behind this topic is the need to create a tool which facilitates the development of further innovative technologies needed to meet some of the challenges presently faced by the steelmaking industry.

1.1.1 Relevance of the EAF steel production route

When considering the current steelmaking methods the relevance of electric arc furnaces (EAFs) for the steel industry becomes evident. There are currently two main steel production categories [1]. The first production route of steel is in basic oxygen furnaces, also referred to as oxygen blown converters or LD converters. The second category of steel production is the production of steel in electric arc furnaces (EAFs) and induction furnaces (IFs). **Table 1-1** shows a summary of the current main steelmaking methods, the corresponding furnace types and the main raw materials needed for each process.

Table 1-1: Overview of steelmaking methods *

Steelmaking: Removing trump elements (e.g. Si, P, Mn) and carbon (< 2 wt%) from iron and adding alloying elements (e.g. Cr, Ni, Mo)		
Furnace/reactor	Basic method	Main raw materials
Basic oxygen steelmaking (BOS): e.g. Basic oxygen furnace (BOF), LD converter (Linz-Donawitz-Verfahren), Klöckner Maxhütte Steelmaking (KMS), Klöckner Oxygen Blowing Maxhütte Steelmaking (K-OBM-S)	Pure oxygen is blown into the liquid iron via supersonic lances to remove the carbon.	Liquid pig iron (70 % to 100 %), steel scrap, oxygen, lime, and other fluxes
Electric arc furnace (EAF)	The raw material is mainly melted by the energy input from the electric arcs. The melting process is accelerated with burners and oxygen injection. Decarburization is achieved by blowing oxygen into the melt with lances and injectors.	Approximately 90 % steel scrap, DRI, HBI, solid pig iron, oxygen, coal, lime, dolomite
Electric induction furnace (IF)	Electricity is used to melt the raw material by induction.	High-quality steel scrap, DRI (up to 40 %)
Open-hearth furnace	Siemens-Martin process. In use in India and Russia.	Pig iron, steel scrap, iron ore

* Based on information from Walker [2] and the Indian Bureau of Mines [1].

According to the 2012 crude steel production statistics published by the Worldsteel Association (www.worldsteel.org) most of the global crude steel produced in 2012 was produced in China (46.9 %) followed by Japan (7.1 %), the United States of America (5.9 %), India (5.1 %) and Russia (4.7 %). According to Walker in 2010 approximately 70 % of this steel was produced in BOFs, 29% in EAFs [2]. According to the statistics published by the Worldsteel Association for the year of 2013, approximately 40 % of the raw steel produced in Europe is obtained via the electric arc furnace route.

1.1.2 Types of electric arc furnaces

Electric arc furnaces are normally characterized according to the type of current used (AC or DC), their capacity (tons of steel) and the transformer rating (in MVA). The type of furnace installed at any specific site depends on many factors: the historical development of the steel works; the steel grades and product sizes; the availability and price of raw materials; the availability and price of energy resources; the relevant current legislation and changes in the legislation concerning energy efficiency and environmental issues. Examples of a DC and an AC electric arc furnace in operation are shown in **Figure 1-1**.

Some of the advantages of DC furnaces are the lower noise level during power-on, less electrode consumption, less costs due to complex roof design and uneven wear of side walls. Most importantly, the level of flicker (non-periodical voltage fluctuations) caused during the power-on phase of DC arc furnaces is lower than that of AC arc furnaces [3]. Some of the disadvantages of DC arc furnaces are higher maintenance costs for the furnace bottom electrode, higher investment costs for electrical equipment and that the DC current and therefore power is limited by the maximum electrode diameter. This influences the time needed for a heat and therefore also the energy losses due to for example cooling during one heat. At present the question of whether a DC or AC electric arc furnace is more advantageous depends mainly on the characteristics of the local electricity grid, especially its susceptibility towards disturbances [3],[4].

The development of UHP (Ultra-High Power) facilities was driven by the need to increase the productivity of EAFs. Increasing the productivity means a reduction in the cost for maintenance and manpower per ton of steel produced. The necessary tap-to-tap time is reduced by increasing the transformer power. UHP furnaces are however only economically feasible if the power-on-time of the steelmaking process makes up more than 70% of the tap-to-tap time [4].

Electric arc furnaces can not only be sorted according to their capacity, transformer rating and the type of current used, they can be further characterized according to the type of process. One such example is the Consteel® EAF process. For a continuous scrap feeding (Consteel®) EAF, such as is described in the CONOX report by Pfeifer et al.[5] or presented by Memoli et al.[6], the preheated scrap is continuously fed into the furnace via conveyor belt, whereby the steel bath is kept covered by a foamy slag. Another example of an EAF type is a shaft EAF such as

that described by Nagai et al.[7]. In this case the melting furnace is directly connected to a scrap preheating shaft.

a) DC EAF (Photo courtesy of Georgsmarienhütte GmbH, Germany)

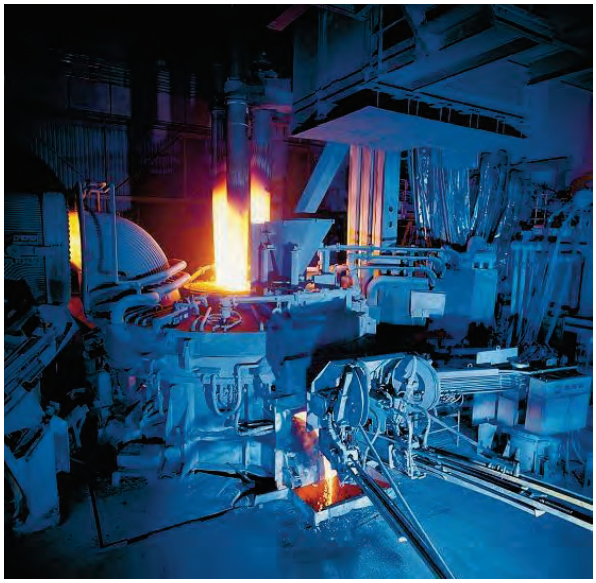

b) AC EAF (Photo courtesy of Siemens VAI Metals Technologies GmbH, Germany)

Figure 1-1: Examples of a DC and an AC EAF

1.1.3 Description of the EAF steelmaking process

Kühn et al.[8] discuss a typical heat of a 130 MVA DC electric arc furnace. **Figure 1-2** was created based on data presented by Kühn et al. and information concerning the operations carried out during an EAF heat given by Kleimt et al.[9]. The time shown in the figure at which a free burning arc is most likely to occur is based on measurements done by Haverkamp et al.[10] at the same DC EAF considered by Kühn et al..

When considering the individual operational parameters shown in Figure 1-2, it must be noted that order and duration of the operations during the process vary, depending not only on the type of furnace, but also on the type of steel being produced and the composition of the raw materials charged.

At the beginning of the process shown in Figure 1-2, the furnace roof is open and the first bucket containing scrap, slag formers and coal, bucket 1, is loaded into the furnace. Thereafter the roof is closed and the electrodes are lowered in order to ignite the arcs. This is the beginning of the first power-on phase (1.).

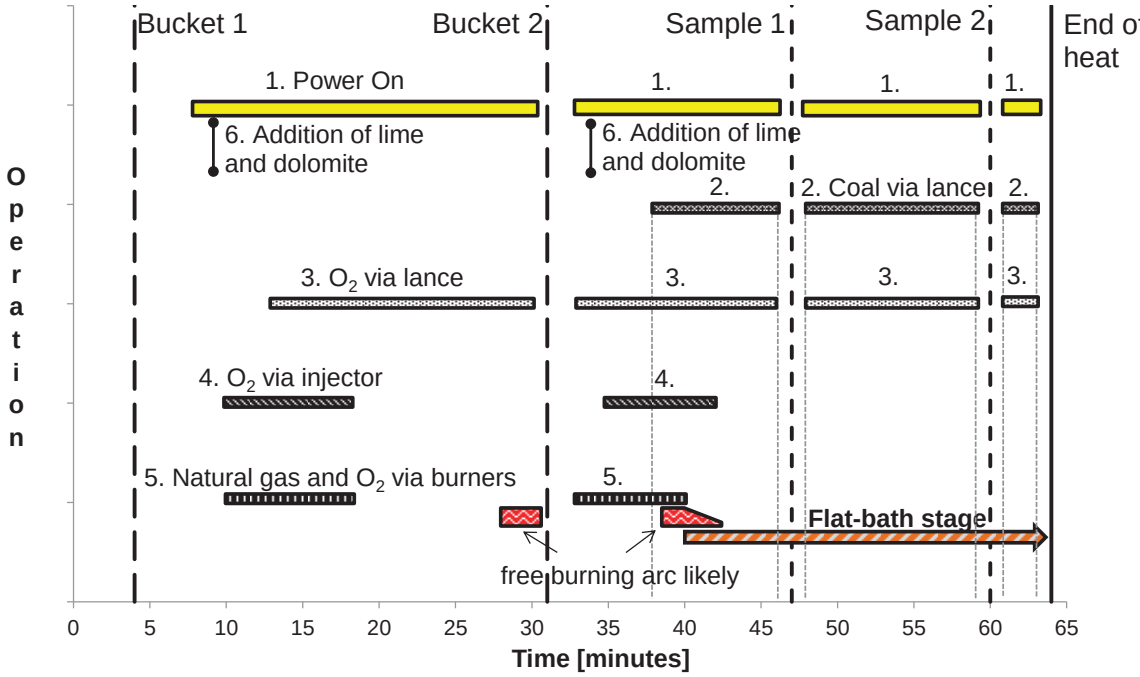

Figure 1-2: Overview of the main operations during an exemplary 130 MVA DC electric arc furnace heat operated with a hot heel (based on information in [8],[9],[10])

The electric energy from the electrodes is used to melt the scrap and achieve and maintain the required melt temperature. Shortly after the ignition of the arcs, the oxygen injectors (4.) and burners (5.) are turned on. The burners are used to accelerate the melting rate of the scrap. The oxygen injectors are used to cut down the steel scrap and combust carbon monoxide, which delivers additional heat. Three minutes thereafter enough molten metal has accumulated in the hearth, when operating with a hot heel. At this point the oxygen lance (3.) is turned on in order to begin decarburization. The oxygen injection into the bath also leads to an increased mixing and accelerates the melting rate of the scrap.

Thirty one minutes into the heat, the lid is opened in order to charge the second bucket containing scrap and lime, bucket 2. As soon as the lid is closed, the arc is reignited and the burners and oxygen injection are reinitiated. Lime and dolomite (6.) are added to the melt during the heat in order to remove impurities (e.g. phosphorus, sulfur, silica) and help form a slag. Once most of the scrap has molten, coal injection via lance (2.) into the melt is started. This, in combination with the oxygen injection

via lance, is done to transport additional heat into the melt. Secondly it leads to the formation of a foamy slag, which is necessary to shield the furnace walls from the intense thermal radiation from the electric arcs.

During the flat-bath phase, which can be assumed to start shortly after fine coal injection into the melt is started, two samples of steel and slag are taken, sample 1 and sample 2, and the temperature of the melt is measured. The heat ends after approximately 64 minutes when the charge is deslagged and then tapped.

It makes sense that a free burning or only partly covered arc is most likely to occur towards the end of the melting down period of the scrap from the first bucket and at the beginning of the flat-bath stage, when foamy slag formation has just been initiated.

When oxygen and carbon are blown into the bath at the same time, the oxygen leads to the oxidation of carbon in the melt ($C + 0.5\ O_2 \rightarrow CO$). Unfortunately it also leads to the oxidation of iron, leading to the formation of FeO. The carbon injected into the bath at the same time dissolves into the melt and reacts with the iron oxide to carbon monoxide ($FeO + C \rightarrow Fe + CO$). This reduces the iron lost due to the oxygen injection during decarburization. In addition the carbon monoxide bubbles generated lead to the foaming of the slag [4].

1.2 Problem definition, objectives and approach

According to the Platts Industry Survey report [11], the 159 respondents to the survey, of whom 51 % where from Western Europe, assessed the biggest challenges faced by the European steel industry as listed in **Table 1-2** below. In the first column the challenges from which the participants could choose are listed. In the second column the percentage of participants who selected the respective challenge as the most relevant is shown.

Table 1-2: Biggest challenges facing the European steel industry in 2013 [11]

Challenges	Percentage
Over-capacity (demand vs. supply)	58.9 %
International competition	12.0 %
Financing and credit availability	10.1 %
EU-climate policy	7.6 %
Cost of raw materials	5.7 %
Rising energy costs	3.2 %
R&D and innovation	1.9 %
Skills shortages and talent retention/development	0.6 %

When asked to describe the current state of the European steel industry at the time the survey was carried out, the overall response was that over-capacity due to the Eurozone crisis, the restrictive environmental policies, rising energy costs, and strong

international competition made it a challenge for the European steelmaking industry to remain competitive.

When considering the costs of steelmaking in an EAF charged mainly with scrap, it can be said that approximately 65 % of the costs are due to the raw materials (scrap and ferroalloys) and 35 % are operating costs. Approximately 40 % of the operating costs are for electricity, fuel and electrodes [4].

One way to address the issues of increasing costs for raw materials and energy is to invest in research with the aim of increasing the efficiency of processes. Furthermore, research with the aim of understanding the mechanisms that cause unwanted emissions during the steelmaking process can facilitate the development of new methods to reduce or counteract pollutants.

Kirschen et al.[12]-[14] performed off-gas measurements at five different AC EAFs and one DC EAF. The averaged energy balances for austenitic steel grade heats for two of the AC EAFs are shown in **Figure 1-3** and **Figure 1-4.** Both EAFs have a steam cooled shell in order to optimize energy recovery, whereby one of them has a steam cooled roof. The averaged energy balances show, that the loss of sensible and latent heat, due to CO and H_2 in the hot off-gas flowing out of the furnace vessel, makes up between 11 % (steam cooled roof and shell) and 16 % (water cooled roof and steam cooled shell) of the total energy input during one heat.

By comparison, the simulation results of a mathematical model developed by Logar et al.[15] for an AC EAF with a conventionally water cooled furnace shell predicts that the flow of off-gas represents 16 % of the total energy input and the cooling approximately 15 %.

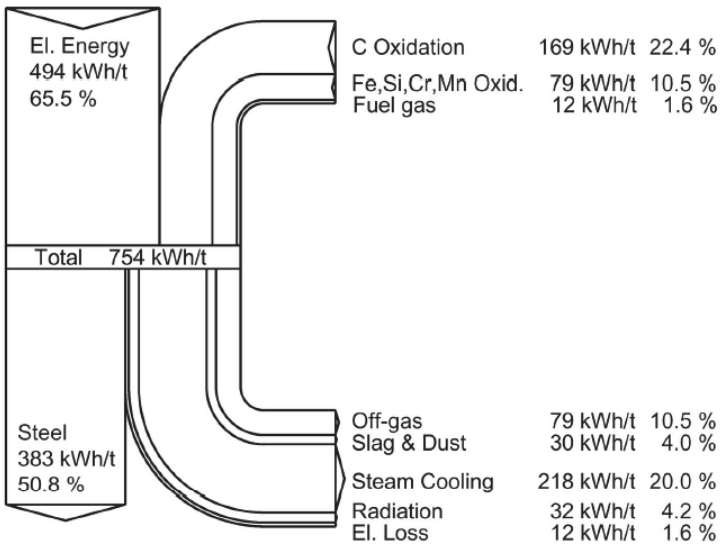

Figure 1-3: Averaged energy balance based on measurements during 24 heats (austenitic grades) for a 75 t EAF with a steam-cooled roof and shell [14]

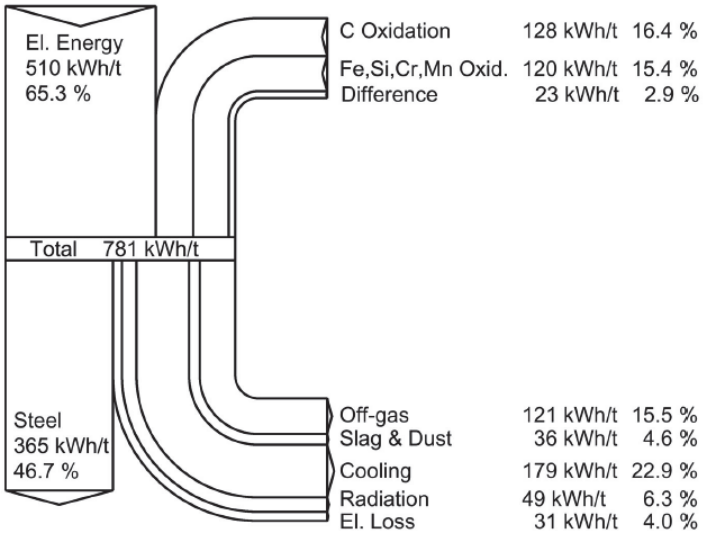

Figure 1-4: Averaged energy balance based on measurements during 7 heats (austenitic grades) for a 145 t EAF with a water-cooled roof and steam-cooled shell [14]

Figure 1-5 shows a Sankey-Diagram for the 130 MVA DC EAF by Kühn [16] for which the main operations during an exemplary heat were illustrated in Figure 1-2. Here the flow of off-gas represents 20 % (7.9 % sensible heat and 12.5 % chemical energy) of the total energy input and the cooling approximately 17 %.

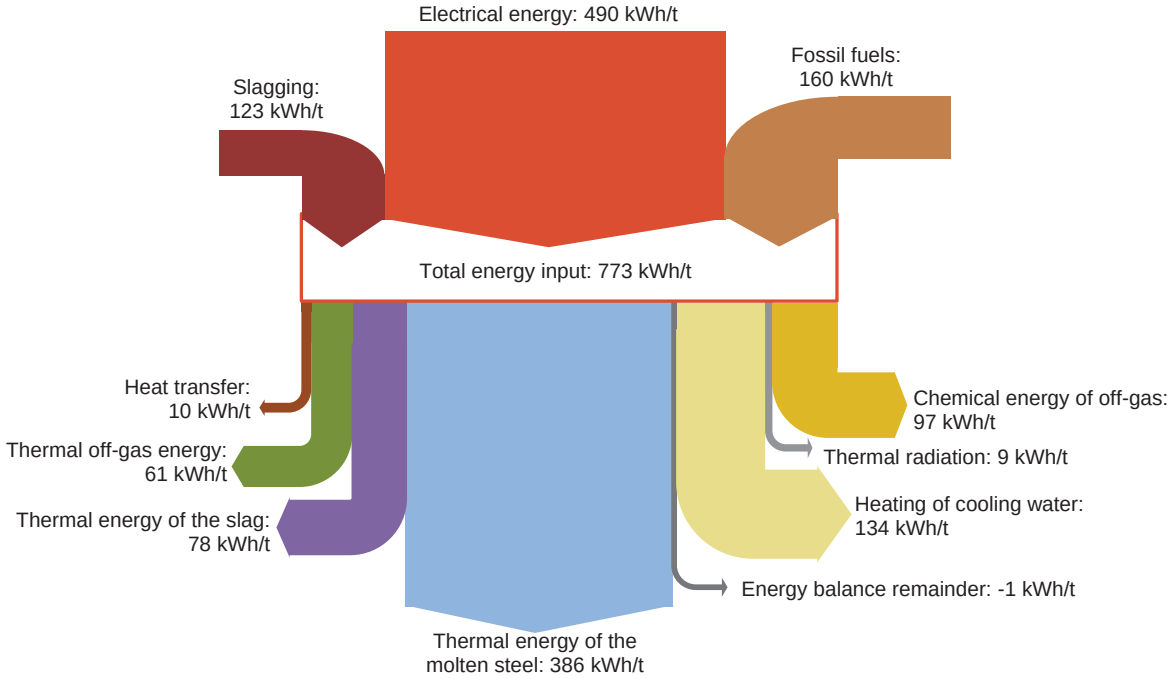

Figure 1-5: Sankey-Diagram for an exemplary heat of a 130 MVA DC EAF [16]

The values above confirm that the energy efficiency of a furnace could be improved by reducing the off-gas and cooling losses and thereby increasing the percentage of total input energy transferred to the steel [16]. This could be achieved by for example

increasing the degree of combustion of CO and H_2 in the furnace before the off-gas exits the vessel.

When comparing values from different investigations it should be noted, that the amount of total energy input lost due to cooling in comparison to that lost due to the thermal off-gas energy leaving the vessel depends on the position at which the off-gas temperature was measured and on the cooling water circuits considered to calculate the cooling water heating.

As will be explained in detail in section 3, the numerical simulation model of the heat and mass transport in an electric arc furnace freeboard presented in this thesis concerns the flat-bath phase of the steelmaking process. In **Figure 1-6** the results of a dynamic energy balance based on off-gas measurements and process data presented by Kleimt et al.[9] for the same 130 MVA DC EAF is shown. It can be seen that during the flat-bath phase, which starts after approximately 45 minutes, the electrical power input is between 80 MW and 90 MW. The cooling losses (roof and vessel walls) are approximately 14 MW and the off-gas losses are greater than 20 MW. It can also be seen that whereas the cooling losses remain fairly stable during the flat-bath phase, the off-gas losses vary. The calculated off-gas losses are dependent on the measured static temperature and off-gas composition. As the sensible temperature remains fairly stable at between 1500 °C and 1600 °C, the variation in off-gas losses is mainly due to a variation in the off-gas composition.

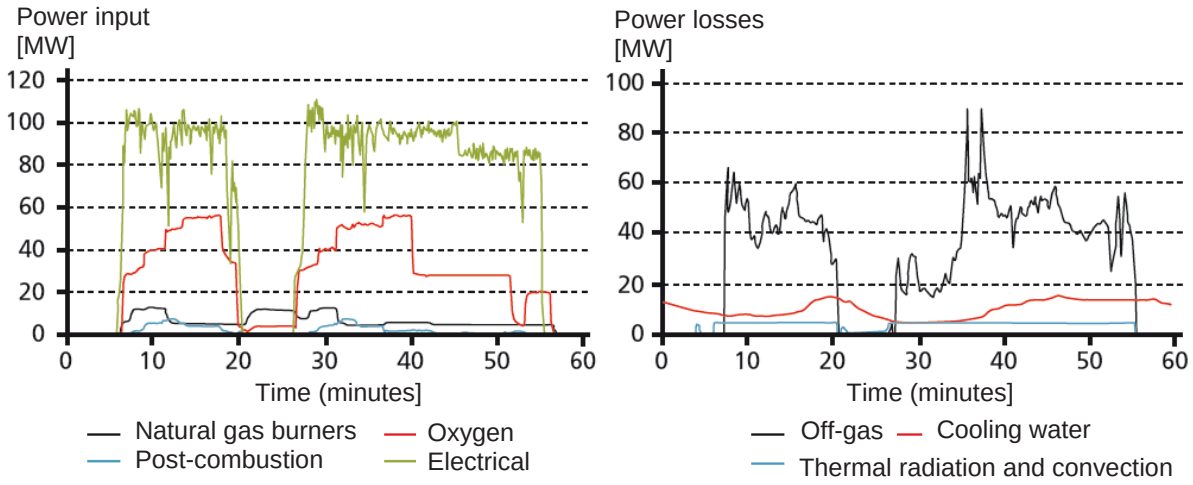

Figure 1-6: Results of a dynamic energy balance for an exemplary heat of a 130 MVA DC EAF [9]

Kleimt et al.[9] use a mathematical dynamic energy and mass balance model to calculate the total energy input needed for a heat. Such mathematical models are very useful as they can be used as a basis for dynamic online process control. However, one of the findings of Kühn et al.[8] is that the positioning of coal lances has a significant influence on the extent of combustion and therefore on the chemical energy of the off-gas. Therefore it can be stated that details, such as the positioning of burners, lances and injectors or the amount of ingress air, can have a significant effect on the off-gas and cooling losses.

The purpose of the numerical EAF model development described in this thesis is to create a tool with which the influence of process innovations on the fluid flow field, energy transport and chemical reactions within the freeboard of an electric arc furnace can be analysed [17]. In contrast to mathematical energy and mass balance EAF models, such as that applied for example by Kleimt et al.[9] and Logar et al.[15], the advantage of the numerical simulation model developed during this thesis is that it can be adapted to investigate the influence of for example the position of lances on the conditions within the furnace.

The main objective of the numerical EAF model at this stage is to qualitatively investigate the influence of the arc region on the amount of post-combustion within the freeboard. The effect of a change in the foamy slag height on the resulting amount of post-combustion is also investigated. The flow fields, temperature distributions, species mass fraction distributions and resulting chemical reactions are evaluated. The simulated energy inputs are compared to the resulting energy losses. The results obtained and the experience gained during the model development are used to outline future developments needed in order to achieve the long term goal of being able to compare the real electric energy input to the modeled energy flows.

2 Current state of research

2.1 Numerical models of the heat and mass transport in an EAF freeboard

There are currently only a few examples of numerical CFD models that attempt to model the entire electric arc furnace freeboard, including not only the thermal radiation exchange between all internal surfaces of the vessel, but also the fluid flow and chemical reactions.

Guo et al.[18] present a radiation model to quantify the radiation energy distribution inside an AC EAF during the power-on phase. This model does not include the influence of the furnace atmosphere, i.e. the fluid flow and chemical reactions. The radiating surface of the arcs is represented by the extended surface of the cylindrical electrodes, deflected outwards from the furnace center. It is assumed that 80 % of the energy released from an arc is transferred in the form of thermal radiation, with 2 % absorbed by the electrode and 18 % directly transferred to the bath. Using the surface of the cylinders representing the arcs and the active power input rate, the energy flux from the surfaces representing the arcs is calculated and applied as a boundary condition. The temperature distribution resulting from the modeled thermal radiation exchange for a free-burning arc length of 152 mm (slag height is 300 mm, arc length is 452 mm and active power is 90 MW) is shown in **Figure 2-1** below.

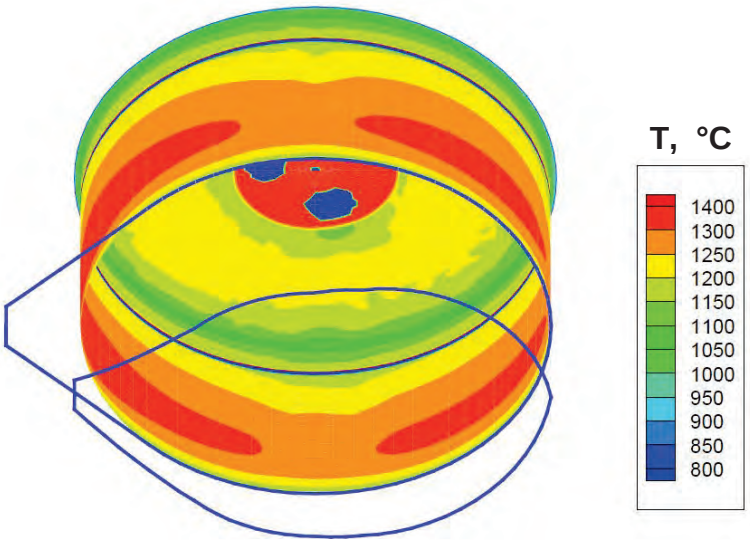

Figure 2-1: Temperature distribution calculated using a radiation model [18]

In addition, in order to check the assumption that 2 % of the electric energy is absorbed by the electrodes, Guo et al.[18] calculate the electrode temperature distribution resulting from Joule heating due to a current of 61.5 kA and thermal conduction. A temperature of 400 K is defined at the top of the electrode. A hot tip temperature between 2000 K and 3600 K and a uniform furnace atmosphere temperature of 400 K are assumed. It is concluded that no more than 5.5 % of the total electric energy flows into the electrodes at the tip. This calculation does however not consider the thermal radiation absorbed by the electrodes from other surfaces, for

example the impingement area of the arc with the bath or the foamy slag surface. In **Figure 2-2** the resulting electrode temperature distribution and a corresponding plot of the temperature with respect to distance from the tip divided by the electrode length are shown.

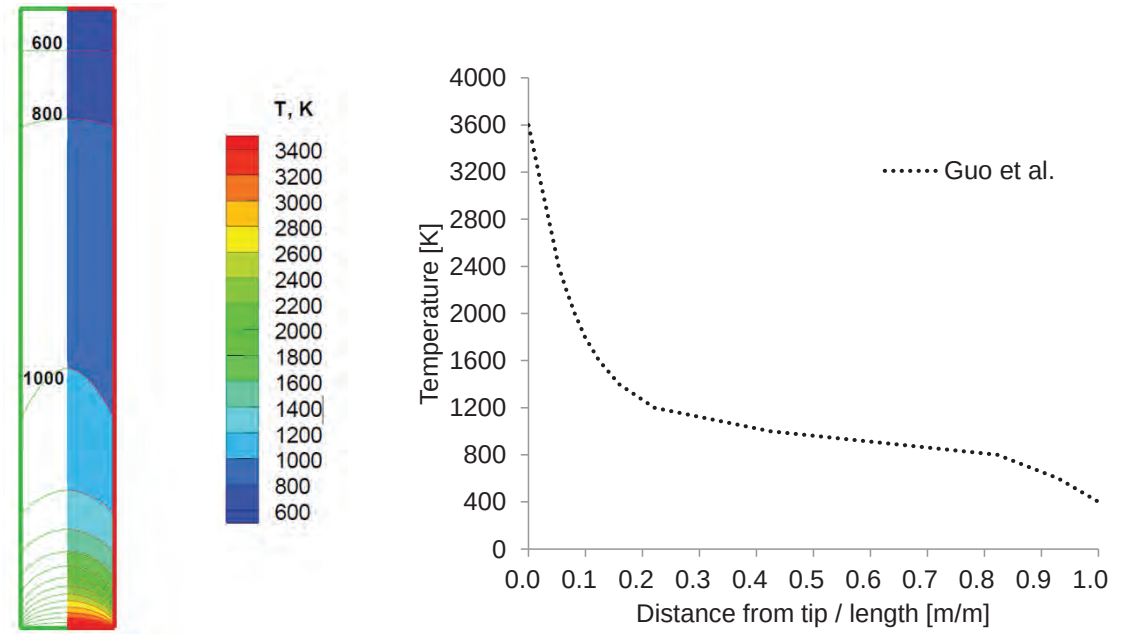

a) Electrode temperature distribution [18]

b) Corresponding plot of electrode temperature distribution

Figure 2-2: Electrode temperature distribution calculated by Guo et al.[18]

Li et al.[19] describe a 3D simulation model for flat-bath conditions inside an AC EAF freeboard. As shown in **Figure 2-3**, the geometry of the model is strongly simplified. It does not include the molten steel and slag. The interior of the electrodes is not included and the electric arc region is not represented in the model.

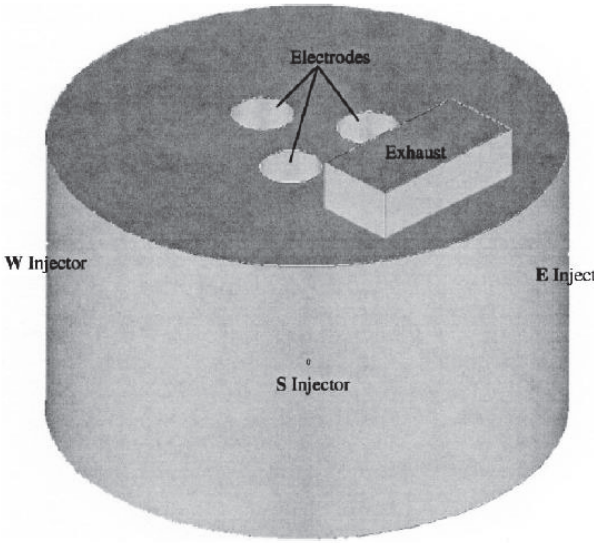

AC furnace capacity	165 t
Internal diameter	5.0 m
Internal height	3.0 m
Electrode diameter	0.61 m
Vent size	1.7 × 0.81 m^2

Figure 2-3: Geometry of the EAF model presented by Li et al.[19]

The model includes the fluid flow, the reversible oxidation of CO to CO_2, convective heat transfer and thermal radiation. In addition, the endothermic gas/solid and gas/liquid surface reaction of CO_2 to CO at the surface of the electrodes and the steel bath is considered in the simulation model using user subroutines. Furthermore the influence of air ingress from the slag door on the flow field and chemical reactions is investigated.

CO is defined to enter the flow field through the bottom flat surface and a total mass flow rate of 1.43 kg/s with a temperature of 298 K of O_2 is injected through four jets in the furnace wall. It is assumed that the wall and roof have a constant temperature of 1573 K (1300 °C) and the bottom surface, which represents the bath surface, is assumed to have a constant temperature of 1773 K (1500 °C). A zero heat flux is assumed at the electrode surfaces.

The aim of the model is to gain insights into the post-combustion using oxygen injectors. The results show, that thermal radiation, dissociation of CO_2, endothermic gas/solid and gas/liquid surface reactions of CO_2 to CO at the surface of the electrodes and bath have a significant effect on the temperature distribution. A comparison of the calculated post combustion with and without air ingress from the slag door led to the conclusion that for the investigated conditions air ingress has a detrimental effect on the post-combustion and should be minimized.

An attempt is made to compare the heat and mass transfer during oxygen injection that occurs during the flat-bath stage to that when a heap of cold scrap is present in the furnace. For this purpose an additional model was generated, in which the lowest surface of the model was adapted to represent the scrap. Around the electrodes a circular area with a diameter of 0.8 m represents the bath surface with a surface temperature of 1773 K (1500 °C). The scrap is modelled as a solid pile surrounding this central area, whereby its surface is defined to have a constant temperature of 873 K (600 °C). The results of this adapted model show that during the flat-bath stage most of the heat generated by the chemical reactions is transferred to the water cooled panels. The efficiency of the heat transfer within the furnace is much better when a pile of cold scrap is present.

Li et al. describe the challenges faced when simulating the chemical reactions. However, the simplified geometry and boundary conditions, for example the definition of fixed temperatures at the inner surfaces, limit the comparability of the results with the real EAF process.

Chan et al.[20] present a 3D model of an AC EAF freeboard for flat-bath conditions. The geometry is shown in **Figure 2-4**. It corresponds to that of an existing AC EAF and includes the furnace freeboard from the surface of the liquid steel bath (flat-bath-stage) to the exit out of the off-gas elbow. The electrodes, burners, roof-ring gap, 4^{th}-hole gap and slag door are all represented. The inside of the electrodes is not included.

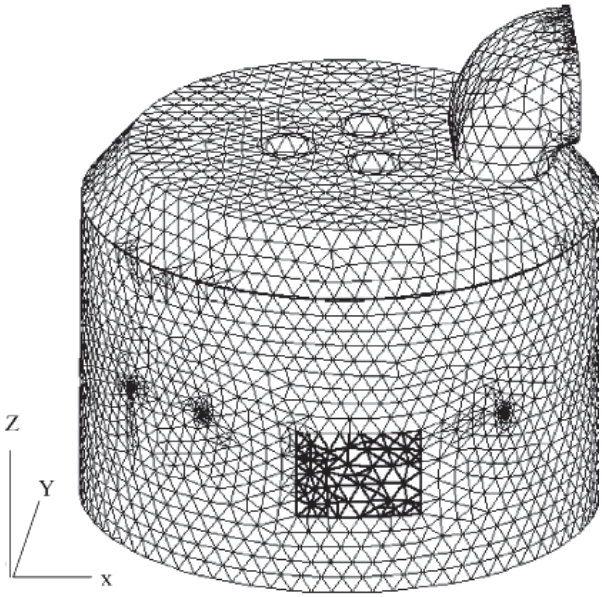

Figure 2-4: Geometry and mesh of the model presented by Chan et al.[20]

The model includes the fluid flow, combustion reactions, heat transfer (convection and thermal radiation), turbulence and NO_x formation. The combustion reactions are calculated using both, the eddy-dissipation concept and finite reaction rates for chemical kinetics, whereby seven species (CH_4, CO, CO_2, H_2, H_2O, O_2, N_2) and a four reaction reduced mechanism are used to simulate the combustion of CH_4 and CO. The NO_x formation is calculated using the extended Zeldovich thermal NO mechanism. The EAF is modeled as a quasi-steady state process.

The furnace wall and roof are defined to have a constant temperature of 1300 K (1027 °C) and the surfaces of the electrodes are assumed to be adiabatic. The bottom surface of the solution domain, representing the slag surface, is defined to be a source of CO, whereby the flow-rate is based on lance oxygen and carbon flow rates, and is defined to have a constant temperature of 1950 K (1677 °C). Air ingress through the slag door and roof-ring gap as well as the inflow of water vapor through the gaps around the electrodes is included.

The primary objective of the simulations is to identify the main mechanisms of NO_x formation and to analyze potential NO_x control strategies when burners and co-jets are in operation. The simulation results show the NO_x emission trends. Chan et al. describe the difficulties encountered in validating the simulation results, for example the lack of information concerning the amount of air ingress through the roof gap and slag door. A further reason for the difficulties could however be the simplified boundary conditions and fairly coarse mesh. Whereas the simplified model used by Li et al.[19] has 350 000 cells, the mesh used for the model shown in Figure 2-4 by Chan et al. has only 82 000 cells. The influence of the arc region with its high temperature zone on the NO_x formation is not investigated.

Henning et al.[21],[22] present a model for a DC arc furnace that includes the fluid flow in the furnace freeboard, as well as the electric arc region, slag, metal bath and different refractory regions.

As shown in **Figure 2-5**, the solution domain represents a 5° axisymmetric slice of the furnace vessel. It is divided into four regions, the arc and freeboard, slag bath, metal bath, and refractory lining. The different regions have a fixed geometry and are each separated by an interface which transfers information concerning electric current, magnetism, heat transfer, and shear forces.

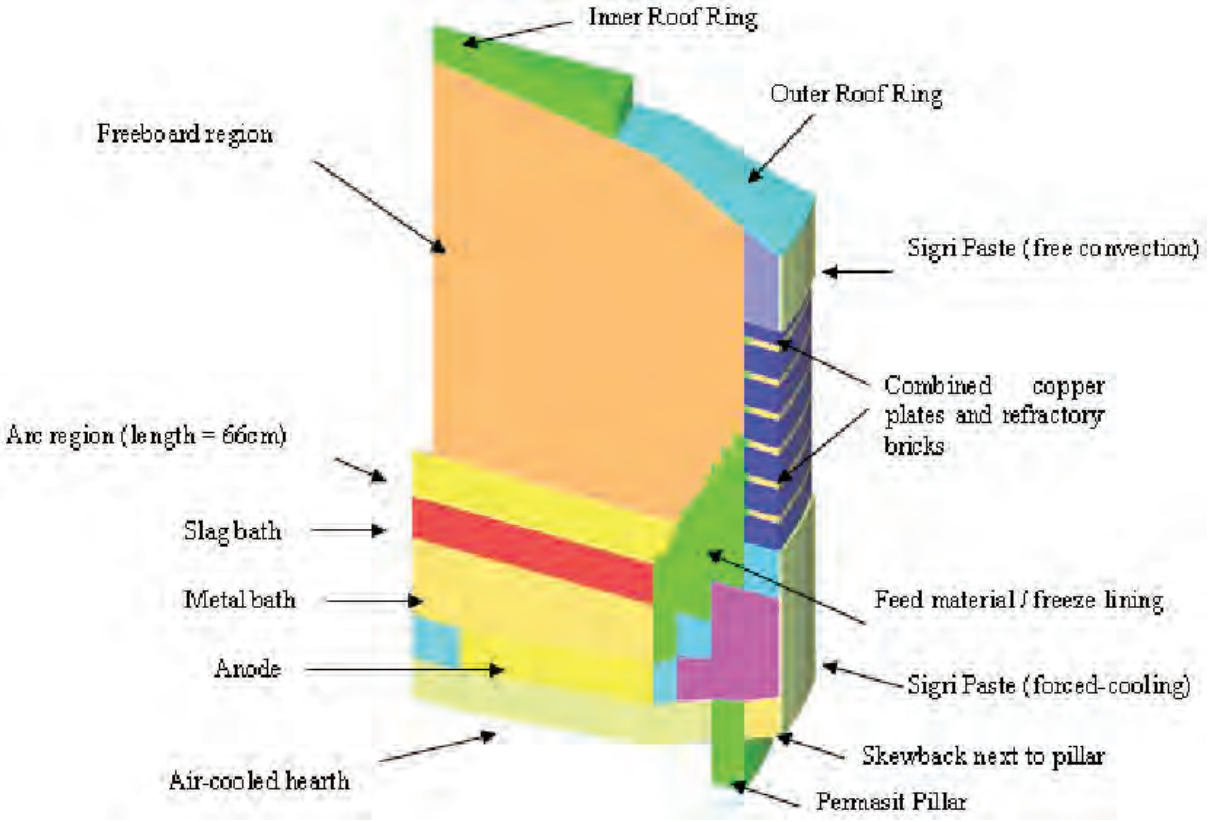

DC Furnace power	40 MW
Hearth diameter	9300 mm
Electrode diameter	610 mm
Arc length	660 mm

Figure 2-5: Solution domain of the model presented by Henning et al.[22]

The fields of electrical potential, electric current, magnetism, heat transfer and radiation are taken into account. The energy absorption processes, for example the metallurgical processes within the bath, are included using an energy absorption model. The gas inside the freeboard is considered to be air. Air ingress, off-gas outflow and the chemical reactions within the freeboard are not considered.

For the simulations the vertical electrode surface is initially defined with a fixed temperature and then later defined to be adiabatic. The electrode tip temperature is set to 4300 K (4027 °C). The outer surface of the vessel wall is defined to be cooled by either forced or natural convection as shown in Figure 2-5.

The aim of the model is to facilitate vessel design by enabling an accurate prediction of the heat fluxes through the walls. It is used to predict the temperature and velocity distributions in all fluid zones of the furnace simultaneously. The side wall heat fluxes are calculated for different arc lengths.

This is the only EAF furnace model that attempts to show the interaction between all fluid zones simultaneously. One of the most interesting results is the comparison, shown in **Table 2-1,** of the energy input defined for heat loss conditions (operating power = heat losses) as opposed to that defined when considering the process energy absorbed in the slag and bath region.

Table 2-1: Comparison of results obtained by Henning et al.[22]

Conditions	Electric current	Operating power	Heat losses	Energy absorption
Heat loss conditions	13 kA	5.71 MW	5.71 MW	-
Process energy absorption	53 kA	46 MW	7.03 MW	39 MW

The heat extracted by the process energy absorption model used by Henning et al. represents the energy absorbed by the endothermic reduction reactions within the slag layer and molten metal bath as well as the energy possibly needed to melt scrap still present in the bath. The necessary magnitude of the energy absorbed by the absorption model to achieve the target process temperature depends on the complex chemical reactions and heat transfer processes within the bath and slag layer.

If one uses the Channel Arc Model (CAM) [23] to represent the electric arc as a cylindrical surface extending from the electrode tip to the bath surface, then for a constant arc length $\ell_{arc,CAM} = 660\,mm$ the arc radius $r_{arc,CAM}$ for a specific arc current $I_{arc,elec}$ can be calculated using eq. (1).

$$j_{arc,CAM} = \frac{I_{arc,elec}}{\pi \cdot r_{arc,CAM}^2} \qquad (1)$$

For a mean electric arc current density $j_{arc,CAM} = 1\ kA/cm^2$ and an electric arc current of $I_{arc,elec} = 13\ kA$ an arc radius of $r_{arc,CAM} = 20\ mm$ results. For $I_{arc,elec} = 53\ kA$ one obtains $r_{arc,CAM} = 41\ mm$.

The calculated temperature profiles in the arc region in **Figure 2-6** clearly show that the higher electric current leads to an increase in the mean temperature of the arc column, which in turn increases the energy input into the solution domain. This is especially evident when considering the temperature distribution along the radius corresponding to the arc column according to the CAM for $\ell_{arc,CAM} = 660\,mm$. Henning et al.[22] explain that the calculated temperatures are over-predicted, as the model used does not take into account the heat absorbed by raw material as it falls through the freeboard and the effect of radiation attenuation due to dust particles within the freeboard.

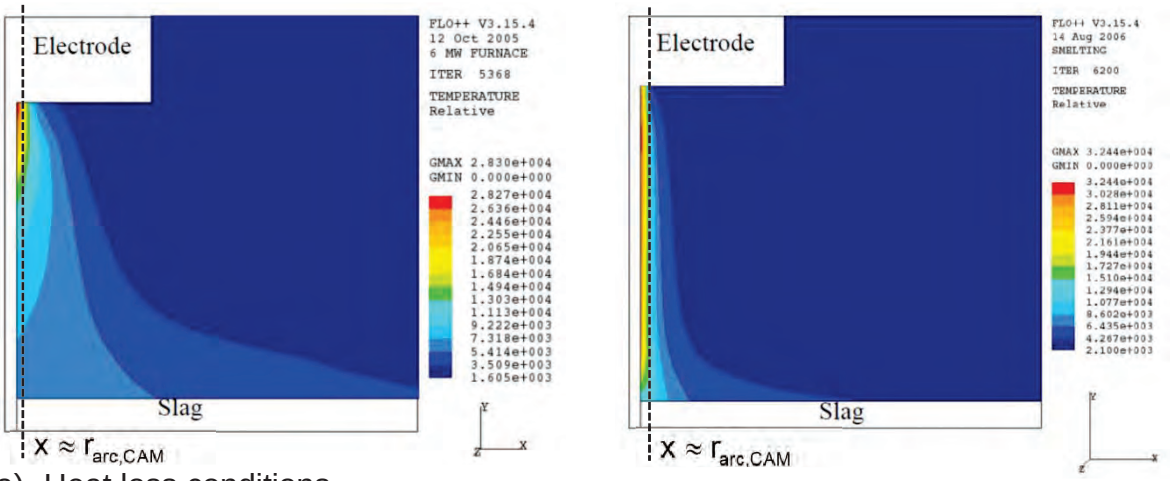

a) Heat loss conditions ($I_{arc,elec} = 13kA$)

b) Process energy absorption conditions ($I_{arc,elec} = 53kA$)

Figure 2-6: Calculated temperature distribution in the arc region by Henning et al.[22]

In **Figure 2-7** and **Figure 2-8** the interrelationship between temperature and velocity distribution which leads to a redistribution of the energy received by the respective neighboring layer can be seen. Due to the strong flow of the fluid leaving the DC plasma arc at the surface of the slag, a corresponding circulatory flow is induced not only in the slag region, but also in the bath. When considering the temperature distributions shown, it must be kept in mind that they correspond to the situation where a heat flux of 39 MW is being drawn out of the slag and metal bath.

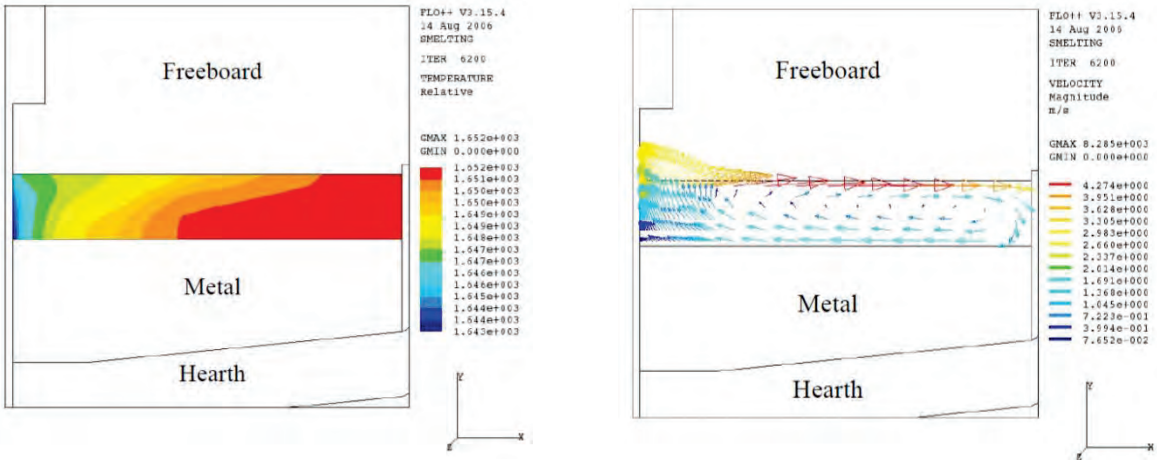

c) Temperature distribution in the slag region

d) Velocity distribution in the slag region

Figure 2-7: Slag temperature and velocity distribution for process energy absorption [22]

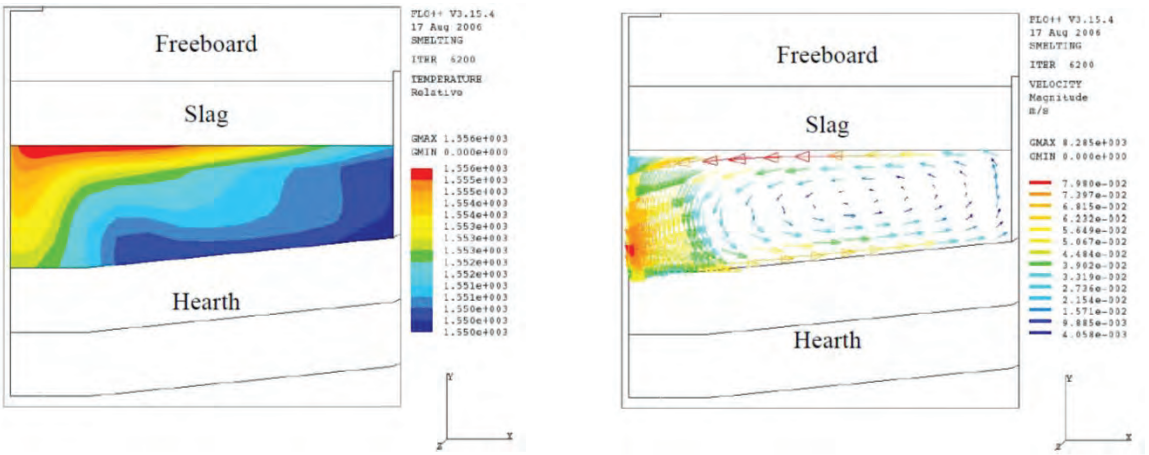

a) Temperature distribution in the bath region

b) Velocity distribution in the bath region

Figure 2-8: Bath temperature and velocity distributions for process energy absorption [22]

Al-Harbi et al.[24] present a 3D CFD numerical simulation model for an AC EAF. As can be seen in **Figure 2-9**, the inside of the electrodes and electric arc region are not included in the solution domain. The numerical mesh used for the simulations has approximately 600 000 cells.

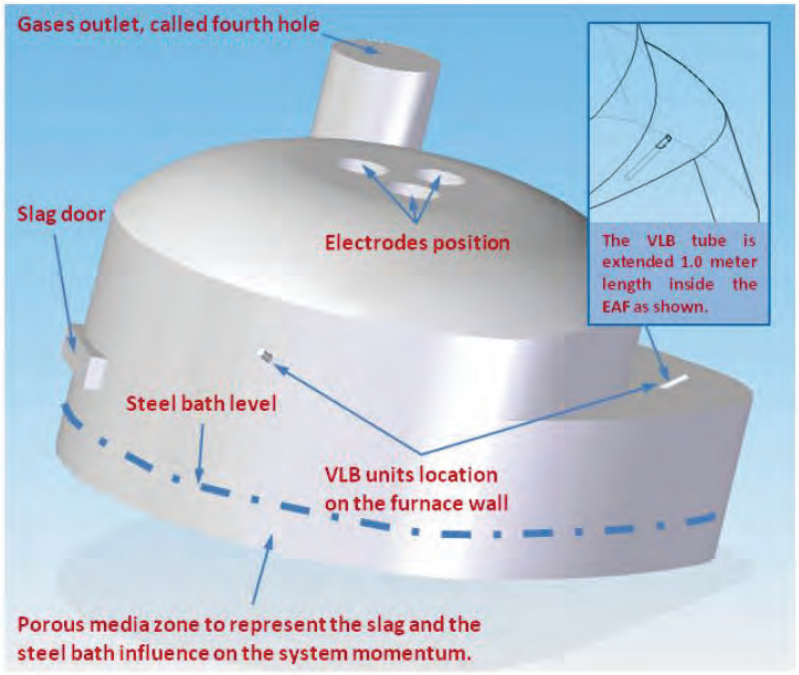

Figure 2-9: A sketch of the geometry of the model by Al-Harbi et al.[24]

The model includes the numerical simulation of the flow field, supersonic oxygen injection, convective heat transfer and thermal radiation. The gas inside the furnace freeboard is defined to be a CO/air species mixture. The decarburization of the steel bath is modeled by defining the bottom surface representing the bath surface as a source of CO. The chemical reactions taking place within the freeboard are not considered. A constant steel bath surface temperature of 1923 K (1650 °C) is

assumed and the water cooled side wall and roof temperatures are defined to be 333 K (60 °C). When the inner surface vessel temperatures calculated for example by Sanchez et al.[26] are considered, it is evident that assuming a uniform side wall and roof temperature of 60 °C is unrealistic.

The model was developed with the aim of investigating causes of low service life of the refractory of the Delta zone during supersonic oxygen injection. The simulations were carried out for two different furnace geometries. The main advantage of the model is the concept used to represent the CO source at the slag layer due to the decarburization of the melt. It is assumed that all the O_2 from the oxygen injection entering a porous layer defined at the slag surface of the model reacts to CO, which enters the solution domain with a temperature of 1923 K (1650 °C). This results in a more realistic inhomogeneous source of CO in comparison to the assumption of a homogenous source for the entire slag layer surface. It does however not take into account the penetration depth and redistribution of the reacting flow of O_2 within the melt. As the inside of the electrodes and electric arc region is not included in the solution domain, the thermal loading of the roof delta due to the reflected radiation from the electric arcs and from the arc region is not considered.

The transient nature of AC arcs necessitates modeling approaches such as that presented by Sanchez et al.[25]. They use the Channel Arc Model (CAM) to investigate the power delivery from the arc in an AC EAF for different gas atmospheres. In another related paper, Sanchez et al.[26] present a model that simulates the influence of the foamy slag height on the hot spot formation on the inside of water cooled panels of an AC EAF.

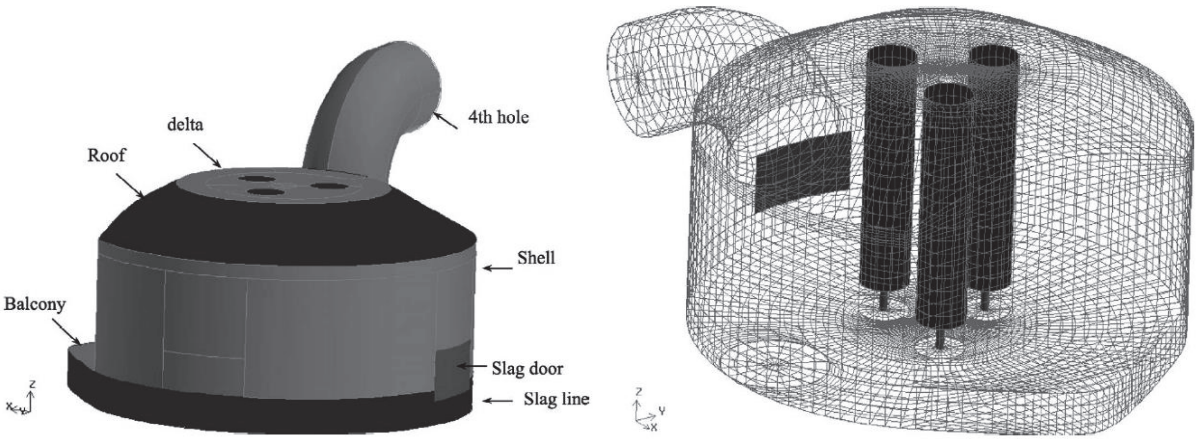

a) Geometry b) Computational domain

Nominal EAF capacity	210 tons
Total active power	120.6 MW
Thermal radiation energy input of the arcs (Heat loss conditions)	30.3 MW
Operating current	85 kA
Electrode diameter	711 mm
Arc length	450 mm

Figure 2-10: Model of an AC EAF presented by Sanchez et al.[26]

The Channel Arc Model (CAM), as presented in [25], is used to calculate the energy input from the electric arcs. These are represented by three cylinders from the tip of the electrodes to the steel bath as shown in **Figure 2-10**. The geometry corresponds to that of an existing industrial AC EAF. The solution domain represents the gas phase above the liquid bath. The insides of the electrodes are not part of the solution domain.

It is assumed, that there are only three energy dissipation modes taking place at the electric arcs: radiation $(P_{r,CAM})$, convection $(P_{conv,CAM})$ and electron flow $(P_{e,CAM})$. The equations given by Sanchez et al. to calculate the energy dissipated by each mode are:

$$P_{r,CAM} = \pi \cdot r_{arc,CAM}^2 \cdot \ell_{arc,CAM} \cdot u_{rad,arc} \quad (2)$$

$$P_{conv,CAM} = \pi \cdot r_{arc,CAM}^2 \cdot \rho_{DC} \cdot \bar{v}_{arc,CAM} \cdot (h_{arc} - h_F) \quad (3)$$

$$P_{e,CAM} = I_{arc,elec} \cdot \left[O_{an} + \frac{5 \cdot k_B \cdot T_{arc}}{2 \cdot e} + U_{an} \right] \quad (4)$$

e	Electron charge, in Coulomb
h_{arc}	Arc specific enthalpy (CAM), in J/kg
h_F	Specific enthalpy of gas surrounding arc (CAM), in J/kg
$I_{arc,elec}$	Electric arc current, in Ampere
k_B	Boltzmann's constant, in J/K
$\ell_{arc,CAM}$	Arc length according to CAM, in m
O_{an}	Work function for the anode, in Volt
$r_{arc,CAM}$	Arc radius according to CAM, in m
T_{arc}	Arc temperature (CAM), in K
U_{an}	Anode drop voltage, in Volt
$u_{rad,arc}$	Arc radiation density, in W/m^3
$\bar{v}_{arc,CAM}$	Average gas velocity of arc (CAM), in m/s
ρ_{DC}	Density of a DC arc, in kg/m^3

According to Sanchez et al. for the maximum voltage of 1210 V and an arc length of 450 mm, the CAM predicts a total power delivery of $P_{r,CAM} + P_{conv,CAM} + P_{e,CAM}$ = 120.6 MW. The corresponding thermal radiation input $P_{r,CAM}$ = 30.3 MW. The energy input of the arcs into the solution domain was defined as a function of the slag height. In other words, leaving the geometry unchanged, the amount of heat radiated from the arc region into the freeboard was varied in the range of 0 MW (slag height = arc length) to 30.3 MW (slag height = 0 mm).

The commercial CFD software FLUENT 6.2.1.6 was used to carry out the numerical simulations. In order to compute the thermal radiation exchange between the inner surfaces, the discrete ordinated (DO) radiation model available in FLUENT was

selected. It is assumed that the off-gas consists only of air, so that absorption of the thermal radiation of the off-gas components is not included in the simulation. The CO entering the freeboard due to the decarburization of the melt is modelled by an air flow out of the bottom flat surface of 3.383 kg/s with a temperature of 1950 K (1677 °C). A constant heat flux is defined at the relevant inner surfaces of the furnace freeboard and a constant temperature profile is defined at the surface of the electrodes. The steady state numerical simulations do not include the chemical reactions within the off-gas.

The results clearly show the influence of the uncovered arc length on hot spot formation on the furnace shell. In **Figure 2-11** the temperature distribution calculated by Sanchez et al. with the model for the case where the slag height is half of the arc length is compared to that when the arc is totally free-burning and the slag height is equal to zero. For a slag layer height of h_{slag} = 0 mm the hot spot temperatures clearly exceed the maximum allowable operating temperature for the surface of the cooling panels of approximately 1800 K [26].

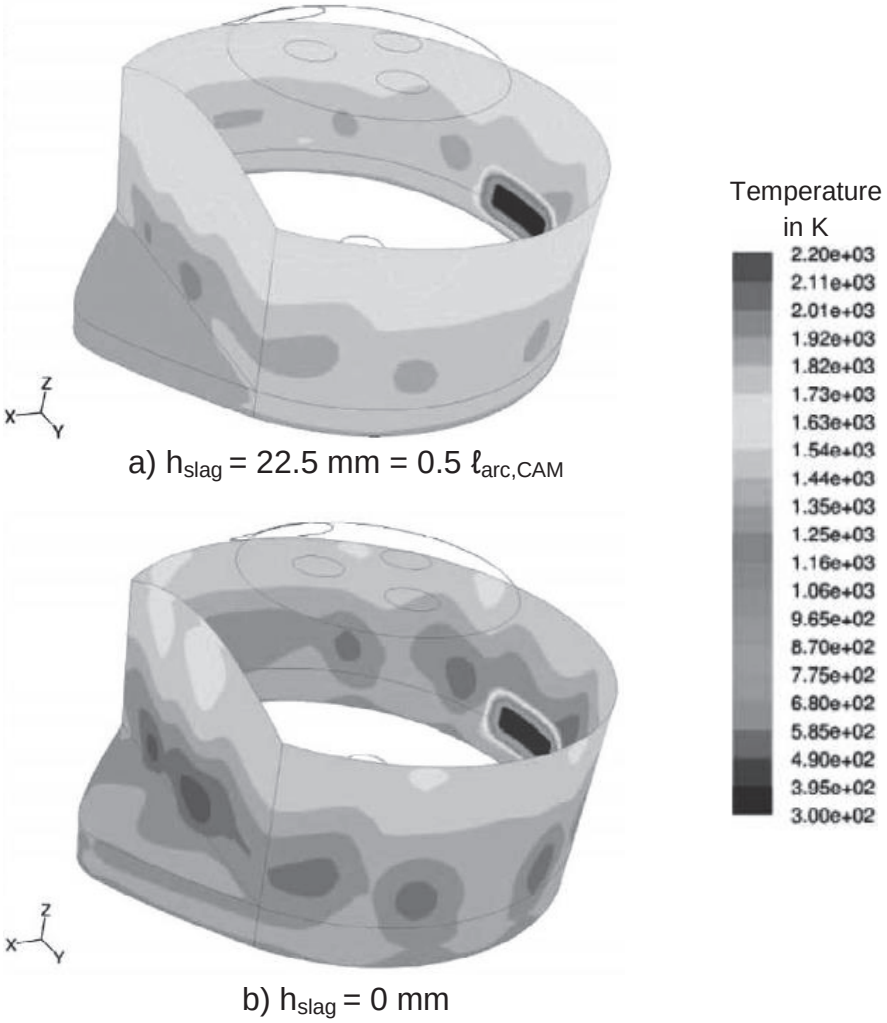

a) h_{slag} = 22.5 mm = 0.5 $\ell_{arc,CAM}$

b) h_{slag} = 0 mm

Figure 2-11: Temperature distribution for $h_{slag} = 0.5 \cdot \ell_{arc,CAM}$ and $h_{slag} = 0.5$ mm [26]

The aim of the simulations carried out by Sanchez et al. was to investigate the influence of the foamy slag height on the hot spot formation. The solution domain of

the presented model does however not include the inside of the electrodes and does not extend below the liquid slag surface. Therefore the effect of the redistribution of the thermal radiation absorbed by the electrodes and by the bath is not reflected in the results. Furthermore the chemical reactions within the off-gas and corresponding increase in the vessel gas temperature are not considered, as the gas inside the furnace is modeled to be air.

Most significantly, in reality the thermal radiation is a function of the local absolute thermal radiation intensity and the view factors. The simulated homogenization of the incident radiation on the walls for larger slag layer heights, reflected by the more homogenous temperature distribution obtained for a slag height of 22.5 mm in comparison to a height of 0 mm (see Figure 2-11), is caused by the fact that the geometry is not adapted to model the different slag heights. Therefore this effect is not realistic. Instead it is caused by the method used to include the effect of a change in slag height.

As explained in section 1.2, the objective of this thesis is the development of a numerical model of the heat and mass transport in an EAF freeboard. Results of the first version of this model are presented in the CONOX report by Pfeifer et al.[5]. The geometry of the model is shown in **Figure 2-12**.

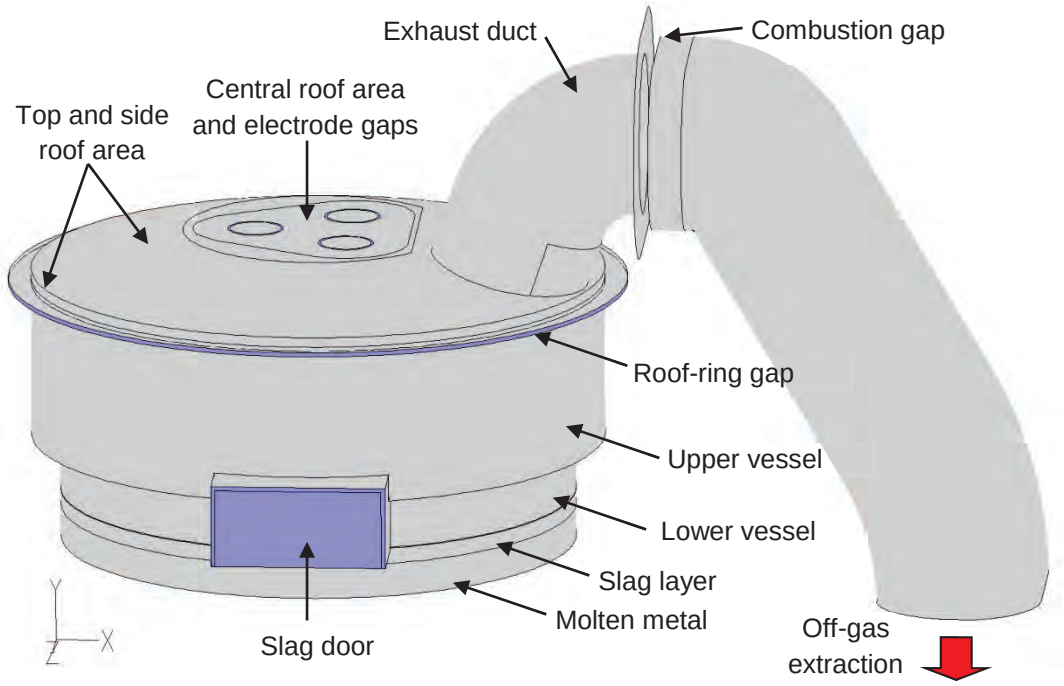

AC Furnace capacity	120 t to 140 t
Internal diameter	6.9 m
Electrode diameter	0.61 m

Figure 2-12: Geometry of the model presented by Pfeifer et al.[5]

The geometry corresponds to that of an existing industrial AC EAF. The solution domain represents not only the gas phase above the liquid bath; it also includes the post-combustion downstream of the air inflow at the post-combustion gap.

The slag layer and the top layer of the bath are included in the solution domain as solid layers in order to simulate a temperature distribution at the surface of the slag layer in dependence of the radiation from the arc region. The inside of the electrodes and the plasma arc columns are not part of the solution domain.

The arc region is modeled based on the channel arc model (CAM), which is described in section 2.2. The electric arcs are represented by three cylinders which extend to the bath surface, whereby a slag layer surrounds two thirds of the arcs, **Figure 2-13**.

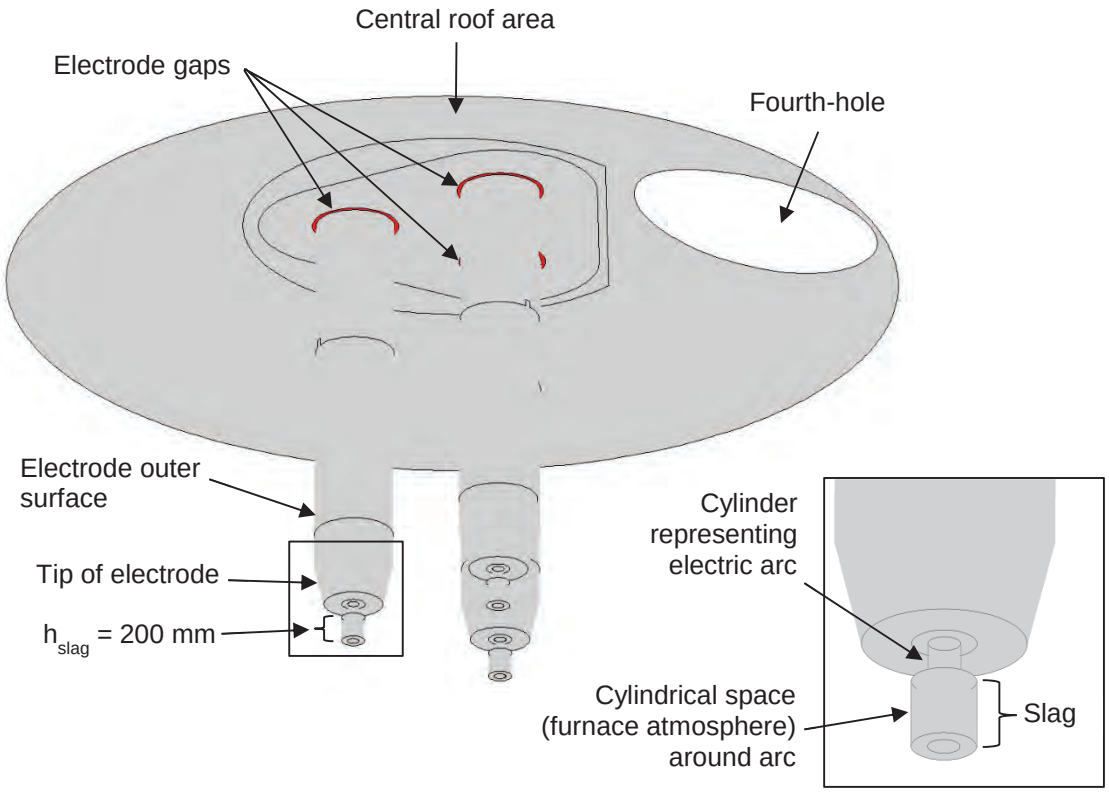

Figure 2-13: Details of the inner geometry of the model presented by Pfeifer et al.[5]

In order to solve the flow field and heat and mass transfer the numerical model was split into two parts. As shown in **Figure 2-14**, the solution domain of Model 1 represents the EAF furnace freeboard. Model 2 includes the off-gas elbow, combustion gap and a section of the off-gas extraction. The two were linked, by first calculating the conditions in the freeboard using Model 1. Afterwards the calculated temperature, velocity and mass fractions distribution at the outlet were defined as the boundary conditions for the inflow into Model 2. The inflow region of the post combustion gap is defined as a pressure outlet.

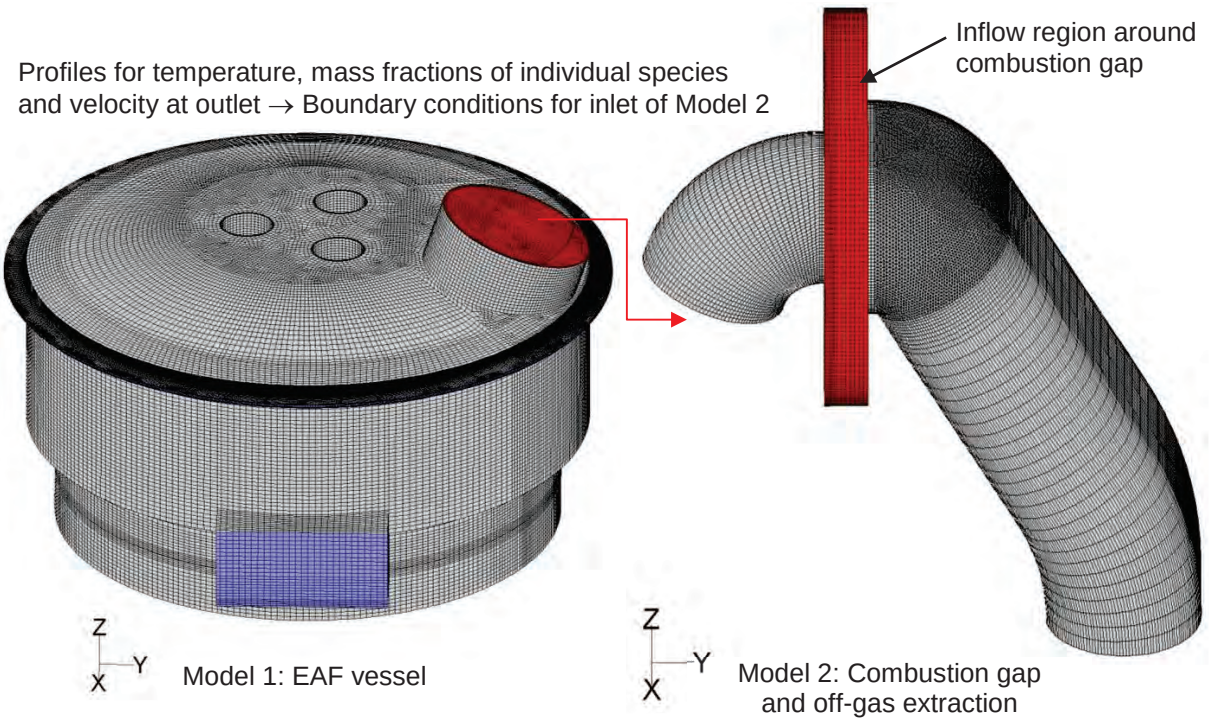

Figure 2-14: Discretised geometry of the numerical model of the EAF [5]

The commercial CFD software FLUENT 12.1.4 was used to carry out the numerical simulations. The gas inside the furnace is defined to consist of the species O_2, N_2, H_2O, CO, CO_2 and NO. The post combustion of CO to CO_2 as well as the reverse reaction is activated in the model. In addition the formation of thermal NO_X according to the extended Zeldovich thermal NO mechanism is calculated. The thermal radiation exchange between the surfaces is modelled using the Discrete Ordinates model, whereby the influence of the absorption of thermal radiation by the species such as CO, CO_2 and H_2O is activated. The influence of a variation of the amount of air ingress at the slag door, roof ring gap and electrode gaps is investigated using the model.

During the state considered, no oxygen injection is taking place, no burners are in operation and the time interval being considered is at the end of the process, when most of the carbon has already been removed from the molten metal. As the electrodes are not part of the solution domain, an adapted temperature profile is defined on the outer electrode surfaces. Similarly, an adapted temperature profile based on the calculations of Ramirez-Argáez et al.[27] is defined at the cylindrical surfaces representing the electric arcs. The temperature at the bottom surface of the solution domain is set to 1873 K (1600 °C).

The only source of CO of in total 0.74 kg/s within the solution domain is defined at the electrode surfaces. This represents the CO entering the flow field due to electrode consumption. A corresponding sink of O_2, calculated based on the stoichiometric coefficients of the reaction of C with O_2 to CO, is also defined. Examples of the simulation results are shown in **Figure 2-15** and **Figure 2-16**.

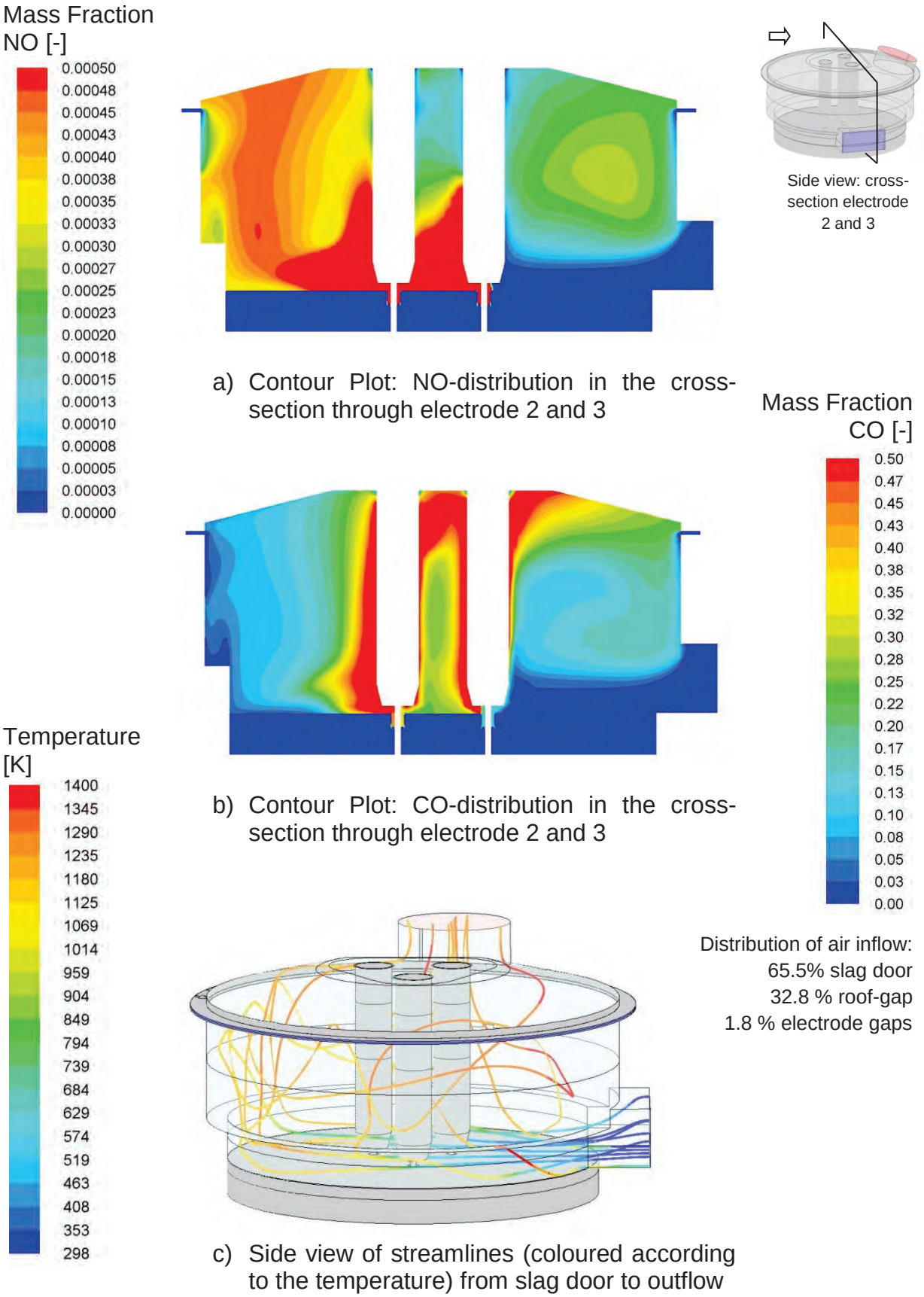

a) Contour Plot: NO-distribution in the cross-section through electrode 2 and 3

b) Contour Plot: CO-distribution in the cross-section through electrode 2 and 3

c) Side view of streamlines (coloured according to the temperature) from slag door to outflow

Figure 2-15: Results obtained with Model 1 [5]

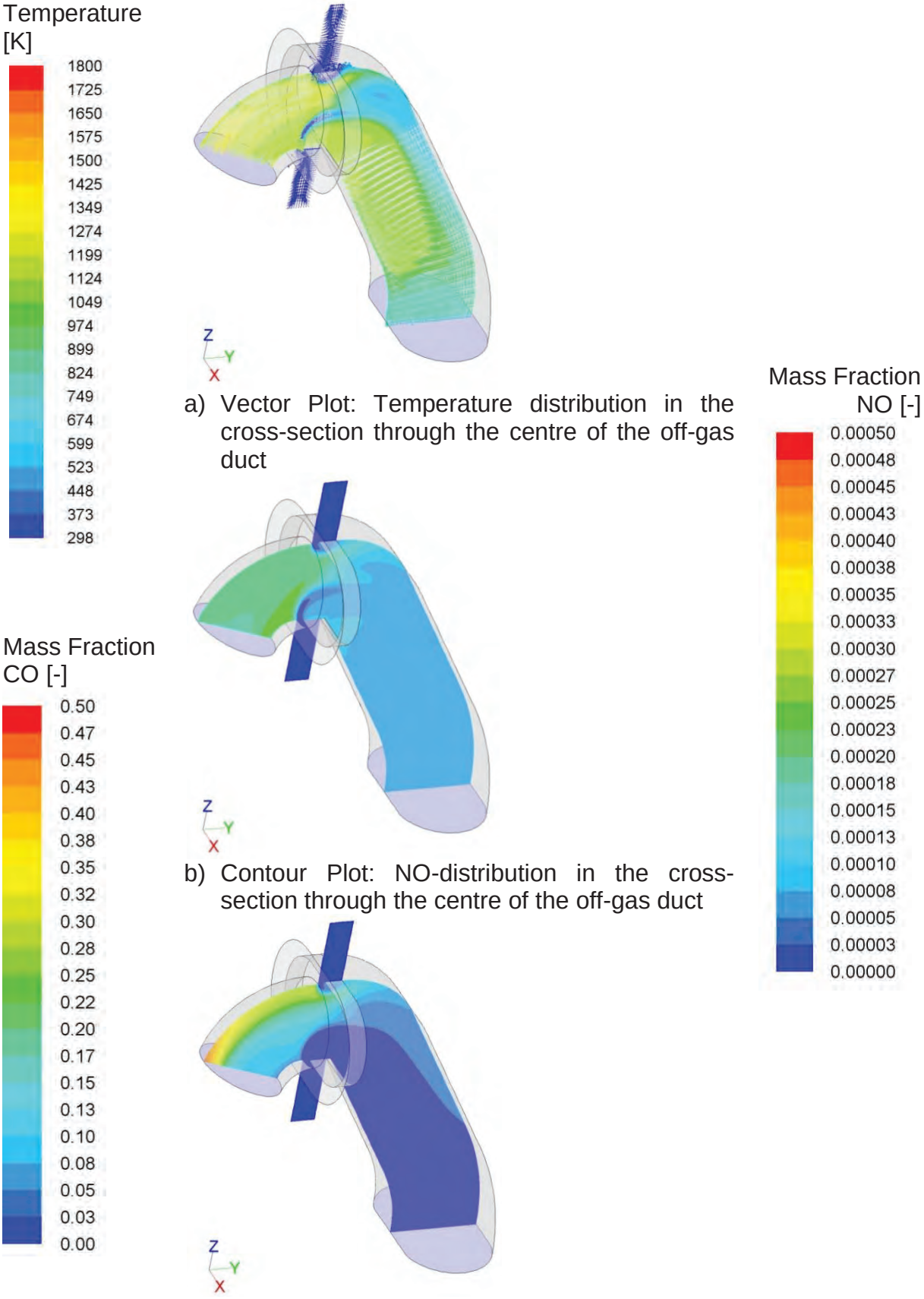

a) Vector Plot: Temperature distribution in the cross-section through the centre of the off-gas duct

b) Contour Plot: NO-distribution in the cross-section through the centre of the off-gas duct

c) Contour Plot: CO-distribution in the cross-section through the centre of the off-gas duct

Figure 2-16: Results obtained with Model 2 [5]

In Figure 2-15 a) the significance of the high temperatures in the arc region on the thermal NO_x formation is evident. In Figure 2-15 b) the effect of the CO source at the electrode surfaces on the CO mass fraction distribution can be seen.

One of the disadvantages of spitting the solution domain into two parts and carrying out the simulations in series is that the influence of the inflowing air and combustion at the post-combustion gap on the residence time of the air inside the freeboard is not reflected by the results. One of the advantages is that the geometry of Model 2 includes an inflow region around the post-combustion gap, which is defined as a pressure outlet. As a result, as shown in Figure 2-16, the amount of air drawn in depends on the calculated flow within the off-gas channel and is not uniformly distributed around the circumference.

The aim of the simulations was to identify the main sources of NO_x formation and investigate the influence of a variation in the amount of air ingress on the amount of NO_x in the off-gas. It was found that even though the heat and mass transfer, post-combustion and formation of thermal NO_x for the conditions considered could be qualitatively simulated with the model, the calculated off-gas composition does not correspond to that measured at the industrial EAF. Pfeifer et al. concluded that the main reason for this is the large uncertainty of the boundary conditions.

In retrospect the difference could also be due to the fact, that the modeling of the plasma arc region is not detailed enough. As will be shown later, the motion of the plasma jets increases the mixing rate of the species within the freeboard and thereby leads to an increase in the post-combustion.

Summarizing, the above described models where generated for different purposes. As a result the researchers concentrated on different aspects of the heat and mass flow within an EAF. When considering the objectives of the model developed during this thesis (refer to section 1.2), the following needs to be further addressed in order to improve the comparability of results obtained with the real process.

(i) The models described above include the electrode surfaces in their solution domain. Theses surfaces are either assumed to be adiabatic, have a constant temperature or a constant temperature profile is defined along the length of the electrodes. Not one of them includes the graphite electrodes themselves in their solution domain. This means that the results do not take the redistribution of heat along the length of the graphite electrodes, which have thermal conductivity of approximately 240 W/(m·K), into account.

(ii) With the exception of the model of Henning et al.[22], the solution domains of the models above do not include the circulation within the slag layer and bath. Therefore they do not include the effect of the redistribution of energy flows caused by the fluid flow, energy sources and energy sinks within the bath and slag layer. The model of Henning et al. is also the only model, with which the amount of energy absorbed within the melt and bath was investigated. During the course of this thesis it was found that in order to be able to truly compare the electrical energy input to the simulated energy flows within an EAF this topic is of great importance.

(iii) Only three models include the arc region. The simulation model of Sanchez et al.[26] concentrates on the effect of the thermal radiation from the arcs on hot spot formation. The other heat transfer mechanisms of the arc region are not included. This is also true for the model of Pfeifer et al.[5], which also does not include for example the effect of the momentum of the plasma jets on the flow field or the energy contribution due to the heating of the gas drawn into and flowing out of the arc region. Only the model of Henning et al.[22], which represents a rotationally symmetric 5° slice of the freeboard of a DC EAF, includes a more detailed modeling of the electric arcs and their effect on the flow field in the freeboard.

(iv) Due to the extreme conditions within the furnace, measurements of the temperature and off-gas composition done in the gap between the elbow and the exhaust duct are needed to validate the chemical reaction scheme chosen in order to simulate the post-combustion within the vessel. Nevertheless, only the model of Pfeifer et al.[5] includes the post-combustion gap.

2.2 Electric arc models

In this section an impression of the development and present state of research concentrating on the mathematical modeling of electric arcs is given. The magneto-fluid dynamic models include a detailed description of individual heat transfer mechanisms taking place in the arc. In contrast, the channel arc model (CAM) is a method with which a time averaged representation of the arcs can be implemented within a model of an entire EAF freeboard, for example as done by Sanchez et al.[26] and Pfeifer et al.[5]. The black-box models are used primarily to represent the electric arcs as an element within a model of the electric circuit of an EAF and could also be a useful tool when developing new ways to represent the arc region within a model of the entire EAF freeboard.

2.2.1 Magneto- fluid dynamic models

Qian et al.[28] present the results of a mathematical model of the arc region. The computational domain of the two-dimensional model, which is schematically shown in **Figure 2-17**, consists of the region between the bottom of the electrode (cathode) and the flat surface of the metal bath (anode). The cathode has a diameter of 250 mm. The distance between the centre of the arc and the border of the solution domain *(ef)* is 250 mm.

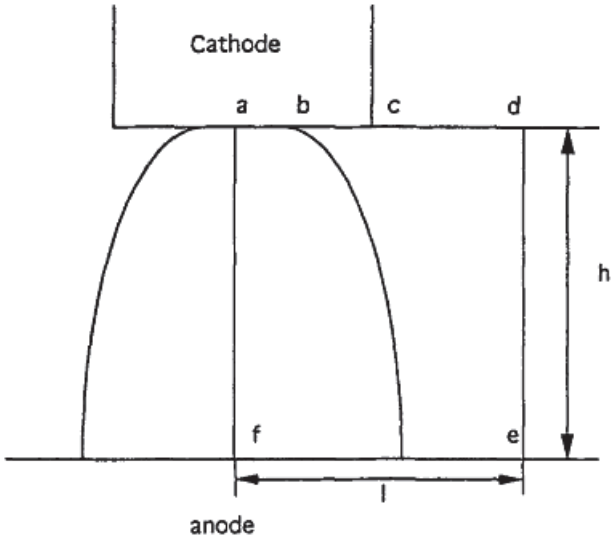

Figure 2-17: Computational domain of the model of Qian et al.[28]

The arc is assumed to be radially symmetric, steady state and in a state of local thermodynamic equilibrium (LTE). The plasma is assumed to be optically thin and neither the effects of metal vapor or the deformation of the bath surface are considered. The relevant equations of conservation of mass, momentum and energy are solved together with the Maxwell equations of the electromagnetic field to calculate the resulting flow and temperature distribution in the plasma region.

Boundary conditions are defined on the borders of the solution domain. The flow velocity is set to equal to zero at *ac* and *fe*. *cd* is defined to have a temperature of 500 K (227 °C) and the axial velocity component here is defined to be equal to zero. Therefore in- and outflow takes place at *de*. It is assumed, that the radial gradients of all variables at *de* are equal to zero. At the bath surface *ef* a constant electric potential ϕ_{elec}, and a constant temperature of 1800 K (1527 °C) is defined. At the cathode spot, surface *ab*, a temperature of 4300 K (4027 °C) and a parabolic electric current distribution according to eq. (5) are assumed. The cathode spot radius is calculated using eq. (6). A value of $4.4 \cdot 10^7$ A/m^2 is used for $j_{cathode}$. *bc* is defined to be adiabatic, in other words the temperature gradient there is equal to zero. For the cathode the boundary condition for the electric potential is approximated using eq. (7).

$$j = 2 \cdot j_{cathode} \cdot \left[1 - \left(\frac{r}{r_{cathode}} \right)^2 \right] \tag{5}$$

$$r_{cathode} = \frac{I_{elec}}{\sqrt{\pi \cdot j_{cathode}}} \tag{6}$$

$$\frac{\partial \phi_{elec}}{\partial z} = \frac{-j}{\sigma_{elec}} \tag{7}$$

$I_{arc,elec}$ Electric arc current, in A

j	Electric current density, in A/m^2
$j_{cathode}$	Average cathode current density, in A/m^2
r	Radius, in m
$r_{cathode}$	Cathode spot radius, in m
ϕ_{elec}	Electric potential, in V
σ_{elec}	Electrical conductivity, in A/(V m)

The electrical conductivity σ_{elec} is considered as a function of temperature and the cathode current is normal to the cathode surface.

Four heat transfer mechanisms are taken into account at the anode surface:

1. Thermal radiation from the plasma.
2. The condensation heat flux, which is a heat source due to the electrons crossing the anode fall potential and entering the anode surface.
3. The transport of thermal energy by the electrons (Thomson Effect)
4. Convection due to the flow of hot plasma at the surface

The equations and boundary conditions were solved using a control-volume-based finite difference approach, whereby the solution procedure was based on the SIMPLE algorithm.

Figure 2-18 shows an example of the temperature and velocity field calculated by Qian et al. using the model presented in [28]. The model does not require an assumption or empirical estimates of the arc shape, as the shape is a result of the model calculations.

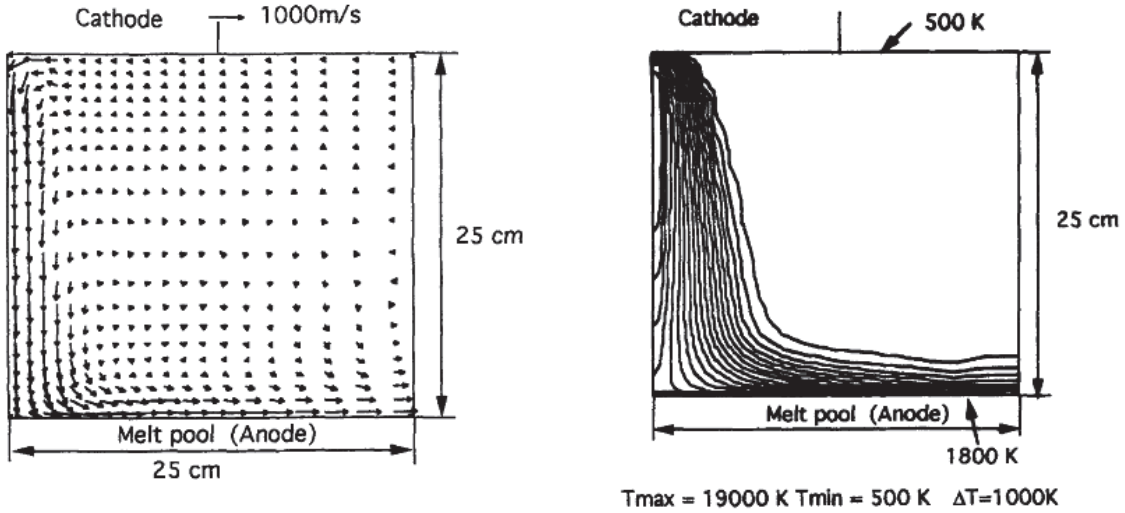

a) Velocity distribution

b) Temperature contours

Figure 2-18: Velocity and temperature distribution for a current of I_{elec} = 50 kA and an arc length of $\ell_{arc} = 250$ mm [28]

The aim of the model development was to obtain a qualitative comparison of the relevance of the four heat transfer mechanisms from the DC arc to the anode, which in this case is the melt pool surface. The calculated radial distributions of these heat transfer components to the anode are shown in **Figure 2-19**.

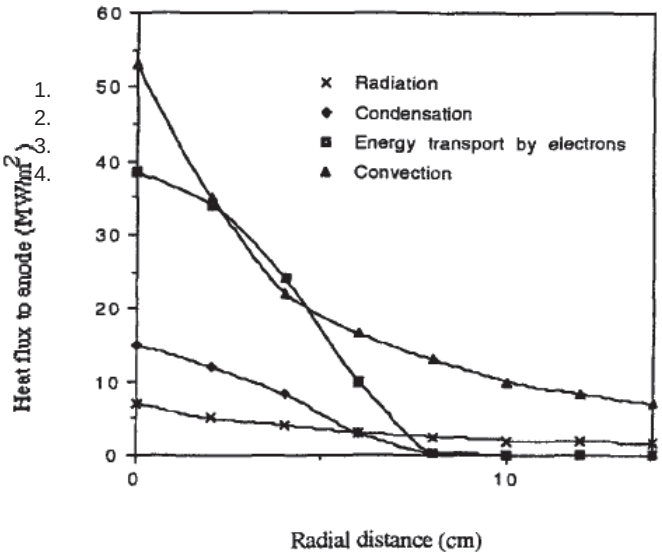

Figure 2-19: Radial distribution of the heat transfer mechanisms to the anode surface for I_{elec} = 50 kA and an arc length of $\ell_{arc} = 250$ mm [28]

In **Table 2-2** the total arc power due to Joule heating in the solution domain ($P_{arc,Joule}$), the total heat flow at the anode surface ($\dot{Q}_{total,anode}$) and the efficiency of the arc obtained with these two values is shown. It was found that using this model the total arc power increases with arc length for a constant electric current. The total heat flow to the anode surface is however seen to be almost independent of the arc length. When one considers the efficiency of the arc, then it becomes clear that the fraction of the joule heat transferred to the anode surface increases for a decrease in arc length.

Table 2-2: Comparison of total Joule heating of the arc and heat transferred at the anode surface [28]

Current/Arc length	$P_{arc,Joule}$ [MW]	$\dot{Q}_{total,anode}$ [MW]	$\dot{Q}_{total,anode}$ / $P_{arc,Joule}$ [%]
50 kA / 250 mm	20.7	5.6	27
50 kA / 150 mm	15.5	5.7	37
60 kA / 250 mm	24.6	7.0	28
60 kA / 150 mm	18.6	7.1	38

When interpreting these results it must always be kept in mind that they correspond to the boundary conditions defined for the model. For example the calculated heat transferred by convection to the anode surface is of course dependent on the constant temperature of 1800 K defined at the anode surface. In reality, the temperature depends on the heat transfer processes and convection taking place in the bath, for example as calculated by Henning et al.[22] .

The model of a DC-plasma arc presented by Alexis et al.[29] was developed to predict heat transfer, electric current density and shear stresses at the lower boundary surface representing the steel bath surface. This information was then used to define boundary conditions for a model used to simulate the fluid flow, heat transfer and electric phenomena in the bath of a DC EAF [30].

The solution domain of the model is shown in **Figure 2-20**. It extends slightly further than that of Qian et al.. The distance from the center of the electrode to the boundary *ef* is 500 mm and the solution domain extends 50 mm upwards from the tip of the simplified electrode geometry. The electrode has a diameter of 160 mm.

In the model presented the arc is treated as a fluid. The thermodynamic properties for air are temperature dependent. It is assumed that the arc is axisymmetric, steady state and in local thermal equilibrium. The effects of metal or graphite vaporization as well as the slag and molten metal surface shape around the impingement area of the arc are not considered in the model. A simplified form of the Maxwell's equations to describe the electric current and magnetic field is used (MHD Approximation[29]). These are solved together with the coupled conservation equations of mass, energy and momentum for cylindrical coordinates. Gravity is not taken into account. The Lorentz force components resulting from the electric field and the induced magnetic field are included in the conservation equations of momentum. The energy conservation equation includes not only the convective and diffusive terms, but also terms for the Joule heating and a thermal radiation source. It also includes a term to take the enthalpy transported due to electron drift (Thompson effect) into account.

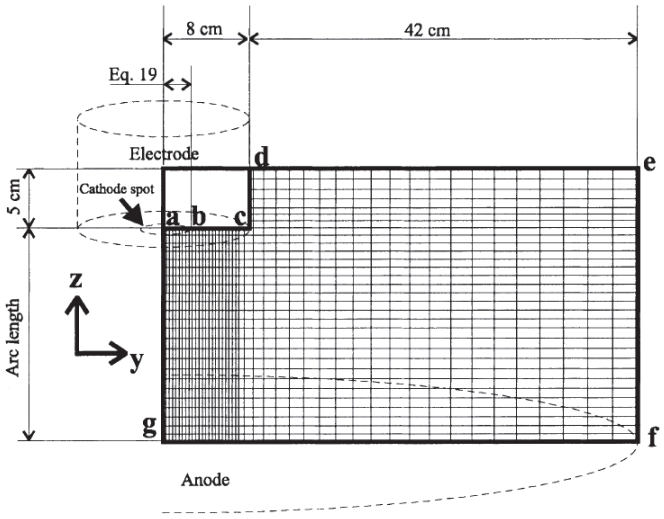

Figure 2-20: Calculation grid of the model presented by Alexis et al.[29]

The boundaries *de* and *ef* shown in Figure 2-20 are defined to be at atmospheric pressure allowing the entrainment or outflow of fluid. The boundaries *bc* and *cd* as well as the surface of the anode *gf* are defined to have a temperature of 1800 K (1527 °C). The temperature at the cathode spot *ab* is defined to be 4000 K (3727 °C). The numerical simulations were carried out using the commercial code PHOENICS.

The treatment of the heat transfer at the cathode spot and anode is especially of interest. As for the model of Qian et al.[28], the electric current density is assumed to be a parabolic function of the radius (see eq. (5) and (6)) and the electric potential is assumed to be zero at the anode surface *fg*. As far as the electric potential calculation is concerned, all other boundaries are treated as symmetry lines. Directly at the cathode, local thermal equilibrium (LTE) is not valid. The energy used to ionize the plasma, leading to a corresponding drop in electrical potential at the cathode, is modeled using an energy source dependent on the cathode electric current density and the cathode fall voltage. At the anode surface the same four heat transfer mechanisms as those analyzed by Qian et al. are considered.

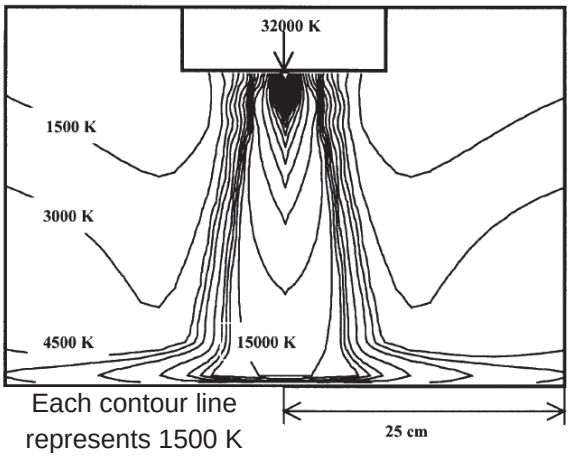

Figure 2-21: Temperature contours determined by Alexis et al.[29] for I_{elec} = 36 kA and an arc length of $\ell_{arc} = 25$ cm

In **Figure 2-21** the temperature isolines for an arc current of 36 kA and an arc length of 250 mm are shown. Due to the different boundary conditions the shape of the contours calculated differs from those of Qian et al. shown in Figure 2-18. This is due to the fact that Qian et al. define the temperature at the sides of the solution domain, where fluid flows into the region, to be 500 K (227 °C). In contrast, Alexis et al. define the gradient of the enthalpy ∂h/∂z at the horizontal border *de* and ∂h/∂r at the vertical border *ef* to be equal to zero. As a result, the model of Alexis et al. results in higher temperatures within the plasma column.

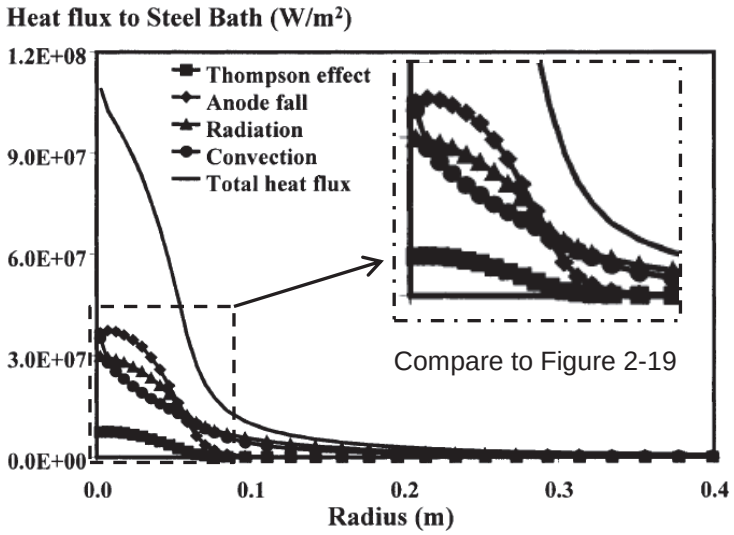

Figure 2-22: Heat transfer mechanisms for an arc current of 36 kA and an arc length of 250 mm calculated by Alexis et al.[29]

By comparing the magnitude of the four different heat transfer mechanisms Alexis et al. come to the conclusion, that for the range of conditions assumed the heat transfer at the anode is dominated by convection and thermal radiation. The contribution of thermal radiation to the total heat transferred at the anode at each respective radius calculated by Alexis et al. (**Figure 2-22**) is larger than that determined by Quian et al. (Figure 2-19) even though the same equation is used. As the same temperature of 1800 K (1527 °C) is assumed at the anode surface, this larger thermal radiation contribution is due to the higher temperatures calculated by Alexis et al. in the plasma column. Whereas for an arc length of 250 mm and an arc current of 50 kA Quian et al. obtain a maximum temperature of 19000 K, Alexis et al. obtain a maximum temperature of 32000 K for the same arc length and an arc current of 36 kA. The contribution of each heat mechanisms will however in reality deviate from those calculated here, depending on the true temperature of the bath close to the impingement area.

Ramirez-Argáez et al.[27] continue the work of Alexis et al. by using the DC arc model to investigate the influence of different atmospheres on the characteristics of the DC arc.

Lago et al.[31] present a DC arc model similar to those previously described. In this model the presence of metal vapour in the plasma gas due to anode erosion is considered. Whereas the subject of the previous models was a DC arc in an electric arc furnace, in this case a free-burning arc between a tungsten electrode and different solid anode materials is investigated. In the case of the EAF the anode surface represents the surface of the molten steel bath with a temperature of approximately 1800 K (1527 °C). Here one has a solid anode with a welding pool in the impingement region of the arc. Whereas for the EAF one has electric currents of between 36 kA and 60 kA with correspondingly long arc lengths between 150 mm

and 300 mm, in this case we have electric currents of 200 A with an arc length of 10 mm.

Blais et al.[32] present a three-dimensional numerical model to simulate the magnetic deflection of an argon DC arc for an electric current of 200 A. First the axisymmetric case without deflection is calculated. Then these results are validated by comparing them to measurements. Thereafter a three-dimensional version of the model is used to calculate the deflection.

The advantage of the setup considered by Lago et al. and Blais et al. in comparison to an electric arc in an EAF is that measurement data exists with which the numerical simulation results can be validated. These two models will however not be described in detail here, due to the assumptions or boundary conditions chosen at the anode surface. Whereas Lago et al. partially neglect the thermal radiation contribution for the calculations where metal vapour is present; Blais et al. consider the anode surface to be adiabatic.

Tarczynski et al.[33]-[35] present a model with which an AC discharge between two electrodes in air is simulated. The geometry of the solution domain is shown in **Figure 2-23**. The areas E_1 and E_2 represent the tips of the two electrodes. D_1 and D_2 represent the sides of the electrodes. Areas A, B and C are the external boundaries of the solution domain.

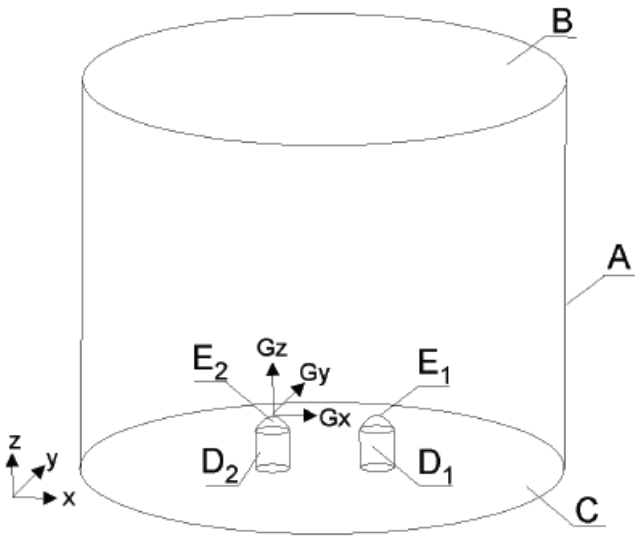

Figure 2-23: Geometry of the model by Tarczynski et al.[33]

Similarly to the models of Qian et al.[28] and Alexis et al.[29] the conservation equations of mass, momentum and energy are solved together with electro dynamic field equations. In this case the numerical simulations where carried out with the commercial CFD software FLUENT. The additional mathematical models needed to take into account the electromagnetic field where included using user-subroutines developed by Tarczynski et al.. In this case the numerical simulations are transient.

A static pressure of 1 atm and a temperature of 2500 K (2227 °C) are assumed at the surfaces A, B, and C. The velocity gradients and scalar electric potential gradients at

these surfaces are defined to be zero. The vector electric potential is defined to be zero at the surfaces. At the electrode tip E_1 a temperature of 3500 K (3227 °C) is defined and the gradients of the electric vector potential are set to be zero. The scalar electric potential is dependent on the electric current density defined at this surface described by eq. (8). In this equation $J_{max} = 1.4 \cdot 10^8$ A/m^2 and $\varpi = 2 \cdot \pi \cdot f$ is the pulsation of the power supply voltage.

$$j_z(x,y) = J_{max} \cdot \exp\left(-b \cdot \sqrt{x^2 + y^2}\right) \cdot \sin(\varpi \cdot t) \quad (8)$$

At the electrode tip E_2 the axial temperature gradient and the scalar electric potential are set equal to zero. As for the surface E1, the gradients of the electric vector potential are defined to be zero.

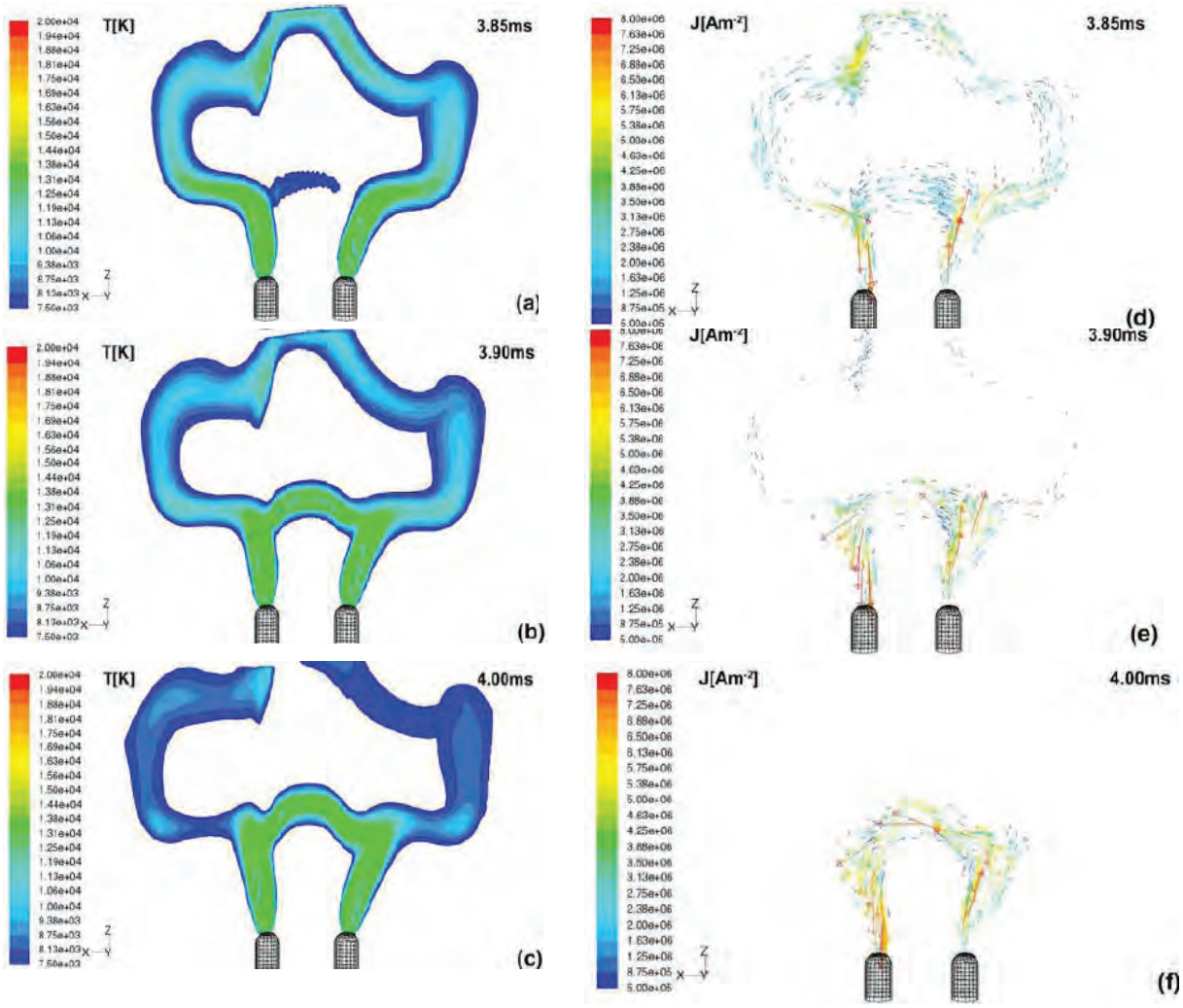

Figure 2-24: Temperature distributions and current density vectors calculated by Tarczynski et al. for a max. electric current of 500 A at atmospheric pressure [35]

The aim of the transient simulation is to investigate the arc movement, especially the formation of new discharge channels and their decay in AC arcs. In **Figure 2-24** simulation results are shown for three steps during one current half-period. The

results show that it is possible to simulate AC arcs using a commercial code such as FLUENT by using user subroutines. It should however be noted, that in this case the composition of the arc plasma is air and one as two electrodes with a fixed position. In the case of an EAF the situation is much more complex. As will be explained later in section 2.3, the composition of the plasma arc varies and possibly depends amongst other things on the slag composition. Furthermore during the flat-bath stage the discharge takes place between three electrodes and the melt surface.

Finally, in conclusion of this outline of the state of affairs concerning magneto fluid dynamic models of electric arcs, Boselli et al.[36] should be mentioned. In this paper a 2D model of a plasma arc welding process (25 to 70 A) is presented. Results, obtained using the assumption of local temperature equilibrium in the plasma column, are compared to those obtained using two-temperature thermal non-equilibrium modeling (2T). Optical emission spectroscopy measurements are used to validate the 2T results.

2.2.2 Channel Arc Model (CAM)

Pfeifer [23] describes the classical channel model for a static electric arc, as developed amongst others by Sakulin [37] and Ahlers et al.[38]. The characterization of plasma and the determination of its thermodynamic material properties are first discussed in detail. Thereafter Pfeifer adapts the classical channel model in order to take the heat transfer due to thermal radiation and convection into account.

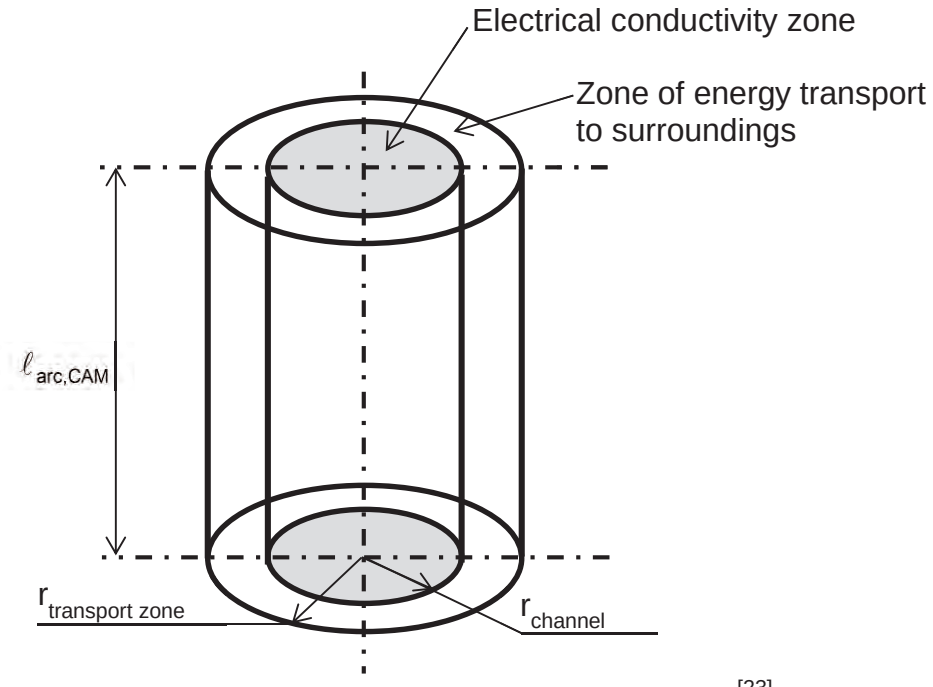

Figure 2-25: Classical electric arc channel model [23]

As shown in **Figure 2-25** for the classical channel model of a stationary DC arc, the arc region is considered to be made of a central clearly defined electrical conductivity zone and an external energy transport zone.

The inner channel is considered to have a temperature which depends on the energy input and output of the arc. The energy generated due to Joule heating in the central

channel is transported by thermal conductivity through the external channel to the surroundings. The temperature of the inner channel is considered to be independent of the radial and axial position within the inner channel. This means that the thermal conductivity $\lambda_{channel}$ for this region is considered to be infinitely large. The electrical conductivity $\sigma_{elec,channel}$ of this zone depends on the temperature, pressure and the arc composition (e.g. air, argon).

In the second zone the temperature decreases from that of the central channel $T_{channel}$ to that of the outer wall $T_{transport\,zone}$. Here the electrical conductivity is considered to be equal to zero and the thermal conductivity is a function of temperature and pressure.

For the adapted version of the classical channel model developed by Pfeifer, the assumption of a clearly defined central electrical conductivity zone is also used. The heat transport mechanisms to the surroundings are however treated differently, as can be seen in **Figure 2-26**.

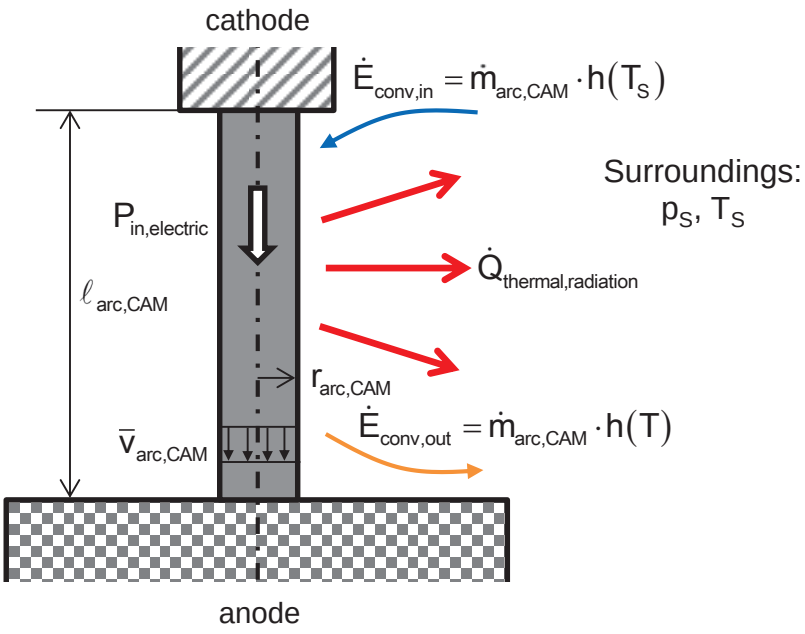

Figure 2-26: Channel model for a stationary arc

The electrical power input ($P_{in,electric}$) and the electrical resistance (R_{arc}) are calculated using the following equations:

$$P_{in,electric} = U_{arc} \cdot I_{arc,elec} = R_{arc} \cdot I^2_{arc,elec} \quad (9)$$

$$R_{arc} = \rho_{elec,arc} \cdot \frac{\ell_{arc,CAM}}{\pi \cdot r^2_{arc,CAM}} = \frac{\ell_{arc,CAM}}{\sigma_{elec,arc} \cdot \pi \cdot r^2_{arc,CAM}} \quad (10)$$

$I_{arc,elec}$ Electric arc current, in A

U_{arc} Arc voltage, in V

$\rho_{arc,elec}$ Specific electrical resistance, in Ω·m or V·m/A

$\sigma_{arc,elec}$ Electrical conductivity, in A/(V·m)

An average arc current density $j_{arc,CAM}$ is assumed.

$$j_{arc,CAM} = \frac{I_{arc,elec}}{\pi \cdot r_{arc,CAM}^2} \tag{11}$$

The mass flow rate in the arc channel is defined in eq. (12).

$$\dot{m}_{arc} = \dot{m}_{arc,inflow} = \dot{m}_{arc,outflow} = \rho \cdot \bar{v}_{arc,CAM} \cdot \pi \cdot r_{arc,CAM}^2 \tag{12}$$

$\bar{v}_{arc,CAM}$ Average velocity in the arc channel, in m/s

ρ Density of flow in arc, in kg/m^3

The mass flow in the arc is caused by compression due to the eigen magnetic forces of the electric current flowing in the arc. This so called Pinch-effect was first proven experimentally by Maecker [39]. Using the equation for the maximum velocity on the arc axis according to McKelliget and Szekely (given in [23]), the mass flow rate in the stationary arc channel can be calculated using:

$$\dot{m}_{arc,CAM} = K \cdot r_{arc,CAM}^2 \cdot \rho^{0.5} \cdot I_{arc,elec}^{0.5} \tag{13}$$

$$K = \left(\frac{K_1}{8} \cdot \pi \cdot \mu_0 \cdot j_{cathode} \right)^{0.5} \tag{14}$$

K_1 = 1.0 (according to Maecker) or K_1 = 5/3 (according to Schoeck and Eckert) $\mu_0 = 1.256637 \cdot 10^6$ H/m (magnetic field constant).

When considering the energy flows for this channel model for a stationary arc the following applies

$$P_{in,electric} = \dot{Q}_{thermal\,radiation} + \left(\dot{E}_{conv,out} - \dot{E}_{conv,in} \right) \tag{15}$$

Pfeifer explains that it is possible to solve the equation above by applying the principle of the minimalized arc voltage postulated by Steenbeck [40].

For a dynamic arc, the variables in equation (9) to (15) are time dependent, as the current is not constant. Furthermore the mass flow rate being drawn into the arc at any specific time is not necessarily equal to the mass flow rate out of the arc.

2.2.3 Black-box models

Black-box models are often used to represent the behavior of an electric arc within a circuit. Such models usually do not require a detailed consideration of the physical processes taking place in the arc region. Detailed information concerning the development and results of such a model for an EAF circuit is published for example by Moghadasian et al.[41] and Logar et al.[42]. The EAF electric circuit model by Logar et al.[42] is represented as a three-phase star AC circuit as shown in **Figure 2-27**.

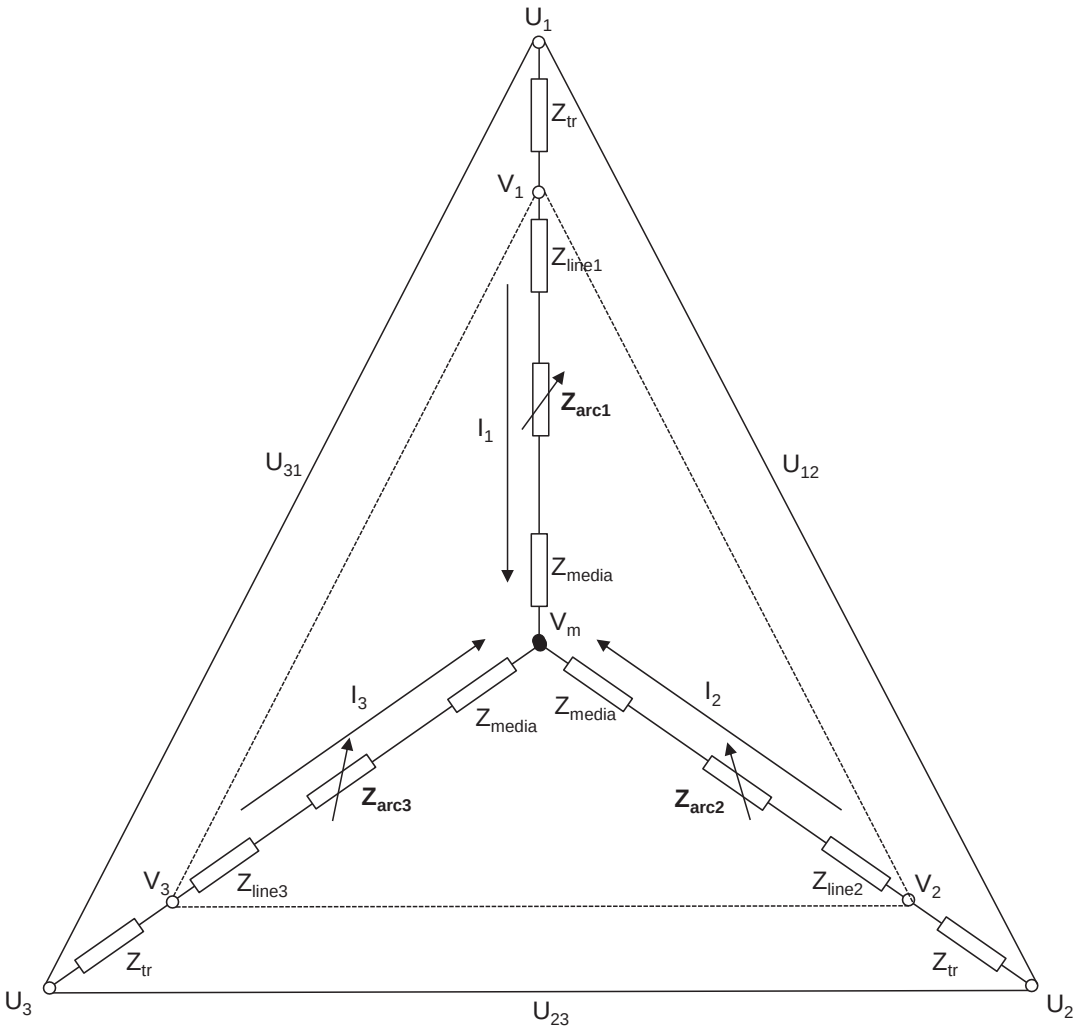

Figure 2-27: Electric model of an EAF by Logar et al.[42]

U_1, U_2, U_3	Phase voltages
U_{12}, U_{23}, U_{31}	Phase to phase voltages
V_1, V_2, V_3	Phase voltages without transformer voltage drop
I_1, I_2, I_3	Phase currents
Z_{tr}	Transformer and reactor impedance
Z_{line}	Line impedance
Z_{arc}	Arc impedance
Z_{media}	Media impedance
V_m	Steel bath potential

Within this circuit, the electric arcs are each modelled as impedance. These impedances of the arcs represent non-linear, time variant loads.

2.3 Experimental investigations

In this section insights gained from experimental investigations are summarized in order to illustrate the complexity of some of the phenomenon that might have to be taken into account when modelling the time-averaged energy input from the arc region during the power-on phase of the steelmaking process in an EAF.

A good reference for information concerning electric arc furnaces is Bowman and Krüger [43]. Amongst other things, the composition of the plasma of the electric arcs is discussed. The importance of the plasma composition, especially the amount of metal vapours, for the electrical conductivity and radiation density of electric arcs is emphasised. It is stated, that whereas at the beginning of a heat the furnace atmosphere consists of dust laden air, for most of the melting period the atmosphere around the arcs will consist of a H_2, CO, CO_2 and iron vapour mixture. If however the arc is submerged by foaming slag, then ionisation of metals from the slag must be taken into account.

The last statement is supported by findings of Aula et al.[44], who discuss the challenges faced when carrying out measurements of the emissions from electric arcs in an industrial AC EAF. For example one of the problems when measuring the emission from an arc is that it is usually hidden from view by scrap or foaming slag. A measurement head protecting an optic fiber was installed in the top of the furnace roof of a 140 t AC industrial arc furnace. Measurements were then carried out for 16 heats. The analysis of the results leads to the hypothesis, that the main source for most of the particles in the plasma arc column is slag. This means that a change in strategy might be necessary when modeling the plasma arc region for arcs that are not free-burning. An example of a typical slag composition obtained by the analysis of slag samples by Aula et al. is 43 % CaO, 27 % SiO_2, 7 % Cr_2O_3, 1 % Fe_2O_3, 6 % Al_2O_3, 6 % MgO, 4 % MnO and 2 % TiO_2.

When considering the energy input of the arc region into the freeboard of the EAF, the following aspect described by Aula et al. must also be considered. It is explained that fuming, referred to by Bowman and Krüger[43] as arc flames, has a big influence on the emission spectrum of the arc. Arc flames are the extremely hot flow exiting an arc region, which consists of a mix of reflected plasma and a flame due to the oxidation of chemical species such as carbon and iron.

In order to understand the thermochemical processes taking place in the arcs, the transformation into plasma of the furnace atmosphere drawn into the arcs must be considered. In **Figure 2-28** and **Figure 2-29** the temperature dependency of the dissociation and ionisation of CO_2 as well as that of air at a fixed pressure of 1 atm for thermochemical equilibrium conditions by Rini et al.[45] are shown.

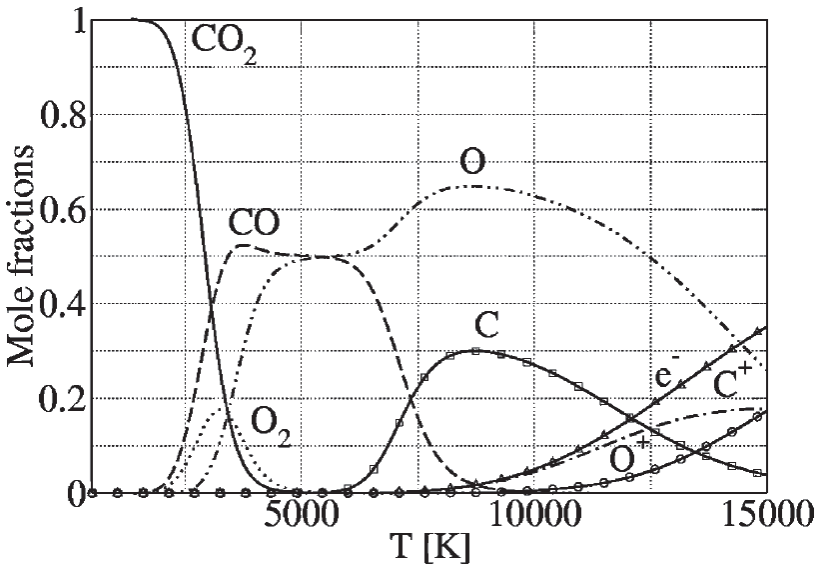

Figure 2-28: Dissociation and ionisation of CO_2 (x_{nO} = 0.67, x_{nC} = 0.33) at 1 atm [45]

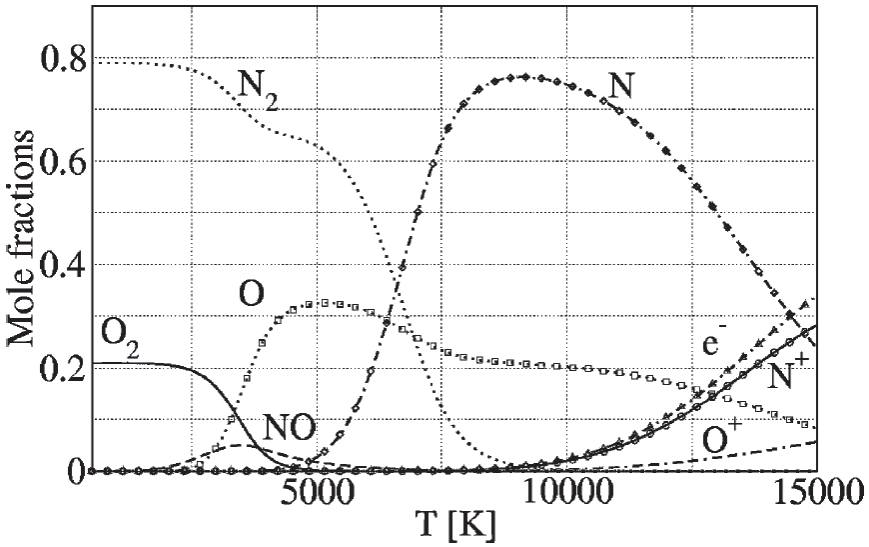

Figure 2-29: Dissociation and ionisation of air (x_{nO} = 0.21, x_{nN} = 0.79) at 1 atm [45]

The dissociation of CO_2 into its atomic elements takes place for temperatures higher than 2500 K. Ionisation, in this case the breakup of atomic elements into positively charged ions and electrons, starts at approximately 7500 K. In comparison, as can be seen in Figure 2-29, air consisting of 21 vol.% O_2 and 79 vol.% N_2 also begins to dissociate at temperatures greater than 2500 K. For temperatures higher than 10000 K the N_2 and O_2 have totally dissociated into their atomic elements and ionisation takes place.

A further paper concerned with the composition and corresponding properties of the electric arcs is that of Barcza et al.[46]. In this case the topic is the occurrence of so-called “side-reactions” in the arc attachment zone, e.g. the reduction of MgO to magnesium vapor or of SiO_2 to silicon monoxide gas. It is explained, that in an open-bath transferred plasma-arc furnace energy is required to maintain the bath in a liquid state and to drive the normally endothermic chemical reactions in the molten metal.

The disadvantages of such a furnace are listed to be the energy losses via radiation from the exposed plasma arc and bath surfaces, as well as the sensible energy loss due to the hot off-gas. It is noted that the feed rate of materials and the input power of the thermal plasma arc must be carefully balanced in order to avoid unwanted side-reactions in the arc attachment zone. These reactions can not only lead to an undesirable loss of elements, but also represent an additional energy loss, as they are endothermic.

Amongst other things Barca et al. investigate the thermal inertia of the bath, i.e. the time needed to heat the slag and bath by 100 °C. The resistance to a change in temperature is explained to be due to the energy needed to heat the slag and metal, shifting of the equilibrium between metal and slag phases, the energy used up by the side-reactions and an increase in the molten bath area.

The energy taken up by the vaporization of elements in the arc attachment zone in a DC or AC arc furnace therefore has an impact on the energy balance of the electric arc furnace. This energy fraction needs to be taken into account in order to be able to compare the true electrical input to that simulated with an EAF model. The question is, what the magnitude of the energy required for such reactions is in comparison to the total energy input of the arc region in an industrial sized electric arc furnace. A further question is, how large the effect of the vaporized species due to side-reactions is on the composition and therefore on the electrical conductivity and radiation density of the arc column.

In a EU steel research project report, Neuschütz et al.[47] describe the results of an experimental investigation of the entrainment of nitrogen in the melt in dependence of the polarity of the electric arc in a laboratory scale plasma melting furnace. They also investigated the influence of different arc atmospheres on the power input of the electric arc. The energy required for the dissociation of the gas components which takes place in an electric arc column depends on the composition of the gas. As a result the voltage drop between the cathode and anode, which increases when the energy required for the dissociation increases, is also dependent on the gas composition of the arc. For bottom stirred melts Neuschütz et al. measured a decrease in the arc voltage. It is surmised that this could be due to an increase in electrical conductivity of the plasma arc caused by bubble-bursting and the resulting increase in the amount of vaporized melt in the arc.

It was furthermore found that DC arc polarity has a relevant influence on the rate of nitrogen pick-up of the melt, referred to as pumping-effect, and on the amount of stirring in the melt. When considering the models described in section 2.2.1 of this thesis, it should therefore be noted that in reality not all the gas components drawn into an electric arc, either flowing from the tip of the electrode to the surface of the melt or in the opposite direction depending on the polarity, flow out of the arc region again.

When considering the magneto fluid dynamic models of DC arc regions summarized in section 2.2.1, the insights gained by Jones et al.[3] concerning the dynamic movement of DC arcs for higher arc currents is also very relevant.

a) Arc current I_{arc} = 500 A, Arc length ℓ_{arc} = 50 mm (cylindrical, steady state arc)

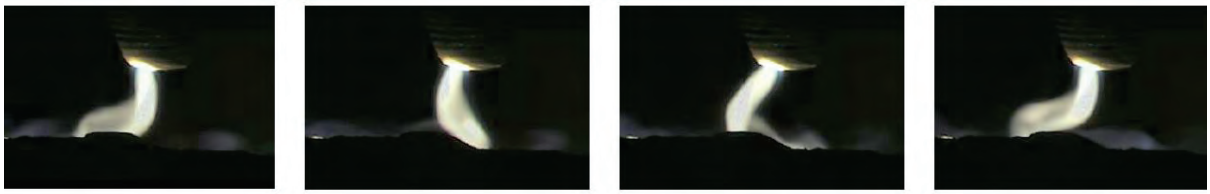

b) Arc current I_{arc} = 1000 A, Arc length ℓ_{arc} = 50 mm (successive frames)

c) Arc current I_{arc} = 2000 A, Arc length ℓ_{arc} = 50 mm (example frames)

Figure 2-30: Images of DC arc motion by Jones et al.[3]

Jones et al. explain that a DC arc in an electric arc furnace is not necessarily a steady state phenomenon with a cylindrical symmetric shape. The correctness of this statement for the experimental conditions during the investigation of Jones et al. is confirmed by images of the arc motion obtained using a high speed video camera, **Figure 2-30**. At low currents the arc column is cylindrical and steady state. The higher the current is the more dynamic the arc movement becomes.

In a previous paper, it had already been proven by Reynolds and Jones et al.[48], that if the time dependent terms in the governing equations are included, it is possible to

model the dynamic nature of DC arcs using a simplified time-explicit finite difference method.

Another of the issues tackled by Jones et al.[3] is the dominance of the energy transfer within the furnace freeboard by the thermal radiation from the arc column. It is argued that the plasma arc gas should not be treated as a black body radiator. This is based on a comparison of the calculated black body volumetric radiation emission of an arc to the volumetric emission calculated based on plasma physics and experimental measurements. This shows that the volumetric radiation emission of nitrogen plasma can be very much lower than that predicted assuming black body radiation. It is furthermore argued that thermal radiation emitted by the plasma is re-absorbed within the plasma column and transferred directly to the bath by close-proximity radiation, convection and conduction. Experimental information is referred to, that suggests that for the conditions considered the thermal radiation from the hot bath surface is the primary mechanism of heat transfer to the vessel walls.

3 EAF model description

3.1 Basic characteristics

Ideally a numerical simulation model of an electric arc furnace should be capable of correctly simulating the heat and mass transfer, turbulent fluid flow, thermal radiation, mixing of off-gas components, chemical reactions and electromagnetic phenomena taking place within the furnace during the individual periods of the steelmaking process. In principle, the commercial CFD software packages available today are equipped with suitable mathematical models for most of these tasks. The main difficulties lie in the transient nature of the process, the size of the solution domain needed for an EAF model and the fact that many of the parameters needed to define boundary conditions are not known.

For example, when considering the scrap melting phase of the steelmaking process, the definition of the material regions within the model would have to be constantly adapted in order to take into account the melting of the scrap and the increasing size of the pool of molten material. As a result, due to the complexity of this particular phase of the process, to the best of the authors knowledge the melting phase is at present not considered in any of the existing numerical EAF models (refer to section 2.1).

Most of the current numerical simulation models consider the flat-bath stage. The relevance of numerical simulation models of the power-on/flat-bath stage depends on the individual electric arc furnace process being considered. For example the flat-bath phase is very important for numerous EAF processes with high amounts of direct reduced iron (DRI) feeding. Such furnaces operate most of the time, in some cases almost 100 % of the time, with a flat-bath [49]. For a continuous scrap feeding Consteel® EAF, such as is presented by Memoli et al.[6], the flat bath stage is also more relevant than for the DC steelmaking process illustrated in Figure 1-2. In this case the flat-bath stage represents approximately 37 % of the total tap-to-tap time.

The numerical simulation model for the heat and mass transport in an electric arc furnace freeboard developed during this thesis represents the power-on/flat-bath stage of the steelmaking process in an exemplary AC electric arc furnace for quasi-steady state heat loss conditions. The term “heat loss conditions” means that the energy flows simulated with the model correspond to the quasi-steady state heat losses during this phase of the heat. The decarburization due to oxygen injection of the melt is taken into account. The exemplary AC EAF has a capacity of 100 tons of steel and a transformer rating of 90 MVA.

In order to generate the model, information concerning the geometry, secondary circuit voltage and current during the flat bath power-on stage and the operation chart for an exemplary heat was needed. The EAF model is based on information supplied by an industrial partner during the course of an investigation of post-combustion in an EAF.

3.2 Arc model

As can be seen by the experimental investigations summarized in section 2.3, it is quite a challenge to model the electric arc region in an AC EAF. In reality, fluid from around each plasma arc is drawn into the plasma column. On entering the arc region this fluid then dissociates and ionizes, whereby the extent of ionization depends on the composition and temperature, Figure 2-28, Figure 2-29. It then moves along as part of the plasma jet and exits it again, whereby due to the dissociation within the arc the chemical composition of the extremely hot fluid leaving the plasma arcs is not the same as when it was drawn in. Furthermore, due to the "pumping effect" described by Neuschütz et al.[47], not all the gas components drawn into an electric arc flow out again.

As can be seen by considering the photos of DC arcs with a high current shown in Figure 2-30, a DC arc in an electric arc furnace is not necessarily a steady state phenomenon with a cylindrical symmetric shape. Furthermore, in the case of alternating current (AC) arcs, the plasma jet changes direction as a function of the AC frequency of 50 Hz. Due to the electromagnetic forces the three arcs influence one another, leading to a rotation of AC arcs around an axis inclined outward towards the furnace wall [50] with a frequency of 100 Hz.

In a first step towards including the influence of the flow in and out of the plasma region on the flow field within the freeboard, the three AC arcs as well as the impingement zone of the arcs through the slag to the metal bath are modeled based on the channel arc model (CAM) [23]. The plasma arcs are not part of the solution domain. Instead they are represented as cylindrical surfaces extending from the electrode tip to the bath surface.

The radius of the cylindrical surfaces representing the arcs was calculated using the channel arc model (CAM) using eq. (11), given in section 2.2.2. For the model a mean electric arc current density $j_{arc,CAM}$ = 1 kA/cm^2 was used [51]. For an arc current of I_{elec} = 63 kA an arc radius of $r_{arc,CAM}$ = 45 mm results from the arc model.

The mass flow rate drawn into each arc was roughly approximated using eq. (13) and (14) [23], section 2.2.2. This corresponds to the mass flow rate through a stationary electric arc according to the CAM. The magnetic field constant is equal to $\mu_0 = 1.256637 \times 10^{-6}$ (kg m)/(A^2 s^2) and an electric arc current density at the cathode $j_{arc,CAM,cathode}$ = 4.40 kA/cm^2 is used. The gas density is approximated using the ideal gas equation and was calculated for an average arc temperature $\bar{T}_{arc}$ = 10000 K at the top of the arc column. This is the temperature calculated approximately at the channel arc radius for a DC arc column using mathematical models such as that of Ramírez-Argáez et al.[27]. A value for the mass flow rate $\dot{m}_{arc}$ = 0.44 kg/s is obtained. This value is only a very rough approximation, as amongst other things the freeboard gas components are in reality dissociating and ionizing as they flow into the arc channel.

In contrast to detailed magneto-fluid dynamic models of DC arcs described in section 2.2.1, this model is meant to be a time-averaged representation of the energy input from the arcs into the freeboard. It is as yet a very rough approximation of the real situation, as it does for example not include the change in direction and rotation of the plasma jets. The model does however include the kinetic energy input due to the arc in- and outflow as well as the energy input due to the heating of the entrained fluid by the arcs. Furthermore the results make it possible to gain an impression of the influence of the arc region on the flow field in the EAF freeboard [17].

3.3 Electrode model

The solution domain of the numerical EAF model by Pfeifer et al.[5] briefly described in section 2.1, does not include the solid graphite electrodes. Instead, the heat transfer from the furnace atmosphere to the electrodes is simulated by defining a constant temperature profile on the outer surfaces of the three electrodes. This temperature profile is based on measured temperature profiles in an industrial EAF presented in a paper by Rafiei et al.[52], **Figure 3-1**.

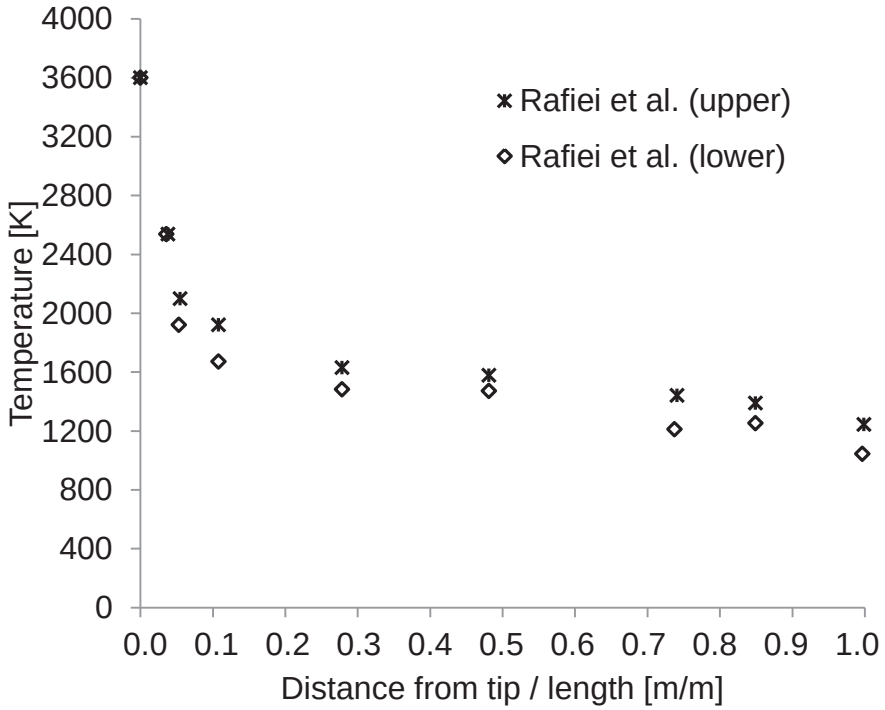

Figure 3-1: Measured electrode temperature profile [52]

An evaluation of the energy balance of the present numerical EAF model led to the conclusion, that the solid electrodes have to be part of the solution domain if the energy flows within the vessel are to be simulated correctly. Consequently, the solid electrodes are now part of the solution domain.

According to the operation chart for an exemplary heat supplied by an industrial partner, an alternating electric current I_{elec} = 63 kA flows through the electrodes during the flat-bath power-on phase considered. This results in Joule heating. It is

calculated based on the method used by Guo et al.[18] to investigate the amount of energy absorbed by the electrodes from the arcs using eq. (16) and (17). A longitudinal electrical specific resistance of the electrodes $\sigma_{electric}$ = 5.2 (Ohm·mm^2)/m, a thermal conductivity $\lambda_{electrode}$ = 240 W/(m·K) and the same temperature of 400 K [18] at the top cross-sectional area at the electrode gaps are assumed.

$$\dot{Q}_{electrode} = I^2_{electrode} \cdot R_{electrode} \tag{16}$$

$$R_{electrode} = \rho_{electrode} \cdot \frac{\ell_{electrode}}{\pi \cdot \frac{d^2_{electrode}}{4}} \tag{17}$$

$R_{electrode}$ Electric resistance, in Ohm

$d_{electrode}$ Electrode diameter, in m

$\ell_{electrode}$ Electrode length, in m

An energy source for all three electrodes of 864 kW (288 kW per electrode) is the result. This is modeled within each electrode as a volumetric heat source $\dot{q}'''_{electrode}$ = 343 kW/m^3 calculated using eq. (18).

$$\dot{q}'''_{electrode} = \frac{\dot{Q}_{electrode}}{V_{electrode}} \tag{18}$$

The temperature at the contact area between arc and electrode is defined to be 3600 K. This is the same value that was assumed for the hot-tip temperature of the CONOX model [5]. In comparison, the approximate sublimation temperature of graphite is 3925 K [52]. The temperature profiles on the electrodes therefore result in dependence of the conduction within the electrodes in combination with the heat transfer taking place at the electrode surface, which is the simulated convection and thermal radiation exchange within the freeboard.

3.4 Thermal radiation model

To model the radiation the CFD code ANSYS FLUENT (Version 14.5) was used. From the radiation models included in the code the discrete ordinates model [53],[54] was chosen to model the thermal radiation exchange. This model was chosen as not only the radiation exchange between the surfaces, but also the gas radiation can be taken into account. With this model a broad range of optical thicknesses can be analyzed, emissivity and dispersion is taken into account and localized sources of heating are not a problem [26].

The radiative heat transfer equation (RTE), eq. (19), is solved for an absorbing medium for a finite number of discrete solid angles, each associated with a vector direction $\vec{s}$ [53].

$$\frac{dI_{rad}(\vec{r},\vec{s})}{ds} + (a+\sigma_s)\cdot I_{rad}(\vec{r},\vec{s}) = a\cdot n^2 \cdot \frac{\sigma T^4}{\pi} + \frac{\sigma_s}{4\pi}\cdot \int_0^{4\pi} I_{rad}(\vec{r},\vec{s})\,\phi(\vec{s}\cdot\vec{s}')\,d\Omega' \tag{19}$$

Each octant of the angular space at any spatial location is discretized into N_θ multiplied by N_ϕ solid angles, called control angles. This results in 8 times N_θ times N_ϕ vector directions. In **Figure 3-2** the angular co-ordinate system for the definition of the solid angles θ and ϕ is shown.

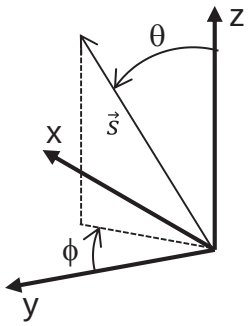

Figure 3-2: Angular co-ordinate system

An angular discretization of $N_\theta = 3$ and $N_\phi = 4$ is used in order to ensure a satisfactory resolution of the thermal radiation, especially around the circumference of the vessel. In addition a pixel resolution for each control angle of 3 times 4 is defined. The composition dependent absorption coefficient of the gas within the vessel is calculated using the weighted-sum-of-grey-gases-model. In this case the absorptivity of the furnace atmosphere is a function of the volume fractions of the species CO_2 and H_2O, which are known to absorb and emit thermal radiation at distinct wave numbers [53]. The implementation of the wsggm-model in FLUENT 14.5 is based on the work of Coppalle et al.[55] and Smith et al.[56]. The refractive index n of the gas mixture is defined to be equal to 1 and the scattering coefficient σ_s defined to be equal to zero.

The resolution chosen for the DO-model was tested using a simplified test model (refer to section 4.2), in which the free-burning arc length is only 50 mm. The temperature distribution on the vessel walls for an angular discretisation of $N_\theta = 3$ and $N_\phi = 4$ (pixel resolution of 3 times 4) is compared to that simulated with $N_\theta = 4$ and $N_\phi = 5$ (pixel resolution of 4 times 5) in **Figure 3-3**.

The results show that the increased resolution leads to a change in the simulated temperature distribution. It is smoother than before, especially around the top circumference of the upper vessel wall. The differences between the maximum and minimum wall surface temperatures are reduced. For example the maximum hot spot temperature drops by 64 K, which is 4 % of the higher value, and in general the temperature peaks are less pronounced than before. The hot spots are however still clearly defined. Their position remains the same and is a result of the position of the electric arcs with respect to the vessel wall. For both simulations it can be seen that convection and thermal radiation exchange of the walls with the cold stream of air from the slag door slightly reduces the hot spot temperatures located to the right of the slag door in comparison to the other two main hot spot positions along the circumference of the vessel.

The higher resolution of the DO-model leads to an increase in the size of the solution file for the test model of 54% and in the necessary random access memory (RAM) of approximately 20%. The necessary computing time is also clearly increased.

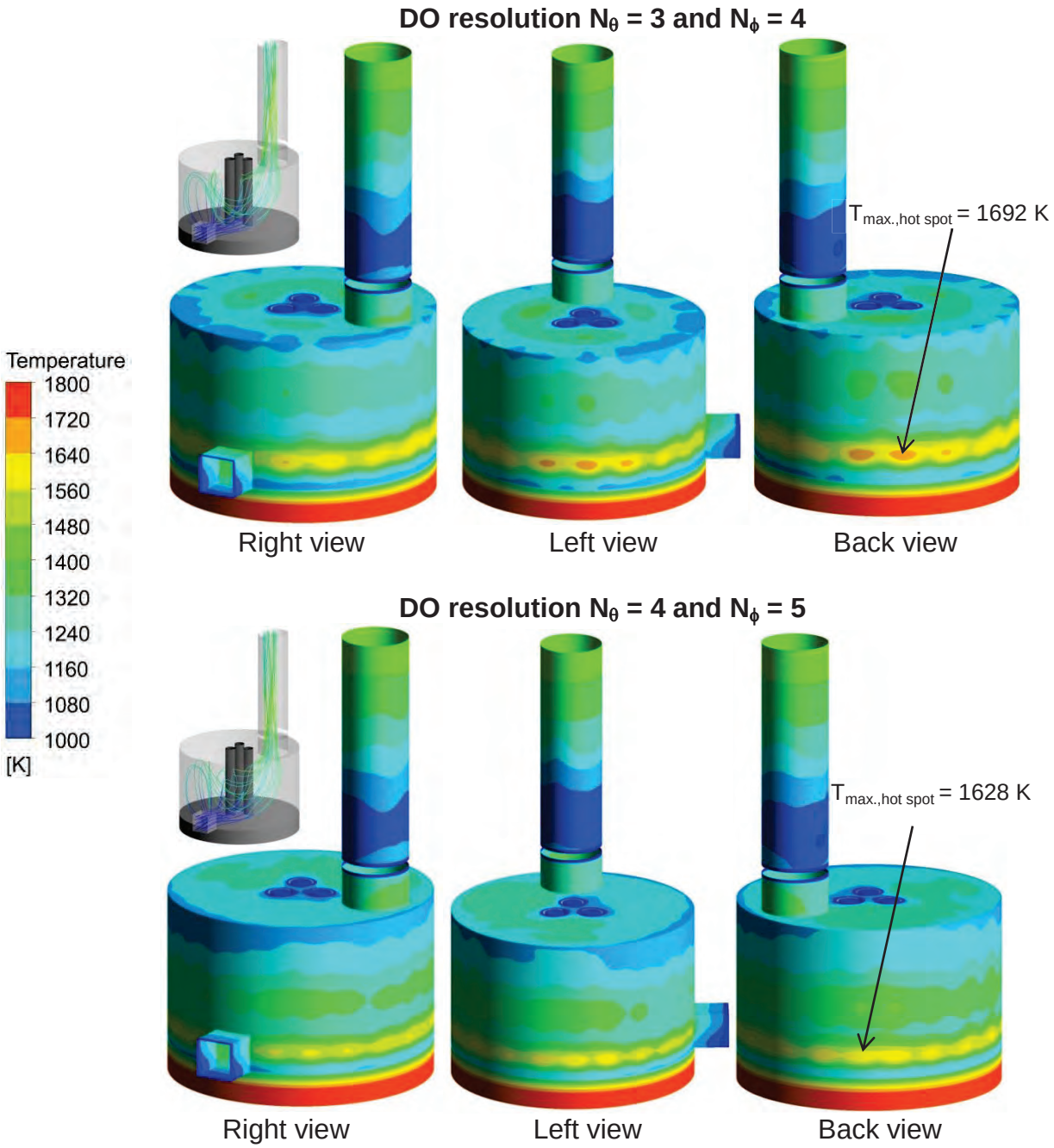

Figure 3-3: Effect of DO-model resolution on hot-spot simulation

As can be seen in Figure 3-3, the simulated temperature distribution on the vessel walls can definitely be improved by an increased resolution of the DO-model. The resulting temperature distribution within the flow field is however only affected close to the walls, **Figure 3-4**. Therefore it was decided that the resolution chosen for the EAF simulation model is sufficient for the present. If however the main goal of the simulation were to be changed, for example to the quantitative investigation of hot

spot temperatures or thermal loading of the cooling panels, then an increased resolution would have to be considered.

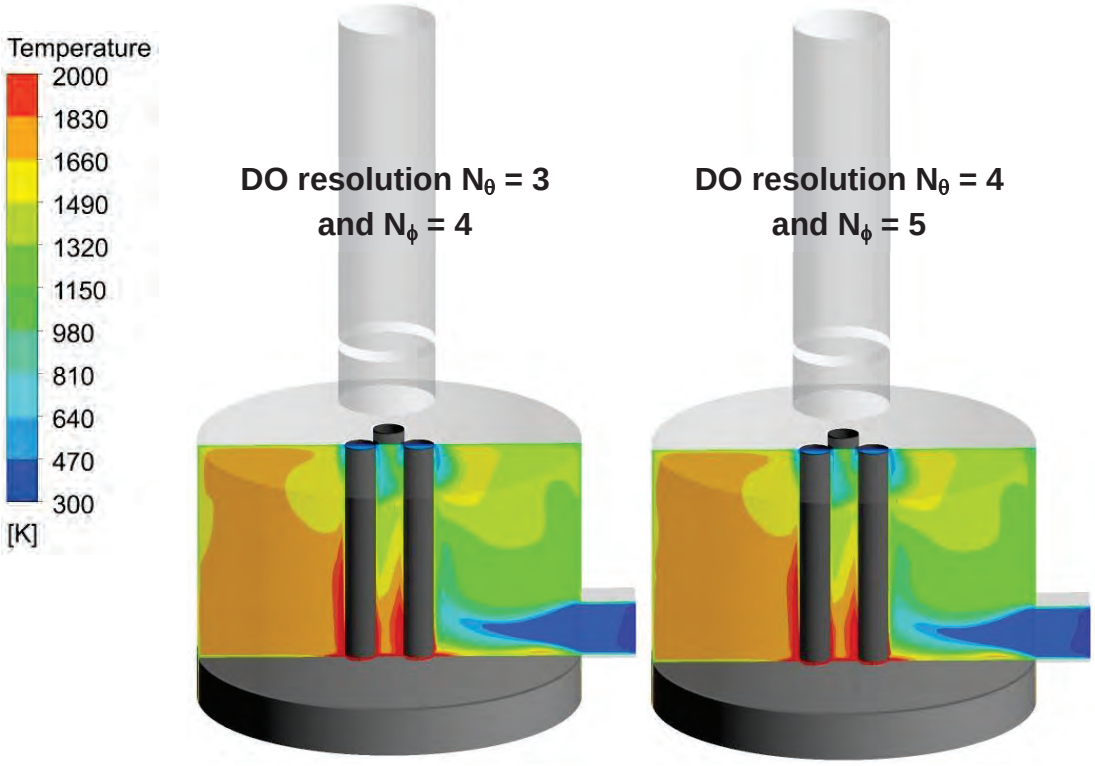

Figure 3-4: Effect of DO-model resolution on flow field temperature distribution

When comparing the hot spots in Figure 3-3 to reality it is important to note, that for the test model and for the final simulation model the influence on the intensity of the hot spot positions caused by the absorption and emission of thermal radiation by particles and fumes, which especially in the arc region is not negligible, is not taken into account. As a result three distinct hot spots can be seen, for example in the left and back views, which correspond to the simulated thermal radiation exchange between the modelled cylindrical arcs and the vessel walls. Furthermore, the influence of plasma jets, referred to by Bowman and Krüger[43] as arc flames, is at present not included, as this would necessitate an inclusion of the plasma flow in the arcs into the model.

The maximum hot spot position determined using the test model is due to the simplified geometry and boundary conditions, Figure 4-5. The more realistic EAF geometry used for the final simulation model has an oval shape and the side walls of the balcony are defined to be made of refractory material.

3.5 Modelling of chemical reactions

Before a suitable model can be chosen to model the chemical reactions taking place, the initial mixing of the reacting species (pre-mixed or non-premixed), the amount of oxygen available relative to that required for total combustion and the rate at which the reactions take place for the conditions being considered must be looked at.

Table 3-1: Conditions in the EAF freeboard (flat-bath period)

Pressure	101.325 kPa (atmospheric pressure)
Temperature of inflow of air	298 K (25 °C)
Off-gas temperatures [8]	Around 1873 K (1600 °C)
Mixing	Inhomogeneous, non-premixed
Air to fuel ratio	Within the furnace the ratio is less than 1, downstream of the post-combustion gap the ratio is greater than 1

When using the RANS approach the following models are available in Fluent (Version 14.5) to model chemical reactions:

- species transport with volumetric reactions (options: laminar finite-rate, finite-rate/eddy dissipation, eddy dissipation or eddy dissipation concept),
- non-premixed combustion model,
- premixed combustion model,
- partially premixed combustion model
- and composition PDF transport.

When considering the conditions within the freeboard listed in **Table 3-1**, only species transport with volumetric reactions, the non-premixed combustion model and the composition PDF transport model would seem to be suitable.

For the non-premixed combustion model the thermochemistry is reduced to a single parameter, the mixture fraction [53]. It is assumed that once the species are mixed, the chemistry is in chemical equilibrium. However a comparison of results from equilibrium calculations with off-gas measurements by Pfeifer et al.[5] shows that the off-gas of an EAF is usually not in thermodynamic equilibrium. This is thought to be due to high off-gas flow rates and the resulting low dwell times within the freeboard. Furthermore, the kinetically controlled oxidation of CO is one of the reactions that determine the time needed until complete combustion is achieved within a combustion chamber. The necessary dwell time is one of the factors that determine the size of a combustion chamber [57]. Therefore the non-premixed combustion model is not suitable for the EAF simulation model, as CO is one of the main furnace atmosphere species.

The probability density distribution function (PDF) transport equation model is suitable to simulate kinetically controlled reactions such as the oxidation of CO [53],[58]. It is however computationally expensive and can only be used to simulate very simple flows for fundamental studies [58].

Therefore species transport with volumetric reactions and the finite-rate/eddy dissipation turbulence chemistry interaction was chosen as the most suitable method available for the EAF model. Furthermore the gas within the furnace is defined to be a mixture of CO, CO_2, H_2O and air (carbon-monoxide-air mixture [53]). This enables the use of the gas-shift reaction available for the oxidation of CO in FLUENT (Version 15.4).

The post combustion of CO to CO_2 was investigated experimentally using a turbulent flow reactor in dependence of the amount of water vapor by Dryer [59]. Dry mixtures of CO and O_2 react very much slower than CO and O_2 mixtures containing water vapor or other hydrogenous species. The gas-shift reaction implemented in FLUENT takes into account the effect of the presence of water on the reaction rate of the oxidation of CO, whereby the following one-step reaction mechanism, Reaction 1, is used.

$$CO + 0.5\ O_2 + H_2O \rightarrow CO_2 + H_2O \qquad \text{(Reaction 1)}$$

Furthermore the dissociation of CO_2 to CO is also taken into account according the one-step mechanism Reaction 2.

$$CO_2 \rightarrow CO + 0.5\ O_2 \qquad \text{(Reaction 2)}$$

The rates of the reactions are calculated according to the Arrhenius expressions as shown by eq. (20) to (23) and in dependence of the turbulent mixing according to the eddy dissipation model, eq. (24) and (25). The smaller of the two values is used.

Arrhenius reaction rate for the species i = 1 to 5 (O_2, CO_2, CO, H_2O, N_2)

$$k_{f,r} = A_r \cdot T^{\beta_r} \cdot e^{\frac{-E_r}{R \cdot T}} \qquad (20)$$

$$\hat{R}_{i,r} = \left(\nu''_{i,r} - \nu'_{i,r}\right) \cdot \left(k_{f,r} \cdot \prod_{j=1}^{N} \left[C_{j,r} \right]^{\eta'_{j,r} + \eta''_{j,r}} \right) \qquad (21)$$

Whereby the term $k_{f,r}$ is the forward rate constant for reaction r and $\hat{R}_{i,r}$ is the Arrhenius molar rate of creation or destruction of species i during reaction r in kmol/(m^3·s) [53].

A_r Pre-exponential factor, in 1/(s·K$^{\beta}$)

β_r Temperature exponent

E_r Activation energy, in J/(kmol)

$C_{j,r}$ Molar concentration of species j in kmol/m^3

$\eta'_{j,r}$ Reactant rate exponent of species j for reaction r

$\eta''_{j,r}$ Product rate exponent of species j for reaction r

$\nu'_{j,r}$ Reactant stoichiometric coefficient of species j for reaction r

$\nu''_{j,r}$ Product stoichiometric coefficient of species j for reaction r

R Universal gas constant, 8314.4621 J/(kmol K)

T Temperature, in K

For Reaction 1 (r = 1) [53]:

$$A_1 = 2.239 \cdot 10^{12}\,1/s \qquad \beta_1 = 0 \qquad E_1 = 1.7 \cdot 10^8 \frac{J}{kmol}$$

$$\nu'_{CO,1} = 1 \qquad \eta'_{CO,1} = 1 \qquad \nu'_{O_2,1} = 0.5 \qquad \eta'_{O_2,1} = 0.25$$

$$\nu''_{CO_2,1} = 1 \qquad \eta''_{CO_2,1} = 0 \qquad \nu''_{H_2O,1} = 0 \qquad \eta''_{H_2O,1} = 0.5$$

For Reaction 2 (r = 2) [53]:

$$A_2 = 5 \cdot 10^8\,1/s \qquad \beta_2 = 0 \qquad E_2 = 1.7 \cdot 10^8 \frac{J}{kmol}$$

$$\nu'_{CO_2,2} = 1 \qquad \eta'_{CO_2,2} = 1$$

$$\nu''_{CO,2} = 1 \qquad \eta''_{CO,2} = 0 \qquad \nu''_{O_2,2} = 0.5 \qquad \eta''_{O_2,2} = 0$$

The net molar rate of creation or destruction $\hat{R}_{net,CO}$ of chemical species CO due to reaction 1 and 2 is the sum of the Arrhenius reaction sources $\hat{R}_{i,r}$ given by eq. (22):

$$\hat{R}_{net,CO} = -2.239 \cdot 10^{12} \frac{1}{s} \cdot e^{\frac{-1.7 \cdot 10^8 \frac{J}{kmol}}{R \cdot T}} \cdot [C_{CO}] \cdot [C_{H_2O}]^{0.5} \cdot [C_{O_2}]^{0.25} +$$

$$5 \cdot 10^8 \frac{1}{s} \cdot e^{\frac{-1.7 \cdot 10^8 \frac{J}{kmol}}{R \cdot T}} \cdot [C_{CO_2}] \qquad (22)$$

As can be seen in eq. (22), the pre-exponential factor of the oxidation of CO is approximately $4.5 \cdot 10^3$ times larger than that of the dissociation of CO_2 to CO. R_i is the net source or sink of chemical species i due to chemical reactions r=1 to N_R in kg/(m^3·s). It is relevant for the mass conservation equation and is given by eq. (23).

$$R_i = M_{w,i} \cdot \sum_{r=1}^{N_R} \hat{R}_{i,r} \qquad (23)$$

$M_{w,i}$ Molecular weight of species i

Eddy dissipation reaction rate

The net source or sink of species i due to reaction r in kg/(m^3 s) is given by the smaller of the two values given by eq. (24) and (25).

$$R_{i,r} = \nu'_{i,r} \cdot M_{w,i} \cdot A \cdot \rho \cdot \frac{\varepsilon}{k} \cdot \min_R \left(\frac{\xi_R}{\nu'_{R,r} \cdot M_{w,R}} \right) \qquad (24)$$

$$R_{i,r} = \nu'_{i,r} \cdot M_{w,i} \cdot A \cdot B \cdot \rho \cdot \frac{\varepsilon}{k} \cdot \frac{\sum_P \xi_P}{\sum_j^N \nu''_{j,r} \cdot M_{w,j}} \qquad (25)$$

M_w Molecular weight

ξ_P Mass fraction of any product species P

ξ_R Mass fraction of a particular reactant R
A Empirical constant equal to 4.0
B Empirical constant equal to 0.5
ρ Density, in kg/m^3

In **Table 3-2** field variables relevant for the chemical reaction rates are given for an exemplary point P within the EAF. In **Figure 3-5** the net molar Arrhenius rate of production of CO in dependence of temperature is shown for the exemplary gas species concentrations. The reaction rate calculated using the finite-rate model depends mainly on the temperature and the molar concentration of the reactants for the gas-shift reaction. By comparison, the reaction rate calculated with the eddy dissipation model depends mainly on the ratio ε/k, the minimum mass fraction of the reactants and the sum of the mass fraction of the products.

Table 3-2: Exemplary field variables simulated in the EAF freeboard *

Concentrations		Mass fractions	
[kmol/m^3]		[%]	
C_{CO}	0.00452	ξ_{CO}	70.3
C_{O2}	0.00012	ξ_{O2}	2.1
C_{CO2}	0.00024	ξ_{CO2}	5.9
C_{H2O}	0.00070	ξ_{H2O}	7.0
C_{N2}	0.00094	ξ_{N2}	14.7
Temperature [K]			1870
Density [kg/m^3]			0.18
ε/k [1/s]			1.87
Turbulent Intensity ($I=\frac{\sqrt{\frac{2}{3}k}}{\bar{v}}$) [%]			31
Net production rate of CO (finite-rate) [kmol/(m^3·s)]			-496.6
Net production rate of CO (eddy dissipation) [kmol/(m^3·s)]			≈ 0

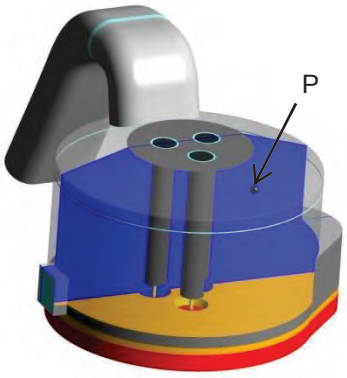

* For Simulation No. 1 at point P:
x = 0.3 m, y =-1.8 m, z = 2.4 m

As can be seen Table 3-2, the kinetic reaction rate of CO for the high temperature at the exemplary point is very fast. However, as the net reaction rate calculated with the eddy dissipation model is almost zero, the simulated combustion of CO at this point is negligible. This is due to the fact, that even though the turbulent intensity is high, the mass fraction of oxygen at the exemplary point is only 2 %. Therefore at point P the turbulent mixing of the reactants limits the combustion of CO.

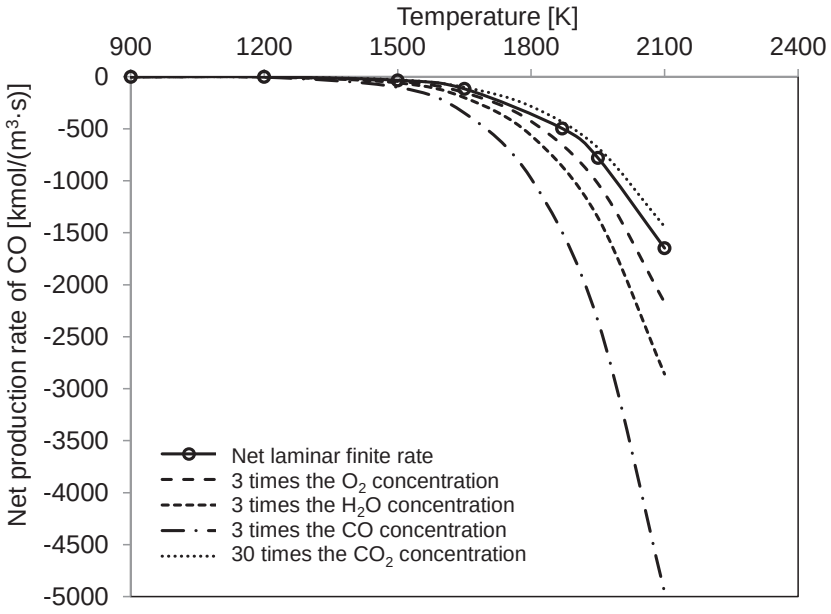

Figure 3-5: Net molar Arrhenius reaction rate for CO

3.6 Conservation equations and turbulence modelling

3.6.1 Mass, momentum and energy conservation

At the start of a numerical CFD simulation an initial field, i.e. start values for the main field variables shown in **Table 3-3**, is specified by the user. Thereafter the flow field, as well as the heat and mass transfer corresponding to the boundary conditions are determined iteratively using the conservation equations and mathematical models chosen during the model generation.

Table 3-3: Main field variables

Variable	Symbol	Unit
x-, y- and z- velocity	v_x, v_y, v_z	m/s
Static pressure	p	Pa
Temperature	T	K
Mass fraction of species i	ξ_i	-
Turbulent kinetic energy	k	m^2/s^2
Turbulent dissipation rate	ε	m^2/s^3

For a Cartesian co-ordinate system (x, y, z) the conservation equations listed below apply. They are explained for example by Welty et al.[60] or White [61] and can also be found as compact vector equations in the FLUENT Theory Guide [53]. As explained in section 4.2, the field values are influenced by the mesh quality and resolution of the gradients. It is an important part of the model development to decide which mathematical models are relevant and most appropriate in order to investigate the phenomena of interest.

Mass conservation equation

$$\frac{\partial \rho}{\partial t} + \nabla \cdot (\rho \cdot \vec{v}) = S_m \tag{26}$$

$\vec{v}$ Velocity vector, in m/s
ρ Density, in kg/m^3
S_m Mass sources, in (kg/s)/m^3

The vector-gradient operator ∇ is defined using the unit vectors in x-, y-, and z-direction i, j, and k as follows

$$\nabla = i \cdot \frac{\partial}{\partial x} + j \cdot \frac{\partial}{\partial y} + k \cdot \frac{\partial}{\partial z} \tag{27}$$

Therefore the divergence of the vector $(\rho \cdot \vec{v})$ which is $\nabla \cdot (\rho \cdot \vec{v})$ can be written as

$$\frac{\partial \rho}{\partial t} + \frac{\partial}{\partial x}(\rho \cdot v_x) + \frac{\partial}{\partial y}(\rho \cdot v_y) + \frac{\partial}{\partial z}(\rho \cdot v_z) = S_m. \tag{28}$$

The local mass fractions (ξ_i) of the furnace atmosphere species O_2, CO_2, CO, H_2O, N_2 are calculated using equation (29) for each species i [53].

$$\nabla \cdot (\rho \cdot \vec{v} \cdot \xi_i) = -\nabla \cdot \vec{J}_i + R_i + S_i \tag{29}$$

In this equation $\vec{J}_i$ is the diffusion flux of each species i due to gradients of concentration and temperature. R_i is the net rate of production of each species i by chemical reaction. S_i is the rate of creation due to sources, such as the volumetric CO source above the slag layer.

Momentum conservation equation (vector equation)

$$\frac{\partial}{\partial t}(\rho \cdot \vec{v}) + \nabla \cdot (\rho \cdot \vec{v}\vec{v}) = -\nabla p + \nabla \cdot (\bar{\bar{\tau}}) + \rho \cdot \vec{g} + \vec{F} \tag{30}$$

$\vec{g}$ Gravitational acceleration vector, in m/s^2
$\vec{F}$ External body force vector, in N/m^3
$\bar{\bar{\tau}}$ Stress tensor

Buoyancy is taken into account by defining a gravitational acceleration of g_z = 9.81 m/s^2. The external body force due to buoyance in N/m^3 is calculated using eq. (31) [53].

$$F_z = \rho \cdot g_z \tag{31}$$

Eq. (30) is the momentum equation written as a vector equation, which is the most compact form. The full non-linear differential momentum equation, where all the

terms are written out in full in their differential form for the x-, y- and z- direction can be found for example in [61].

Energy conservation equation (vector equation)

$$\frac{\partial}{\partial t}(\rho \cdot E) + \nabla \cdot \left[\vec{v} \cdot (\rho \cdot E + p)\right] = \nabla \cdot \left[k_{eff} \cdot \nabla T - \sum_j h_j \cdot \vec{J}_j + (\bar{\bar{\tau}}_{eff} \cdot \vec{v})\right] + S_h \quad (32)$$

$$E = h - \frac{p}{\rho} + \frac{v^2}{2} \quad (33)$$

The effective conductivity k_{eff} is equal to the sum of the fluid conductivity and the turbulent conductivity. The variable $\vec{J}_j$ is equal the diffusion flux of species j. The energy source term S_h includes the heat of chemical reaction and all user defined energy sources, for example the Joule heating defined in the electrodes. The third term on the right hand side of eq. (32) represents the energy transported due to viscous dissipation.

3.6.2 Turbulence

It is a well-known fact that fluid behavior is different depending on whether the flow is laminar (smooth and steady) or turbulent (fluctuating and agitated) [61]. The main measure of turbulence is the Reynolds number given by eq. (34).

$$Re = \frac{\rho \cdot v_{ch} \cdot \ell_{ch}}{\mu} \quad (34)$$

v_{ch} - Characteristic velocity magnitude, in m/s

μ - Dynamic viscosity, in kg/(s·m)

ℓ_{ch} - Characteristic length or flow scale, in m

In a chapter concerning the scales of turbulent motion, Pope[62] explains the following concerning v_{ch} and ℓ_{ch}. Turbulence can be considered to be composed of eddies of different sizes. An eddy is conceived to be a turbulent motion localized within a region of size ℓ. This region can also be occupied by smaller eddies at the same time. The eddies in the largest size range are characterized by the length scale ℓ_0, which is comparable to the characteristic length ℓ_{ch}. The characteristic velocity of these eddies is on the order of the root mean square turbulence intensity, which in turn is comparable to the characteristic velocity magnitude v_{ch}.

When considering this explanation it becomes clear that it is not trivial to define the characteristic velocity and length for the flow in an EAF, so as to be able to determine the Reynolds number. However it is easy to recognize that the flow within the furnace is not smooth and steady, i.e. laminar. The flow is definitely turbulent. Therefore a choice must be made whether to model the turbulence in detail using the DNS (Direct Numerical Simulation) method, or to calculate the flow with the help of a suitable

turbulence model. DNS involves solving the Navier-Stokes-equations, i.e. the full differential form of the conservation equations listed above, and necessitates a very fine discretization. Therefore it is only possible for investigations concerning a small solution domain. A good example of such a case is the simulation of the buoyancy dominated turbulent flow around a bluff body presented by Kang et al.[63].

For the simulation of the flow in an electric arc furnace however, using DNS is not an option. Therefore a suitable turbulent model must be selected. Several turbulence models are available in order to model the influence of the mean fluctuations of flow properties on the conservation equations, as shown in **Figure 3-6** (based on information in [53] and [61]). It is important to understand, that existing turbulent-flow theory is semi-empirical. It is concerned with the mean flow properties only and the mean of the fluctuations, not their rapid variations [61]. This means that in the case of a turbulent flow the simulation results, for example the velocity components or pressure, correspond to the mean values.

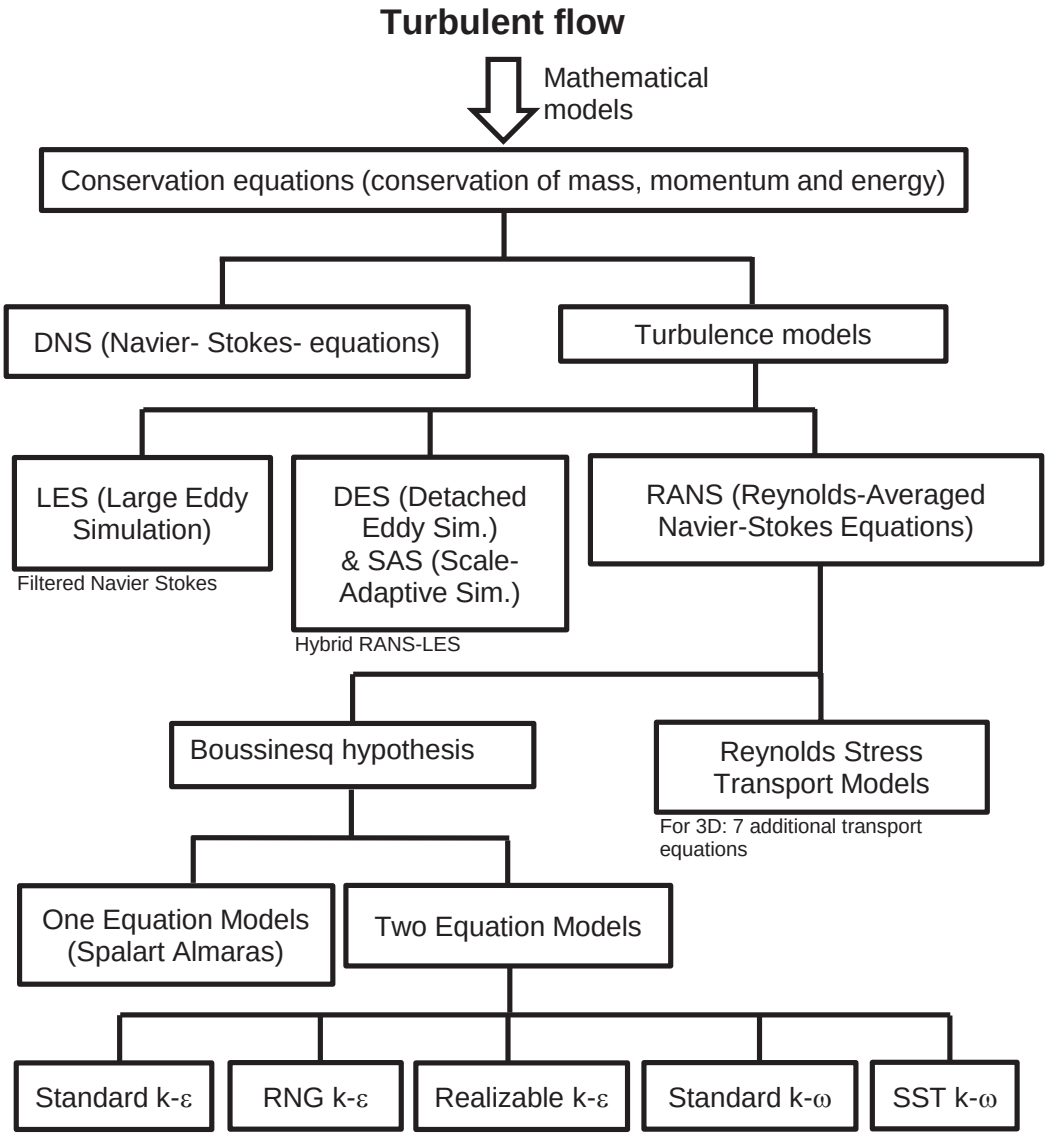

Figure 3-6: Summary of currently available turbulence models

For the simulation the realizable k-ε model with standard wall functions for the near wall treatment was selected to simulate the turbulent viscous flow. This choice is mainly based on the fact, that for the conditions investigated the convergence of the simulated heat of reaction using this combination of turbulence model and wall-functions was good.

The realizable k-ε model is based on the RANS (Reynolds-Averaged Navier-Stokes-equations) approach. The conservation equations are modified by describing each scalar ϕ (e.g. velocity component, pressure or shear stress) in term of its mean value and fluctuation, as shown in eq. (35).

$$\phi(t) = \bar{\phi} + \phi' \tag{35}$$

Applying the RANS approach leads to the momentum equations containing mean values and mean products of fluctuating values [61],[64]. These additional terms, see eq. (36) and (37) below, representing the effects of turbulence are referred to as Reynolds stresses and turbulent scalar fluxes [64].

$$\rho \cdot \overline{u_i' u_j'} \qquad \text{Reynolds stresses} \tag{36}$$

$$\rho \cdot \overline{u_i' \phi'} \qquad \text{Turbulent scalar fluxes} \tag{37}$$

The Reynolds-Averaged Navier-Stokes equations (RANS) in this form cannot be solved directly, as there are more unknowns than equations. The system of equations in this form is not “closed”. This problem is usually solved by expressing the Reynolds stress tensors and turbulent scalar fluxes as functions of the mean values and empirical parameters [64], as shown in eq. (38).

$$-\rho \cdot \overline{u_i' u_j'} = \mu_t \left(\frac{\partial \bar{u}_i}{\partial x_j} + \frac{\partial \bar{u}_j}{\partial x_i} \right) - \frac{2}{3} \cdot \rho \cdot \delta_{ij} \cdot k \tag{38}$$

Eq. (38) is referred to as the eddy-viscosity model, whereby δ_{ij} is called the Kronecker delta and k is the turbulent kinetic energy defined according to eq. (39) [64]

$$k = \frac{1}{2} \cdot u_i \cdot u_i = \frac{1}{2} \cdot \left(\overline{u_x' u_x'} + \overline{u_y' u_y'} + \overline{u_z' u_z'} \right). \tag{39}$$

One such approach is the Boussinesq hypothesis, which relates the Reynolds stresses, which are actually convective acceleration terms [61], in terms of the mean velocity gradients [53]. Using the realizable k-ε model means that the two additional transport eq. (40) and (41) are solved in addition to the conservation equations. The first transport equation is for the turbulent kinetic energy k and the second is for the turbulent dissipation rate ε [53]. The turbulent dissipation ε represents the rate with which the turbulent energy is irreversibly transformed into internal energy [64].

$$\frac{\partial}{\partial t}(\rho \cdot k) + \frac{\partial}{\partial x_j}(\rho \cdot k \cdot u_j) = \frac{\partial}{\partial x_j} \left[\left(\mu + \frac{\mu_t}{\sigma_k} \right) \cdot \frac{\partial k}{\partial x_j} \right] + G_k + G_b - \rho \cdot \varepsilon - Y_M + S_k \tag{40}$$

$$\frac{\partial}{\partial t}(\rho \cdot \varepsilon) + \frac{\partial}{\partial x_j}(\rho \cdot \varepsilon \cdot u_j) =$$

$$\frac{\partial}{\partial x_j}\left[\left(\mu + \frac{\mu_t}{\sigma_\varepsilon}\right) \cdot \frac{\partial \varepsilon}{\partial x_j}\right] + \rho \cdot C_1 \cdot S_\varepsilon - \rho \cdot C_2 \cdot \frac{\varepsilon^2}{k + \sqrt{\upsilon \cdot \varepsilon}} + C_{1\varepsilon} \cdot \frac{\varepsilon}{k} \cdot C_{3\varepsilon} \cdot G_b + S_\varepsilon \qquad (41)$$

G_k Generation of k due to mean velocity gradients

G_b Generation of k due to buoyancy

Y_M Contribution of fluctuating dilation in compressible turbulence to the overall dissipation rate

$\sigma_k, \sigma_\varepsilon$ Turbulent Prandtl numbers

S_k, S_ε User defined source terms

$C_{1\varepsilon} = 1.44,\ C_2 = 1.9,\ \sigma_k = 1.0,\ \sigma_\varepsilon = 1.2$

Eq. (42) is used to calculate the turbulent viscosity, also referred to as the eddy viscosity.

$$\mu_t = \rho \cdot C_\mu \cdot \frac{k^2}{\varepsilon} \qquad (42)$$

For the realizable k-ε model C_μ is not constant. It is computed in dependence of mean strain and rotation rates, the angular velocity of the system rotation and the turbulent fields [53]. The default values suggested by FLUENT were used for the model constants.

More in-depth information concerning turbulent theory, including a detailed description of the turbulent theory concerning wall-functions used to model the near wall regions for turbulent flows, is given by Ferziger and Perić [64].

3.6.3 Wall functions and wall surface roughness

Boundary conditions are needed to model the effect of walls on the heat transfer and fluid flow. When using the k-ε turbulence model, the following is appropriate [64] for n=0, whereby n is the coordinate normal to the wall and v_t is the velocity component tangential to the wall:

$$k_{n=0} = 0 \qquad \text{and} \qquad \frac{\partial \varepsilon}{\partial n}_{n=0} = 0 \qquad \text{or} \qquad \varepsilon_{n=0} = \mu \cdot \left(\frac{\partial \overline{v}_t}{\partial n}\right)^2$$

For the FLUENT software version 14.5 used for the EAF model the value for the surface roughness at a wall has a relevant effect on the near-wall flow. In this case, roughness effects at walls are included by applying the *law of the wall for mean velocity modified by roughness* [53]

$$\frac{u_p \cdot u^*}{\frac{\tau_w}{\rho}} = \frac{1}{\kappa} \cdot \ln\left(E \cdot \frac{\rho \cdot u^* \cdot y_p}{\mu}\right) - \Delta B. \qquad (43)$$

The dimensionless velocity u^* is given by eq. (44). The variable u_p is the mean velocity of the fluid at the near-wall node P which is located a distance y_p away from the wall.

$$u^* = C_\mu^{\frac{1}{4}} \cdot k^{\frac{1}{2}} \tag{44}$$

The value defined for the surface roughness height K_s is used to determine the type of roughness regime (smooth, transitional or rough) by determining the value for the non-dimensional roughness height K_s^+ using eq. (45).

$$K_s^+ = \frac{\rho \cdot K_s \cdot u^*}{\mu} \tag{45}$$

Thereafter ΔB is determined according to the equation for the specific roughness regime by using the value defined for the roughness constant C_s. For example, for the fully rough regime, ΔB is calculated using

$$\Delta B = \frac{1}{\kappa} \cdot \ln\left(1 + C_s \cdot K_s^+\right). \tag{46}$$

Eq. (43) is then applied to evaluate the shear stress at the wall and other wall functions for the mean temperature and turbulent functions [53].

With FLUENT Version 14.5 the modeling above is applied by the software when using standard wall functions in combination with the realizable k-ε model.

Please Note: The treatment of surface roughness was not the same for previous versions of FLUENT and is not necessarily the same for other commercial CFD Software, even if the same turbulence and near wall models are chosen.

When using wall-functions problems can arise in separated flows, especially within the separation and reattachment region [64]. Contrary to the standard k-ε model the realizable k-ε model is able to simulate flow separation [65]. The flow within the freeboard of an EAF is complex and includes such separation and reattachment regions (refer to section 5.2.1). Therefore it is especially important to monitor the convergence and stability of the results.

It is possible that during a later stage of the model development, when different boundary conditions or the inclusion of burners are being considered, an alternative choice for the turbulent modeling and wall functions will become necessary.

New investigations could be helpful when reevaluating the models chosen. For example in a paper by Iaccarino [66] concerning the challenge of choosing the correct turbulence and near wall modeling, the results obtained using selected turbulence models when simulating turbulent separated flow with the commercial CFD Software programs FLUENT, Star CD and CFX are compared. The results of another interesting investigation concerning flow separation, during which thirteen different turbulence models implemented in OpenFoam were compared, are given in a project

report by Furbo et al.[65]. In this report it is concluded, that for the case considered the RNG k-ε model, realizable k-ε model and k-ω model deliver acceptable results.

The topic of turbulent modeling is still being intensively researched. Therefore it is advisable to keep abreast of new developments, as the models and their implementation in commercial codes are constantly being adapted.

4 Model implementation

4.1 Geometry

The geometry of the model shown in **Figure 4-1** was generated using the commercial software SolidWorks (2011 SP2.0). The graphite electrodes, the arc region (excluding the plasma arcs) and the post-combustion gap are all part of the solution domain. Burners, lances or injectors are not included in order to reduce the necessary mesh size [17]. The flow within the molten steel bath and foamy slag layer are not included in the simulation. Instead the foamy slag is modelled as a solid layer and only a part of the bath, also considered as a solid, is included. In **Table 4-1** and **Figure 4-2** the main dimensions of the model are given.

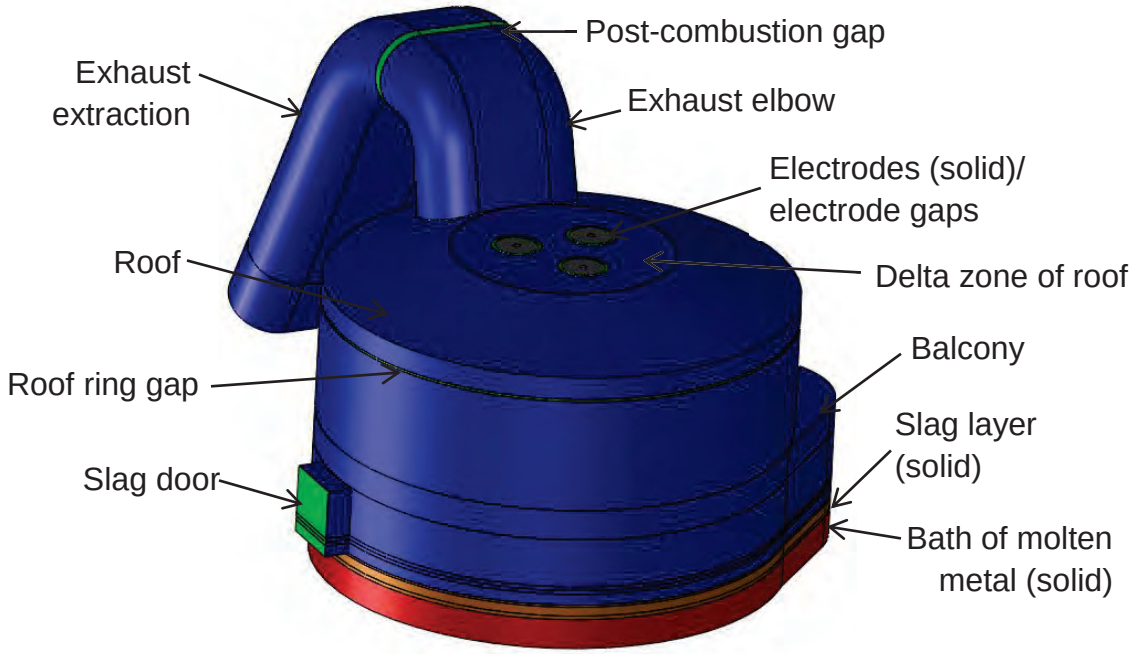

Figure 4-1: 3D view of the geometry of the model

Table 4-1: Main dimensions of the EAF model

Geometry of EAF Model	
Vessel diameter / Electrode pitch diameter	6.100 m / 1.200 m
Height of vessel from surface of bath to top of roof	3.824 m
Height and width of slag door	0.900 m / 0.900 m
Area of 4th-hole	2.090 m^2
Size of electrode gaps and roof gap	0.040 m / 0.030 m
Height of steel bath layer (solid)	0.400 m
Height of slag layer (solid)	0.170 m
Height of slag CO source layer	0.030 m
Diameter of electrodes (solid)	0.559 m
Electric arc length and radius	0.400 m / 0.045 m
Arc region: length of negative velocity inlet and mass flow inlet	0.050 m

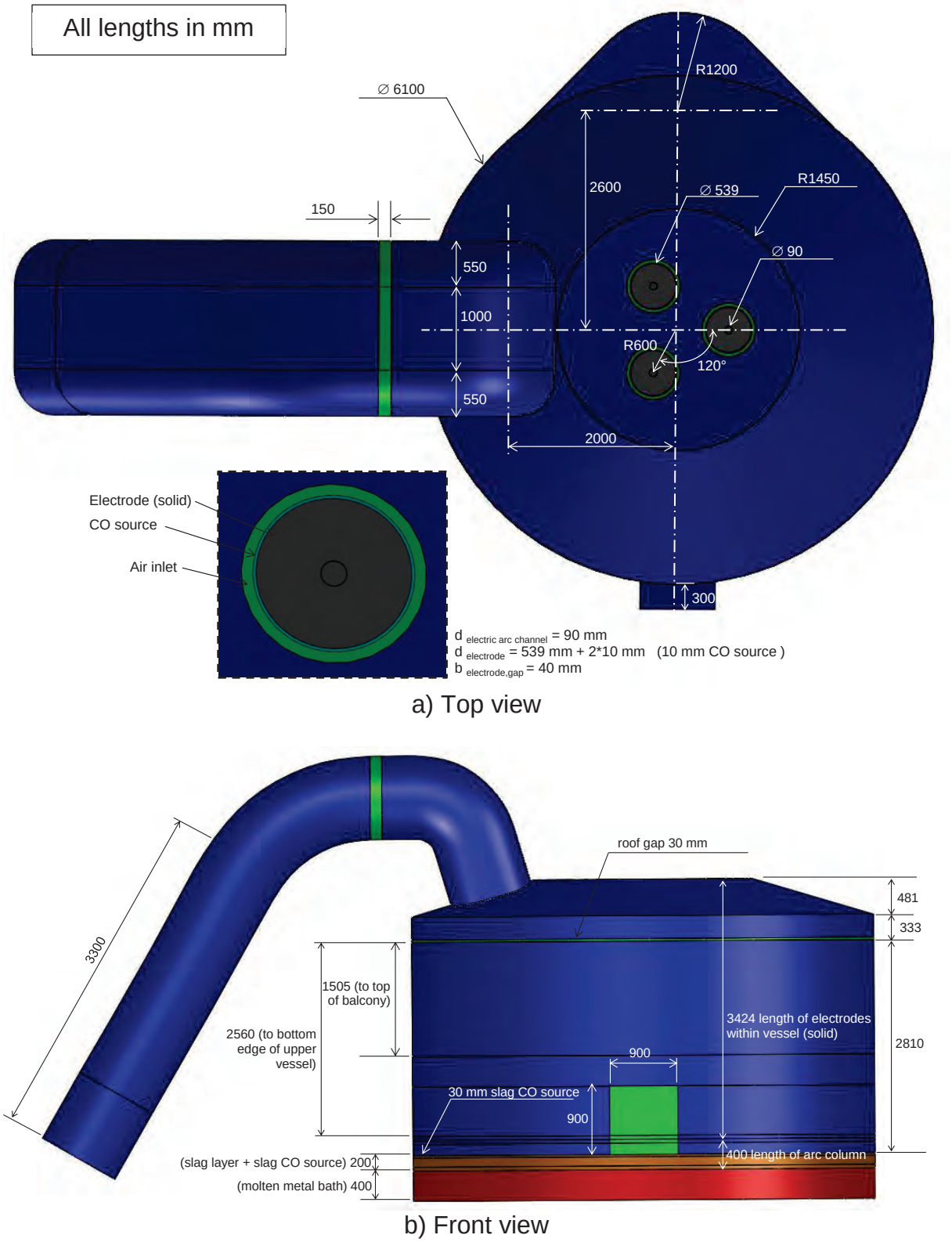

Figure 4-2: Main dimensions of the EAF model

The solid slag and molten metal bath layer allow a certain extent of absorption and redistribution of energy from the arc region. This is reflected by the resulting temperature distribution on the boundary to the furnace atmosphere at the slag

surface. The validity of using this method is discussed in more detail in the results section.

Two source regions are defined in the model. The first is the slag CO source layer. In this layer, similarly to the method chosen by Al-Harbi et al.[24], a volumetric source of CO is defined in order to simulate the hot carbon monoxide entering the freeboard due to the decarburization of the melt. The second region is a 10 mm thick layer around each electrode (see Figure 4-2.a). In this second region a volumetric carbon monoxide source and corresponding oxygen sink is defined in the model in order to simulate the electrode consumption.

The graphite electrodes within the solution domain are modelled to be cylindrical with a length of 3.424 m. This corresponds to an arc column height of 400 mm. The geometry of the electrodes, slag layer and arc columns can be seen in **Figure 4-3**.

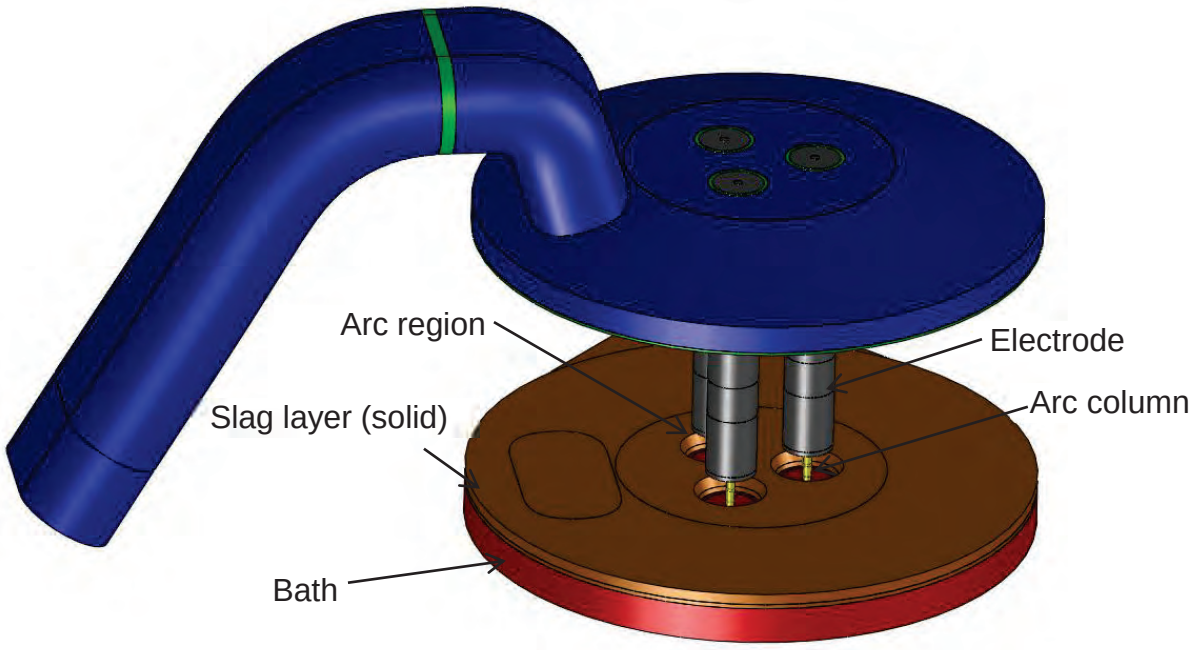

Arc region: Conical frustum with d_{bottom} = 639 mm and $\alpha = 23°$

Figure 4-3: Geometry of the electrodes and arc region

It is assumed that the arc columns extend down to the bath surface and that the thrust of the plasma flow displaces the slag around the column, forming a conical frustum. At this stage of the model development, the indentation in the surface of the molten steel bath due to effect of the arcs thrust is not taken into account. As the simulations are steady state, the transient deflection of the arc columns due to their mutual electromagnetic interaction is not modelled. The arc column radius was calculated based on the channel arc model (refer to section 3.2). The inside of the arc columns, i.e. the flow within the arcs, is not part of the solution domain.

As explained in section 5.1, an additional numerical simulation was carried out for a slag height of 350 mm. This was also done using the geometry generated with SolidWorks described in this section. The change in slag height was implemented by redefining the volumes up to 350 mm above the bath to be part of the solid slag

layer. The new slag CO source layer was defined to be the 50 mm thick layer on top of this new solid slag region. The amount of CO entering the solution domain per m^3 in the source layer was adapted, so that the same mass flow rate of CO enters the solution domain as before. The two resulting geometry versions are compared in **Figure 4-4**.

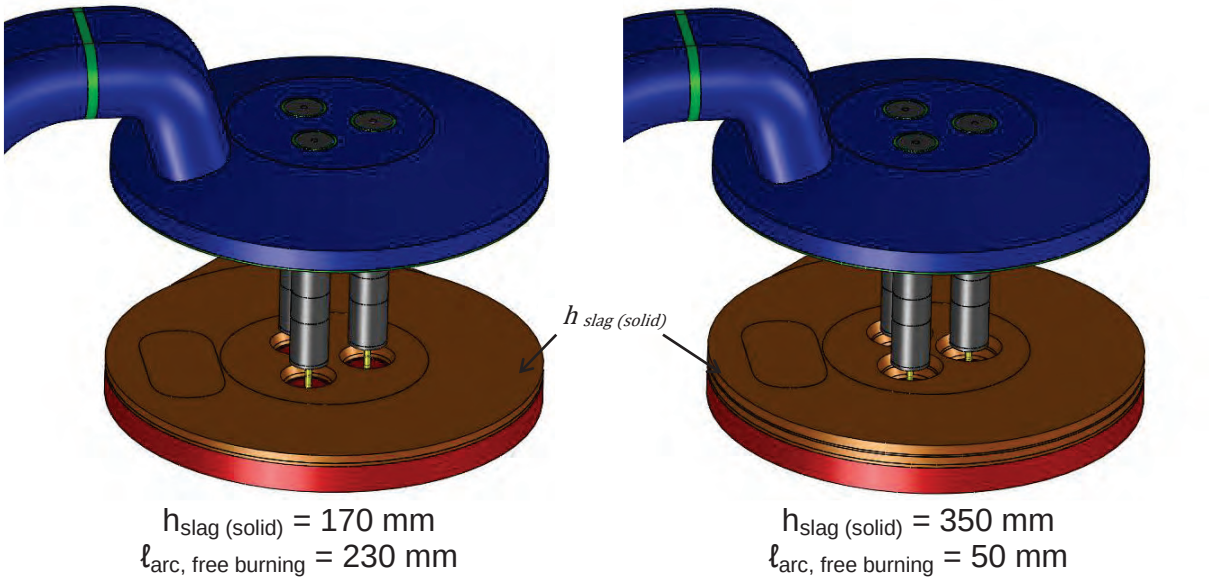

Figure 4-4: Comparison of the geometries for two slag heights (ℓ_{arc} = 400 mm)

Changing the slag height leads to a change in the free burning length of the arc column. As will be shown in the results section of this report, the free-burning arc length influences how much of the thermal radiation from the arc directly reaches the vessel walls and how much is absorbed and redistributed by the slag layer and bath.

4.2 Discretisation

4.2.1 Influence of boundary conditions on convergence of simulations

The discretisation of a solution domain has a large influence on the quality and convergence of numerical simulation results. Therefore a mesh sensitivity study is necessary to check that the gradients within the solution domain are sufficiently resolved.

A mesh that is more than suitable to calculate the flow field without chemical reactions, is not necessarily fine enough to resolve the resulting species gradients and to simulate the turbulent mixing within the flow when species transport and chemical reactions are considered. It is therefore important to carry out the mesh sensitivity study with the relevant boundary conditions. Even though a simplification of the conditions for the mesh sensitivity study saves a lot of calculation time, it can lead to the wrong conclusions.

The statements made above are confirmed by the insights gained during an additional study concerning the influence of boundary conditions on the convergence

of simulation results done during this thesis. The study was carried out with a simplified version of the EAF geometry. In **Table 4-2**, **Figure 4-5** and **Figure 4-6** the mesh quality, geometry, discretisation and results of the test model which support the statements made are shown.

Table 4-2: Mesh quality of test model

Number of elements	Average Orthogonal Quality	Aspect Ratio: Percentage of elements with a value smaller than 10	Average Skewness
460307	0.97	100	0.11
Ideal Value	1	100	0

The simplified geometry allows the generation of a structured mesh with a very good quality. Nevertheless, when the ratio of the mass flow rate of carbon monoxide from the slag layer to the amount of air flowing in at the slag door is reduced, the following is observed. The change in the mass flow rate of CO leads to a change in the chemical species gradients within the flow field. This in turn leads to instability of the simulated sum of the heat of reaction as shown in Figure 4-6. Therefore a change in boundary conditions can lead to the need to reconsider the discretisation.

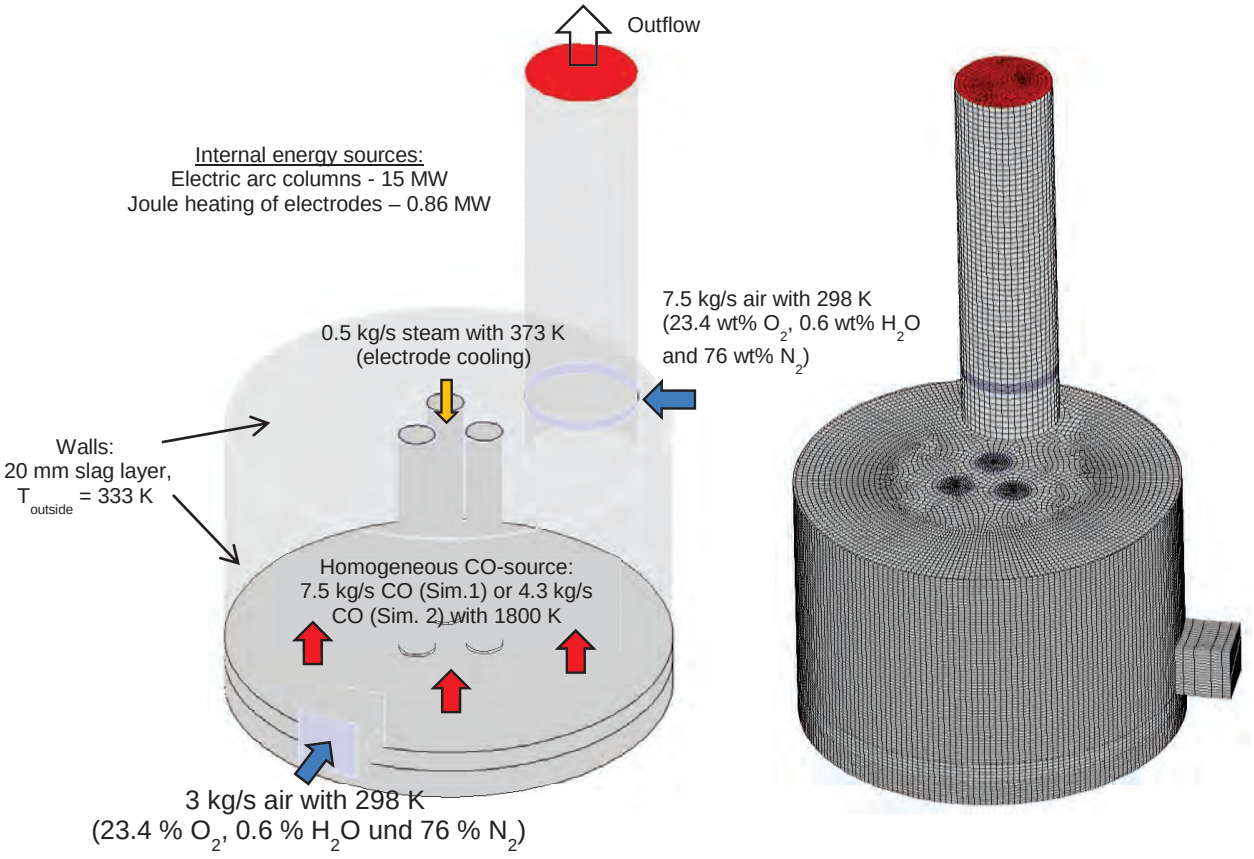

a) Geometry and boundary conditions b) Discretisation

Figure 4-5: Test model geometry, boundary conditions and discretisation

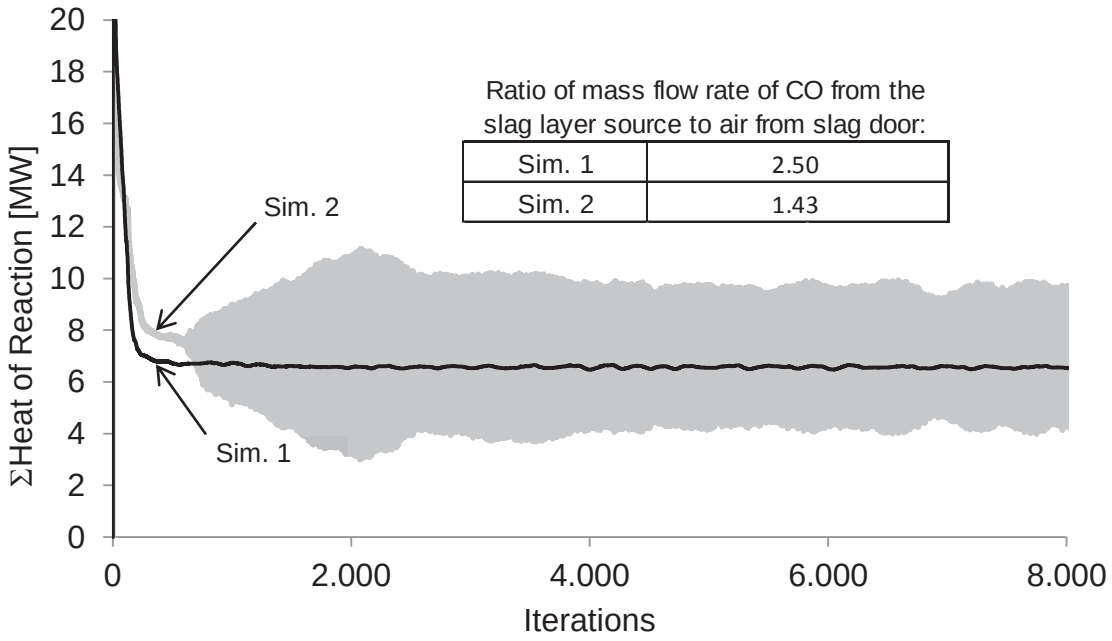

Figure 4-6: Convergence of test model results for different ratios of CO to air

Simulation 1 and 2 were initialised in exactly the same way, starting with the calculation of the flow field and species transport. Then the simulation of the combustion of CO to CO_2 and the reverse reaction of CO_2 to CO were activated. Whereas Simulation 1 converges very well, Simulation 2 becomes unstable around 610 iterations after the calculation of chemical reactions has been activated.

The investigation described above and further observations made during the mesh sensitivity study for the final EAF model led to the conclusion, that it is not sufficient to assess the convergence of a simulation based solely on the residuals output by the simulation software. A first measure is to monitor the convergence of the most relevant variables, for example at the outflow. In addition, it is necessary to evaluate the quality of the simulation results by carrying out the following logical steps:

1. Mass balance: The incoming mass flow rate (all inflows and sources) of all gas species elements (N, O, C and H) is compared to the outgoing mass flow rate (outflows and sinks). This is done to check the conservation of the mass of individual elements and can be carried out whether chemical reactions take place or not.
2. Energy balance: The sum of all energy flows at boundaries of the solution domain, taking into consideration the heat of reaction within the solution domain, is calculated to check the conservation of energy.
3. The convergence and stability of the sum of heat of reaction ($\Delta\dot{E}_{chem.Reac}$) within the solution domain during the simulation must be monitored.

4.2.2 Mesh sensitivity study

Three meshes with an increasing number of elements were generated for the mesh sensitivity study carried out for the final EAF model. The meshing was carried out using the software ANSYS Workbench 14.5.

The geometry (Figure 4-1) is divided into 202 volumes. The volumes were meshed step by step in order to ensure that the discretization of the regions with high gradients is fine enough. The meshing is structured in order to minimize the number of cells. Wherever possible the volumes were meshed using the sweep method, with the element size and number of elements on the edges being adjusted in order to ensure that the cell layer at all surfaces corresponds to the wall functions chosen. There is only one solution domain. The solid regions (electrodes, foamy slag layer and bath layer) are thermally coupled to the fluid regions at the respective boundary [17].

The three meshes were used for simulations with the boundary conditions identical to the reference boundary conditions described in section 4.4. The characteristics of each mesh are listed in **Table 4-3**.

Table 4-3: Mesh quality of discretisation for the final EAF model

Mesh	Number of elements	Average Orthogonal Quality	Aspect Ratio: Percentage of elements with a value smaller than 10	Average Skewness
1	912250	0.958	88.8	0.120
2	1966424	0.961	96.7	0.122
3	4079071	0.962	96.2	0.098
Ideal Value		1	100	0

The simulation results were evaluated according to the procedure described in the previous section. The results are shown in **Table 4-4**. The oscillation of the sum of the heat of reaction was determined by calculating the average difference from the mean value in percent for the last 100 iterations of the quasi-steady state simulation.

Table 4-4: Evaluation of simulation results

Mesh	No. of elements	**Mass conservation**	**Energy conservation**	**Convergence of the heat of reaction**
		$\Delta\dot{m}_{Element,in-out,max}$	$\Delta\dot{E}_{in-out}$	Average difference to mean value of $\Delta\dot{E}_{chem.Reac}$
1	912250	1.2 %	3.1 %	5.1 %
2	1966424	0.4 %	2.6 %	0.1 %
3	4079071	0.5 %	3.2 %	0.1 %

Even though the values in Table 4-4 indicate that mesh no. 2 would be sufficient, mesh no. 3 was used to generate the results presented in section 5 of this report. The finer discretisation leads to a better resolution of the details of the flow field, especially in the region between the electrodes. Mesh no. 3, which when excluding the post-combustion gap, off-gas extraction, solid slag and bath layer has

approximately 3 200 000 cells, is very fine in comparison to the discretization of Li et al.[19] (350 000 cells), Chan et al.[20] (82 000 cells) and Sanchez et al[26] (72 604 nodes). Therefore it was decided not to create a fourth mesh with an even finer discretization.

Mesh no. 3 is a hybrid mesh which consists to 96 % of hexahedron cells, the rest being tetrahedron, wedge and pyramid cells. Due to the slope of the roof and exhaust elbow geometry it was not possible to completely avoid cells with a low quality. However only 0.05 % of the total number of cells have an orthogonal quality below 0.1 and only 1.0 % of all the cells have a skewness greater than 0.8. No numerical instability due to these cells, which are mainly located in the roof and elbow, was in evidence [17]. In **Figure 4-7** the discretisation of the final EAF model (mesh no. 3) is shown.

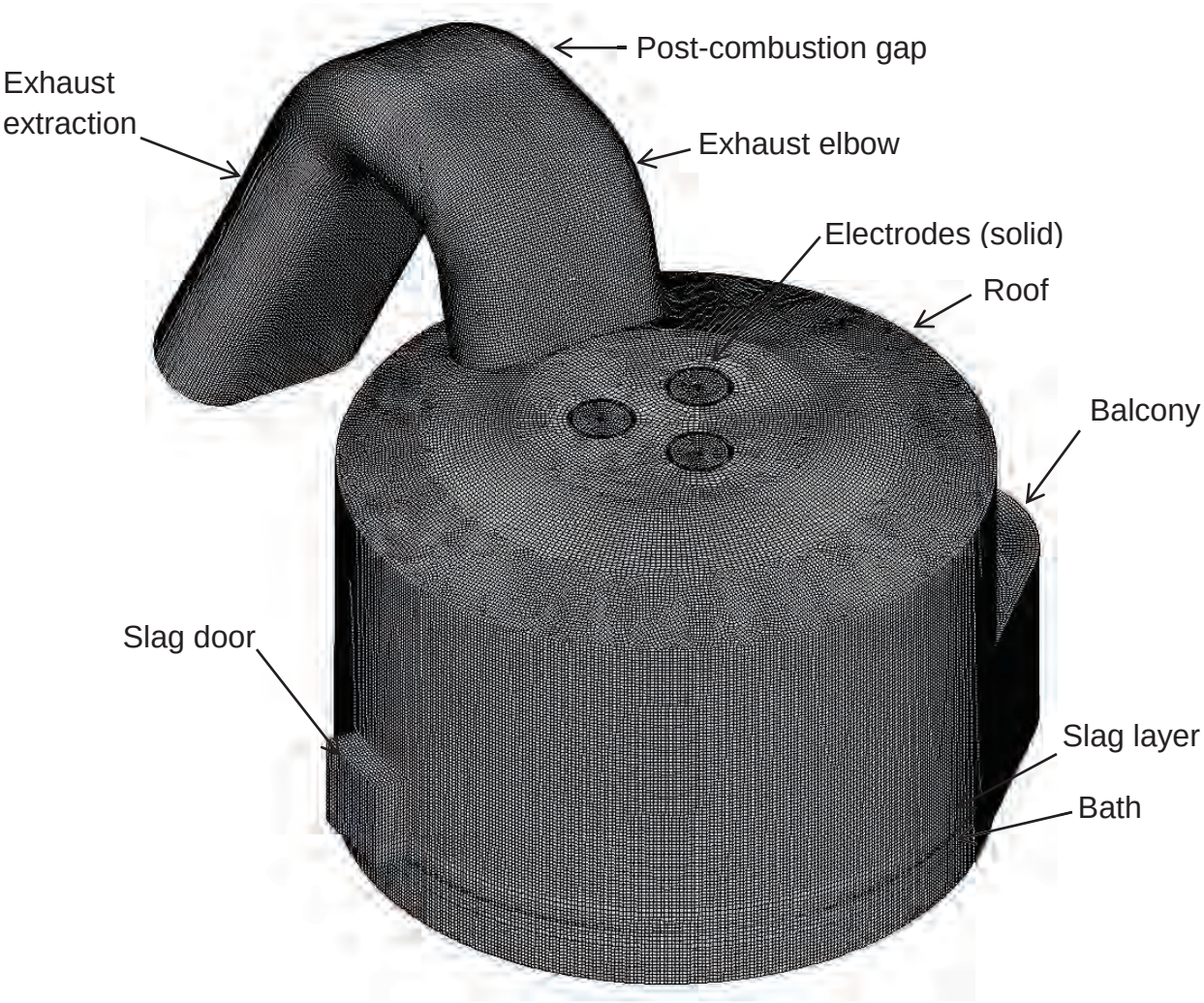

Figure 4-7: Discretisation

4.3 Material properties

4.3.1 Fluids

The furnace atmosphere is defined to consist of a CO-air mixture. The species considered within this mixture are O_2, CO_2, CO, H_2O (vapour) and N_2.

An operation pressure of 101325 Pa is defined for the model, whereby the reference point is located at the centre of the inflow to the slag door 400 mm above the bath surface. The reference temperature is 298 K (25 °C). An operational density of 1.175 kg/m^3 is specified, which corresponds to the density of air (23.4 wt. % O_2, 76.0 wt. % N_2, 0.6 wt. % H_2O) calculated with the ideal gas law for the operation pressure and reference temperature.

The density of the mixture with n = 5 species is calculated using the incompressible ideal gas law eq. (47). This is permissible, as the static pressure difference between the inflow at the slag door and the outflow out of the vessel is less than 500 Pa for the boundary conditions considered. In comparison to the ideal gas law for a pressure difference relative to the operation pressure of 500 Pa, using the incompressible ideal gas law leads to an error in the calculated air density at 298 K of only 0.5 %.

$$\rho = \frac{p_{op}}{R \cdot T \cdot \sum_{i=1}^{n} \frac{\xi_i}{M_{w,i}}} \tag{47}$$

ρ	Density of mixture, in kg/m^3
$M_{w,i}$	Molecular weight of species i, in kg/mol
ξ_i	Mass fraction of species i, in kg/kg
p_{op}	Operating pressure defined for the simulation, in Pa
R	Universal gas constant, R = 8.314472 J/(K mol)
T	Temperature, in K

The temperature dependent material properties defined for the furnace atmosphere are given in **Table 4-5** and **Table 4-6** (Source: FLUENT, Release Version 14.5, Revision 14.5.7, 2013). The constants (K_1 to K_5) given correspond to the polynomial equation below. As shown in **Figure 4-8**, if the constants of two polynomials are given for a material property, then the polynomials coincide at 1000 K.

$$\text{Property}(T) = K_1 + K_2 \cdot T + K_3 \cdot T^2 + K_4 \cdot T^3 + K_5 \cdot T^4 \tag{48}$$

Table 4-5: Fluid thermal properties (1) *

Fluid	Thermal conductivity [W/(m K)]	Viscoscity [kg/(m s)]	Specific heat [J/(kg K)]	Molecular weight [g/mol]	Heat of formation [kJ/(mol)]
O_2	$K_1 = 0.003921754$ $K_2 = 8.081213 \cdot 10^{-5}$ $K_3 = -1.354094 \cdot 10^{-8}$ $K_4 = 2.220444 \cdot 10^{-12}$ $K_5 = -1.416139 \cdot 10^{-16}$	$K_1 = 7.879426 \cdot 10^{-6}$ $K_2 = 4.924946 \cdot 10^{-8}$ $K_3 = -9.851545 \cdot 10^{-12}$ $K_4 = 1.527411 \cdot 10^{-15}$ $K_5 = -9.425674 \cdot 10^{-20}$	300 K ≤ T ≤ 1000 K $K_1 = 834.8265$ $K_2 = 0.292958$ $K_3 = -0.0001495637$ $K_4 = 3.413885 \cdot 10^{-7}$ $K_5 = -2.278358 \cdot 10^{-10}$ 1000 K ≤ T ≤ 5000 K $K_1 = 960.7523$ $K_2 = 0.1594126$ $K_3 = -3.270885 \cdot 10^{-5}$ $K_4 = 4.612765 \cdot 10^{-9}$ $K_5 = -2.952832 \cdot 10^{-13}$	31.9988	0
CO_2	0.0145	$1.37 \cdot 10^{-5}$	300 K ≤ T ≤ 1000 K $K_1 = 429.9289$ $K_2 = 1.874473$ $K_3 = -0.001966485$ $K_4 = 1.297251 \cdot 10^{-6}$ $K_5 = -3.999956 \cdot 10^{-10}$ 1000 K ≤ T ≤ 5000 K $K_1 = 841.3765$ $K_2 = 0.5932393$ $K_3 = -0.0002415168$ $K_4 = 4.522728 \cdot 10^{-8}$ $K_5 = -3.15313 \cdot 10^{-12}$	44.00995	-393.5324
CO	0.025	$1.75 \cdot 10^{-5}$	300 K ≤ T ≤ 1000 K $K_1 = 968.3898$ $K_2 = 0.4487877$ $K_3 = -0.001152217$ $K_4 = 1.656882 \cdot 10^{-6}$ $K_5 = -7.34637 \cdot 10^{-10}$ 1000 K ≤ T ≤ 5000 K $K_1 = 897.9305$ $K_2 = 0.4282316$ $K_3 = -0.0001671392$ $K_4 = 3.023444 \cdot 10^{-8}$ $K_5 = -2.05137 \cdot 10^{-12}$	28.01055	-110.54

* Source: FLUENT, Release Version 14.5, Revision 14.5.7, 2013

Table 4-6: Fluid thermal properties (2) **

Fluid	Thermal conductivity [W/(m K)]	Viscoscity [kg/(m s)]	Specific heat [J/(kg K)]	Molecular weight [g/mol]	Heat of formation [kJ/(mol)]
H_2O	K_1 = -0.007967996 K_2 = 6.881332·10^{-5} K_3 = 4.49046·10^{-8} K_4 = -9.09994·10^{-12} K_5 =6.1733·10^{-16}	K_1 =-4.418944·10^{-6} K_2 = 4.687638·10^{-8} K_3 = -5.389431·10^{-12} K_4 = 3.202856·10^{-16} K_5 =4.919179·10^{-22}	300 K ≤ T ≤ 1000 K K_1 = 1563.077 K_2 = 1.603755 K_3 =-0.002932784 K_4 = 3.216101·10^{-6} K_5 =-1.156827·10^{-9} 1000 K ≤ T ≤ 5000 K K_1 = 1233.234 K_2 = 1.410523 K_3 =-0.0004029141 K_4 = 5.542772·10^{-8} K_5 =-2.949824·10^{-12}	18.01534	-241.838
N_2	K_1 = 0.004737109 K_2 = 7.271938·10^{-5} K_3 = -1.122018·10^{-8} K_4 = 1.454901·10^{-12} K_5 =-7.871726·10^{-17}	K_1 = 7.473306·10^{-6} K_2 = 4.083689·10^{-8} K_3 = -8.244628·10^{-12} K_4 = 1.305629·10^{-15} K_5 = -8.177936·10^{-20}	300 K ≤ T ≤ 1000 K K_1 = 979.043 K_2 = 0.4179639 K_3 =-0.001176279 K_4 = 1.674394·10^{-6} K_5 =-7.256297·10^{-10} 1000 K ≤ T ≤ 5000 K K_1 = 868.6229 K_2 = 0.4416295 K_3 =-0.000168723 K_4 = 2.996788·10^{-8} K_5 =-2.004386·10^{-12}	28.0134	0

** Source: FLUENT, Release Version 14.5, Revision 14.5.7, 2013

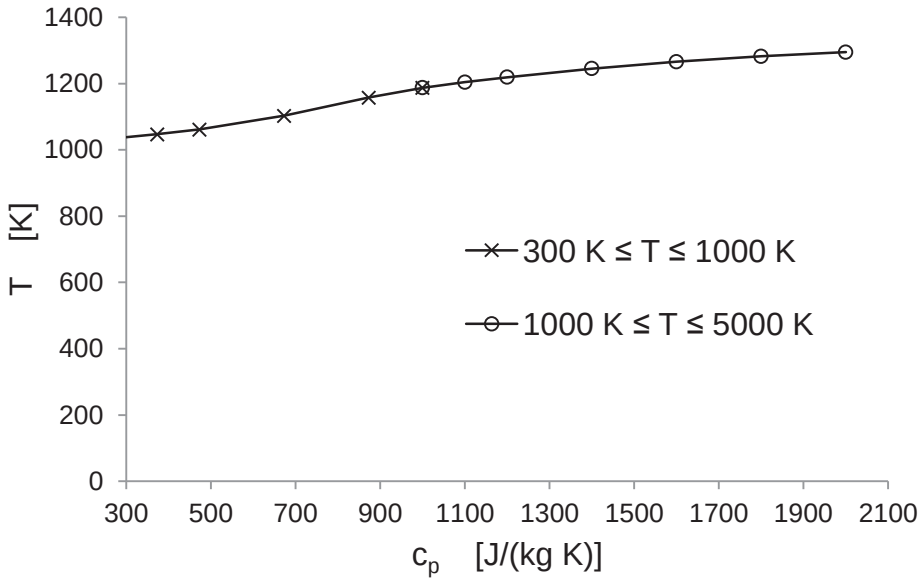

Figure 4-8: Temperature dependent c_p for CO

Amongst other things, the specific heat ($c_{p,i}$) is needed to calculate the energy transported into or out of the solution domain at sources, sinks, inlets and at the outflow. For this the enthalpy of the mixture must be known. It is calculated using the equations below.

$$h = \sum_{i=1}^{n} \xi_i \cdot h_i \tag{49}$$

$$h_i = \int_{T_{ref}}^{T} c_{p,i}\, dT \tag{50}$$

4.3.2 Solids

The solid electrodes are included in the solution domain. Furthermore, the geometry of the EAF model includes a solid layer of slag and a solid layer representing the bath. As will be explained in more detail in section 4.4.4, a layer of slag is considered to be present on the inner side of the vessel walls. The relevant material properties defined for these solid regions are given **Table 4-7**.

Table 4-7: Material properties of solids [5]

Material	Thermal conductivity [W/(m K)]	Emissivity [-]
Graphite	240	1
Refractory material	2.4	0.6
Slag (layer on vessel walls)	2.4	0.6
Dust (layer on exhaust extraction walls)	2.4	0.6
Slag (layer on top of bath)	8.8	1
Bath	80	-

The material values were based on those of the predecessor EAF model used by Pfeifer et al.[5] and on approximate values available for the materials in literature. The effective thermal conductivity assumed for the layers representing the foamy slag layer and the bath was estimated and adapted in dependence of the resulting maximum slag layer temperature.

When considering these values, it should be noted that for example the slag composition within an EAF varies during a heat and also depends on the steel being produced. Furthermore the nature (e.g. composition, thermal properties) and thickness of the layer of slag and dust, which accumulates on the inner vessel surfaces, is in reality not homogeneous and varies with time depending on the conditions.

4.4 Boundary conditions

4.4.1 Inflows, outflows and sources

Slag CO source

For the EAF model the slag CO source is based on information in the exemplary operation chart supplied by an industrial partner during a research project. According to this operation chart, an oxygen mass flow rate of 4.28 kg/s is injected into the melt using a lance and burners during decarburization. At the same time carbon is injected into the melt. It is assumed that the oxygen reacts completely with the injected carbon in the melt to CO according to the reaction C + 0.5 $O_2 \rightarrow$ CO. Thereby, simplifying, the fact that a part of the injected oxygen is consumed by the slagging reactions is not taken into account. The corresponding CO mass flow rate is calculated as follows:

$$\dot{m}_{CO} = 2 \cdot \dot{m}_{O_2} \cdot \frac{M_{CO}}{M_{O_2}} \tag{51}$$

M_{O_2} = 0.0319988 kg/mol and M_{CO} = 0.0280101 kg/mol

A carbon monoxide mass flow rate of 7.5 kg/s is the result. It is assumed to have a temperature of 1823 K (1550 °C). This is defined in the model, simplifying in comparison to the method chosen by Al-Harbi et al.[24], as a homogeneous volumetric source of CO in the 30 mm high layer on top of the solid slag layer.

CO source and O_2 sink due to electrode consumption

At this stage of the model development, it was decided to define a fixed source of CO due to electrode consumption. M. Grant et al.[67] use a value of 2.72 kg/ton of steel (6 lbs/ton) for the electrode consumption during one heat. For a capacity of 100 tons and a tap-to-tap time of approximately 55 minutes, this corresponds to a graphite electrode consumption of 0.082 kg/s. For the EAF model an electrode consumption of 0.08 kg/s was assumed. Using eq. (52) and (53), this corresponds to a source of CO of 0.187 kg/s and a corresponding O_2 sink of 0.107 kg/s.

$$\dot{m}_{O_2} = 0.5 \cdot \dot{m}_C \cdot \frac{M_{O_2}}{M_C} \tag{52}$$

$$\dot{m}_{CO} = \dot{m}_C \cdot \frac{M_{CO}}{M_C} \tag{53}$$

M_C = 0.0120107 kg/mol

The energy source and sink due to electrode consumption is implemented in the EAF model using the user subroutine given in section 9.1. The O_2 drawn out of the solution domain represents an energy sink which depends on the local fluid flow temperature in each source volume cell. Similarly, it is assumed that the CO entering the solution domain due to electrode consumption has the same temperature as that

of the O_2. Therefore the input of the subroutine is the local temperature in each volume source cell (*cell_T_source*).

With this temperature the enthalpy of the O_2 and CO is calculated using the constants given in Table 4-5 and eq. (52) and (53). The output of the subroutine is the net energy source (*source*) resulting from the inflowing CO (*COsource*) and O_2 drawn out of the solution domain (*O2source*) in each source volume cell.

Mass flow inlets and outflow area

The static pressures at the inlets are defined relative to the operating pressure, i.e. relative to an absolute static pressure of 101.325 kPa. A relative static pressure of 0.01 Pa is defined at the slag door, roof gap, electrode gaps and combustion gap.

At all inlet areas, implemented in the model as mass flow inlets, the direction of the incoming flow is specified to be normal to the inlet area. A turbulent intensity of 5 % is assumed. The turbulent length scale is defined to be 0.07 times the respective hydraulic diameter, as suggested in the FLUENT Users Guide [53].

Air is defined to have a composition of 23.4 wt% O_2, 0.6 wt% H_2O and 76 wt% N_2 (21.03 vol% O_2, 0.96 vol% H_2O and 78.01 vol% N_2) and a temperature of 298 K (25 °C). At all air inlets, an external black body temperature of 298 K is specified.

The total mass flow rate of air flowing into the furnace vessel, not including inflow at the post-combustion gap, is estimated to be 3 kg/s. This is distributed amongst the slag door, roof ring gap and the electrode gaps according to the size of each inlet area. As the temperature and therefore density is the same, an average inlet velocity of 1.585 m/s results at all of these inlets. The amount of air flowing in at the post-combustion gap is estimated to be 7.65 kg/s.

It is assumed that in total 0.5 kg/s of steam with a temperature of 373 K (100 °C) enters the vessel through the three electrode gaps due to electrode cooling. In order to take into account the thermal radiation losses through the electrode gaps, an external black body temperature of 373 K is specified.

The outflow area is defined as a pressure outlet, whereby the average gauge-pressure, i.e. pressure relative to the operating pressure, is defined to be $p_e = -350$ Pa. This means that the pressure p_f at the outlet face of each fluid volume adjacent to the outlet area is calculated using eq. (54).

$$p_f = 0.5 \cdot (p_c + p_e) + dp \tag{54}$$

In this case p_f is a function of the interior cell pressure at the neighboring exit-face p_c and dp, which is the difference in pressure value between p_e and the latest calculated average pressure for the boundary [53]. The external black body temperature specified for the thermal radiation losses through the outflow area is estimated to be 860 K. As backflow is possible at a pressure outlet, a backflow turbulent intensity of 5% with a temperature of 1500 K is specified. The composition of the backflow is defined to be 60 wt% CO, 0.4 wt% H_2O and 39.6 wt% N_2. Even though no backflow is expected,

the specified temperature and composition of the backflow is relevant, as sensible values can lead to the solution converging faster.

All the inflows, sources and outflows, with the exception of those in the arc region (refer to section 4.4.3), are shown in **Figure 4-9**. Summarising, 3 kg/s air flows into the vessel, with 7.65 kg/s flowing in at the post-combustion gap. If all the sources and sinks defined in the EAF model (capacity = 100 tons of steel, vessel diameter = 6.1 m) are considered, this results in a total off-gas mass flow rate of 18.73 kg/s.

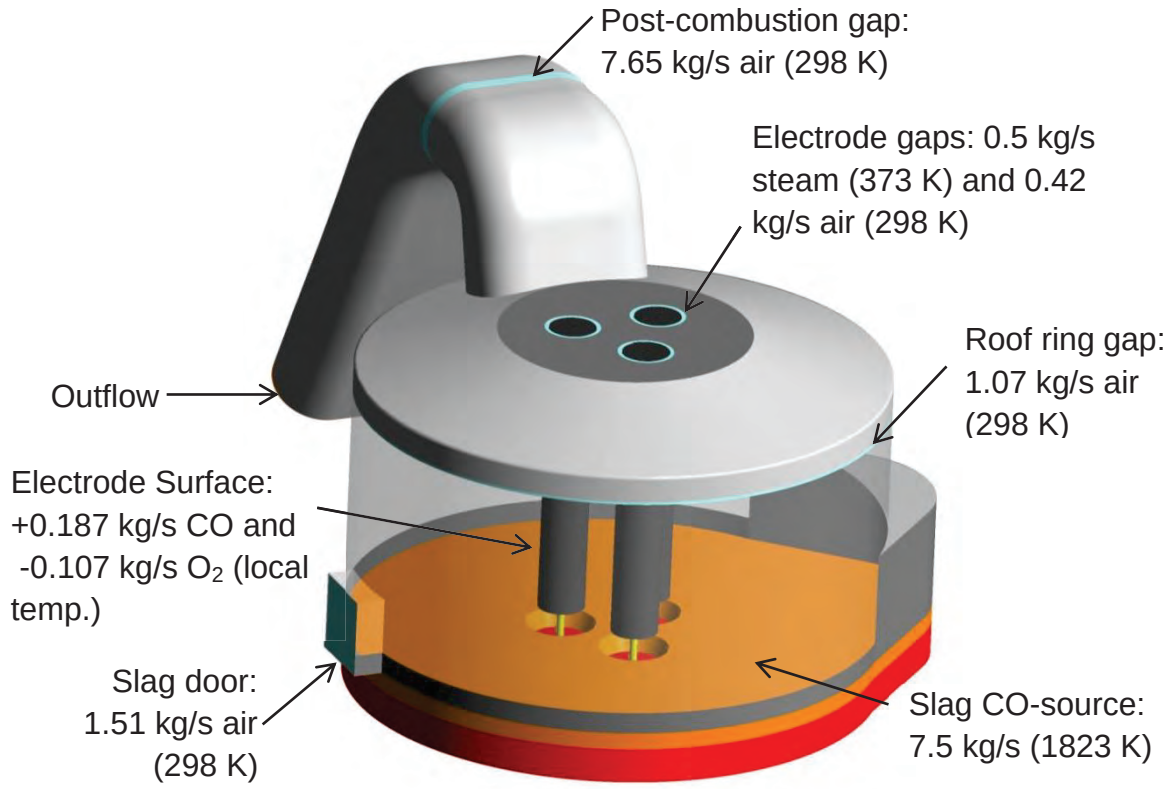

Figure 4-9: Inflows, outflows and sources

By comparison, consider the amount of air flowing into the vessel and at the post-combustion gap of the CONOX model [5] during the power-on flat bath phase without oxygen injection for decarburization. In the case of this larger AC EAF (capacity m_{tap} = 120 to 140 tons of steel, vessel diameter d_{upper_vessel}= 6.900 m), the amount of ingress air was determined to be approximately $\dot{m}_{ingress\_air}$ = 3.52 kg/s. This was calculated by comparing and evaluating off-gas measurements done in the post-combustion gap and further downstream in the exhaust extraction system during an exemplary heat. The amount flowing in at the post-combustion gap was $\dot{m}_{post\_combustion\_air}$ = 9.81 kg/s, corresponding to a total off-gas mass flow rate of $\dot{m}_{total,off-gas}$ = 13.64 kg/s.

At this stage of the model development burners, lances or injectors are not included in the model, as the main emphasis is to qualitatively investigate the influence of the arc region on the amount of post-combustion within the freeboard (refer to

section 1.2). This simplification also has the advantage that it leads to a significant reduction in the necessary mesh size. Furthermore, as explained at the end of section 3.6.3, the inclusion of burners or injectors in the model will probably lead to the necessity to reconsider the turbulent modeling and wall functions.

4.4.2 Electrodes

The outer electrode surfaces are defined to be a thermally coupled non-slip walls with a roughness height K_s = 5 mm and an emissivity of 1 [17].

4.4.3 Electric arc region

The electric arc column is divided into three segments, **Figure 4-10**. Directly under the electrode tip a negative velocity inlet is defined. Here fluid from the furnace atmosphere is drawn into the column with a velocity of 338 m/s. The velocity was adapted during the simulation, so that the mass flow rate drawn out of the solution domain at the top of the arc column is the same as that defined to be flowing back into the solution domain at the base of the column. The value of the velocity therefore depends on the inflow mass flow rate determined in section 3.2, the area chosen to model the inflow region at the top of the arc column and the density of the inflow. The density depends on the temperature and composition, which is a result of the flow field and chemical reactions simulated. When compared to the radial velocities of up to around 400 m/s determined by Quian et al.[28] for the inflow into a 36 kA, 300 mm long DC arc, 338 m/s is acceptable [17]. The intense thermal radiation is taken into account by defining an external black body temperature of 5500 K for the inlet.

The second segment of the arc column is defined to be a moving surface with a surface roughness of 5 mm. It is defined to have a velocity directed downward of 375 m/s. This velocity value was chosen based on the results obtained by Qian et al.[28], Figure 2-18, and is meant to include the effect of the arc jet stream on the fluid adjacent to it in the arc region. The thermal radiation is simulated by defining the surface to have a constant temperature of 5500 K.

The third segment at the base of the column, directly above the melt, is defined to be a mass flow outlet of 0.44 kg/s. The outflow temperature is assumed to be equal to that of the time averaged thermal radiation temperature of the AC arc channels of 5500 K [17]. Thermal radiation is taken into account by defining an external black body temperature of 5500 K. Based on the observation of the simulation results obtained during the development of the model, the outflow is defined to have a composition of 100 wt% CO. It was observed that a fairly stable vortex forms in the arc region of each electrode with only a small amount of “fresh” fluid being entrained from the surrounding atmosphere (refer to section 5.2.1). As there is a large amount of CO flowing out of the slag during decarburization, it makes sense that of the species considered in the EAF model CO is the one most likely to dominate in the vortex. Furthermore, due to the dissociation and ionization of the gas within the electric arc, any CO_2 drawn into the arcs will have dissociated to CO, see Figure 2-28.

The surface representing the arc/electrode interface is defined to have a constant temperature of 3600 K. The contact area between arc and bath is defined to be adiabatic.

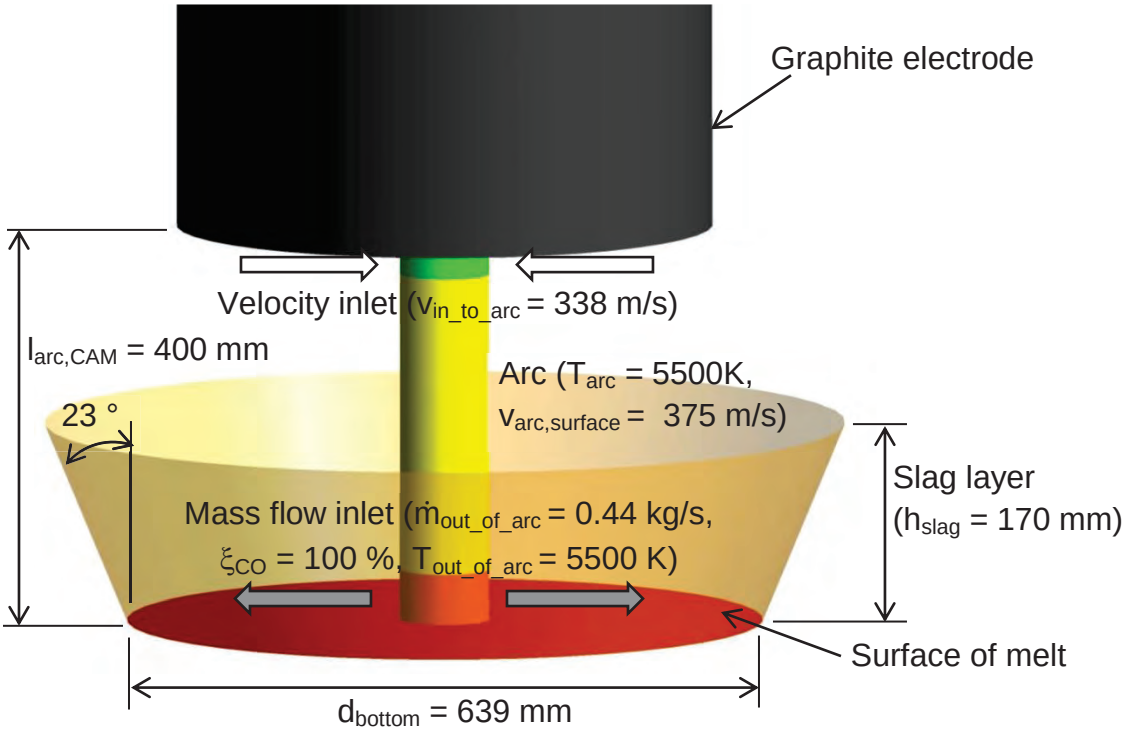

Figure 4-10: Electric arc region

The reason why a temperature of 5500 K was defined to simulate the thermal radiation for all three segments is that in this case there is not one arc with a constant direct electric current. Instead there are three arcs with an alternating current. The temperature defined therefore represents the time averaged temperature of these AC arc columns. As this temperature is unknown, it was varied during the development of the model to determine its influence on the resulting hot spot temperatures at the furnace vessel wall.

With their detailed magneto- fluid dynamic model of a 44 kA DC arc with a length of 300 mm in an air atmosphere Ramírez-Argáez et al.[27] simulate arc temperatures of between 5200 K and 13000 K at the corresponding arc channel radius of the DC arc of 45 mm (CAM). These values were used by Pfeifer et al.[5] for the predecessor version of the EAF model to define a time averaged temperature profile on the surfaces representing the AC arcs. In contrast to a DC arc, the current flowing in the three AC arc fluctuates as a function of the AC frequency of 50 Hz. Therefore, in order to estimate the time averaged arc temperature, a temperature profile with temperatures of between 9882 K and 3953 K was applied [5], by assuming that the three AC arcs would result in thermal radiation comparable to that of a steady DC arc of similar length and intensity. This temperature profile corresponds to an average temperature of the arc channel surfaces of 7538 K. As this temperature lead to unacceptably high temperatures at the vessel walls, it was decreased to 5500 K [17].

As will be discussed in detail in the results section of this thesis, the determination of a correct value for the time averaged arc temperature is one of the challenges that need to be further addressed for future models.

It is not possible to model the change of the form and flow direction of the AC arcs using a quasi-steady state model. Even DC arcs do not necessarily have a stationary rotationally symmetric shape, Figure 2-30. The advantage of the time averaged model of the arc region used in this numerical EAF model in comparison to the previous models is that several of the heat transport mechanisms taking place in a real arc region are represented:

- Heat transfer due to thermal radiation
- The net energy input due to the temperature increase of the flow drawn into and flowing out of the arc column
- The energy input due to the fact that the arc plasma jets have an effect on the circulation within the furnace
- The energy input due to the increased amount of combustion of CO within the furnace due to the improved mixing
- Heat transfer due to convection between the arc column and the fluid adjacent to it in the arc region

When evaluating the comparability of the concept used during this thesis to reality, there is still a large potential for improvement. Nevertheless, in its present form the results help to understand the effect of the different energy input mechanisms of the arc region on the heat and mass flow within the furnace vessel freeboard. The current EAF model is a basis with which a further improvement of the representation of the arc region is now possible.

4.4.4 Surfaces

During the flat-bath stage the melt is usually overheated. The melting range of a specific steel type depends on its alloying elements. For example in data sheets available in the internet for stainless steel type 305, which is an austenitic chromium-nickel stainless steel, a melting range of 1672 K to 1727 K (1399 °C to 1454 °C) is given, whereby for steel type 409, which is a stabilized ferritic stainless steel, a melting range of 1753 K to 1803 K (1480 to 1530 °C) is specified. For the EAF model the bottom boundary of the solid melt layer, which is also the lowest boundary of the solution domain, is defined to have a constant temperature of 1823 K (1550 °C).

The boundary between the modeled solid slag and solid melt region is defined to be thermally coupled. The upper surface of the solid slag layer, at which convection and thermal radiation to the freeboard takes place, is defined to be a thermally coupled non-slip surface with a roughness height of 5 mm. In **Figure 4-11** the different boundary definitions of the outer surfaces are shown.

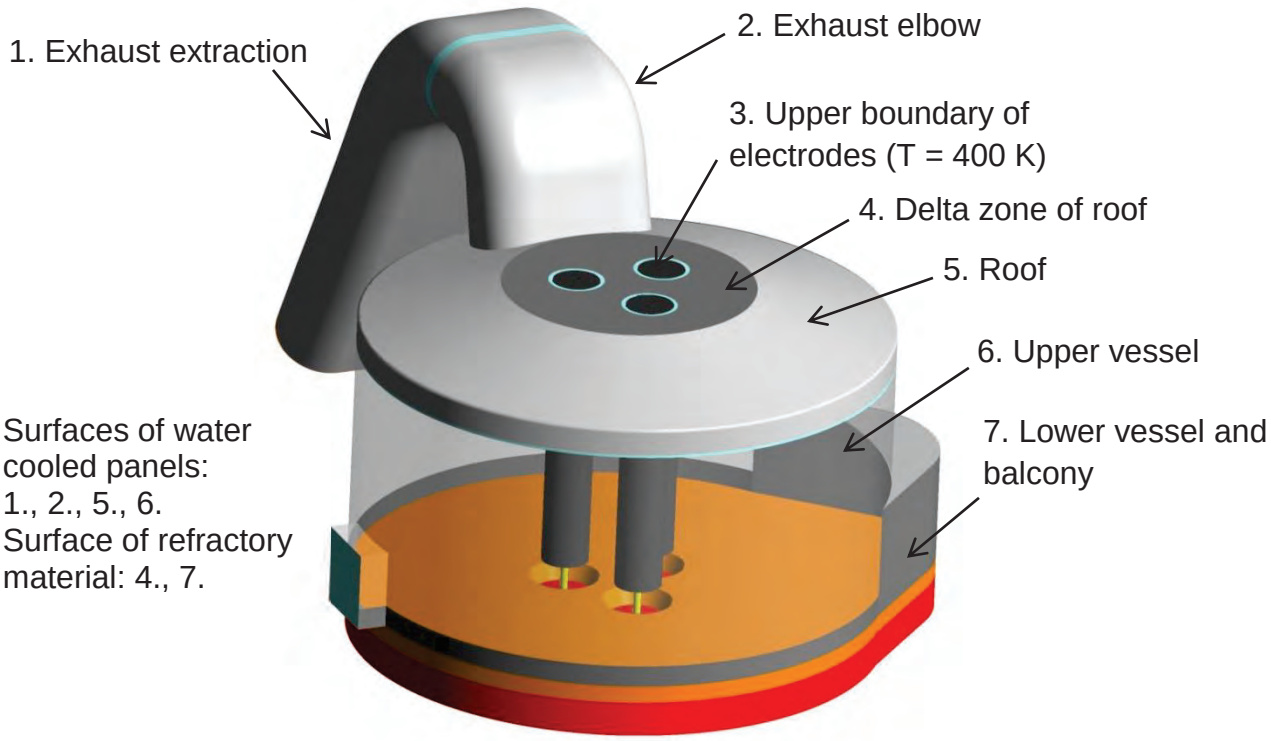

Figure 4-11: Surfaces of the model

Heat is transported away from the upper vessel, roof, exhaust elbow and exhaust extraction by water cooled panels. In general the thermal loading of individual panels depends on their position with respect to the slag line, burners and injectors. Therefore the design of the panels differs. The walls of the lower vessel are usually made up of fire bricks and other refractory materials. The inner surface of both the upper and lower vessel in the freeboard is mostly coated with a layer of slag, whose composition, thickness and roughness is not homogeneous and changes continuously during a heat as new material solidifies on the surface or melts, depending on the conditions and thermal loading [17].

For the numerical EAF model these boundaries are defined as walls with a roughness height K_s = 5 mm and a roughness constant C_s = 0.5. The walls of the upper vessel, roof and exhaust elbow are assumed to have a solid slag coating with a thickness of 20 mm. The walls of the exhaust extraction are assumed to have an equivalent 20 mm thick coating of dust. An external temperature, at the outside surface of the slag/dust layer, of 333 K (60 °C) is specified for these cooled surfaces.

The walls of the lower vessel, balcony and delta zone of the electrodes are defined to consist of refractory material with a thickness of 500 mm which is cooled by natural convection and thermal radiation to the ambient on the outside of the vessel. An external heat transfer coefficient of 5 W/(m^2·K), a free stream temperature and ambient temperature of 298 K (25 °C) and an external emissivity of 0.85 is defined.

5 Results

5.1 Overview of simulations

Three simulations, referred to in this section as Simulation 1, 2 and 3, were carried out with the EAF model. In **Table 5-1** a summary of the defined mass flow rates into the freeboard for all three simulations is shown. **Table 5-2** gives an overview of the differences between the three simulations.

Table 5-1: Mass flow rates into the freeboard

Location	Mass flow rate	Temperature
Simulation 1, 2 and 3		
CO source at slag surface	7.5 kg/s	1823 K
Air inflow through combustion gap	7.65 kg/s	298 K
Air inflow through slag door	1.51 kg/s	298 K
Air inflow through roof gap	1.07 kg/s	298 K
Air inflow through electrode gaps	0.42 kg/s	298 K
Steam inflow at electrode gaps	0.50 kg/s	373 K
CO source and O_2 sink at electrode surfaces	0.19 kg/s CO (-0.11 kg/s O_2)	Local gas temperature
Simulation 1 and 3		
Mass flow rate of furnace atmosphere into each arc	0.44 kg/s	Local gas temperature
Mass flow rate of CO out of each arc	0.44 kg/s	5500 K
Simulation 2		
Mass flow rate of furnace atmosphere into each arc	0.0 kg/s	-
Mass flow rate of CO out of each arc	0.0 kg/s	-

Simulation 1 is the reference simulation. In this case the arc in- and outflow is taken into account and the slag height of 170 mm means that the free-burning arc length is 230 mm. As can be seen in Table 5-1, the difference between Simulation 1 and 2 is that the arc in- and outflow is not taken into account in Simulation 2. Instead the velocity inlet and mass flow outlet at the top and base of each arc column, described in detail in section 4.4.3, are redefined to be a surface with a roughness of 5 mm and with a temperature of 5500 K. A comparison of the results of Simulation 1 and 2 enables an evaluation of the influence of the inclusion of the energy input due to the heating and increase in momentum of the furnace atmosphere drawn into and flowing out of the arc region on the resulting energy flows and post combustion within the furnace freeboard. Simulation 1 and 2 were carried out using the geometry and

mesh described in section 4. With the exception of the arc in- and outflow, all the other boundary conditions for Simulation 1 and 2 are identical.

The difference between Simulation 1 and 3 is that whereas for Simulation 1 a slag height of 170 mm and a corresponding free-burning arc length of 230 mm are considered, for Simulation 3 the free-burning arc length is only 50 mm with an increased slag height of 350 mm. As the geometry of the EAF model was divided into volumes in order to allow a structured meshing, only a redefinition of the material of the relevant volumes above the slag layer was necessary in order to adapt the EAF model for Simulation 3, section 4.1. Therefore the same mesh as for Simulation 1 and 2 was used. The aim of Simulation 3 is to investigate the influence of a change in the free-burning arc length from 230 mm to a free-burning arc length of only 50 mm on the conditions within the freeboard. The motivation for this is that a free-burning arc length of 230 mm occurs only seldom during a normal steelmaking heat, as such a large free-burning arc length leads to the formation of hot spots on the inner surface of the upper vessel wall. These can lead to perforation of the water cooled panels, if the hot spot temperature exceeds 1800 K (1527 °C) [26]. By comparing the results of Simulation 1 and 3, a qualitative estimate of the magnitude of the influence of the flow in the arc region on the post-combustion of CO to CO_2 within the freeboard in dependence of the free-burning arc length can be made. The boundary conditions of Simulation 1 and 3 are identical.

Table 5-2: Differences between the simulations

Name	Comparison of arc region conditions
Simulation 1	With arc in- and outflow, slag height = 170 mm, arc length = 400 mm free-burning arc length = 230 mm
Simulation 2	Without arc in- and out-flow, slag height = 170 mm, arc length = 400 mm free-burning arc length = 230 mm
Simulation 3	With arc in- and outflow, slag height = 350 mm, arc length = 400 mm free-burning arc length = 50 mm

For all three simulations the flow field is characterised by first illustrating the streamlines of the flow starting at the slag door, roof-ring gap and electrode gaps. Streamlines make it possible to understand the three-dimensional nature of the flow. In addition, the simulated flow fields are characterised with the help of normalized vector plots of the velocity distribution. Thereafter the resulting temperature distributions within the vessel, on the vessel walls, on the slag surface and electrodes are shown. These lead to a better understanding of the redistribution of the energy input of the electric arcs within the furnace. Contour plots of the simulated mass fractions of CO, O_2, and CO_2 show the mass transfer within the freeboard and the

dependence of the post-combustion within the freeboard on the temperature distribution as well as the extent to which the incoming O_2 mixes with the CO.

In order to generate the vector and contour plots, three cross-sectional planes were defined. The origin of the co-ordinate system, X = Y = Z = 0.0 m, is located at the surface of the bath in the centre of the vessel. The cross-sectional planes are shown in **Figure 5-1**. In addition to the results discussed in this chapter, further results of the simulations are given in the appendix (section 9.2).

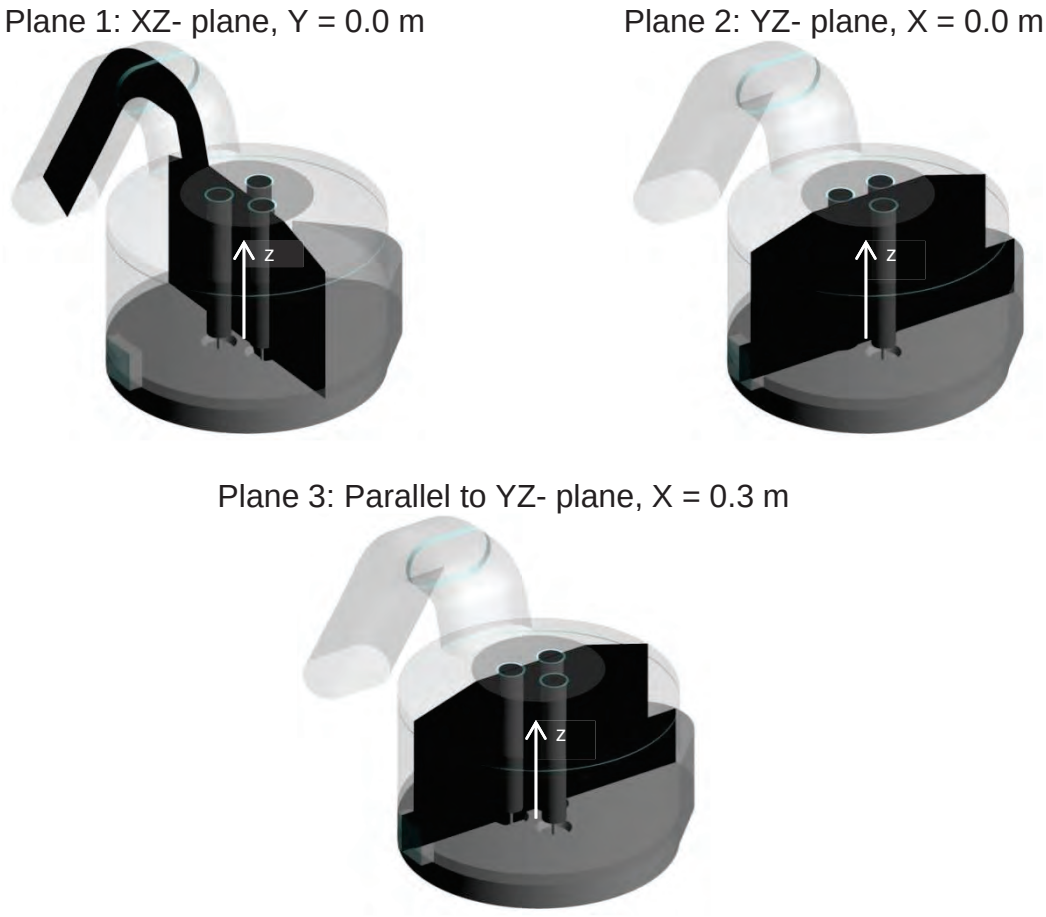

Figure 5-1: Cross-sectional planes defined to generate the vector and contour plots

5.2 Arc region modelling

5.2.1 Flow field

In **Figure 5-2** the resulting streamlines from the slag door with and without arc in- and outflow are compared. It is evident that the inclusion of the arc in- and outflow has a marked effect on the flow field. There is an increased circulation with higher velocity magnitudes within the entire freeboard, which is evident when considering the velocity vectors shown in **Figure 5-3.**

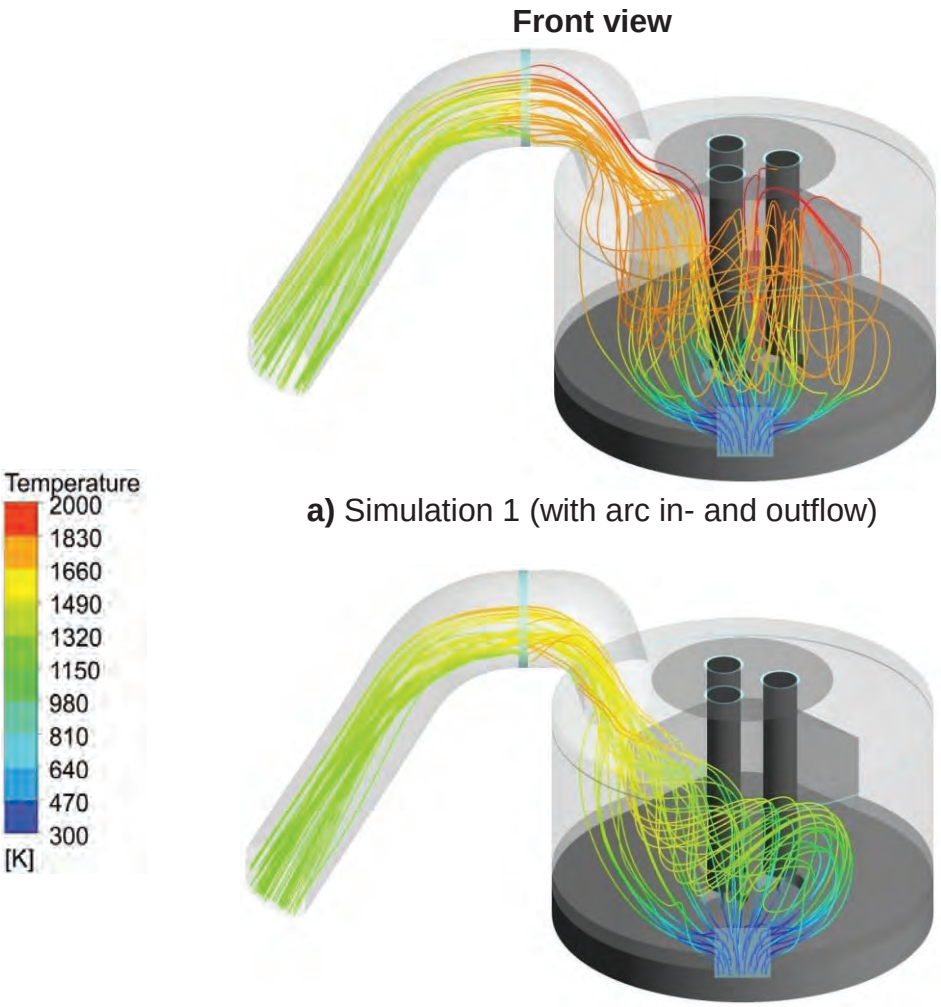

a) Simulation 1 (with arc in- and outflow)

b) Simulation 2 (without arc in- and outflow)

c) Simulation 1 (with arc in- and outflow)

d) Simulation 2 (without arc in- and outflow)

Figure 5-2: Streamlines from slag door coloured according to the temperature of the furnace atmosphere for Simulation 1 and 2

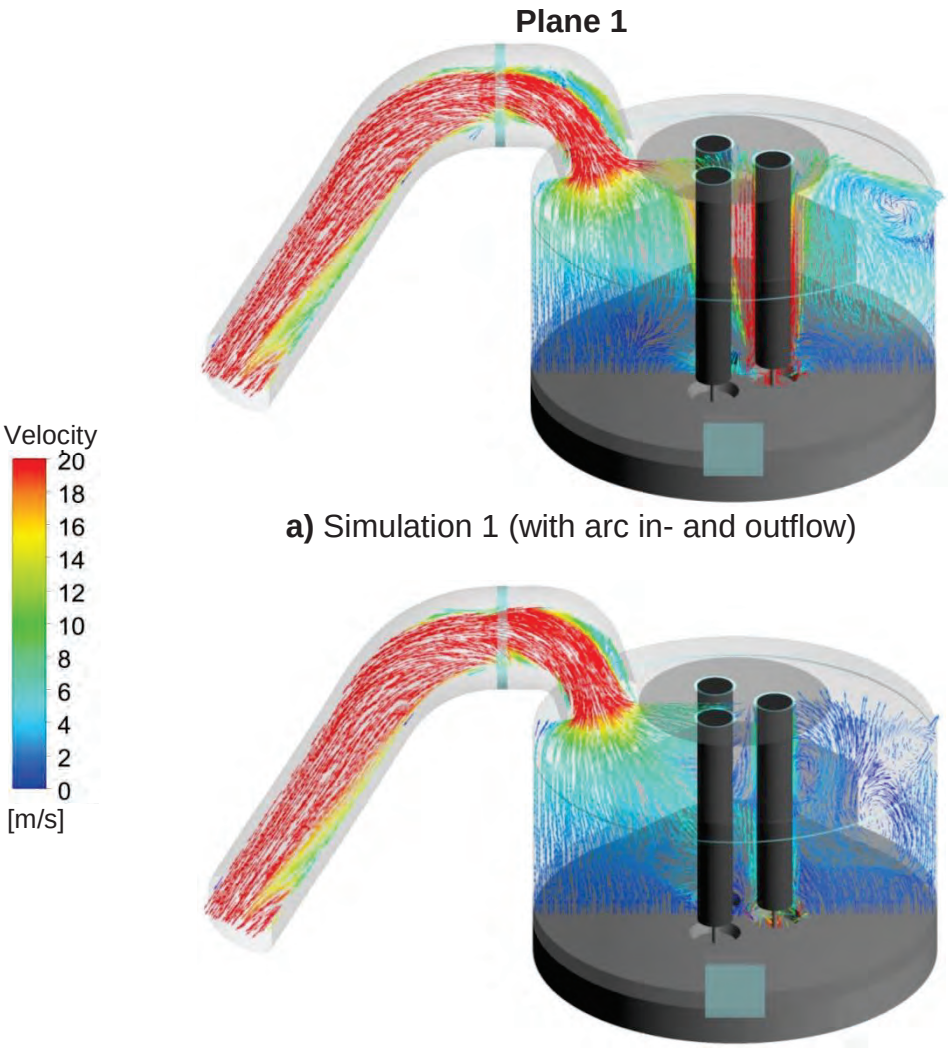

a) Simulation 1 (with arc in- and outflow)

b) Simulation 2 (without arc in- and outflow)

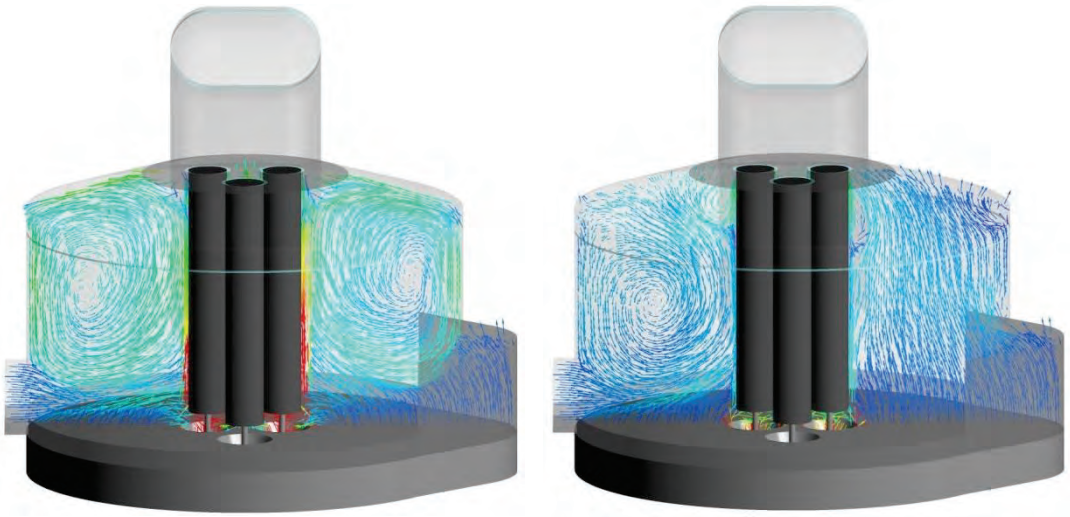

c) Simulation 1 (with arc in- and outflow)

d) Simulation 2 (without arc in- and outflow)

Figure 5-3: Comparison of normalized velocity vectors in plane 1 and 3 for Simulation 1 and 2

For both simulations the mass flow rate of air from the slag door of 1.51 kg/s, which has an initial temperature of 298 K and an initial velocity of 1.585 m/s, is diverted upwards and mixes with the flow of CO coming up out of the slag layer. This mass flow rate of CO has an initial velocity of approximately 1.4 m/s and a temperature of 1823 K (1550 °C). In the case of Simulation 1, in addition to the mass flow rate of CO coming out of the slag layer and the ingress air flowing in at the slag door, roof gap and electrode gaps, a mass flow rate of furnace atmosphere of 0.44 kg/s is drawn into each arc with a velocity of 338 m/s. Furthermore 0.44 kg/s of CO with a temperature of 5500 K and an average velocity of 506 m/s flows back into the freeboard at the base of each arc.

The difference between the flow patterns in Figure 5-2a, Figure 5-2c and Figure 5-2b, Figure 5-2d is therefore that due to the momentum and temperature of the flow in the arc region the surrounding furnace atmosphere is firstly heated and secondly accelerated upward. The upward acceleration is especially evident when comparing the velocity vectors around the electrodes in Figure 5-3**.**

Contrary to the AC EAF model of Chan et al.[20] described in section 2.1, who assume that buoyancy effects are negligible, in this EAF simulation model the vertical body forces F_z due to the gravitational acceleration are taken into account. The vertical body forces are calculated according to eq. (31) in section 3.6.1. Consequently the simulated increased circulation is not just due to the exchange of momentum between the incoming air and the vortices in the arc region, to a certain extent it is also due to a difference in buoyancy forces. As shown in **Figure 5-4,** due to the in- and outflow in the arc region the temperatures of the furnace atmosphere between the electrodes of Simulation 1 are higher than those of Simulation 2.

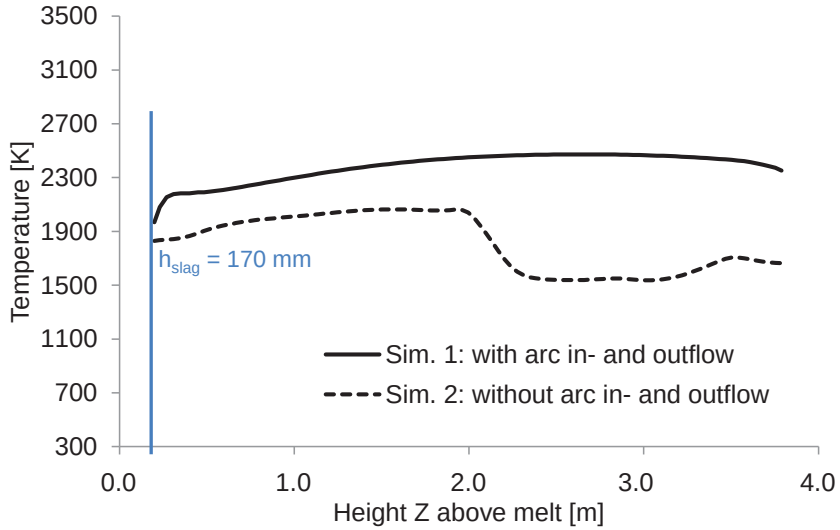

Figure 5-4: Temperature versus height along the Z-axis in the centre of the upper vessel (X = 0.0 m; Y = 0.0 m) for Simulation 1 and 2

The resulting difference in buoyancy is clear when considering the distribution of the vertical body force due to buoyance in N/m^3 shown in **Figure 5-5**. This shows that the

furnace atmosphere in the centre of the electrodes experiences different buoyancy forces for Simulation 1 than for Simulation 2, which will slightly increase the acceleration of the furnace atmosphere directly around the electrodes. Furthermore the difference in buoyancy of the cold ingress air in comparison to the CO rising up out of the slag leads to the conclusion, that especially if ingress air is to be considered it is important to take buoyancy into account in the simulation model, as its influence on the flow field is not negligible.

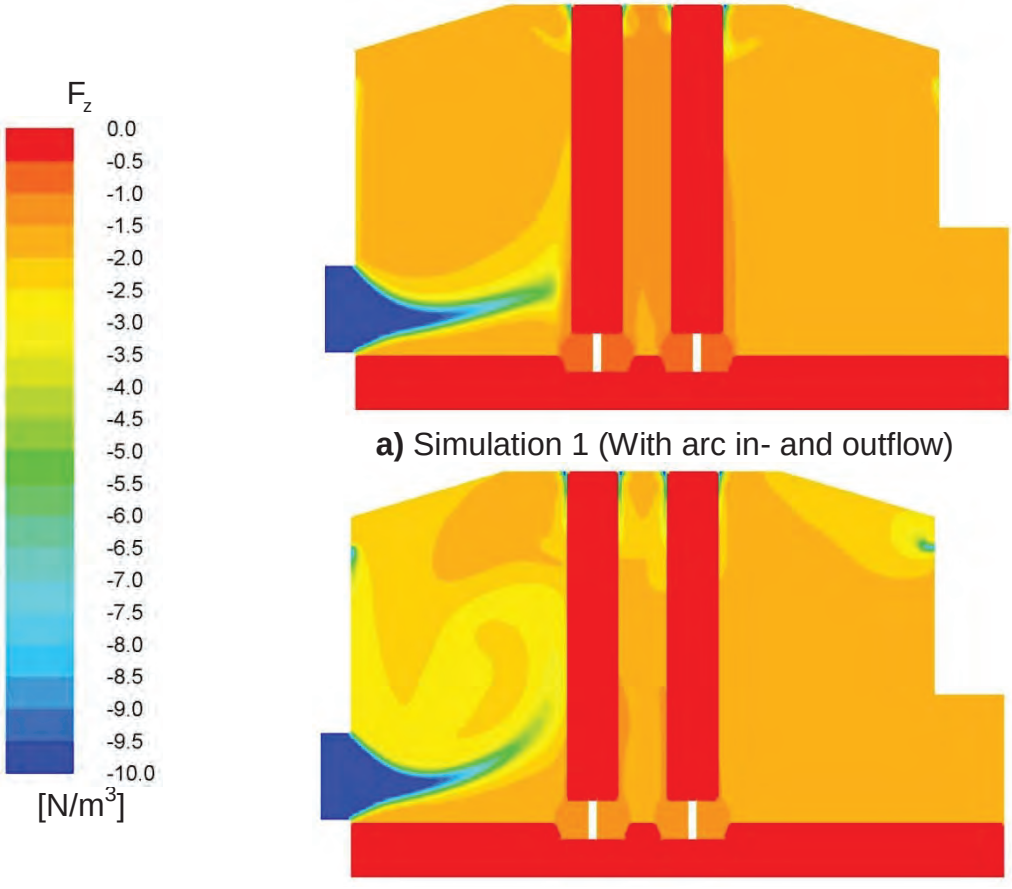

a) Simulation 1 (With arc in- and outflow)

b) Simulation 2 (Without arc in- and outflow)

Figure 5-5: Vertical body force distribution due to buoyancy in plane 3 for Simulation 1 and 2

The velocity vectors in the arc region are shown in **Figure 5-6**. A downward velocity of -375 m/s is defined at the surfaces representing an arc channel for both simulations. As a result, a swirling flow pattern, which almost has the form of a circle torus, results around each arc for both simulations. Due to the arc in and outflow taken into account in Simulation 1, the corresponding circulation in the arc region is much stronger with higher velocities which have a larger effect on the surrounding furnace atmosphere.

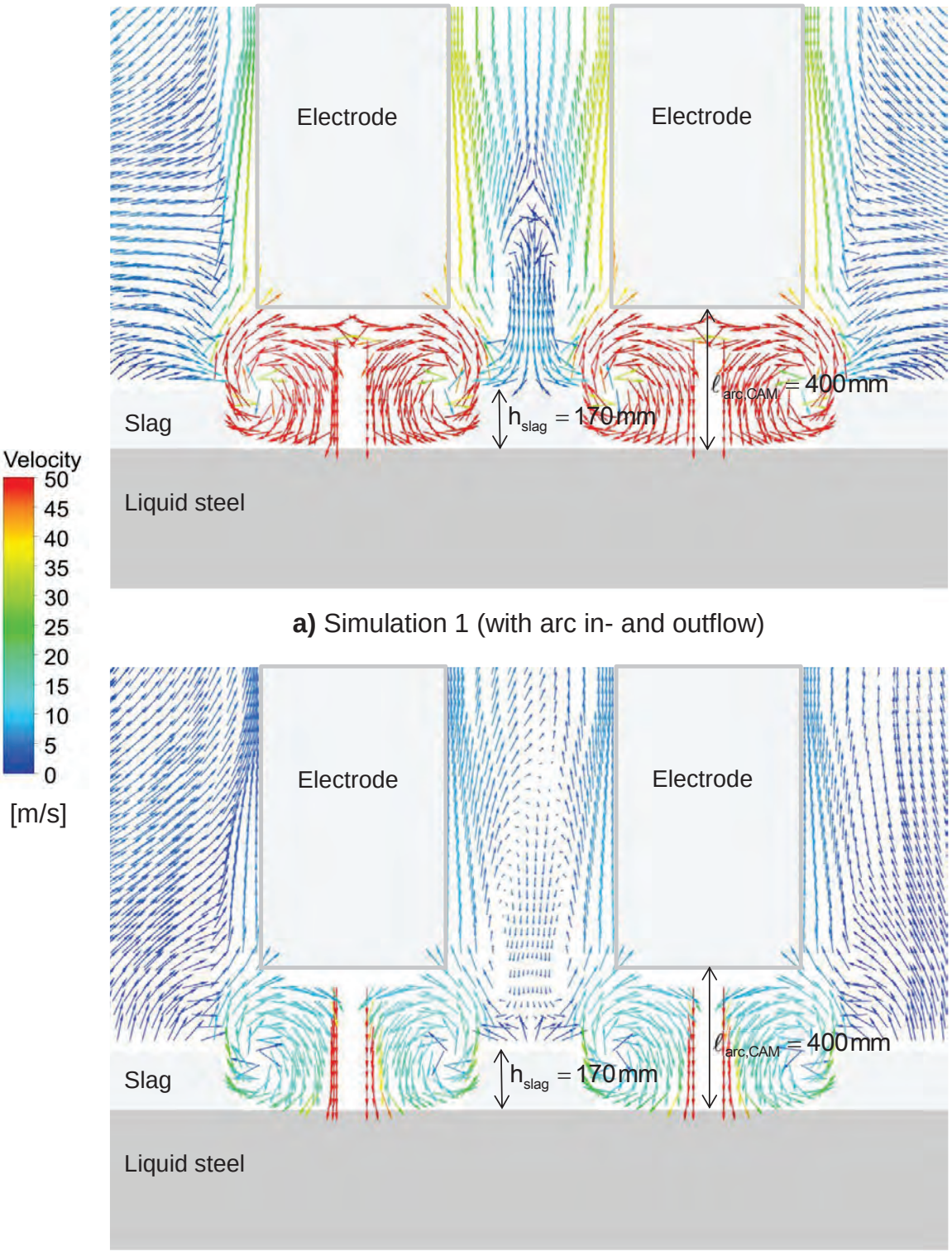

a) Simulation 1 (with arc in- and outflow)

b) Simulation 2 (without arc in- and outflow)

Figure 5-6: Normalized velocity vectors around the arc region in plane 3 (parallel to YZ- plane, X = 0.3 m) for Simulation 1 and 2

For Simulation 1 the defined inlet velocity of the arc inflow was varied during the simulation, until the defined mass flow rate out of the arcs is equal to the arc inflow. This was necessary as the mass flow rate into the arcs is dependent on the resulting composition and temperature of the furnace atmosphere drawn in at the inlet. The

simulated mass flow rate into the arcs can be calculated with eq. (55) using the defined inlet velocity, the resulting inflow density, which depends on the local gas temperature and composition, and the inlet area. As was explained in section 3.2, this value is only an approximation of the true mass inflow, as the gas components are in reality dissociating and ionizing as they flow into the arcs.

$$\dot{m}_{arc,inflow} = \rho_{arc,inflow} \cdot v_{arc,inflow} \cdot A_{arc,inlet} \quad (55)$$

For Simulation 1 the final inflow velocity is defined to be 338 m/s. The resulting composition of the inflow is 0.052 wt% O_2, 1.149 wt% N_2, 98.563 wt% CO, 0.114 wt% CO_2 and 0.122 wt% H_2O with an average temperature of 3666 K (3393 °C). Therefore the density, according to the incompressible ideal gas law, is 0.0931 kg/m^3. For this inlet velocity the resulting total mass flow rate into the arcs is only 0.12 % higher than that flowing out of the arcs.

5.2.2 Temperature distributions

A comparison of the temperature distribution within the freeboard with and without arc in- and outflow is shown in **Figure 5-7**. The path of the ingress air flowing in at the slag door, roof-ring gap and electrode gaps can be easily identified. Due to the increased circulation and higher upward velocities around the electrodes for Simulation 1, the air coming in at the electrode gaps initially does not penetrate as far into the vessel as for Simulation 2. When looking at the temperature distributions, the same seems to be the case for the ingress air from the roof-ring gap.

However, if the streamlines from the electrode gaps and roof-ring gap in **Figure 5-8** are considered, it is clear that the increased circulation resulting from the modelling of the arc region of Simulation 1 leads to an improved mixing of the ingress air with the hot CO within the entire freeboard.

The temperature distribution within the freeboard depends on the flow field, convection, thermal radiation exchange and on the energy generated due to post-combustion within the vessel. The contour plots shown in Figure 5-7 are therefore a result of the interaction of these heat and mass transport phenomena and chemical reactions.

Due to the inclusion of the graphite electrodes in the solution domain, their simulated three-dimensional temperature distribution, shown in **Figure 5-9**, results from the interaction of thermal radiation exchange, Joule heating, thermal conduction along the electrodes and convective heat transfer at the electrode outer surfaces. The temperature distribution on the slag surface, which is modeled as a solid, depends not only on convection and thermal radiation exchange, but also on thermal conduction within the slag and melt layer.

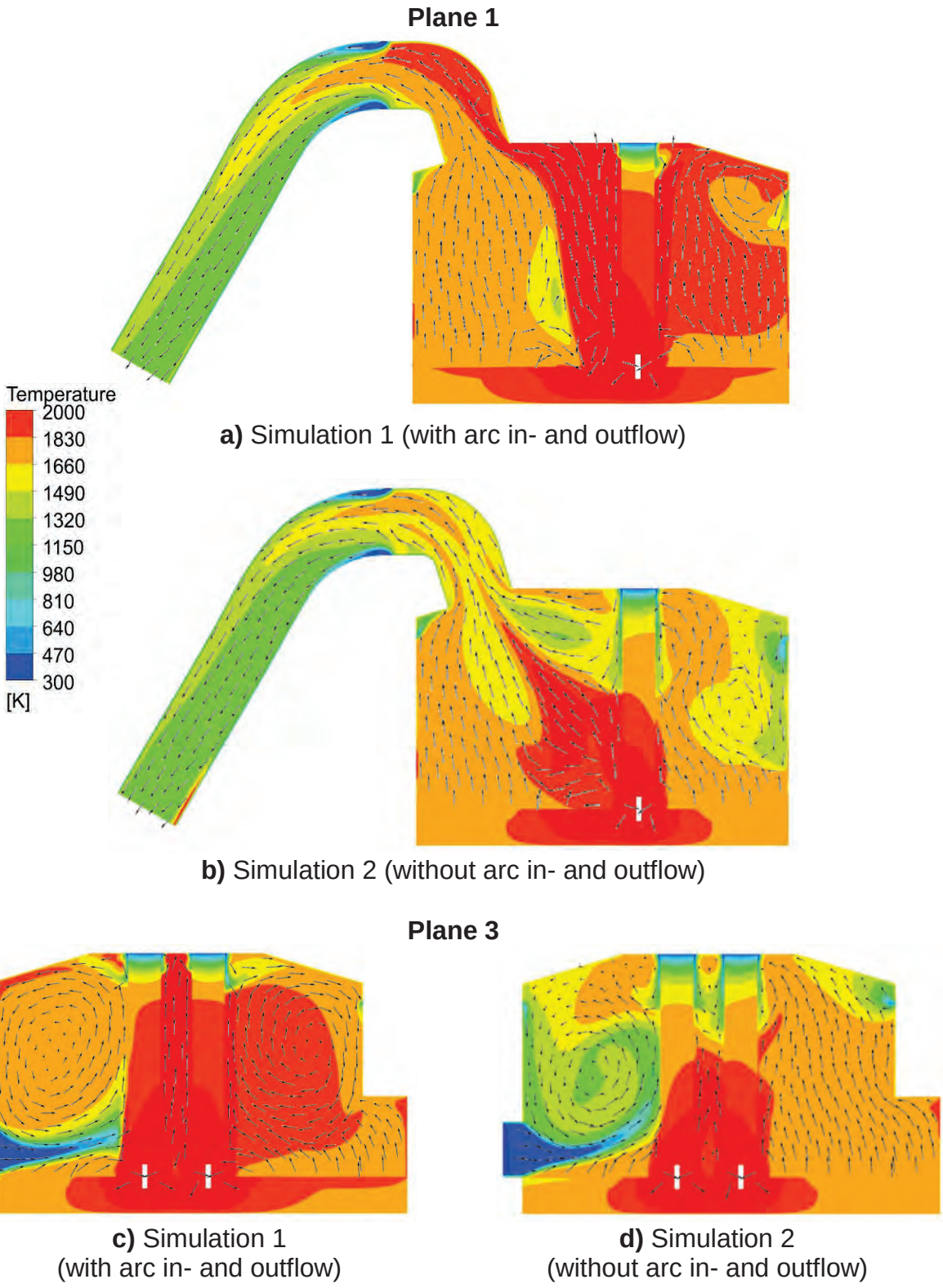

Figure 5-7: Temperature distribution for Simulation 1 and 2

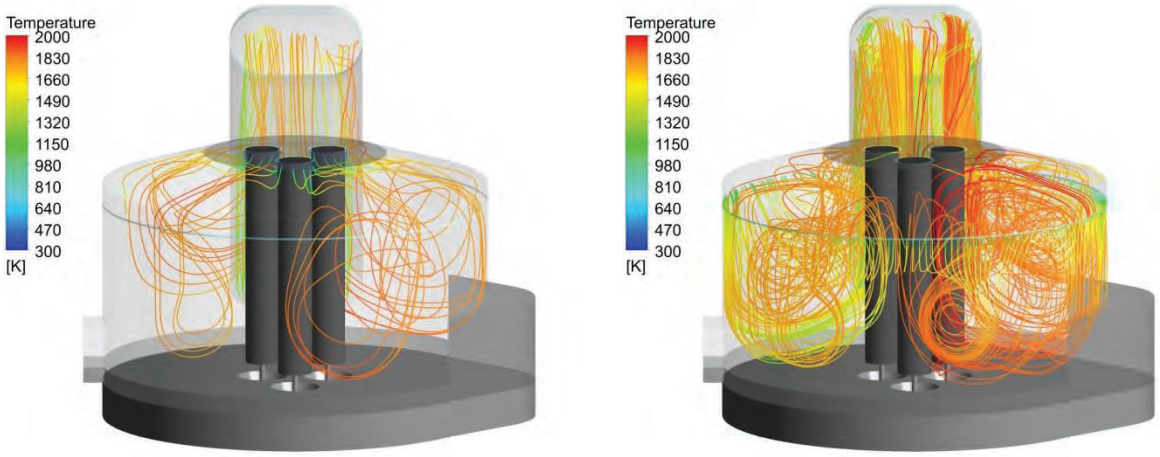

a) Sim. 1 - Electrode gaps streamlines **b)** Sim. 1 - Roof-ring gap streamlines

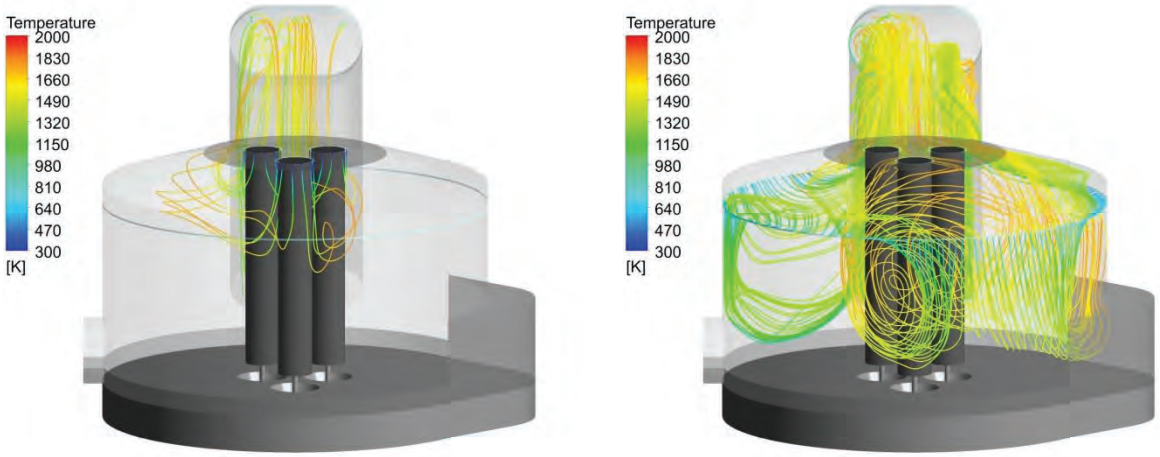

c) Sim. 2 - Electrode gaps streamlines **d)** Sim. 2 - Roof-ring gap streamlines

Figure 5-8: Streamlines from the electrode gaps and roof-ring gap for Sim. 1 and 2

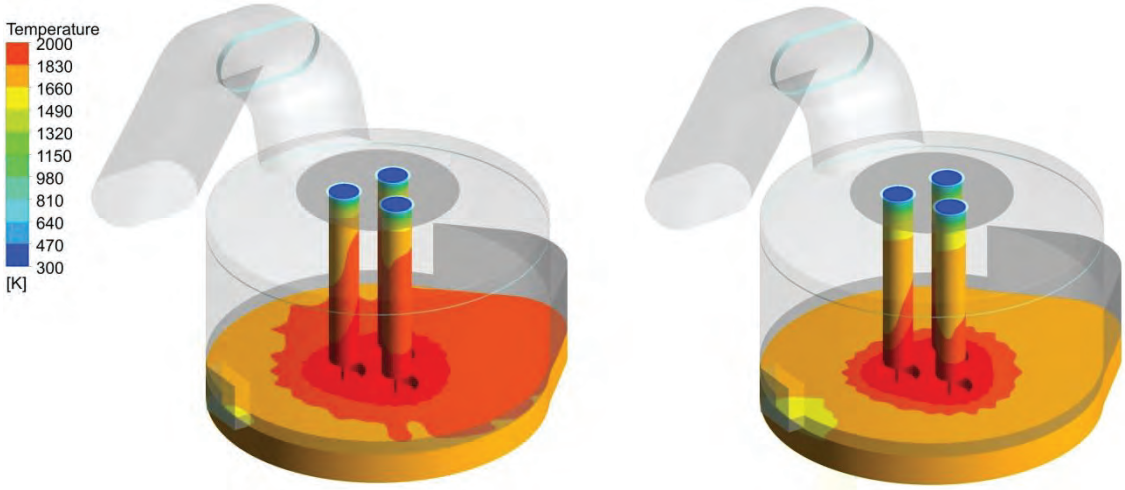

a) Sim. 1 (With arc in- and outflow) **b)** Sim. 2 (Without arc in- and outflow)

Figure 5-9: Temperature distributions on the electrode and slag surfaces for Simulation 1 and 2

The inclusion of the arc in- and outflow leads to a definite increase in the temperature distribution on the slag surface and on the electrodes surfaces. One of the reasons for the higher temperatures in the balcony region on the slag surface is an increased amount of thermal radiation received from the furnace atmosphere, which also has a higher temperature than for Simulation 2 (see Figure 5-7). The thermal radiation absorption coefficient, which is a function of the volume fraction of H_2O and CO_2, is shown in **Figure 5-10**.

a) Sim. 1 (With arc in- and outflow) **b)** Sim. 2 (Without arc in- and outflow)

Figure 5-10: Absorption coefficient in Plane 3 (Sim. 1 and 2)

There is water vapor defined to be entering the furnace at the electrode gaps due to electrode cooling. As a result of the increased circulation, this H_2O is more thoroughly mixed into the furnace atmosphere (see Figure 5-8.a), leading to an increase in the thermal radiation absorption coefficient within the freeboard. This is the variable a in the radiative transfer equation (section 3.4), which has an influence on the amount of thermal radiation absorbed by the thermal atmosphere and therefore also on the amount emitted as specified by the radiative transfer equation. Furthermore, the improved mixing leads to a higher post-combustion of CO to CO_2. This also contributes towards the difference in absorption coefficients of Simulation 1 in comparison to those of Simulation 2.

The temperature versus length on the inner side (X = -330.5 mm; Y = 0.0 mm) and outer side (X = -869.5 mm; Y=0.0) of the electrode furthest away from the 4^{th}-hole is shown in **Figure 5-11**. The maximum temperature difference between the side facing the other electrodes and the side facing towards the EAF vessel wall is 402 K, which is approximately 15% of the average electrode temperature at that height above the melt.

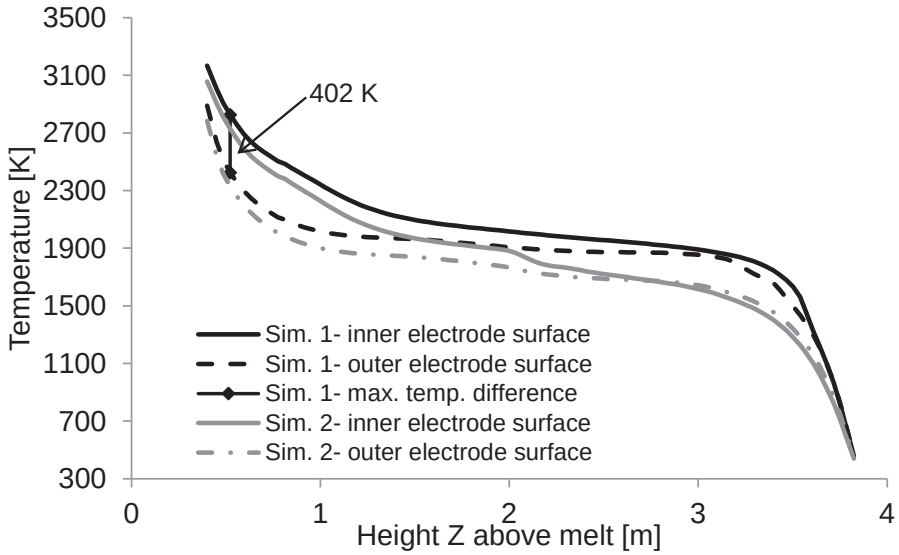

Figure 5-11: Temperature profiles on electrode surface furthest from slag door

The temperature distributions on the outer surfaces of the EAF model are dependent on convection and thermal radiation exchange. They are shown in **Figure 5-12**.

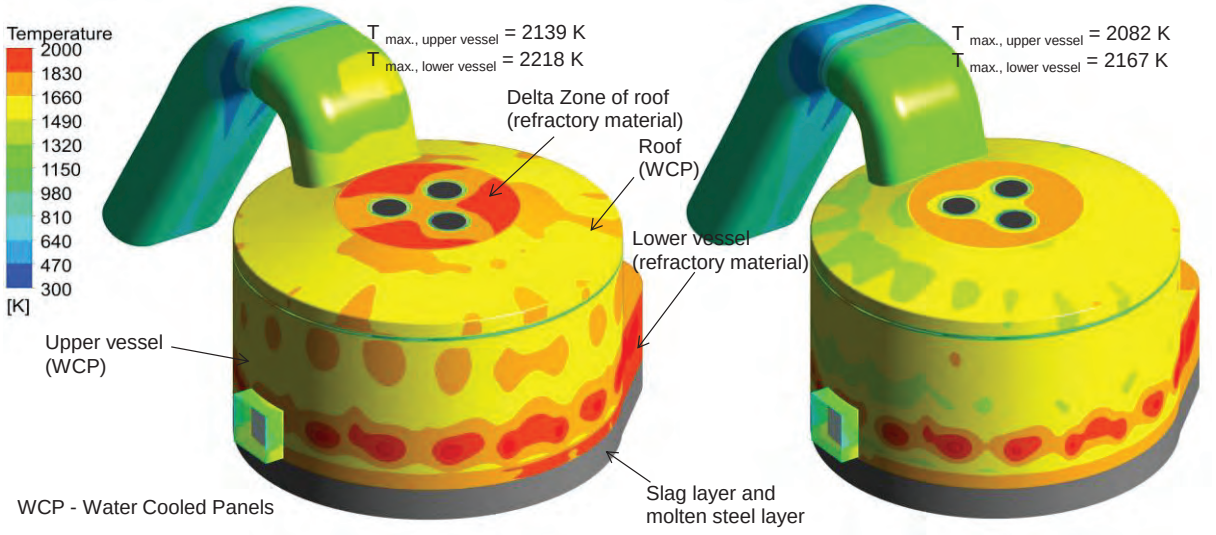

a) Sim. 1 (With arc in- and outflow) **b)** Sim. 2 (Without arc in- and outflow)

Figure 5-12: Temperature distributions on the outer walls above the slag layer

The maximum hot spot temperatures in Figure 5-12 are slightly higher than they would be using a resolution of $N_\theta = 4$ and $N_\phi = 5$ for the DO thermal radiation model (refer to section 3.4). The maximum hot spot temperature of the upper vessel of Simulation 1, which is 2139 K, is only 57 K higher than that of Simulation 2. The higher temperatures on the walls of Simulation 1 reflect the energy input due to the arc in- and outflow and increased post-combustion. The hot spot temperatures of both simulations would in reality cause the slag layer protecting the water cooled panels to melt. Due to the fact that the maximum allowable temperature to avoid perforation of the panels is approximately 1800 K [26], these hot spot temperatures

are not reached in reality during the flat-bath phase in an EAF. The reason for this discrepancy will be discussed in detail in section 6.

5.2.3 Mass transfer and post-combustion

The effect of the increased mixing on the mass transfer can be seen by considering the resulting mass fraction distributions of the most relevant species.

In **Figure 5-13** and **Figure 5-14** the mass fractions of CO and O_2 are shown. The local kinetic reaction rate of CO and O_2 to CO_2 is dependent on temperature and the molar concentration of the reactants and products, whereby the concentration of H_2O also plays an important role. In addition the eddy dissipation reaction rate depends on the turbulent mixing.Due to the relatively large amount of CO coming out of the slag, even if the furnace atmosphere were perfectly mixed, the sub-stoichiometric amount of ingress air would correspond to an air-fuel equivalence ratio of only λ = 0.16. This limits the amount of post-combustion. Due to the high temperatures the kinetic reaction rates are fairly high. As shown in section 3.5, it is the turbulent mixing rate which limits the amount of post-combustion simulated in the EAF vessel.

In **Figure 5-15** the resulting mass fraction distribution of CO_2 of Simulation 1 and 2 are compared.

The total amount of CO_2 leaving the EAF vessel through the 4th hole for Simulation 1 and Simulation 2 is compared in **Table 5-3.** The mass flow rate of CO_2 out of 4th hole of Simulation 1 is 78 % higher than for Simulation 2. Due to the resulting higher sum of heat of reaction within the vessel, this corresponds to an increased energy input due to post-combustion within the vessel of 1.28 MW.

Table 5-3: Post-combustion within the EAF vessel (Sim.1 and 2)

Simulation	$\dot{m}_{CO_2,4^{th}-hole}$	$\Delta\dot{E}_{chem.Reac.,EAF\,vessel}$
1	0.455 kg/s	2.92 MW
2	0.255 kg/s	1.64 MW

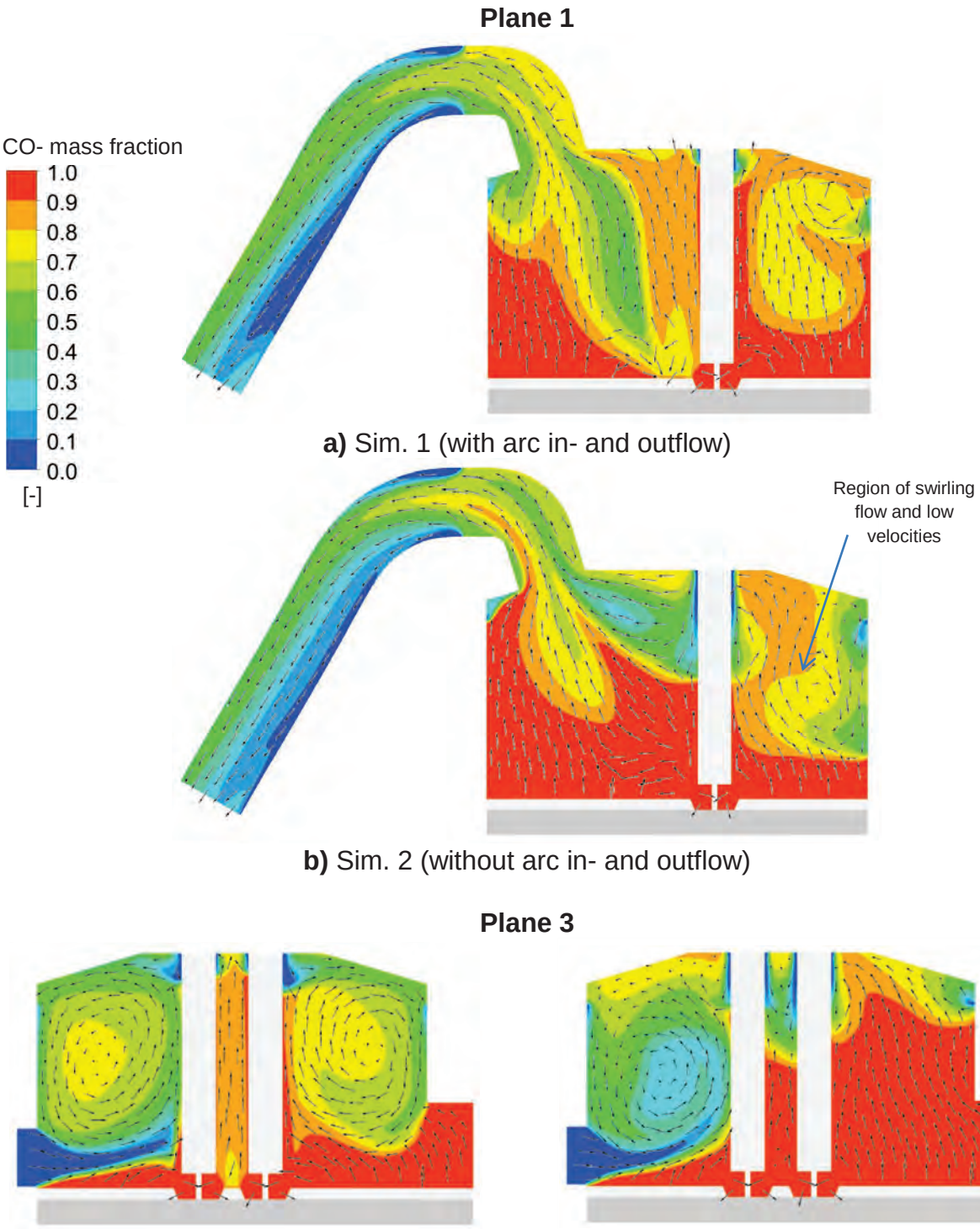

a) Sim. 1 (with arc in- and outflow)

b) Sim. 2 (without arc in- and outflow)

c) Sim. 1 (with arc in- and outflow) **d)** Sim. 2 (without arc in- and outflow)

Figure 5-13: CO Mass fraction distribution for Simulation 1 and 2

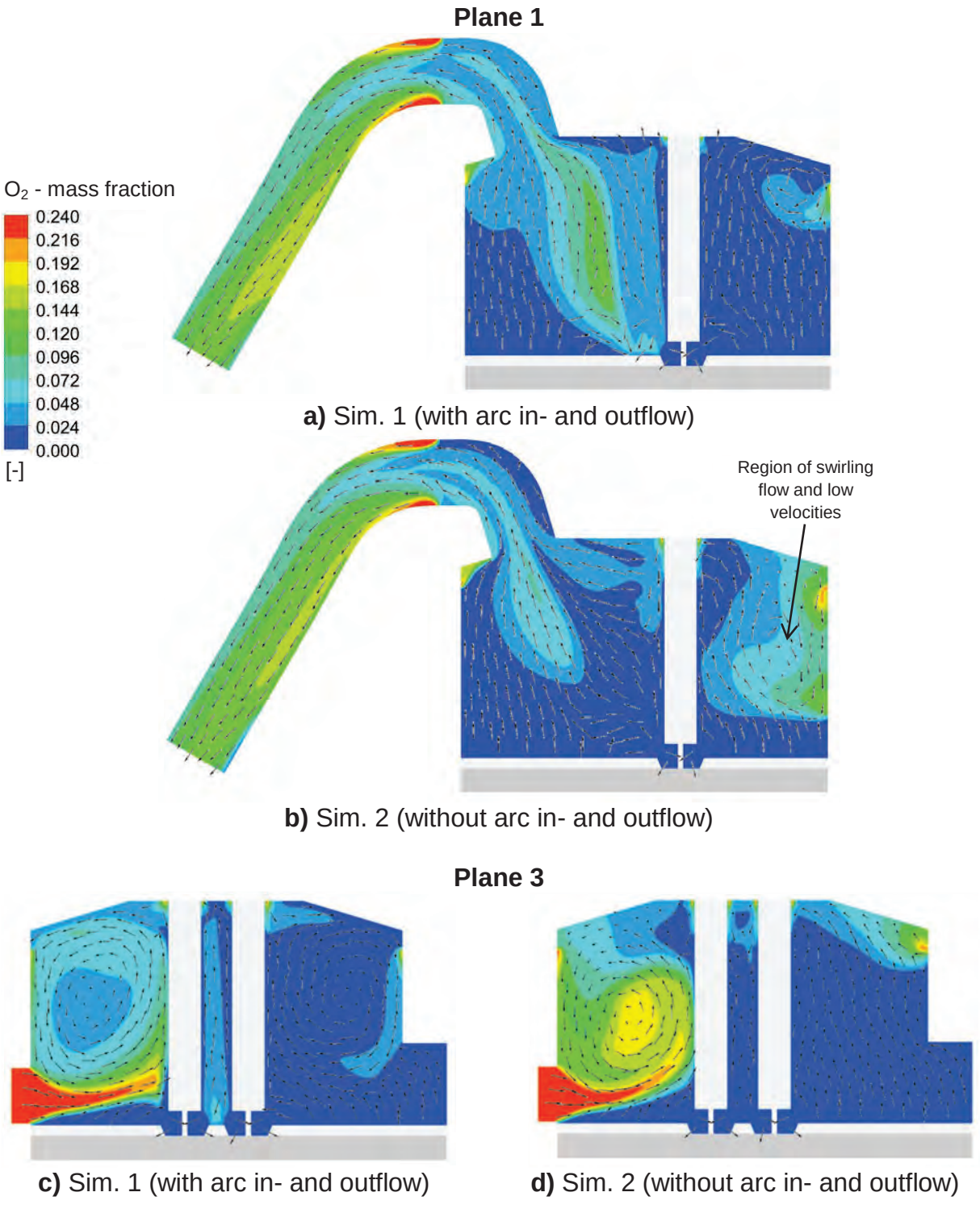

a) Sim. 1 (with arc in- and outflow)

b) Sim. 2 (without arc in- and outflow)

c) Sim. 1 (with arc in- and outflow)

d) Sim. 2 (without arc in- and outflow)

Figure 5-14: O_2 Mass fraction distribution for Simulation 1 and 2

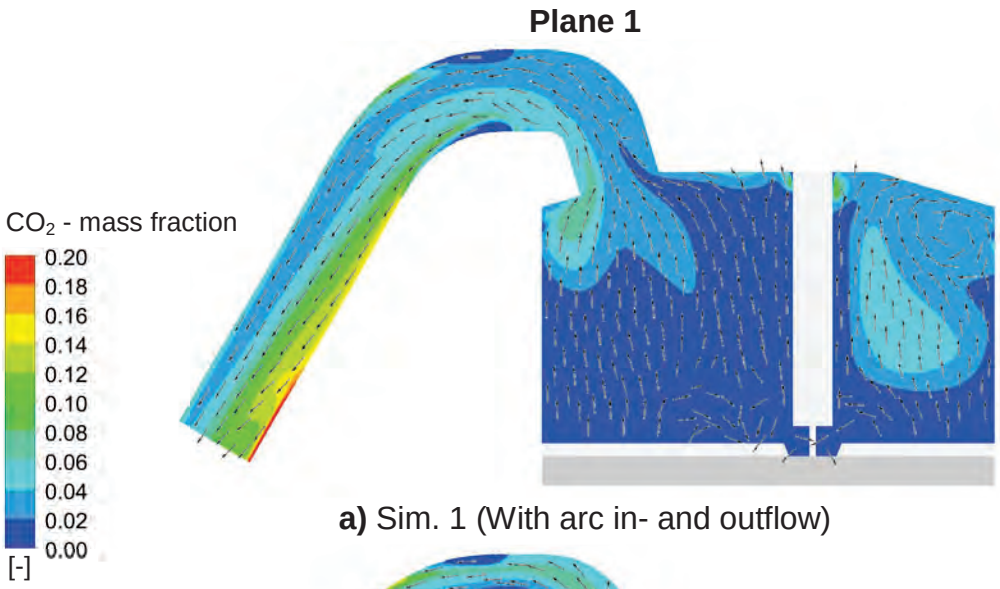

a) Sim. 1 (With arc in- and outflow)

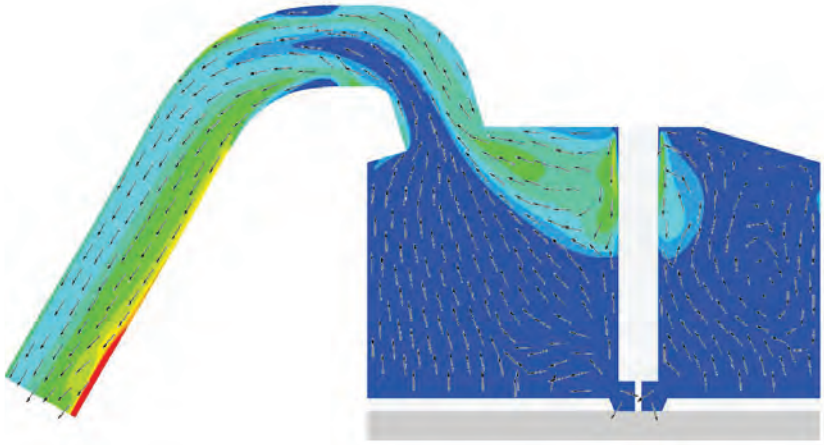

b) Sim. 2 (Without arc in- and outflow)

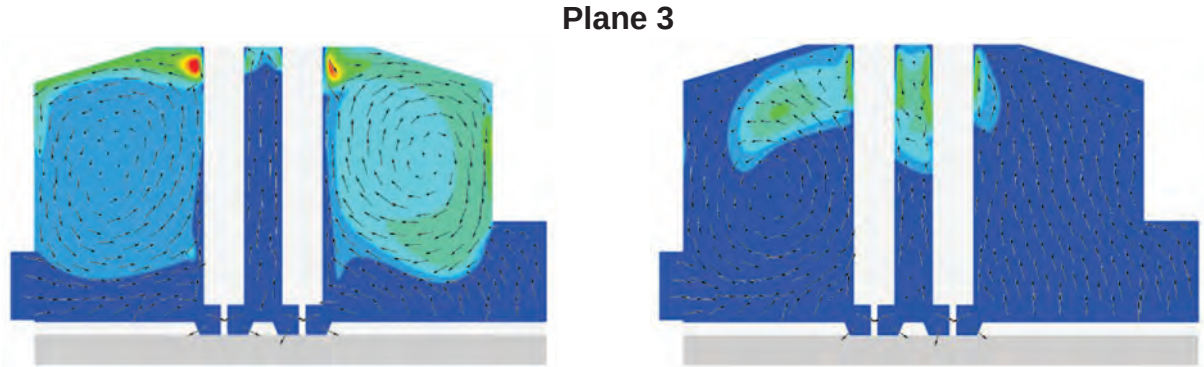

c) Sim. 1 (With arc in- and outflow)

d) Sim. 2 (Without arc in- and outflow)

Figure 5-15: CO_2 Mass fraction distribution for Simulation 1 and 2

5.2.4 Residence time

In general, if there is a sufficient amount of oxidant present, then combustion takes place according to the kinetic reaction rate and the dwell time is important so that a complete combustion can be achieved. The dwell time until a particular streamline leaves the vessel, which is also referred to as residence time, depends on the

velocity and the path length. In process engineering, one of the values used to evaluate the performance of a flow reactor is the space-time τ. This is defined according to eq. (56) [68]. In this case $\tau_{Sim.1}$ = 1.7 s and $\tau_{Sim.2}$ = 1.9 s.

$$\tau = \frac{V_{reactor}}{\dot{V}_{reactor}} \tag{56}$$

In **Figure 5-16** the dwell time and velocity of the streamlines from the slag door are compared. Most of the streamline dwell times up to the 4th hole do not correspond to the space-time value, as the EAF vessel is not a simple steady state ideal flow tube reactor. The furnace atmosphere is not ideally mixed and contains stagnation and recirculation regions. A region of low velocities and swirling flow on the right hand side of the slag door leads to comparatively high dwell times for a group of streamlines from the roof ring gap for Simulation 2. As the local CO reaction rate is low, this is however not reflected by the CO_2 distribution within the vessel (Figure 5-15).

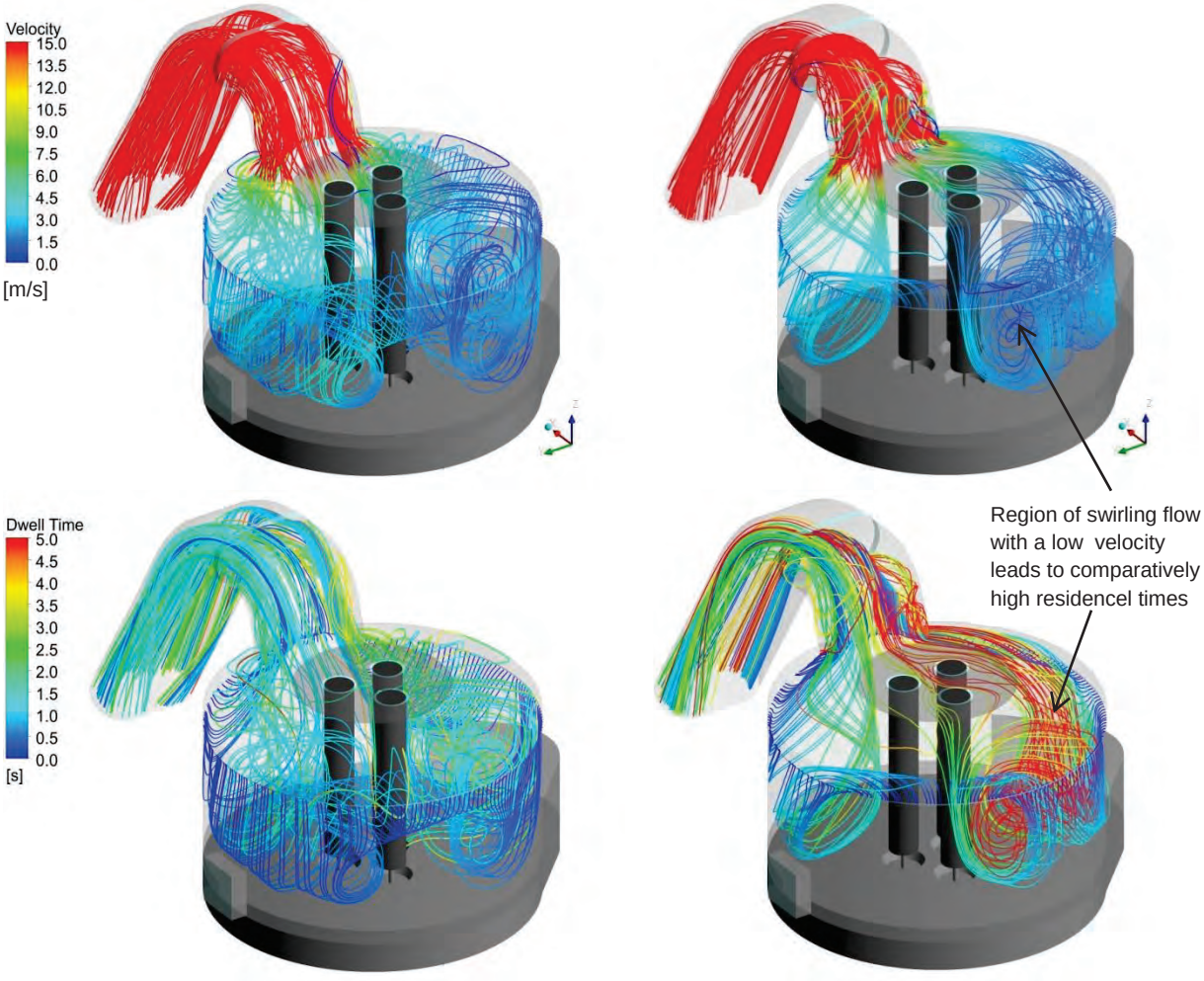

a) Sim. 1 (With arc in- and outflow) **b)** Sim. 2 (Without arc in- and outflow)

Figure 5-16: Velocity and dwell time of roof ring gap streamlines (Sim. 1 and 2)

Therefore, due to the three-dimensional nature of the flow field and for the low mass fraction of available oxygen during this phase of the heat in most parts of the EAF

vessel, it is not that easy to interpret the effect of dwell time on the total post combustion. This is due to the fact, that the gas species are not homogeneously distributed and flow field variables, such as the temperature and velocity, are not constant. Furthermore, in some parts of the furnace the resulting reaction rate along sections of a particular streamline is almost negligible. Therefore the amount of CO_2 formed along the path of that streamline is not proportional to the total streamline path length and corresponding total dwell time.

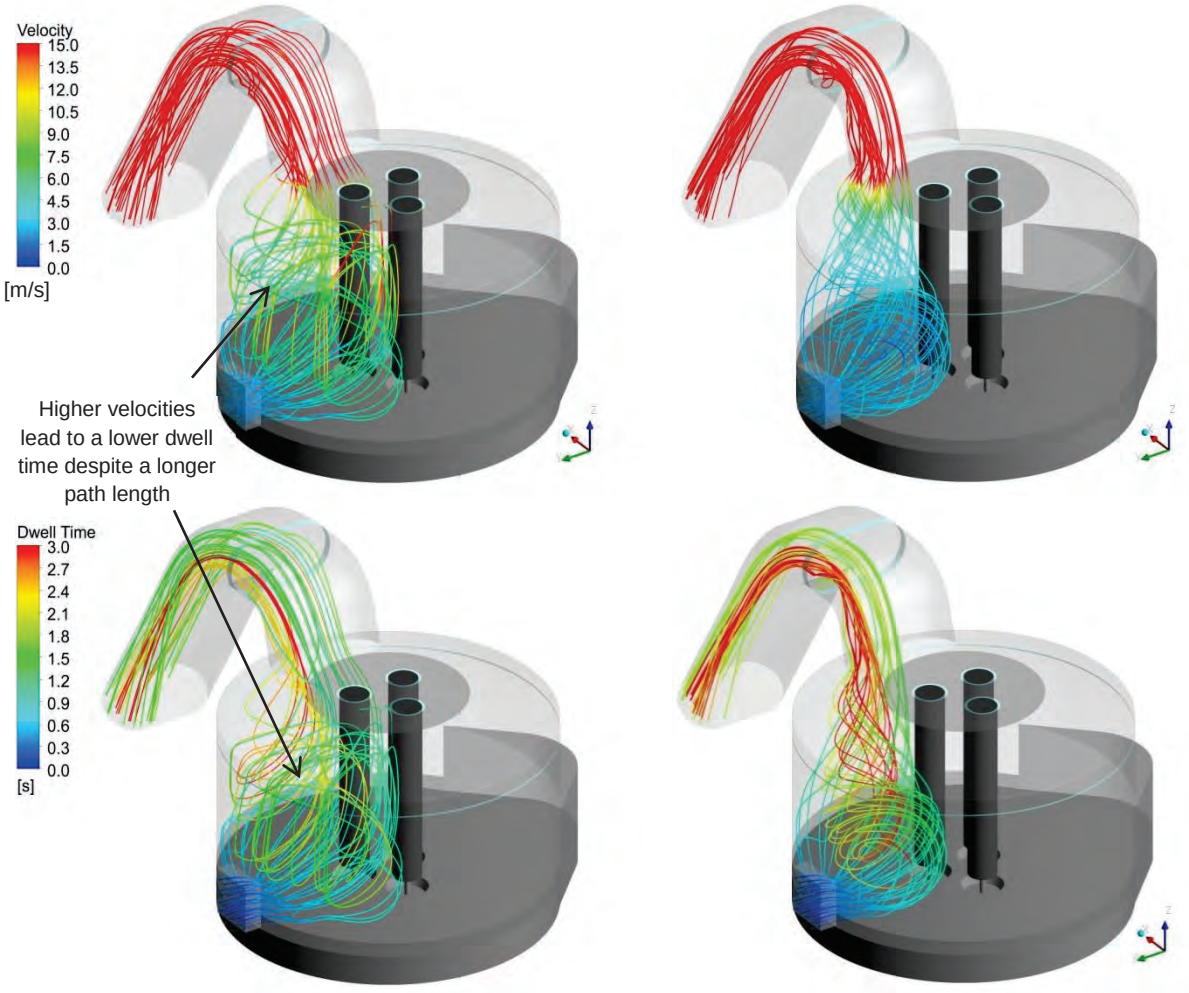

a) Sim. 1 (With arc in- and outflow) **b)** Sim. 2 (Without arc in- and outflow)

Figure 5-17: Velocity and residence time of slag door streamlines (Sim. 1 and 2)

Furthermore, as the velocity varies along the streamlines, a longer path length within the furnace does not necessarily mean a higher dwell time (**Figure 5-17**). On the other hand, as is the case for Simulation 1, a longer path length which passes through a greater fraction of the furnace volume can mean an improved mixing. This in turn leads to increased post combustion (Figure 5-15.a and c).

5.2.5 Energy flows

The results presented in the previous sections show that the modelling of the arc region has a large influence on the flow field, temperature distribution and post-combustion. The energy flows taken into account in the EAF model are shown in **Figure 5-18**.

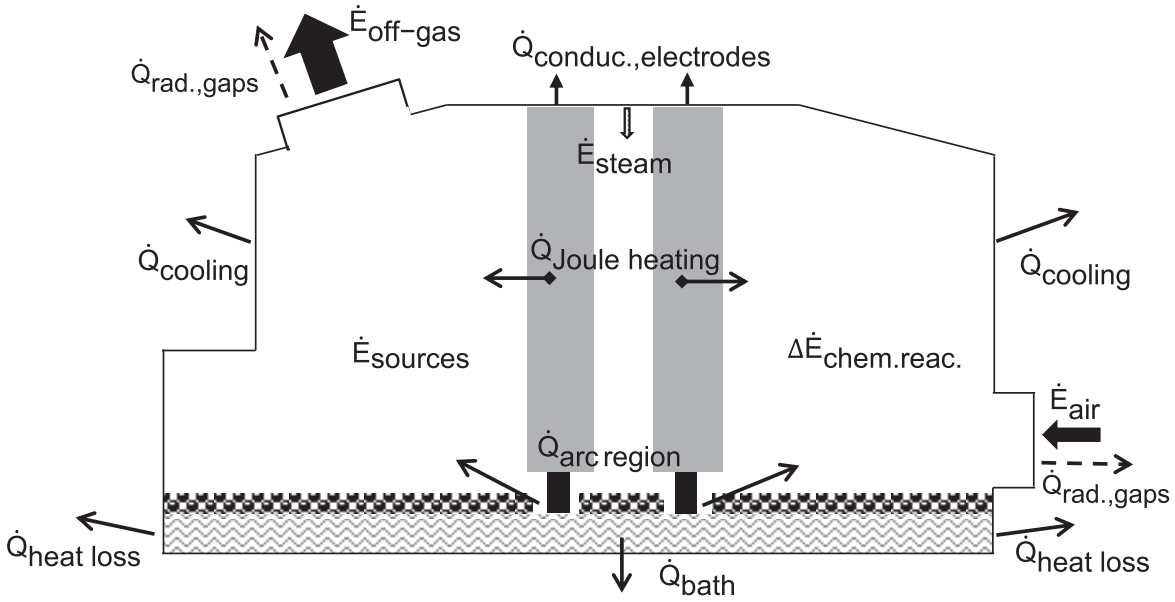

Figure 5-18: Energy flows in the EAF model

As the CFD simulations are steady state, the total energy input represents the power needed to cover the losses. These, as shown in Figure 1-6 in section 1.2, are due to the cooling by the water cooled panels, heat losses at the outer vessel surfaces, the loss of thermal radiation through gaps and openings, as well as the loss of energy due to the sensible and latent heat in the off-gas. The energy balance equation valid for the solution domain is therefore eq. (57), whereby the terms on the left hand side are the energy flows into the domain and on the right hand side are the energy flows out of the domain.

$$\dot{Q}_{arc\,region} + \dot{Q}_{Joule\,heating} + \dot{E}_{air} + \Delta\dot{E}_{chem.reac.} + \dot{E}_{steam} + \dot{E}_{sources} =$$

$$\dot{Q}_{bath} + \dot{Q}_{cooling} + \dot{Q}_{heat\,loss} + \dot{E}_{off-gas} + Q_{conduc.,electrodes} + Q_{rad.,gaps} \qquad (57)$$

$\dot{E}_{air}$	Energy inflow of air
$\Delta\dot{E}_{chem.reac.}$	Net energy input due to oxidation/dissociation of CO/CO_2
$\dot{E}_{off\text{-}gas}$	Energy outflow of off-gas
$\dot{E}_{sources}$	Net energy input due to CO sources and O_2 sink
$\dot{E}_{steam}$	Energy inflow of steam due to electrode cooling
$\dot{Q}_{arc\,region}$	Energy input from arc region
$\dot{Q}_{bath}$	Net energy outflow at bottom surface of model
$\dot{Q}_{conduc.electr.}$	Energy outflow by conduction at top surface of electrodes

$\dot{Q}_{cooling}$ Energy outflow due to cooling with the water cooled panels

$\dot{Q}_{heat\,loss}$ Heat losses at the outer surfaces of the walls made of refractory material

$\dot{Q}_{Joule\,heating}$ Joule heating of the electrodes

$\dot{Q}_{rad.,gaps}$ Energy loss due to thermal radiation out of the slag door, electrode gaps, roof-ring gap, post-combustion gap and off-gas outflow

The energy input from the arc region plus the Joule heating of the electrodes $\dot{Q}_{arc\,region} + \dot{Q}_{Joule\,heating}$, represents the simulated electric power input from the secondary circuit. It is much smaller than the true electric power input from the secondary circuit, as the simulated value represents the amount needed, in addition to the other four energy inflows in eq. (57), to cover the stationary power losses.

The modelled energy input to the solution domain due to the arc region, referred to as $\dot{Q}_{arc\,region}$ in eq. (57), is a sum of the individual terms in **Figure 5-19**, calculated using eq. (58). The individual terms correspond to the choice of energy balance system boundary of the electric arc model in the solution domain, which are the surfaces, top, bottom and side, of the three cylinders representing the electric arcs. The plasma arcs themselves are not included in the solution domain.

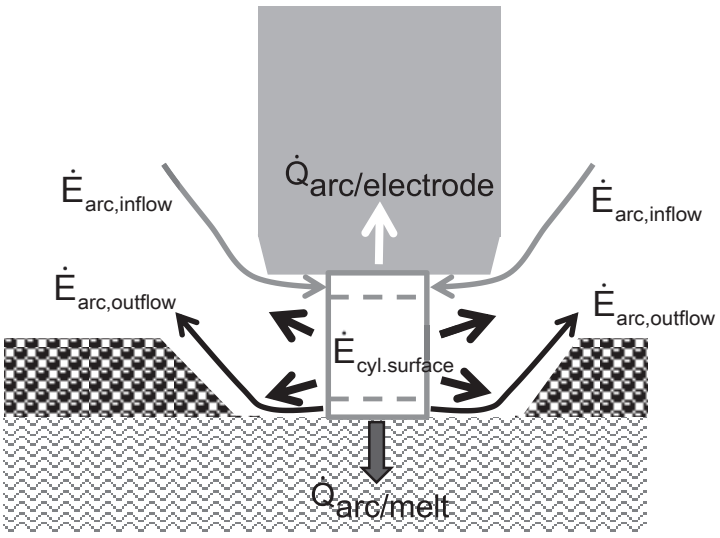

Figure 5-19: Energy flows modeled in arc region

$$\dot{Q}_{arc\,region} = \dot{Q}_{arc\,/\,electrode} + \dot{Q}_{arc\,/\,melt} + \dot{E}_{cylindrical\,suface} + \dot{E}_{arc,outflow} - \dot{E}_{arc,inflow} \quad (58)$$

$\dot{E}_{arc,inflow}$ Energy outflow out of solution domain due to gas atmosphere being drawn in at the top of the arc columns (the electric arcs are not included in the solution domain)

$\dot{E}_{arc,outflow}$ Energy input into solution domain due to flow out of the arc channel at the base of the arc columns

$\dot{E}_{cyl.surface}$ Net energy input due to thermal radiation exchange and convection at the cylindrical surface

$\dot{Q}_{arc/electrode}$ Energy input at plasma/electrode interface

$\dot{Q}_{arc/melt}$ Energy input at plasma/melt interface

A constant temperature of 3600 K is defined at the arc/electrode interface and at present the surface representing the arc/melt interface is defined to be adiabatic (section 4.4.3). Therefore, for the present model $\dot{Q}_{arc/electrode}$ depends on the temperature distribution resulting in the electrodes and $\dot{Q}_{arc/melt} = 0$. In **Table 5-4** the resulting energy flows in the arc region of Simulation 1 and 2 are compared.

Table 5-4: Energy input of the arc region for Simulation 1 and 2

Sim.	$\dot{Q}_{arc\,region}$ [MW]	$\dot{E}_{cyl.surface,therm.rad.}$ [MW]	$\dot{E}_{cyl.surface,conv.}$ [MW]	$\dot{E}_{arc,outflow} - \dot{E}_{arc,inflow}$ [MW]	$\dot{Q}_{arc/electrode}$ [MW]
1	18.73	15.39	0.07	3.26	0.008
2	15.67	15.48	0.18	Not included	0.012

For Simulation 1 the net thermal radiation from the arc column with the surroundings represents 82.2 % of $\dot{Q}_{arc\,region}$. The second largest energy contribution is due to the in- and outflow, which makes up 17.4 %. In the case of Simulation 2 the total energy input is 3.06 MW lower than that of Simulation 1 and the net thermal radiation exchange makes up 98.8 % of the energy input of the arc region. A comparison of the energy inputs and outputs for the solution domain up to the 4'th-hole is given in **Table 5-5** and **Table 5-6**. $\dot{E}_{off\text{-}gas,4^{th}-hole}$ is the energy flow of the off-gas leaving the vessel through the 4'th-hole.

Table 5-5: Energy inflows (Sim. 1 and 2)

Sim.	$\dot{E}_{total,in}$ [MW]	$\dot{Q}_{arc\,region}$ [MW]	$\dot{E}_{source,CO,slag}$ [MW]	$\Delta\dot{E}_{chem.reac.}$ [MW]	$\dot{Q}_{Joule\,heating} + \dot{E}_{air} + \dot{E}_{steam} + \dot{E}_{source,CO,electrode} - \dot{E}_{sink,O_2,electrode}$ [MW]
1	36.30	18.73	13.48	2.92	1.17
2	31.88	15.67	13.48	1.64	1.09

Table 5-6: Energy outflows (Sim. 1 and 2)

Sim.	$\dot{E}_{total,out}$ [MW]	$\dot{E}_{off\text{-}gas,4^{th}-hole}$ [MW]	$\dot{Q}_{cooling} + \dot{Q}_{heat\,loss}$ [MW]	$\dot{Q}_{bath} + Q_{conduc.,electrodes} + Q_{rad.,gaps}$ [MW]
1	-35.14	-20.69	-11.99	-2.46
2	-31.08	-17.93	-11.11	-2.04

Not only is the energy input of the arc region increased for Simulation 1, the higher temperatures lead to an increase in the post-combustion within the vessel, which in turn leads to an overall increase in the simulated energy input within the vessel of

4.42 MW. The energy input due to the 7.5 kg/s of 1823 K (1550 °C) hot CO defined to be entering the freeboard at the slag surface is the same for both simulations and represents 37 % of the total energy input for Simulation 1 and 42 % for Simulation 2.

As both simulations are steady state, the energy losses represent the quasi-steady state heat losses during the flat-bath phase of the EAF heat. This means that transient changes in the amount of energy stored by the melt and EAF vessel are not included in the simulated energy flows. Therefore, in accordance with the steady state energy conservation equation, eq. (32) (section 3.6.1), the increase in total energy input of Simulation 1 leads to an equivalent increase in the energy losses. Whereas the energy losses due to heat transfer through the vessel walls increase by 7.9 %, the amount of energy lost due to the flow of off-gas out of the vessel increases by 15.4 %. The conclusions gained from these results are discussed in detail in section 6. The values above show that for the discretization, turbulent modeling and chemical reaction modeling chosen $\Delta\dot{E}_{in-out,Sim.1} = 3.2\,\%$ and $\Delta\dot{E}_{in-out,Sim.2} = 2.5\,\%$. The difficulties that have to be overcome when addressing the convergence of these stationary simulations are mentioned at the end of section 3.6.3 and discussed in detail in section 4.2.1.

5.3 Slag layer height

Simulation 1 has a free burning arc length of 230 mm. The increased slag height of Simulation 3 leads to a free burning arc length of only 50 mm. All other boundary conditions and the mesh are identical. In this section the resulting change in the heat and mass flow is evaluated.

5.3.1 Flow field

In **Figure 5-20** the streamlines from the slag door of Simulation 1 and Simulation 3 are compared. For both simulations the mass flow rate of air from the slag door is 1.51 kg/s and has an initial temperature of 298 K. The inlet velocity of Simulation 1 is 1.585 m/s. The increased slag layer height leads to a reduction in the inlet area of the slag door of Simulation 3. Therefore in this case the inlet velocity at the slag door is 1.902 m/s.

The increase in slag height leads to a completely different streamline pattern. The circulation and mixing of the air from the slag door is clearly decreased. Despite the higher inlet velocity the air is deflected upwards more strongly by the flow of CO out of the slag surface. This is because there is not such a strong circulation region above the inflow counteracting the upward deflection, as is the case for Simulation 1. This can be seen in **Figure 5-21**, where the normalized velocity vectors in plane 3 are compared. For Simulation 3 the slag door air takes a much more direct route through the freeboard to the 4th hole.

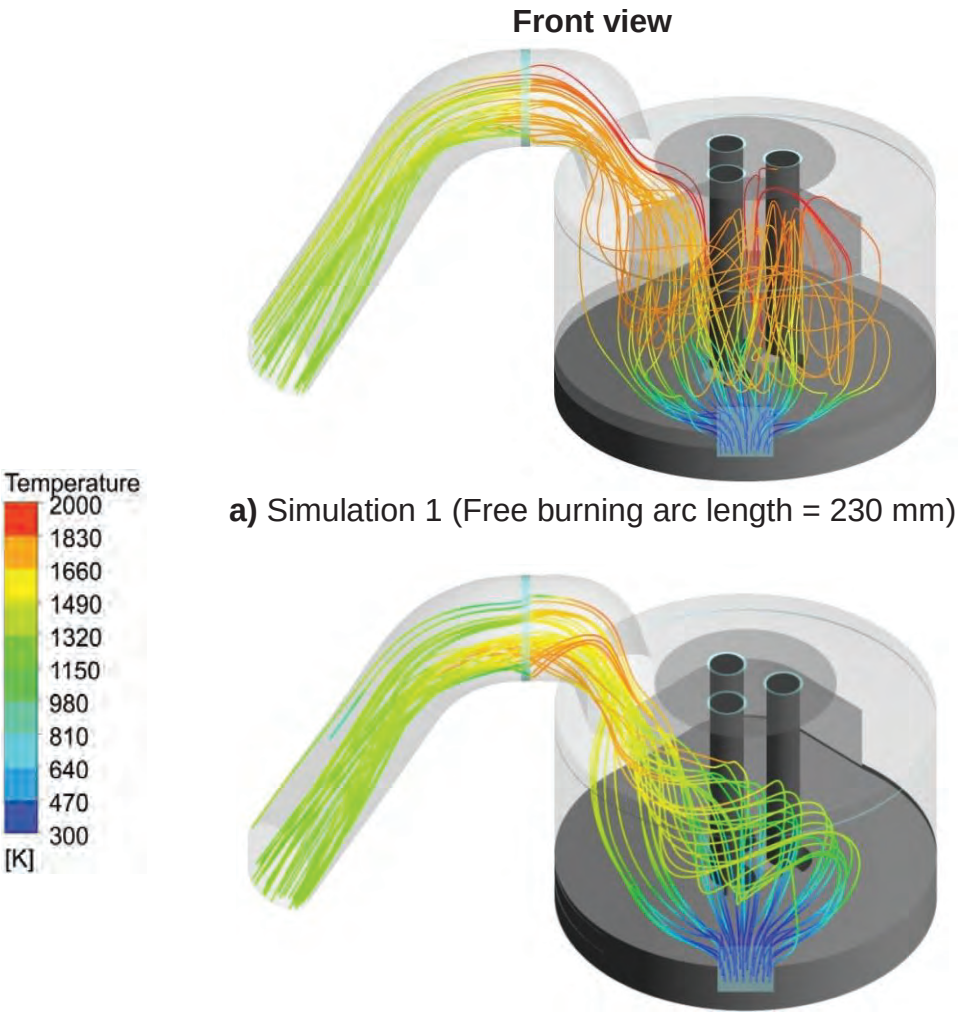

a) Simulation 1 (Free burning arc length = 230 mm)

b) Simulation 3 (Free burning arc length = 50 mm)

c) Simulation 1 (Free burning arc length = 230 mm)

d) Simulation 3 (Free burning arc length = 50 mm)

Figure 5-20: Streamlines from slag door (Simulation 1 and 3)

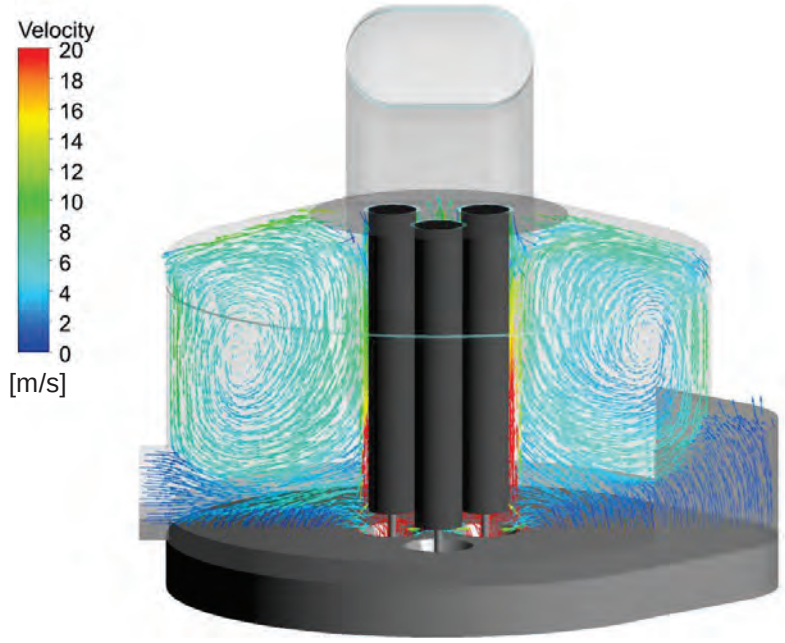

a) Simulation 1 (Free burning arc length = 230 mm)

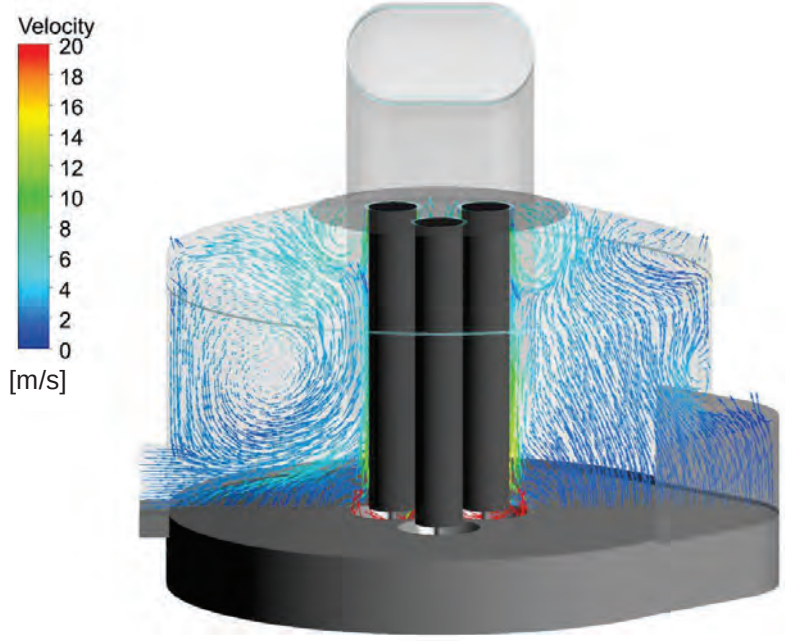

b) Simulation 3 (Free burning arc length = 50 mm)

Figure 5-21: Comparison of normalized velocity vectors in plane 3 (Sim. 1 and 3)

As for Simulation 1, an acceleration of the hot fluid around the electrodes upwards can be seen in Figure 5-21. This is mainly due to an exchange of momentum with the vortices in the arc region and to a lesser extent due to buoyancy forces. The velocities upwards in the proximity of the electrodes are however lower for Simulation 3 than for Simulation 1. Therefore the air and steam entering at the electrode gaps initially penetrate further down into the vessel.

The velocity vectors in the arc region are compared in **Figure 5-22.**

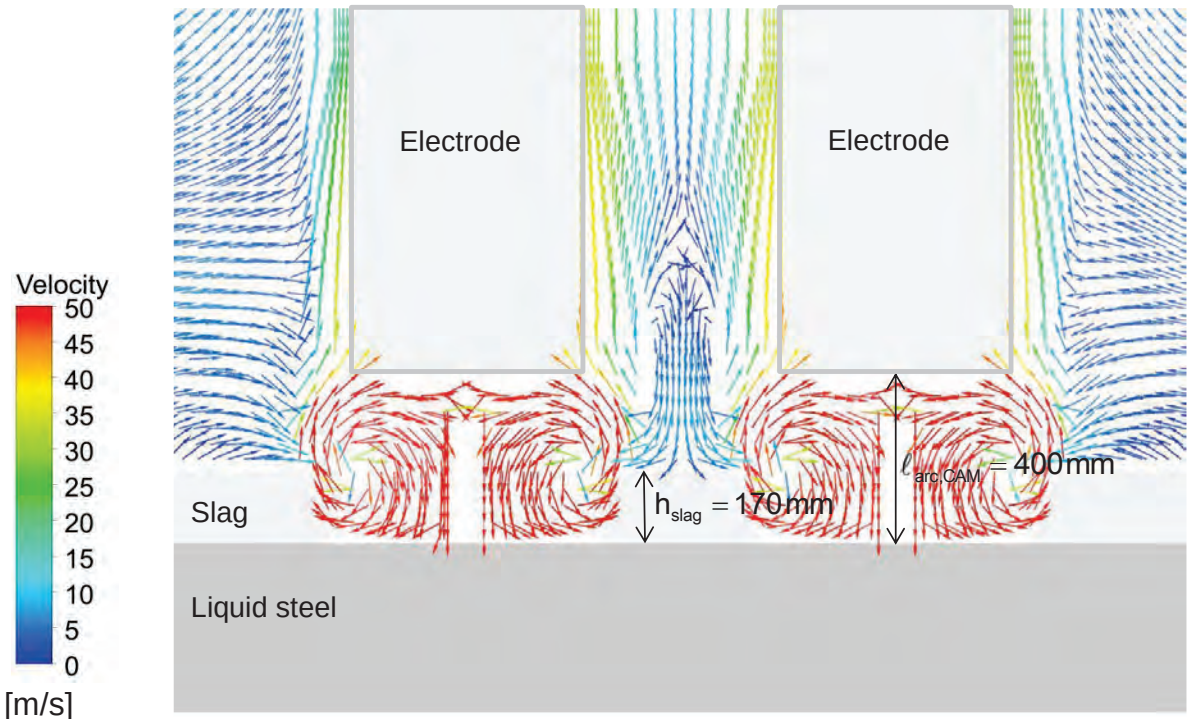

a) Sim. 1 (Free burning arc length = 230 mm)

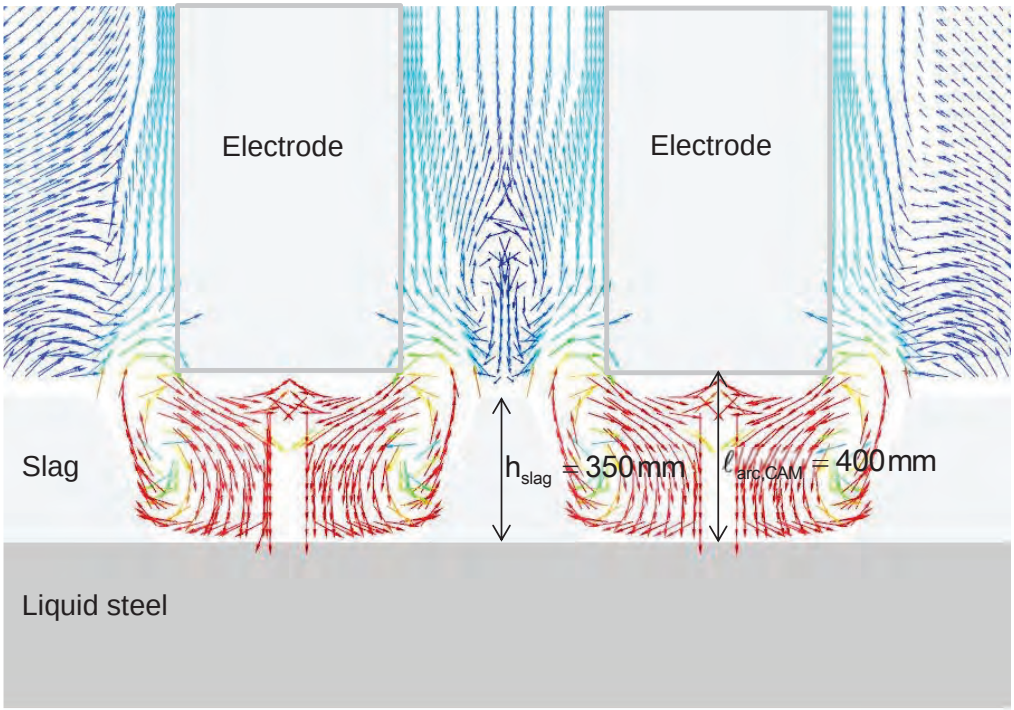

b) Sim. 3 (Free burning arc length = 50 mm)

Figure 5-22: Normalized velocity vectors in the arc region in plane 3 (Sim. 1 and 3)

The velocity vectors clearly show that in the case of Simulation 3 the vortices in the arc region are more contained within the slag layer and have less opportunity to interact with the flow in the freeboard. As a result less momentum is transferred from

the vortices to the furnace atmosphere, leading to the reduction in circulation and lower velocities. For Simulation 3 the lower velocities around the arc region lead to a longer dwell time of the flow around the electrodes (**Figure 5-23**), whereby this central flow of mainly CO hardly mixes with the surrounding furnace atmosphere, until it meets the ingress air from the electrode gaps in the upper region of the vessel.

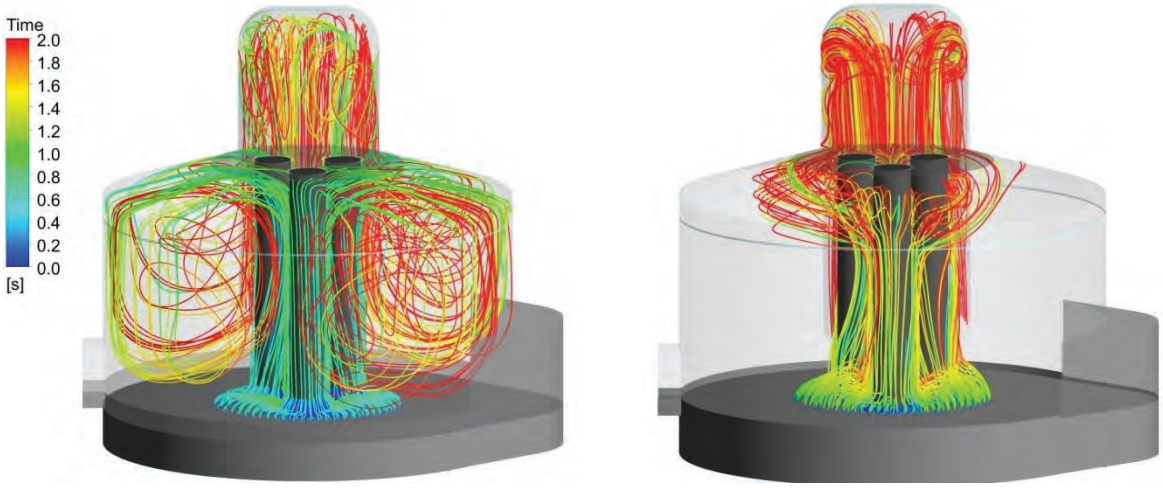

a) Simulation 1
(Free burning arc length = 230 mm)

b) Simulation 3
(Free burning arc length = 50 mm)

Figure 5-23: Time along streamlines from centre of slag surface (radius = 1.450 m)

5.3.2 Temperature distributions

For Simulation 1 the resulting composition of the inflow into the arcs is 0.052 wt% O_2, 1.149 wt% N_2, 98.563 wt% CO, 0.114 wt% CO_2 and 0.122 wt% H_2O with an average temperature of 3666 K (3393 °C). For Simulation 3 the resulting composition of the inflow is 99.999 wt% CO with an average temperature of 4258 K (3985 °C), which is 592 K higher than for Simulation 1.

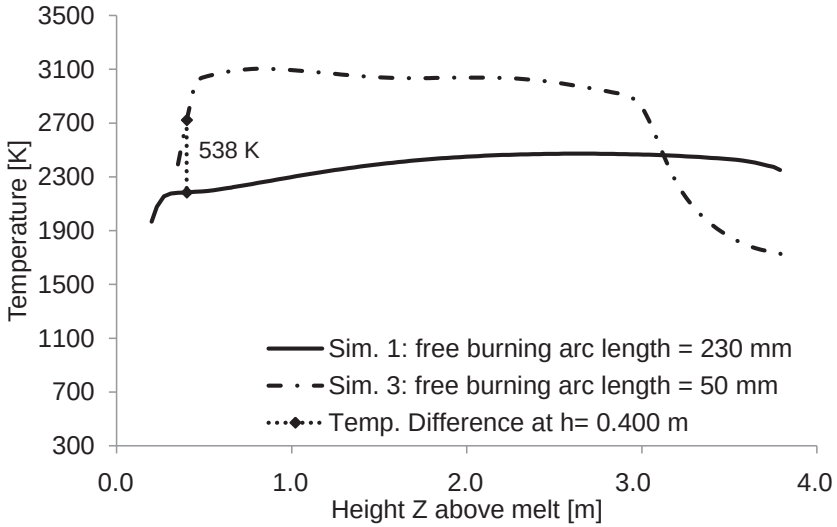

Figure 5-24: Temperature versus height along the Z-axis in the centre of the upper vessel (X = 0.0 m; Y = 0.0 m) for Simulation 1 and 3

The simulated temperature distributions between the electrodes in the centre of the freeboard are compared in **Figure 5-24**. It is evident that the increase in slag height leads to a definite increase in the temperature of the furnace atmosphere between the electrodes. This is due to the higher temperatures in the region of the arc vortices of Simulation 3 (**Figure 5-25**) and due to the reduced mixing with the relatively cooler furnace atmosphere.

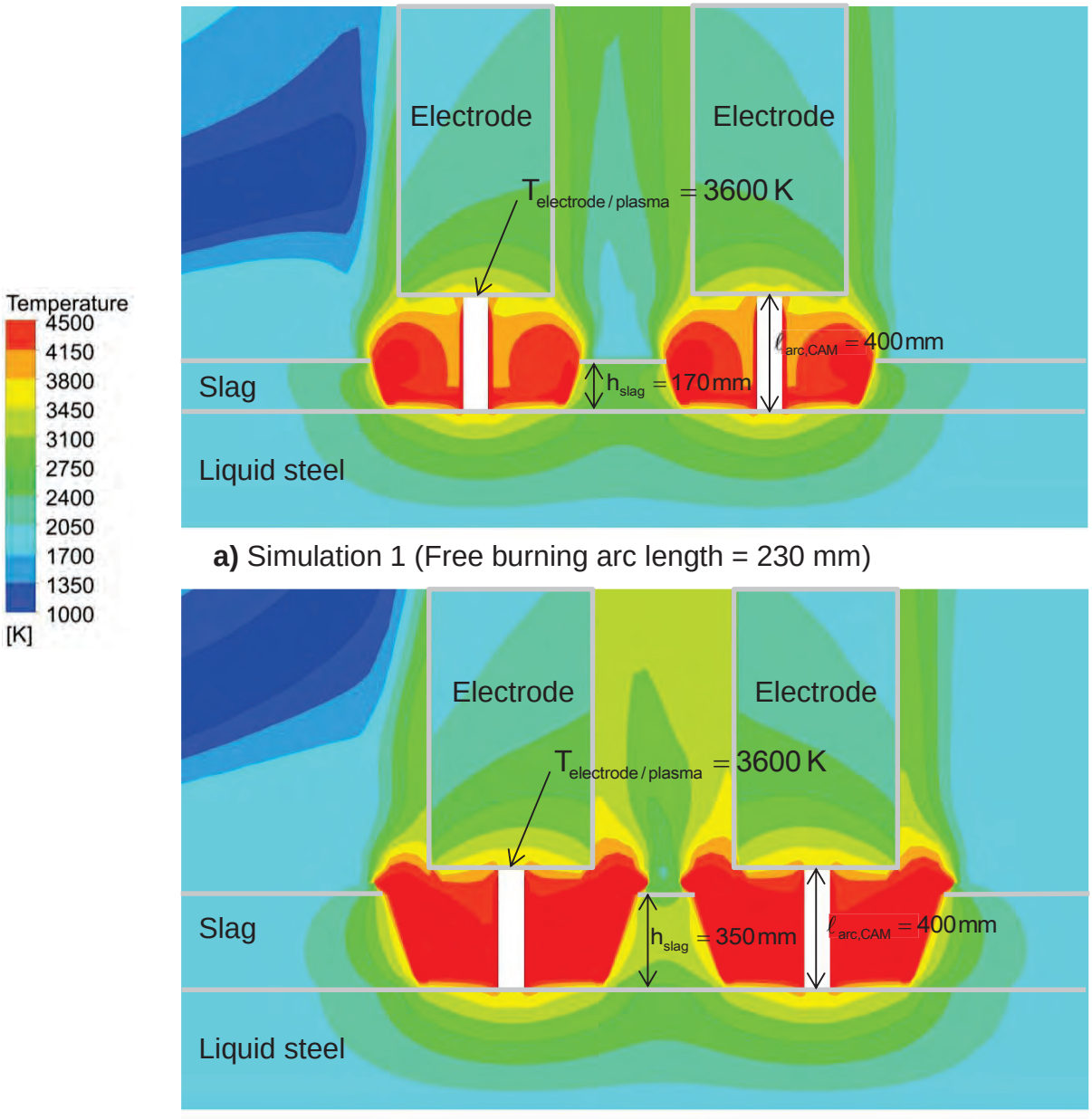

a) Simulation 1 (Free burning arc length = 230 mm)

b) Simulation 3 (Free burning arc length = 50 mm)

Figure 5-25: Temperature distribution in the arc region in plane 3 (Sim. 1 and 3)

Due to the increased temperatures around the tip of the electrodes in the case of a slag height of 350 mm the corresponding electrode consumption would be higher than for a slag height of 170 mm.

The temperature gradients at the tip of the electrodes show, that the definition of a constant temperature of 3600 K at the boundary between the plasma column and electrode should be reconsidered for both cases. According to the work by for example Alexis et al.[29] for a current direction from the electrode to the melt this interface is the position where the highest temperatures at the electrode tip are to be expected. At this stage of the model development, the plasma melt interface is as yet defined to be adiabatic. This is another aspect which could be improved for future models.

The difference in temperature distribution of Simulation 1 and 3 around the electrodes can also be seen in **Figure 5-26**.

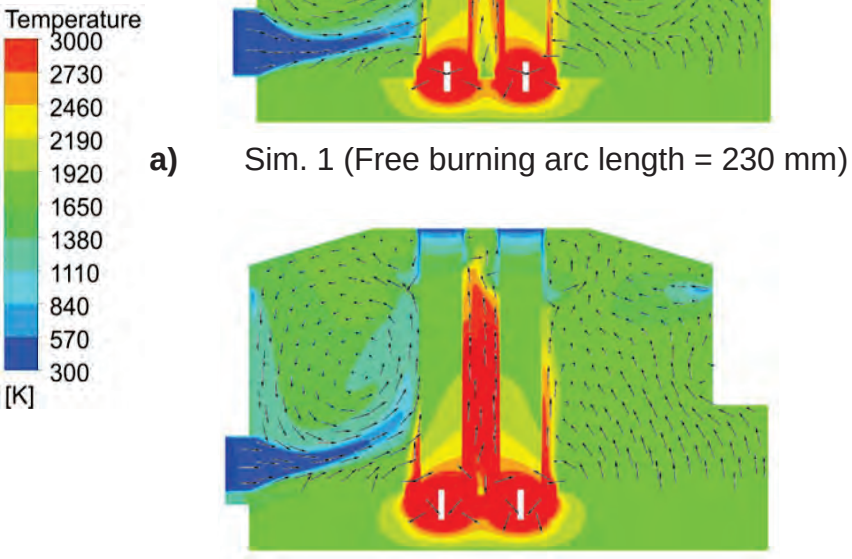

a) Sim. 1 (Free burning arc length = 230 mm)

b) Sim. 3 (Free burning arc length = 50 mm)

Figure 5-26: Temperature distribution in plane 3 (Sim. 1 and 3)

The region of temperatures higher than 2000 K in the center of the freeboard of Simulation 3 (**Figure 5-27**) corresponds to the path of the streamlines shown in Figure 5-23.b.

The lowest boundary of the solution domain, the bottom of the melt, is defined to have a constant temperature of 1823 K. An important fact, which becomes evident when evaluating the results shown in this section, is that this boundary is too close to the arc region. In order to simulate the redistribution of the energy within the vessel more accurately the circulation and corresponding convection in the bath should be included in all future models of the EAF vessel.

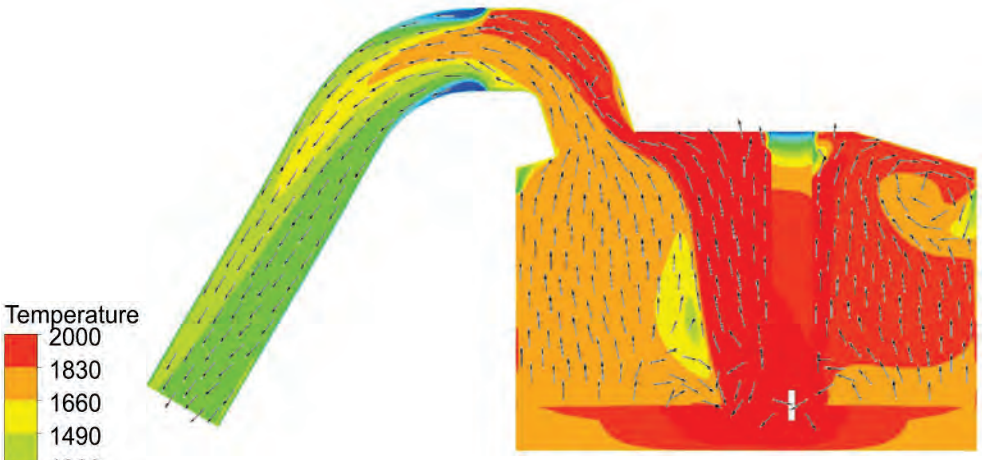

a) Sim. 1 (Free burning arc length = 230 mm)

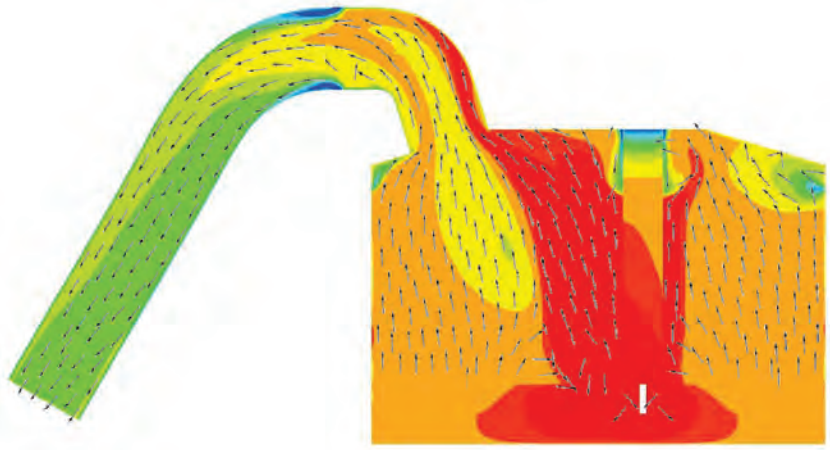

b) Sim. 3 (Free burning arc length = 50 mm)

Figure 5-27: Temperature distribution in Plane 1 (Sim. 1 and 3)

The simulated absorption coefficient distribution, which determines the amount of thermal radiation absorbed by the furnace atmosphere, is illustrated in **Figure 5-28**.

a) Simulation 1
(Free burning arc length = 230 mm)

b) Simulation 3
(Free burning arc length = 50 mm)

Figure 5-28: Absorption coefficient in Plane 3 (Sim. 1 and 2)

The adsorption coefficient, which is a function of the mass fraction of H_2O and CO_2, is in both cases negligible between the electrodes. This confirms that the higher temperatures here are not due to thermal radiation exchange, but due to the

interaction of the CO flowing out of the slag layer with the vortices in the arc region and heat transfer with the slag surface around the base of the electrodes.The temperature distributions on the outer surfaces of the EAF model, which are dependent on convection and thermal radiation exchange, are shown in **Figure 5-29**.

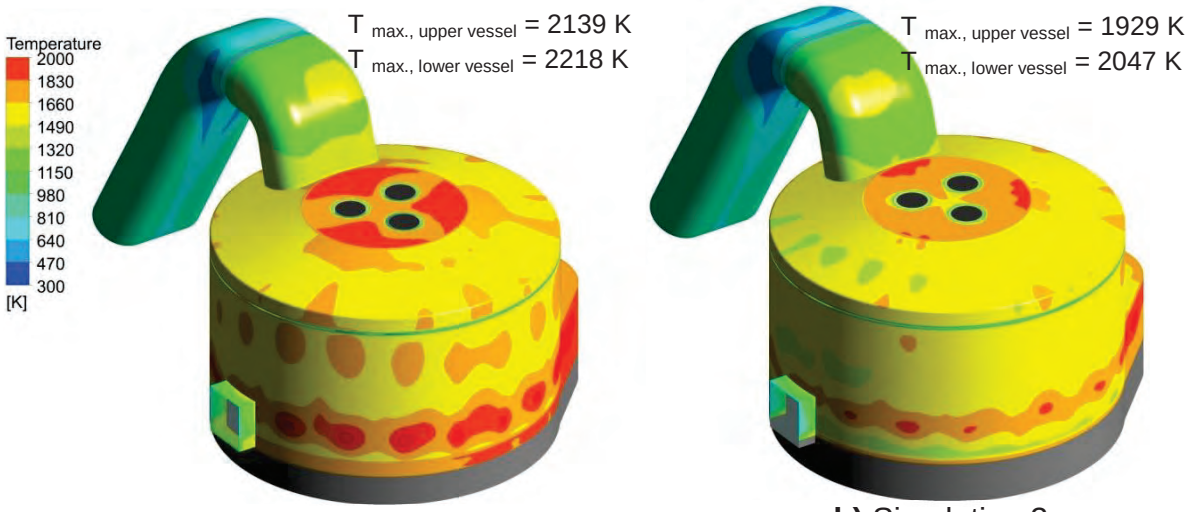

a) Simulation 1
(Free burning arc length = 230 mm)

b) Simulation 3
(Free burning arc length = 50 mm)

Figure 5-29: Temperature distributions on the inner surfaces of the vessel walls (Simulation 1 and 3)

As expected, the increase in slag height leads to a reduction in the amount of thermal radiation from the arcs to the upper vessel walls. As a result, the maximum hot spot temperatures are also clearly reduced. The maximum temperature of the upper vessel of Simulation 1 is much closer to the maximum allowable temperature of 1800 K [26]. The position of the main hot spots is unchanged.

5.3.3 Mass transfer and post-combustion

The total amount of CO_2 leaving the EAF vessel through the 4th hole for Simulation 1 and Simulation 3 is compared in **Table 5-7.** The mass flow rate of CO_2 out of 4th hole of Simulation 1 is 62 % higher than for Simulation 3. The reason for this is the reduced circulation within the freeboard and the corresponding decrease in the mixing of air and CO.

Table 5-7: Post-combustion within the EAF vessel (Sim.1 and 3)

Simulation	$\dot{m}_{CO_2,4^{th}\text{-hole}}$	$\Delta\dot{E}_{chem.Reac.,EAF\ vessel}$
1	0.455 kg/s	2.92 MW
3	0.281 kg/s	1.81 MW

The difference in the amount of post combustion within the vessel leads to a higher sum of the heat of reaction for Simulation 1. This corresponds to an increased energy input due to post-combustion within the vessel of 1.11 MW.

The post combustion within the vessel for Simulation 3 depends on the flow field and temperature distribution discussed in detail in the previous sections, as well as on the

resulting mass fraction distributions (**Figure 5-30**). As for Simulation 1, it is the turbulent mixing rate which limits the amount of post-combustion simulated in the EAF vessel.

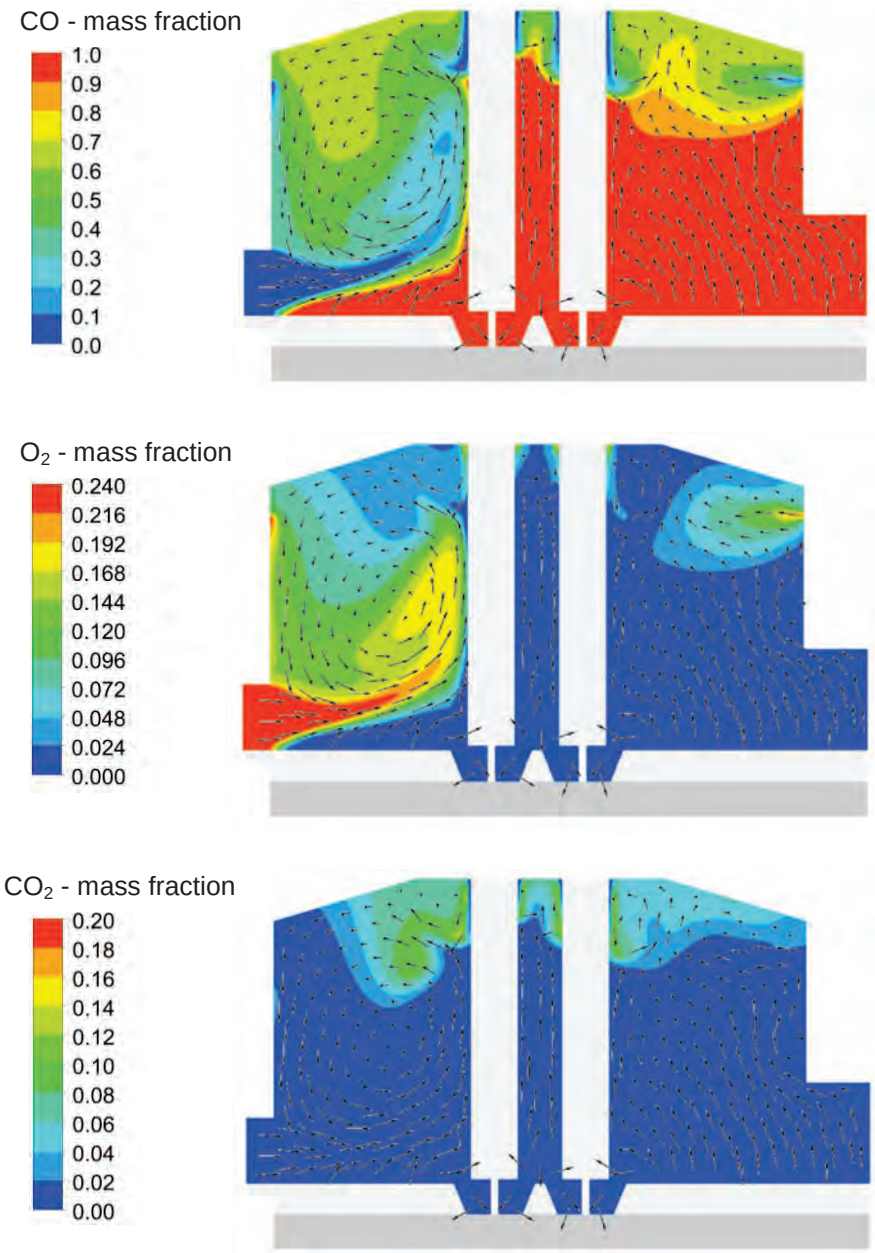

Figure 5-30: Post combustion in plane 3 of Sim. 3 (Free burning arc length = 50 mm)

5.3.4 Energy flows

In **Table 5-8** the energy flows in the arc region of Simulation 1 and 3 are compared. The energy input of the arc region of Simulation 3 is 2.11 MW lower than that of Simulation 1. Firstly, due to the resulting higher temperatures in the vortices of the arc region, the temperature difference between the arc in- and outflow ($\Delta T_{arc,out\text{-}in,Sim1}$=1834 K and $\Delta T_{arc,out\text{-}in,Sim3}$=1242 K) is 592 K lower. Secondly, due to the higher temperatures of the slag surrounding the arc columns (Figure 5-25), the amount of net thermal radiation exchange from the arcs to the surrounding surfaces is also reduced.

The values in Table 5-8 also show that in the case of Simulation 3 the defined temperature of 3600 K at the arc/electrode tip interface leads to 0.014 MW being drawn out of the solution domain at this small boundary. By comparison, 0.008 MW flows into the solution domain at this boundary for Simulation 1. In reality the processes taking place at the electrode tip/plasma interface are extremely complex. This is also the case for the impingement area of the arc with the bath. The consideration in the EAF simulation model of the processes taking place in these two regions and their effect on the energy balance of the solution domain needs to be further developed.

Table 5-8: Energy input of the arc region (Simulation 1 and 3)

Sim.	$\dot{Q}_{arc\,region}$ [MW]	$\dot{E}_{cyl.surface,therm.rad.}$ [MW]	$\dot{E}_{cyl.surface,conv.}$ [MW]	$\dot{E}_{arc,outflow} - \dot{E}_{arc,inflow}$ [MW]	$\dot{Q}_{arc/electrode}$ [MW]
1	18.73	15.39	0.07	3.26	0.008
3	16.62	14.42	0.04	2.17	-0.014

A comparison of the main energy inputs and outputs for the solution domain up to the 4th-hole is given in **Table 5-9**. The lower energy input of the arc region and reduction in energy input within the vessel due to post-combustion are reflected by a corresponding decrease in the energy flows out of the solution domain. Both simulations are steady state and therefore the steady state continuity equation ensures that the decrease in energy input is equated by an equal decrease in the energy output.

Table 5-9: Main energy flows (Simulation 1 and 3)

Sim.	$\dot{E}_{total,in}$ [MW]	$\dot{Q}_{arc\,region}$ [MW]	$\dot{E}_{sources,CO,slag}$ [MW]	$\Delta\dot{E}_{chem.reac.}$ [MW]	$\dot{E}_{off\text{-}gas,4^{th}-hole}$ [MW]	$\dot{Q}_{cooling} + \dot{Q}_{heat\,loss}$ [MW]
1	36.30	18.73	13.48	2.92	-20.69	-11.99
3	33.08	16.62	13.48	1.81	-18.89	-11.23

The method of using a constant temperature to simulate the time averaged energy input of the AC arc columns needs to be investigated in more detail. The results evaluated in this section show the effect that the temperature defined has on the simulated energy distribution within the EAF freeboard.

An alternative method would be to include the arc column in the solution domain as a solid and to define a volumetric energy source within the cylindrical columns. When considering the results it however becomes evident, that a more detailed investigation of the energy mechanisms in the arc region of DC and AC arcs is required, so that a more accurate time averaged model of the arcs can be developed. The results clearly show that it is not only the thermal radiation, but also the transfer of momentum of the arc vortices, leading to a corresponding change in mixing and post-combustion, which need to be considered.

5.4 Validation of Results

Validating the results of a numerical simulation model of an electric arc furnace is a challenge. This is due in part to the transient and complex nature of the processes taking place within the furnace (section 2.3). Further reasons are the high temperatures and electromagnetic interference during the power-on phase [17]. In addition, as explained in section 1.1.3, the order and duration of the operations during the steelmaking process vary, depending not only on the type of furnace, but also on the type of steel being produced and the composition of the raw materials charged. Therefore the comparability of measurements from different EAFs to simulation results is limited.

Another good example which illustrates the challenges of validating the results is the lack of information concerning the amount and inflow distribution of air ingress into an industrial furnace. To the best of the author's knowledge, no measurements or other direct information concerning the air inflows through the slag door, electrode gaps and roof ring gap during a heat is available. As can be seen when considering the results in section 5.2.3 and 5.3.3, these have a direct influence on the amount of post-combustion within the furnace. This gives an indication of the challenges faced not only concerning the validation of results, but also the definition of boundary conditions for the simulations.

Nevertheless, in order to qualitatively evaluate the results of the EAF simulation model, the calculated electrode temperature profiles and energy flows are compared to values available in the literature.

5.4.1 Electrode temperature profile

In **Figure 5-31** the electrode temperature profile simulated with the numerical EAF model is compared to that measured with an infrared pyrometer during EAF operation by Rafiei et al.[52] and to that determined by Guo et al.[18] .

For the electrode model of Guo et al. the electrode diameter is d_{elec} = 610 mm and the electrode length l_{elec} = 4 m. For the temperature profile plotted a temperature at the tip of $T_{elec,tip}$ = 3600 K and at the top of $T_{elec,top}$ = 400 K are assumed. In addition a homogenous furnace atmosphere temperature of $T_{furnace}$ = 400 K is used. In the case of the measurements of Rafiei et al. the electrode diameter is d_{elec} = 600 mm and the electrode length l_{elec} = 5.400 m. The measurements were carried out during normal operation of an AC EAF for an alternating electric current of 64 kA [52].

Due to the differences in electrode length from the electrode tip to the top of the EAF vessel, which is 3.424 m for the EAF model, the values are plotted with respect to the distance from the tip divided by the respective electrode length.

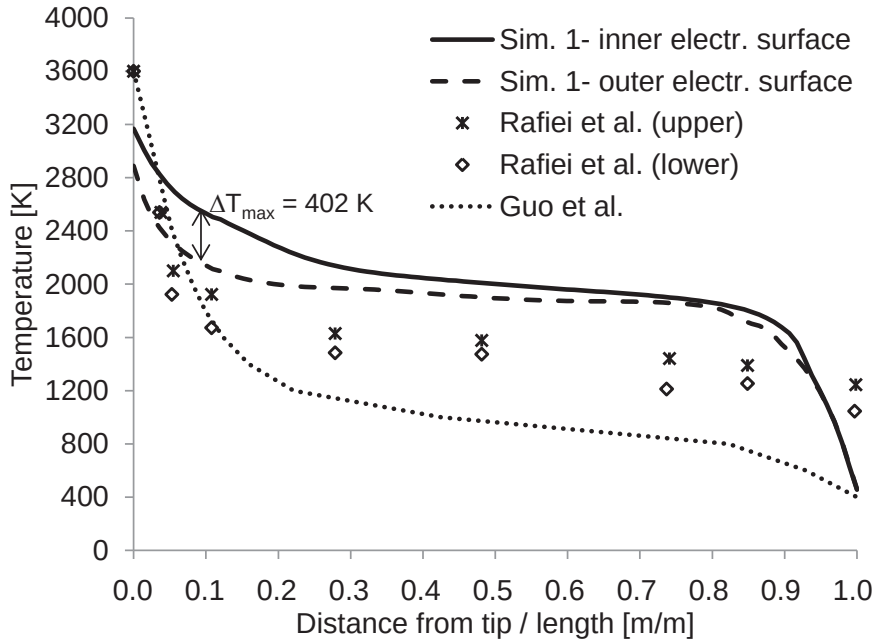

Figure 5-31: Comparison of electrode temperature profiles

In Figure 5-31 it can be seen, that in comparison to the measurements the assumed temperature of 400 K at the top of the electrode by Guo et al. and used for the EAF model is too low [17]. It leads to a sharp drop in temperature towards the top of the electrode which is not reflected by the measurements. The temperatures simulated with the EAF model agree better to those measured than those of Guo et al. This is due to the assumed furnace atmosphere of 400 K used by Guo et al. Even though the slope of the central part of the simulated profile obtained using the EAF model is similar to that measured, the temperatures are higher. Unfortunately, Rafiei et al. do not clearly describe how and when the temperature measurements were done, only stating that they were done at a distance of approximately 5 m from the electrodes. In order to be able to measure the temperature profile of the entire electrode length, it's most likely that this was done during charging, so that the temperatures would tend to be rapidly dropping during the measurement. The difference between the measured and simulated profile at the electrode tip is a consequence of the simplified electrode geometry.

In conclusion, the electrode temperature profile simulated using the EAF model shows that the thermal radiation exchange between the electrodes leads to a difference in temperature at the respective height that is not negligible. For future versions of the model the electrode top temperature should be reconsidered and the shape of the electrodes at the tip adapted [17].

5.4.2 Energy Flows

In the introduction of this thesis the relevance of off-gas and cooling losses during the EAF steelmaking process were discussed. It was mentioned that the simulation results of a mathematical model developed by Logar et al.[15] for an AC EAF with a conventionally water cooled furnace shell predicts that the flow of off-gas represents

16 % of the total energy input and the cooling approximately 15 %. In comparison the Sankey-Diagram for the 130 MVA DC EAF by Kühn [16] shows that the flow of off-gas represents 20 % (7.9 % sensible heat and 12.5 % chemical energy) of the total energy input and the cooling approximately 17 %.

In the case of the numerical simulations done with the EAF model, the total energy input is equal to the quasi-steady state heat losses during the flat-bath period of the EAF heat. In other words the transient superheating of the melt, the heating of the furnace vessel and all other transient energy sources and sinks in the molten metal bath are not included in the model. Furthermore these off-gas and cooling losses determined by Logar et al.[15] and Kühn[16] quoted above represent the sum of the losses in comparison to the total energy input for an entire heat, not just the flat-bath phase. Therefore it is not possible to validate the model results by comparing them to the above values. It can however be deduced, that the off-gas temperatures simulated using the EAF model in the off-gas elbow (see Figure 5-27) lie in a range which agrees with the off-gas temperatures measured by Kühn et al. during coal injection of approximately 1600 °C [8].

Similarly to the numerical EAF model, the results of Guo et al.[18] also correspond to the quasi-steady state heat loss conditions, as their model does not take any transient heating, sources and sinks into account. The heat extracted by the cooling water simulated using their radiation model for an arc length of 452 mm varies between 12 and 15 MW. In their model the furnace atmosphere is not considered and so no values for the off-gas heat losses are given. These values are comparable to those determined with the numerical EAF model developed. For a free burning arc length of 230 mm (Simulation 1) the cooling and heat losses are determined to be 11.99 MW and for a free-burning arc length of 50 mm (Simulation 3) the resulting cooling and heat losses are 11.23 MW.

Using a dynamic energy balance Kleimt et al.[20] calculated the heat extracted by the cooling water during the refining phase to be approximately 14 MW for an exemplary heat of a 140 t industrial DC EAF (Figure 1-6). This would also indicate that the cooling losses calculated with the numerical EAF model lie in an acceptable range. The off-gas losses determined by Kleimt et al. are larger than 20 MW and vary between 20 MW and almost 60 MW in dependence of the varying off-gas composition. In comparison, using the numerical EAF model the off-gas losses are determined to be 20.69 MW for a free burning arc length of 230 mm (Simulation 1) and 18.89 MW for a free-burning arc length of 50 mm (Simulation 3).

6 Conclusions and Recommendations

The topic of this thesis is the development of a mathematical model for the heat and mass transport in an electric arc furnace freeboard. The main objective was to create a tool with which the influence of process innovations on the fluid flow field, energy transport and chemical reactions within the freeboard of an electric arc furnace can be analysed.

The model developed during this thesis and the results obtained deliver valuable information which help one to understand the heat and mass transfer processes taking place within the EAF freeboard. The results clearly show the importance of the different aspects of the modelling parameters and boundary conditions. Even though as yet the model is only a rough approximation of the true situation during the flat-bath phase of the process, the experience gained is a solid basis which enables a goal orientated further development of the model.

It can be concluded, that in order to be able to model the redistribution of the energy flows within the furnace correctly, it is essential to include the solid electrodes. Most importantly, the effect of the in- and outflow into the arc region cannot be neglected. It represents one of the relevant energy input mechanisms of the arc region and leads to an increased mixing and post-combustion of the gas species within the furnace [17].

In its present form, the model can already be used to quantify the effect of changes, for example the amount of ingress air or a change in slag height, on the heat and mass transfer within the freeboard. Nevertheless, during the model development and evaluation of the results obtained, several important insights were gained concerning necessary future developments of the model.

In **Figure 6-1** the energy flows simulated in the present model are compared to those recommended based on the experience gained. The temperature distributions and energy flows simulated with the present model show, that the solution domain needs to be extended in order to include the energy transport and energy sources within the bath. This is essential in order to be able to improve the modeling of the energy flows within the EAF.

The inclusion of the bath in the solution domain would enable the implementation of methods, for example user subroutines, to include the following in the simulation model:

- the net amount of energy input due to chemical reactions in the bath ($\Delta\dot{E}_{chem.reac.,melt}$),
- the energy input due to Joule heating of the melt ($\Delta Q_{Joule\,heating,melt}$),
- the redistribution of energy due to the bath circulation and corresponding heat losses at the outer surface of the lower vessel,
- and transient effects, such as the transient superheating of the bath.

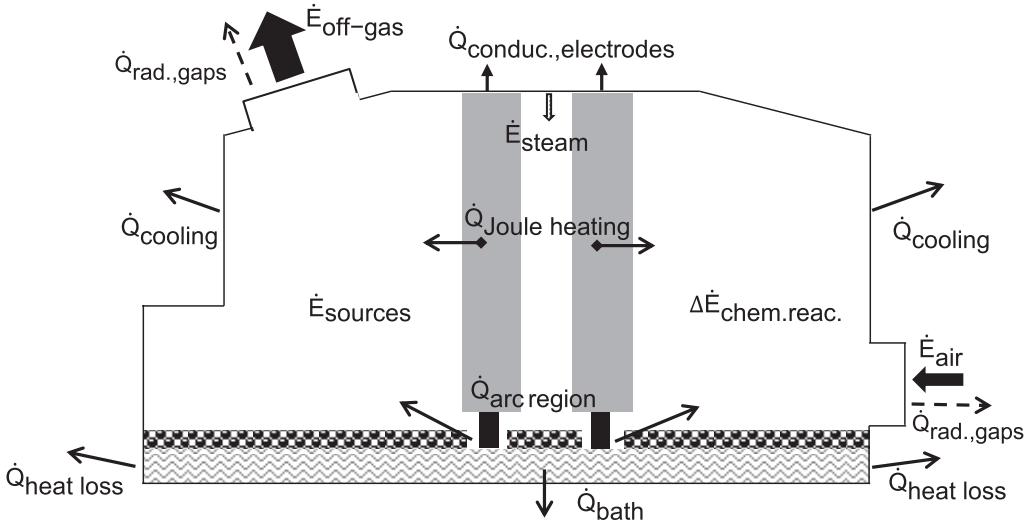

a) Energy flows of present EAF model

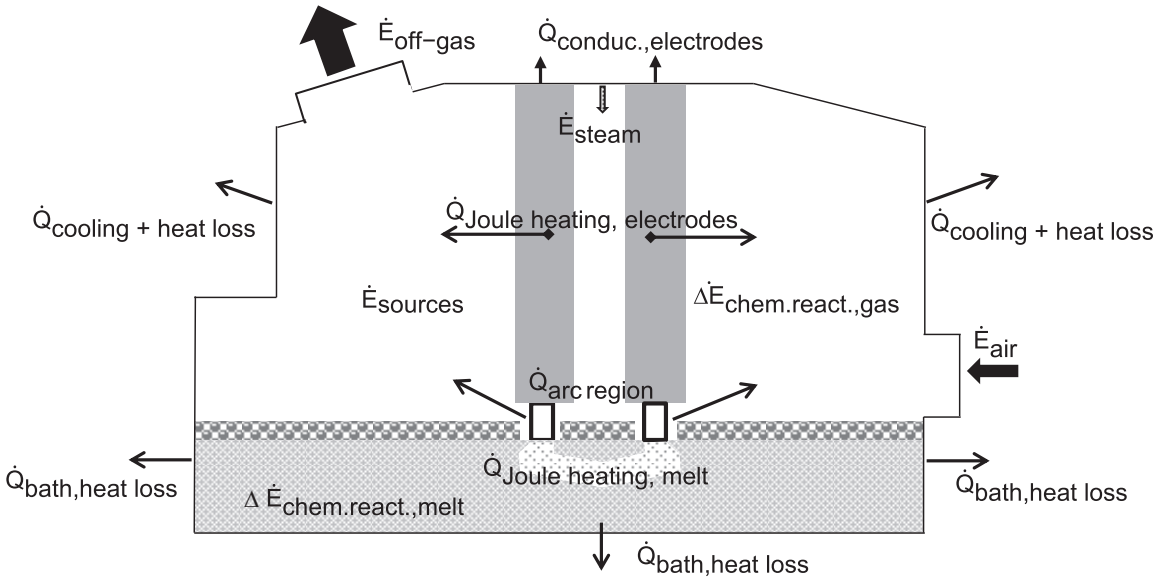

b) Recommended future modelling of energy flows

Figure 6-1: Conclusions concerning size of solution domain and energy flows

In addition, in order to enable a quantitative comparison of the true energy input of an EAF during the flat bath phase to the simulated energy flows, a more in-depth investigation of the energy mechanisms in the arc region is necessary. The aim of such an investigation would be to develop a time averaged model of the arc region, so that the time-averaged effect of the individual energy transport phenomena of the arc region could be better included in the EAF simulation model. This would greatly increase the usefulness of the model as a tool to for example predict the thermal loading of the cooling panels.

An improved modelling of the energy flows and the arc region are the most important issues for the future development of the model. Before these two issues are solved, a more detailed modelling of other aspects of the heat and mass flow within the furnace

need not be attempted, as most phenomena are dependent on the correct modelling of the temperature distribution and energy input within the vessel.

For the sake of completeness a list of other aspects which are also relevant for future model developments is included here as follows:

- The use of a user subroutines to improve the accuracy of the calculation of the thermal radiation absorption coefficient better suited to the extreme conditions within the EAF vessel
- A more detailed modelling of the chemical reactions within the furnace using multi-step chemical reaction mechanisms
- An increased resolution of the discrete ordinates thermal radiation model
- The development of a method to simulate the temperature dependant electrode consumption and resulting CO source and O_2 sink at the electrode surface
- The effect of particles in the off-gas on the absorption of thermal radiation by the furnace atmosphere
- The implementation of a method to better simulate the non-homogeneity of the source of CO flowing out of the slag due to oxygen injection (modelling of the C and O_2 injection)
- The question of how to better qualitatively validate the simulation results of future models should be addressed.

7 Summary

The topic of this thesis is the development of a numerical model for the heat and mass transport in an electric arc furnace freeboard. Approximately 40 % of the raw steel produced in Europe is currently obtained via the electric arc furnace route. Some of the challenges presently faced by European steelmakers are increasing costs for raw materials and energy, as well as strict environmental policies. By considering energy flow diagrams of the steelmaking process in EAFs it can be concluded, that the energy efficiency can be improved by reducing off-gas and cooling losses. This can be achieved by increasing the degree of combustion of CO and H_2 in the furnace. A better understanding of the mechanisms that cause unwanted emissions during the steelmaking process can help to develop new methods to reduce or counteract pollutants.

The long term motivation behind the topic of this thesis is therefore to create a numerical EAF model which enables the analysis of the influence of process innovations on the conditions within an EAF. The advantage of a numerical simulation model is that the influence of such innovations on the conditions within the furnace can be investigated in detail. The main objective of the EAF model at this stage is to qualitatively investigate the influence of the arc region on the amount of post-combustion within the freeboard. The effect of a change in the foamy slag height on the resulting amount of post-combustion is also investigated.

The numerical EAF model represents the power-on/flat-bath stage of the steelmaking process in an exemplary AC electric arc furnace for quasi-steady state heat loss conditions. The flat bath period represents approximately 37 % of the tap-to-tap time of a conventional heat. The exemplary conventional AC EAF has a tapping capacity of 100 tons, a transformer rating of 90 MVA and and an inner vessel diameter of 6.1 m.

A simplified time-averaged arc model based on the channel arc model was developed in order to include the influence of the arc region on the conditions within the freeboard. The plasma arcs are not part of the solution domain, but are represented as cylindrical surfaces extending from each electrode tip to the bath surface. In contrast to the arc modeling of other numerical EAF models, this model includes the kinetic energy input due to the arc in- and outflow as well as the energy input due to the heating of the entrained furnace atmosphere in the arcs. This is achieved by dividing the arc column into three segments. A negative velocity inlet is defined at the top of each arc where furnace atmosphere is drawn into each column. At the base of each arc a corresponding mass flow outlet is defined, where the hot gas reenters the freeboard. The arc channel radius and arc mass flow rate are approximated using the channel arc model. A temperature of 5500 K was defined to simulate the time averaged thermal radiation temperature for all three segments. This arc model enables the qualitative investigation of the influence of the arc region on the amount of mixing and therefore post-combustion of CO to CO_2 within the freeboard.

In contrast to previous numerical EAF models, the three graphite electrodes are part of the solution domain. The Joule heating due to the 63 kA flowing through the electrodes is taken into account by a corresponding volumetric heat source. The temperature profiles of the electrodes therefore result in dependence of the simulated thermal conduction within the electrodes as well as the heat transfer due to convection and thermal radiation exchange at the electrode surfaces.

The discrete ordinates thermal radiation model available in the CFD code ANSYS FLUENT (Version 14.5) was chosen to model the thermal radiation exchange between the surfaces of the EAF freeboard. An angular discretization of $N_\theta = 3$ and $N_\phi = 4$ with a pixel resolution for each control angle of 3 times 4 is used in order to ensure a satisfactory resolution of the thermal radiation. The composition dependent absorption coefficient of the furnace atmosphere within the vessel is calculated with the weighted-sum-of-grey-gases-model.

The option species transport with volumetric reactions and the finite-rate/eddy dissipation turbulence chemistry interaction is used to calculate the mass transfer and chemical reactions within the freeboard. The furnace atmosphere is defined to be a mixture of CO, CO_2, H_2O, N_2 and O_2. The post combustion of CO to CO_2 is simulated according to the gas-shift reaction available for the oxidation of CO in FLUENT (Version 14.5). The realizable k-ε model with standard wall functions for the near wall treatment was selected to simulate the turbulent viscous flow.

The geometry of the EAF simulation model extends from the uppermost layer of the metal bath to the beginning of the off-gas extraction downstream of the post-combustion gap. In contrast to other numerical EAF models it therefore not only includes the electrodes, but also the post-combustion gap. The foamy slag is modelled as a solid layer and the top layer of the steel bath, also considered as a solid, is included. These two layers allow the simulation of downward absorption and redistribution of energy from the arc region, which is reflected by the resulting temperature distribution at the foamy slag layer surface. Burners, lances or injectors are not included at present.

The geometry is divided into 202 volumes. These were meshed step by step in order to ensure that the discretization of the regions with high gradients is fine enough. Only one solution domain is necessary, as the solid regions are thermally coupled to the fluid regions at the respective boundaries. The final mesh was chosen based on the results of a mesh sensitivity study. The final structured hybrid mesh, which consists to 96 % of hexahedron cells, has 4079071 elements.

The main inflows, sources and sinks can be summarized as follows:

- The decarburization of the molten metal bath is taken into account by the definition of a homogenous source of CO at the surface of the foamy slag layer, corresponding to a total CO mass flow rate of 7.5 kg/s with a temperature of 1823 K (1550 °C).

- An average graphite electrode consumption of 0.082 kg/s is assumed and modelled by a corresponding CO source and O_2 sink at the electrode surfaces.
- A relative static pressure of 0.01 Pa is defined at all inlets. The operating pressure is 101.325 kPa. A total mass flow rate of ingress air of 3 kg/s with a temperature of 298 K (25 °C) is defined to enter the freeboard through the slag door, roof gap and electrode gaps. An air mass flow rate of 7.65 kg/s flows in at the post-combustion gap.
- It is assumed that 0.5 kg/s of steam with a temperature of 373 K (100 °C) enters the vessel through the three electrode gaps due to electrode cooling.

The bottom boundary of the solid melt layer is defined to have a constant temperature of 1823 K (1550 °C). The upper vessel, roof, exhaust elbow and exhaust extraction are cooled by water cooled panels. The inner surfaces of the upper vessel, roof and exhaust elbow are defined to have a 20 mm thick solid slag coating and the walls of the exhaust extraction are assumed to have an equivalent 20 mm thick coating of dust. An external temperature, at the outer surface of the slag/dust layer, of 333 K (60 °C) is specified for these cooled surfaces. The walls of the lower vessel, balcony and delta zone of the roof are defined to consist of refractory material with a thickness of 500 mm, which is cooled by natural convection and thermal radiation to the ambient on the outside of the vessel.

Three simulations were carried out using the EAF simulation model. In Simulation 1 the arc in- and outflow is taken into account and the slag height of 170 mm means that the free-burning arc length is 230 mm. The only difference between Simulation 1 and 2 is that the arc in- and outflow is not taken into account in Simulation 2. By comparing the results, the influence of the inclusion of the energy input due to the heating and increase in momentum of the furnace atmosphere drawn into and flowing out of the arc region on the conditions within the furnace freeboard is evaluated.

The difference between Simulation 1 and 3 is that for Simulation 3 the free-burning arc length is only 50 mm due to an increased slag height of 350 mm. By comparing the results, the influence of the flow in the arc region on the post-combustion of CO to CO_2 within the freeboard in dependence of the free-burning arc length is investigated.

For all three simulations the resulting flow field in the EAF freeboard is characterised using streamlines of the flow starting at the slag door, roof-ring gap and electrode gaps. Furthermore the resulting flow fields are characterised with the help of normalized vector plots of the velocity distributions. In addition the temperature distributions within the vessel, on the vessel walls, on the slag surface and electrodes are shown. Contour plots of the simulated mass fractions of CO, O_2, and CO_2 show the mass transfer within the freeboard and the dependence of the post-combustion on the temperature distribution as well as the turbulent mixing.

The resulting energy flows of the three simulations are evaluated, in order to investigate the influence of the arc modelling on the simulated post-combustion and resulting energy inputs and losses. As the simulations are steady state, the energy

flows corresponds to the heat loss conditions. This means that the total energy input represents the power needed to cover the losses and that a decrease in energy input is equated by an equal decrease in the energy output. The simulated energy input from the arc region plus the defined Joule heating of the electrodes, represents the simulated electric power input from the secondary circuit. It is much smaller than the true electric power input from the secondary circuit, as the simulated value represents the amount needed, in addition to the other energy inflows, to cover the stationary power losses.

The modelling of the arc region has a large influence on the flow field, temperature distribution and post-combustion. The comparison of the results of Simulation 1 and 2 shows, that due to the inclusion of the arc in- and outflow the energy input of the arc region is increased and there is an increase in the circulation within the vessel. The correspondingly higher temperatures and circulation lead to an increase in the post-combustion of CO to CO_2 within the freeboard. The inclusion of the arc in and outflow therefore leads to an overall increase in the simulated energy input within the vessel of 4.42 MW. It can therefore be concluded, that the influence of the arc in- and outflow should not be neglected in future EAF models.

A comparison of the results of Simulation 1 and 3 shows, that an increased slag height not only protects the cooling panels from the thermal radiation of the arcs. It also leads to a reduction in the interaction between the flow in the arc region and in the freeboard. This in turn leads to less circulation within the freeboard, which reduces the amount of mixing of CO from the slag layer with the ingress air. Therefore the amount of post-combustion in the freeboard is also reduced. An increase in the slag height from 170 mm to 350 mm, leads to a reduction in the total simulated energy input within the solution domain of 3.22 MW.

The results show that the EAF simulation model developed during this thesis delivers valuable information which helps to understand the heat and mass transfer processes taking place within the EAF freeboard. Furthermore, several important insights were gained concerning necessary future developments of the model. Firstly, the solution domain needs to be extended in order to include the heat and mass transfer processes taking place within the molten metal bath. This is essential in order to be able to improve the modeling of the energy flows within the EAF. In addition, a more in-depth investigation of the energy mechanisms in the arc region is necessary. The aim of such an investigation would be to develop a time averaged model of the arc region, so that the time-averaged effect of the individual energy transport phenomena of the arc region can be better included in the EAF model.

8 References

[1] **Government of India, Ministry of Mines, Indian Bureau of Mines, Ore dressing division:** Iron & Steel – Vision 2020, August 2011, p. 50

[2] **Walker, K.:** The basics of iron and steelmaking – Part 2, Steel Times International, May/June 2012, p. 45

[3] **Jones, R.T.; Reynolds, Q.G.; Curr, T.R.:** Some myths about DC arc furnaces, South African Pyrometallurgy 2011, South African Institute of Mining and Metallurgy, Johannesburg, 2011, pp. 15 - 32

[4] **Toulouevski, Y.N.; Zinurov, I.Y.:** Innovation in Electric Arc Furnaces (Scientific Basis for Selection), Springer Verlag, (2010), p. 2

[5] **Pfeifer, H.; Echterhof, T.; Voj, L.; Gruber, J.; Jung, H.-P.; Lenz, S.; Beiler, C.; Cirilli, F.; De Miranda, U.; Veneri, N.; Bressan, E.:** EUR 25078 - Control of nitrogen oxide emission at the electric arc furnace - CONOX, European Commission, Luxembourg, (2012), pp. 92 - 126

[6] **Memoli, F.; Guzzon, M.; Giavani, C.:** The Evolution of Preheating and the Importance of Hot Heel in Supersized Consteel® Systems, Iron & Steel Technology, January (2012), pp. 70 – 78

[7] **Nagai, T.; Sato, Y.; Kato, H.; Fujimoto, M.; Sugasawa, T.:** The most advanced power saving technology in EAF, METEC and 2nd ESTAD 2015, Stahlinstitut VDEh, Düsseldorf, (2015), pp. 1 - 5

[8] **Kühn, R.; Geck, H.G.; Schwerdtfeger, K.:** Continuous Off-gas measurement and Energy Balance in Electric Arc Steelmaking, ISIJ Int., 45 (2005), p.1587

[9] **Thomé-Kozmiensky, K.J.; Goldmann, D.:** Recycling und Rohstoffe, Band 5, Erhöhung der Energie- und Materialeffizienz der Stahlerzeuging im Lichtbogenofen, TK Verlag Karl Thomé-Kozmiensky, Neuruppin, (2012), pp. 367 - 391

[10] **Haverkamp, V.; Krüger, K.; Dettmer, B.:** Spectrometer-Based Real-Time Measurement of the Electric Arc Radiation in a DC-EAF, Proc. of 30th JSI, Fédération Française de l'Acier, Paris, (2012), p. 33

[11] **Platts (McGraw Hill Financial):** Industry Survey Report – Trends in the European Steel Industry, 9th Annual Steel Markets European Conference, 2013

[12] **Pfeifer, H.; Kirschen, M.; Simeos, J.P.:** Thermodynamic analysis of EAF electrical energy demand, Proc. of 8th European Electric Steelmaking Conference, European Coal and Steelmaking Community, Birmingham, 2005, p. 1 - 19

[13] **Kirschen, M.; Velikorodov, V.; Pfeifer, H.; Kühn, R.; Lenz, S.; Loh, J.; Schaefers, K.:** Off-gas measurements at the EAF primary dedusting system, Proc. of 8th European Electric Steelmaking Conference, European Coal and Steelmaking Community, Birmingham, England, 2005, p. 1 - 11

[14] **Kirschen, M.; Pfeifer, H.; Wahlers, F. J.:** Mass and Energy Balances of Stainless Steel EAF, Proc. of 7th European Electric Steelmaking Conference, European Coal and Steelmaking Community, Venice, Italy, 2002, p. 2.3

[15] **Logar, V.; Dovžan, D.; Škrjanc, I.:** Modeling and Validation of an Electric Arc Furnace: Part 2, Thermo-chemistry , ISIJ Int. 2012, 52, pp. 413 - 423

[16] **Kühn, R.:** Untersuchungen zum Energieeinsatz in einem Gleichstromlichtbogenofen zur Stahlerzeugung, Dissertation, Technische Universität Clausthal, 2002, Shaker Verlag

[17] **Gruber, J.C.; Echterhof, T.; Pfeifer, H.:** Investigation on the Influence of the Arc Region on the Heat and Mass Transport in an EAF Freeboard using Numerical Modeling, steel research int., Online Version, March 2015, pp. 1 - 14

[18] **Guo, D.; Irons, G.:** Radiation Modeling in an EAF, AISTech 2004 Proceedings, Vol. 1, pp. 991-999

[19] **Li, Y.; Fruehan, R.J.:** Computational Fluid-Dynamics Simulation of Post-combustion in the Electric-Arc Furnace, Metall. Mater. Trans. B, 34B (2003), p. 333

[20] **Chan, E.;** Riley**, M.; Thomson, M.J.; Evenson, E.J.:** Nitrogen Oxides (NO_x) Formation and Control in an Electric Arc Furnace (EAF): Analysis with Measurements and Computational Fluid Dynamics (CFD) Modeling, ISIJ Int., 44 (2004), pp. 429 - 438

[21] **Henning, B.; Shapiro, M.; le Grange, L.A.:** DC Furnace Containment Vessel Design using Computational Fluid Dynamics, Proc. of 10th International Ferroalloys Congress, SAIMM, Johannesburg, (2004), pp. 565 - 574

[22] **Henning, B.; Shapiro, M.; le Grange, L.A.:** Improving CFD Analysis of DC Furnace Operation by refining and addition of Transportation Phenomena Models, Proc. of 11th International Ferroalloys Congress, SAIMM, Johannesburg, (2007), pp. 654 - 665

[23] **H. Pfeifer:** Energetische Untersuchung der Plasmatechnik bei der Stahlerzeugung, Stahleisen, Düsseldorf, (1992), p. 57

[24] **Al-Harbi, M.N.; Mishra, S.K.; Maity, M.; Al-Turky, S.:** Computational Fluid-Dynamics Simulation of the Electrical Arc Furnace toward the Optimize the Service Life of Delta Refractory, Proc. of METEC InSteelCon 2011 (Session 15), Stahlinstitut VDEh, Düsseldorf, (2011), pp. 1 - 9

[25] **Sanchez, J.L.G.; Ramirez-Argáez, M.; Conejo, A.N.:** Power Delivery from the Arc in AC Electric Arc Furnaces with Different Gas Atmospheres, steel research int. 80 (2009), No. 2, pp. 113-120

[26] **Sanchez, J.; Conejo, A.; Ramirez-Argáez, M.:** Effect of Foamy Slag Height on Hot Spots Formation inside the Electric Arc Furnace Based on a Radiation Model, ISIJ Int., 52(2012), 804.

[27] **Ramirez-Argáez, M.; Gonzáles-Rivera, C.; Trápaga, G.:** Mathematical Modeling of High Intensity Electric Arcs Burning in Different Atmospheres ISIJ Int., Vol. 49 (2009), No. 6, pp. 796-803

[28] **Qian, F.; Farouk, B.; Mutharasan, R.:** Modeling of Fluid Flow and Heat Transfer in the Plasma Region of the dc Electric Arc Furnace, Metallurgical and Materials Transactions B, Volume 26B (1995), pp. 1057-1067

[29] **Alexis, J.; Ramírez, M.; Trápaga, G.; Jönsson, P.:** Modeling of a DC Electric Arc Furnace - Heat Transfer from the Arc, ISIJ Int., Vol. 40 (2000), No. 11, pp. 1089-1097

[30] **Ramírez, M.; Alexis, J.; Trápaga, G.; Jönsson, P.; McKelliget, J.:** Modeling of a DC Electric Arc Furnace - Mixing in the Bath, ISIJ Int., Vol. 41 (2001). No. 10, pp. 1146-1155

[31] **Lago, F.; Gonzalez, J. J.; Freton, P.; Gleizes, A.:** A numerical modelling of an electric arc and its interaction with the anode: Part I, J. of Physics, Inst. Of Physics publishing, 2004, p. 883

[32] **Blais, B.; Proulx, P.; Boulos, M. I.:** Three-dimensional numerical modelling of a magnetically deflected dc transferred arc in argon, J. of Physics D (Applied Physics), Vol. 36 (2003), pp. 488-496

[33] **Daszkiewicz, T.; Tarczynski, W.:** Discharge channel displacement simulation in AC arc, Archives of Electrical Engineering, Vol. 59 (1-2), 2010, p. 35

[34] **Tarczynski, W.; Daszkiewicz, T.:** Switching Arc Simulation, Przeglad Elektrotechniczny (Electrical review), R. 88 Nr 7b, 2012, p. 60

[35] **Tarczynski, W.; Daszkiewicz, T.:** A new method of determining a new discharge channel time point in a switching arc, Przeglad Elektrotechniczny (Electrical review), R. 89 Nr 1a, 2013, p. 122

[36] **Boselli, M.; Colombo, V.; Ghedini, E.; Gherardi, M.; Sanibondi, P.:** Two-temperature modelling and optical emission spectroscopy of a constant current plasma arc welding process, J. of Physics D (Applied Physics), Vol. 46 (2013), pp. 1 - 11

[37] **Sakulin, M.:** Rechnerische Bestimmung der Kennlinien von Gleichstrom-lichtbögen mit Hilfe von Kanalmodellen, Elektrowärme Int. 40 (1982), B1, p. 18

[38] **Ahlers, H.; Timm, K.:** Untersuchungen von frei brennenden Gleichstrom-lichtbögen bis 12 MW an Elektrostahlöfen – Teil 2: Modellbildung, Elektrowärme Int. 45 (1987), B6, p. 291

[39] **Maecker, H.:** Plasmaströmungen in Lichtbögen infolge eigenmagnetischer Kompression, Zeitschrift für Physik, Bd. 141, 1955, pp. 198 - 216

[40] **Steenbeck, M.:** Eine Prüfung des Minimums- Prinzips für thermische Bogensäulen an Hand neuer Meßergebnisse, Wiss. Veröffentlichung aus dem Siemens Konzern 19 (1940), p. 59

[41] **Moghadasian, M.; Alenasser, E.:** Modeling and Artificial Intelligence-Based Control of Electrode System for an Electric Arc Furnace, J. Electromagnetic Analysis & Applications, 2011, p. 47

[42] **Logar, V.; Dovžan, D.; Škrjanc, I.:** Mathematical Modeling and Experimental Validation of an Electric Arc Furnace, ISIJ Int., Vol. 51 (2011), No. 3, pp. 382 - 391

[43] **Bowman, B.; Krüger, K.:** Arc Furnace Physics, Stahleisen GmbH, Düsseldorf, 2009

[44] **Aula, M. ; Leppänen, A. ; Roininen, J. ; Heikkinen, E. ; Vallo, K. ; Fabritius, T.; Huttula, M.:** Characterization of Process Conditions in Industrial Stainless Steelmaking Electric Arc Furnace Using Optical Emission Spectrum Measurements, Metallurgical and Materials Transactions B, Volume 45B (2014), pp. 839 - 849

[45] **Rini, P.; Degrez, G.:** Elemental Demixing in Air and Carbon Dioxide Stagnation Line Flows, J.l of Thermophysics and Heat Transfer, Vol. 18, No. 4, 2004, pp. 511 - 518

[46] **Barcza, N.A.; Curr, T.R.; Jones, R.T.:** Pure and Applied Chemistry, Vol. 26 (1990), No. 9, pp. 1761-1772

[47] **Neuschütz, D.; Hauck, A.; Giesler, M.; Stüber, A.:** Stoffübergang bei plasmabeheizten Stahlschmelzen, EU Steel Research Project Report (1997), EUR 17803 DE

[48] **Reynolds, Q.G.; Jones, R.T.; Reddy, B.D.:** Mathematical and computational modeling of the dynamic behavior of direct current plasma arcs, The 12th International Ferroalloys Congress, Helsinki, Finland, 2010, p. 789

[49] **Alameddine, S.; Bowman, B.:** Particularities of melting DRI in AC and DC Arc Furnaces, Archives of Metallurgy and Materials, Vol. 53, Issue 2, polish Academy of Sciences, 2008, pp. 411 - 417

[50] **Jones, J.A.T.; Bowman, B.; Lefrank, P.A.:** The Making, Shaping and Treating of Steel, 11th Edition, Electric Furnace Steelmaking , The AISI Steel Foundation, 1999, pp. 525 - 660

[51] **Jordan, G.R.; Bowman, B.; Wakelam, D. :** Electrical and photographic measurements of high-power arcs, British Steel Corporation, Swindon Laboratories, Moorgate, England, 1970, p. 1089

[52] **Rafiei, R.; Kermanpur, A.; Ashrafizadeh, F.:** Numerical thermal simulation of graphite electrode in EAF during normal operation, Ironmaking and Steelmaking, Vol. 35 (2008), Nr. 6, pp. 465 - 472

[53] **ANSYS®:** ANSYS FLUENT Theory Guide, Release 14.5, ANSYS, (2013)

[54] **Raithby, G.D.; Chui, E.H.:** J. of Heat Transfer 1990, 112, p. 415

[55] **Coppalle, A.; Vervisch, P.:** The Total Emissivities of High-Temperature Flames, Combustion and Flame, 49, 1983, pp. 101 - 108

[56] **Smith, T.F.; Shen, Z.F.; Friedman, J.N.:** Evaluation of Coefficients for the Weighted Sum of Grey Gases Model, J. Heat Transfer, 104, 1982, pp. 602 - 608

[57] **Joos, F.:** Technische Verbrennung – Verbrennungstechnik, Verbrennungs-modellierung, Emissionen, Springer Verlag, 2006

[58] **Javadi, M.; Moghiman, M.; Zamani, A.:** Arrhenius Law Modification for Turbulent Combustion Modeling, 3rd Fuel & Combustion Conference of Iran, Iranian Combustion Institute, 2010

[59] **Dryer:** The reaction of carbon monoxide and oxygen in the presence of water, AFOSR Scientific Report, 1972, pp. 125 - 139

[60] **Welty, J.R.; Wicks, C.E.; Wilson, R.E.; Rorrer, G.:** Fundamentals of Momentum, Heat and Mass transfer, 4th Edition, John Wiley and Sons Inc., New York (2001)

[61] **White, F.M.:** Fluid Mechanics, Second Edition, McGraw and Hill International Editions, Mechanical Engineering Series, Singapore (1986)

[62] **Pope, S.B.:** Turbulent flows, Cambridge University Press, United Kingdom, Cambridge (2001), S. 183

[63] **Kang, S.; Iaccarino, G.; Ham, F.:** DNS of buoyancy-dominated turbulent flows on a bluff body using the immersed boundary method, Journal of Computational Physics, 228 (2009), pp. 3189 - 3208.

[64] **Ferziger, J.H.; Perić, M.:** Numerische Strömungsmechanik, Springer Verlag, Berlin, 2008

[65] **Furbo, E.; Harju, J.; Nilsson, H.:** Evaluation of Turbulence models for Prediction of Flow Separation at a Smooth Surface, Report in Scientific Computing Advanced Course, Institutionen För Informationsteknologi, Uppsala Universitet, June 2009

[66] **Iaccarino, G.:** Predictions of a Turbulent Separated Flow using Commercial CFD Codes, J. of Fluid engineering, Vol. 123, December 2001, p. 819

[67] **Grant, M.G.:** Principles and Strategy of EAF Post-Combustion, 58th Electric Furnace Conference, Orlando (USA), November 2000

[68] **Levenspiel, O.:** Chemical Reaction Engineering, 3rd Edition, John Wiley and Sons, 1999, p. 93

9 Appendix

9.1 User subroutine - Energy source/sink due to electrode consumption

```
/*
**********************************************************************************************
**

This UDF specifies the temperature dependant energy source due to CO and O2
mass in- and outflow (electrode consumption)

**********************************************************************************************
****/

/*/ for energy source: h=integral Cp*dt wobei cp=f(T)/ */

#include “udf.h”

DEFINE_SOURCE(cell_T_source, cell, thread, dS, eqn)

{

   real source, DCOsource, DO2source;
   real JGRvol;

/*  */

   real JGRmflowCO, JGRTerm1CO, JGRTerm2CO, JGRTerm3CO;
   real k11CO, k12CO, k13CO, k14CO, k15CO;
   real k21CO, k22CO, k23CO, k24CO, k25CO;
   real JGRtermTCO, jgraCO, jgrbCO, jgrcCO, jgrdCO, jgreCO;

/*  */

   real JGRmflowO2, JGRTerm1O2, JGRTerm2O2, JGRTerm3O2;
   real k11O2, k12O2, k13O2, k14O2, k15O2;
   real k21O2, k22O2, k23O2, k24O2, k25O2;
   real JGRtermTO2, jgraO2, jgrbO2, jgrcO2, jgrdO2, jgreO2;

/*  */

   real JGRbildhCO, JGRbildhO2;
   real COsource, O2source;


   JGRvol = 0.209425921;
   JGRmflowCO = 0.186568;
   JGRmflowO2 = -0.106568;

/*  */
```

```
/* values for CO */
/* --------------*/
    JGRTerm1CO = 301420.2967;
    JGRTerm2CO = 1076005.6167;
    JGRTerm3CO = 1063481.5693;
    JGRbildhCO = -3946005.19;
/* Cp konstants for region between 300K and 1000K */
    k11CO = 968.3898;
    k12CO = 0.4487877;
    k13CO = -0.001152217;
    k14CO = 1.65688E-06;
    k15CO = -7.34631E-10;
/* Cp konstants for region  between 1000K and 5000K */
    k21CO = 897.9305;
    k22CO = 0.4282316;
    k23CO = -0.000167139;
    k24CO = 3.02344E-08;
    k25CO = -2.05137E-12;
/*  */
/* values for O2 */
/* --------------*/
    JGRTerm1O2 = 261170.2769;
    JGRTerm2O2 = 971230.8983;
    JGRTerm3O2 = 1030649.7846;
    JGRbildhO2 = 0.0;
/* Cp konstants for region between 300K and 1000K */
    k11O2 = 834.8265;
    k12O2 = 0.292958;
    k13O2 = -0.000149564;
    k14O2 = 3.41389E-07;
    k15O2 = -2.27836E-10;
/* Cp konstants for region between 1000K and 5000K */
    k21O2 = 960.7523;
    k22O2 = 0.1594126;
    k23O2 = -3.27089E-05;
    k24O2 = 4.61277E-09;
    k25O2 = -2.95283E-13;
```

```
    if (C_T(cell,thread) <= 1000.)
  {
   jgraCO = k11CO*C_T(cell,thread);
   jgrbCO = (k12CO*C_T(cell,thread)*C_T(cell,thread))/2;
   jgrcCO = (k13CO*C_T(cell,thread)*C_T(cell,thread)*C_T(cell,thread))/3;
    jgrdCO =
(k14CO*C_T(cell,thread)*C_T(cell,thread)*C_T(cell,thread)*C_T(cell,thread))/4;
    jgreCO =
(k15CO*C_T(cell,thread)*C_T(cell,thread)*C_T(cell,thread)*C_T(cell,thread)*C_T(cell
,thread))/5;
   JGRtermTCO = jgraCO+jgrbCO+jgrcCO+jgrdCO+jgreCO;
   COsource = JGRmflowCO*(JGRtermTCO-JGRTerm1CO)/JGRvol;
/*  */
   jgraO2 = k11O2*C_T(cell,thread);
   jgrbO2 = (k12O2*C_T(cell,thread)*C_T(cell,thread))/2;
   jgrcO2 = (k13O2*C_T(cell,thread)*C_T(cell,thread)*C_T(cell,thread))/3;
    jgrdO2 =
(k14O2*C_T(cell,thread)*C_T(cell,thread)*C_T(cell,thread)*C_T(cell,thread))/4;
    jgreO2 =
(k15O2*C_T(cell,thread)*C_T(cell,thread)*C_T(cell,thread)*C_T(cell,thread)*C_T(cell
,thread))/5;
   JGRtermTO2 = jgraO2+jgrbO2+jgrcO2+jgrdO2+jgreO2;
   O2source = JGRmflowO2*(JGRtermTO2-JGRTerm1O2)/JGRvol;
/*  */
    source = COsource + O2source;
```

9.1.1.1.1 /* energy source realative to 298.15 K */

```
   jgraCO = k11CO;
   jgrbCO = k12CO*C_T(cell,thread);
   jgrcCO = k13CO*C_T(cell,thread)*C_T(cell,thread);
   jgrdCO = k14CO*C_T(cell,thread)*C_T(cell,thread)*C_T(cell,thread);
    jgreCO =
k15CO*C_T(cell,thread)*C_T(cell,thread)*C_T(cell,thread)*C_T(cell,thread);
   JGRtermTCO = jgraCO+jgrbCO+jgrcCO+jgrdCO+jgreCO;
```

```
    DCOsource = JGRmflowCO*(JGRtermTCO)/JGRvol;

/*   */

    jgraO2 = k11O2;
    jgrbO2 = k12O2*C_T(cell,thread);
    jgrcO2 = k13O2*C_T(cell,thread)*C_T(cell,thread);
    jgrdO2 = k14O2*C_T(cell,thread)*C_T(cell,thread)*C_T(cell,thread);

     jgreO2                                                                    =
k15O2*C_T(cell,thread)*C_T(cell,thread)*C_T(cell,thread)*C_T(cell,thread);

    JGRtermTO2 = jgraO2+jgrbO2+jgrcO2+jgrdO2+jgreO2;
    DO2source = JGRmflowO2*(JGRtermTO2)/JGRvol;

/*   */

     dS[eqn] = DCOsource + DO2source;

   }

     else

   {

    jgraCO = k21CO*C_T(cell,thread);
    jgrbCO = (k22CO*C_T(cell,thread)*C_T(cell,thread))/2;
    jgrcCO = (k23CO*C_T(cell,thread)*C_T(cell,thread)*C_T(cell,thread))/3;

     jgrdCO                                                                    =
(k24CO*C_T(cell,thread)*C_T(cell,thread)*C_T(cell,thread)*C_T(cell,thread))/4;

     jgreCO                                                                    =
(k25CO*C_T(cell,thread)*C_T(cell,thread)*C_T(cell,thread)*C_T(cell,thread)*C_T(cell
,thread))/5;

          JGRtermTCO = jgraCO+jgrbCO+jgrcCO+jgrdCO+jgreCO;

    COsource     =     JGRmflowCO*((JGRtermTCO-JGRTerm3CO)+(JGRTerm2CO-
JGRTerm1CO))/JGRvol;

/*  */

    jgraO2 = k21O2*C_T(cell,thread);
    jgrbO2 = (k22O2*C_T(cell,thread)*C_T(cell,thread))/2;
    jgrcO2 = (k23O2*C_T(cell,thread)*C_T(cell,thread)*C_T(cell,thread))/3;

     jgrdO2                                                                    =
(k24O2*C_T(cell,thread)*C_T(cell,thread)*C_T(cell,thread)*C_T(cell,thread))/4;
```

```
    jgreO2 =
(k25O2*C_T(cell,thread)*C_T(cell,thread)*C_T(cell,thread)*C_T(cell,thread)*C_T(cell
,thread))/5;

    JGRtermTO2 = jgraO2+jgrbO2+jgrcO2+jgrdO2+jgreO2;

    O2source = JGRmflowO2*((JGRtermTO2-JGRTerm3O2)+(JGRTerm2O2-
JGRTerm1O2))/JGRvol;

/*  */

    source = COsource + O2source;
```

9.1.1.1.2 /* energy source realative to 298.15 K */

```
   jgraCO = k21CO;
   jgrbCO = k22CO*C_T(cell,thread);
   jgrcCO = k23CO*C_T(cell,thread)*C_T(cell,thread);
   jgrdCO = k24CO*C_T(cell,thread)*C_T(cell,thread)*C_T(cell,thread);

    jgreCO =
k25CO*C_T(cell,thread)*C_T(cell,thread)*C_T(cell,thread)*C_T(cell,thread);

   JGRtermTCO = jgraCO+jgrbCO+jgrcCO+jgrdCO+jgreCO;
   DCOsource = JGRmflowCO*(JGRtermTCO)/JGRvol;

/*   */

   jgraO2 = k21O2;
   jgrbO2 = k22O2*C_T(cell,thread);
   jgrcO2 = k23O2*C_T(cell,thread)*C_T(cell,thread);
   jgrdO2 = k24O2*C_T(cell,thread)*C_T(cell,thread)*C_T(cell,thread);

    jgreO2 =
k25O2*C_T(cell,thread)*C_T(cell,thread)*C_T(cell,thread)*C_T(cell,thread);

   JGRtermTO2 = jgraO2+jgrbO2+jgrcO2+jgrdO2+jgreO2;
   DO2source = JGRmflowO2*(JGRtermTO2)/JGRvol;

/*   */

    dS[eqn] = DCOsource + DO2source;

  }


    return source;
```

9.2 Overview of simulation results

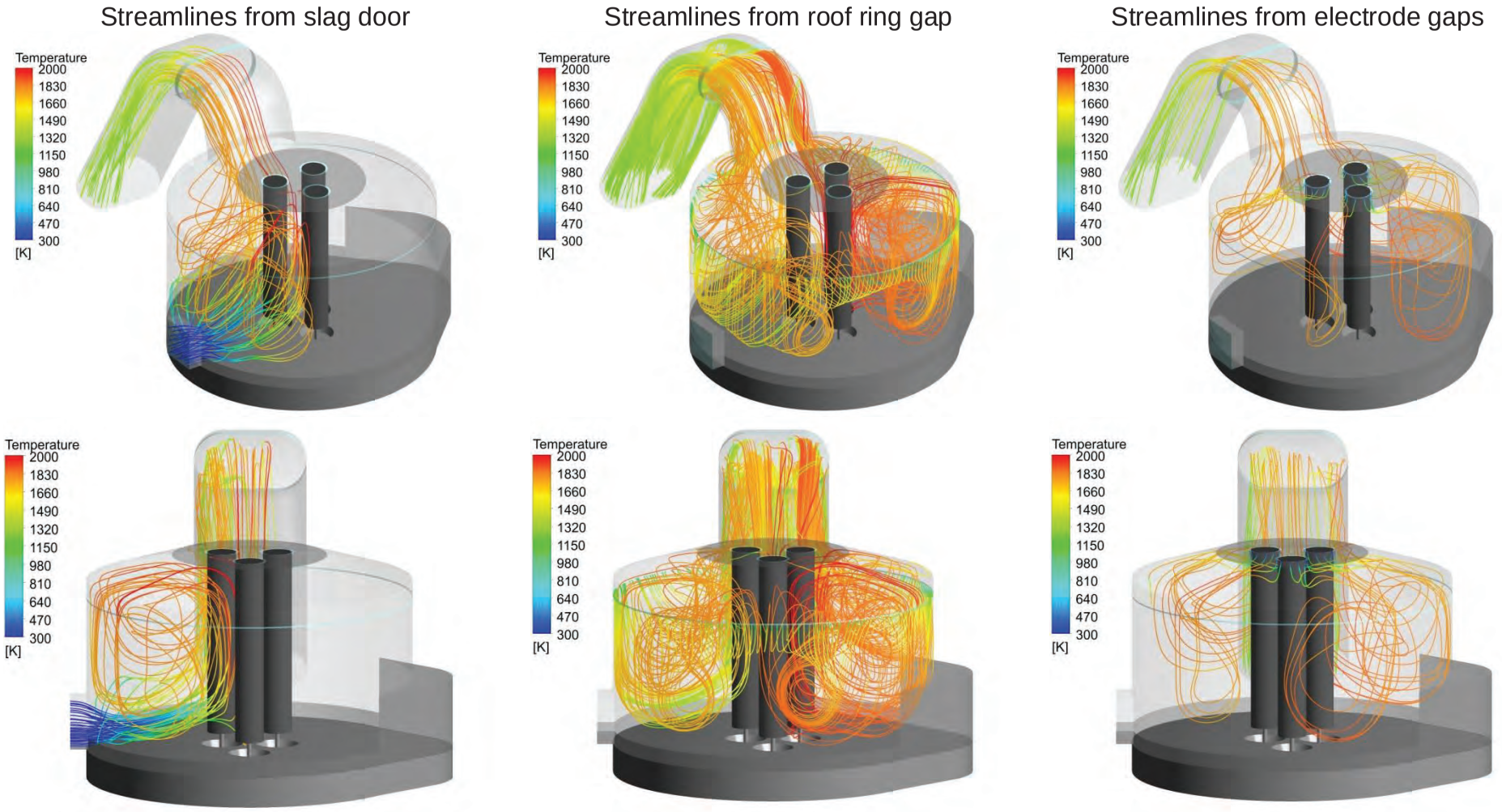

Figure 9-1: Streamlines (Sim. 1 – with arc in and outflow, free burning arc length = 230 mm)

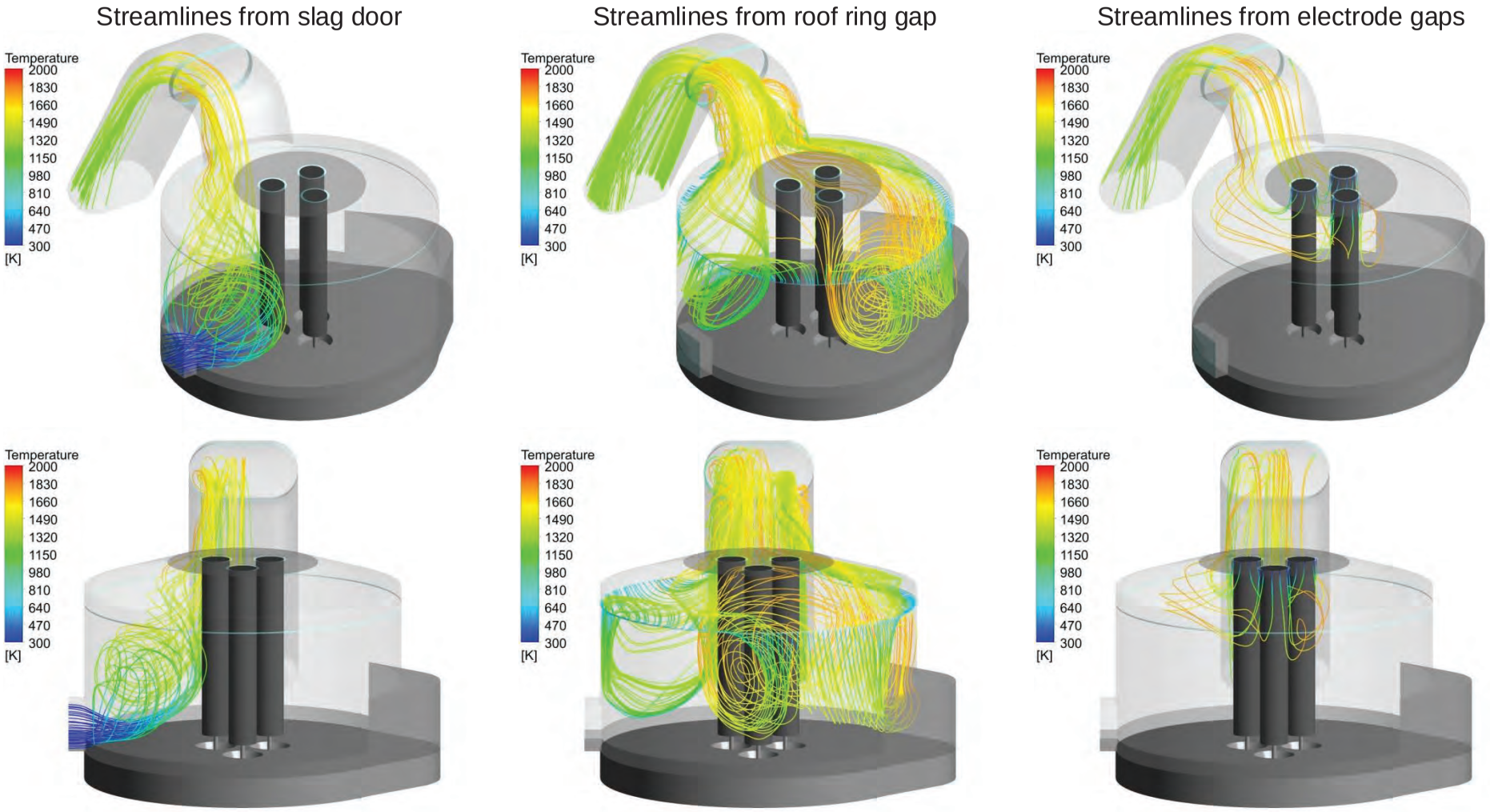

Figure 9-2: Streamlines (Sim. 2 - without arc in and outflow, free burning arc length = 230 mm)

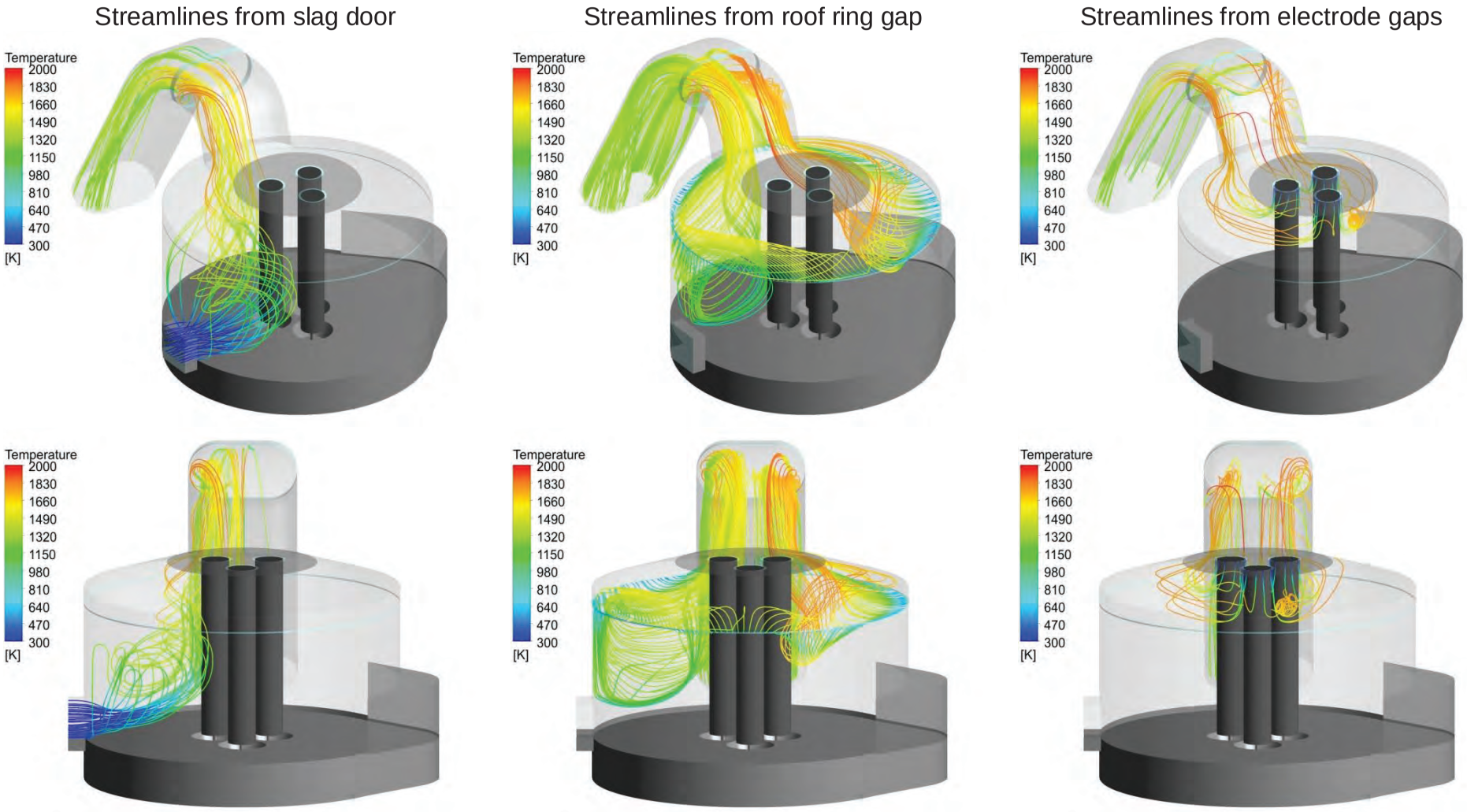

Figure 9-3: Streamlines (Sim. 3 - with arc in and outflow, free burning arc length = 50 mm)

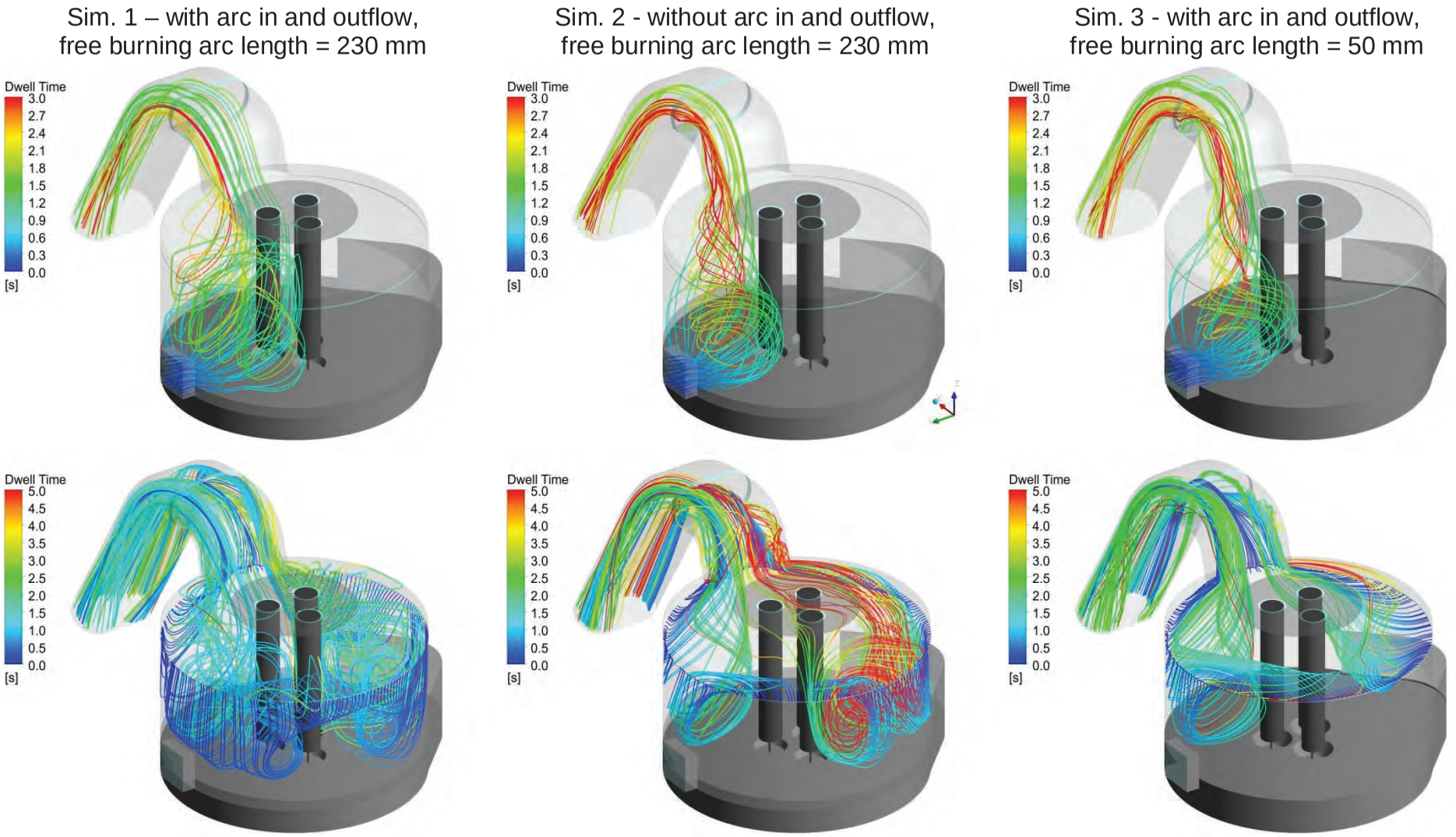

Figure 9-4: Comparison of residence times along streamlines

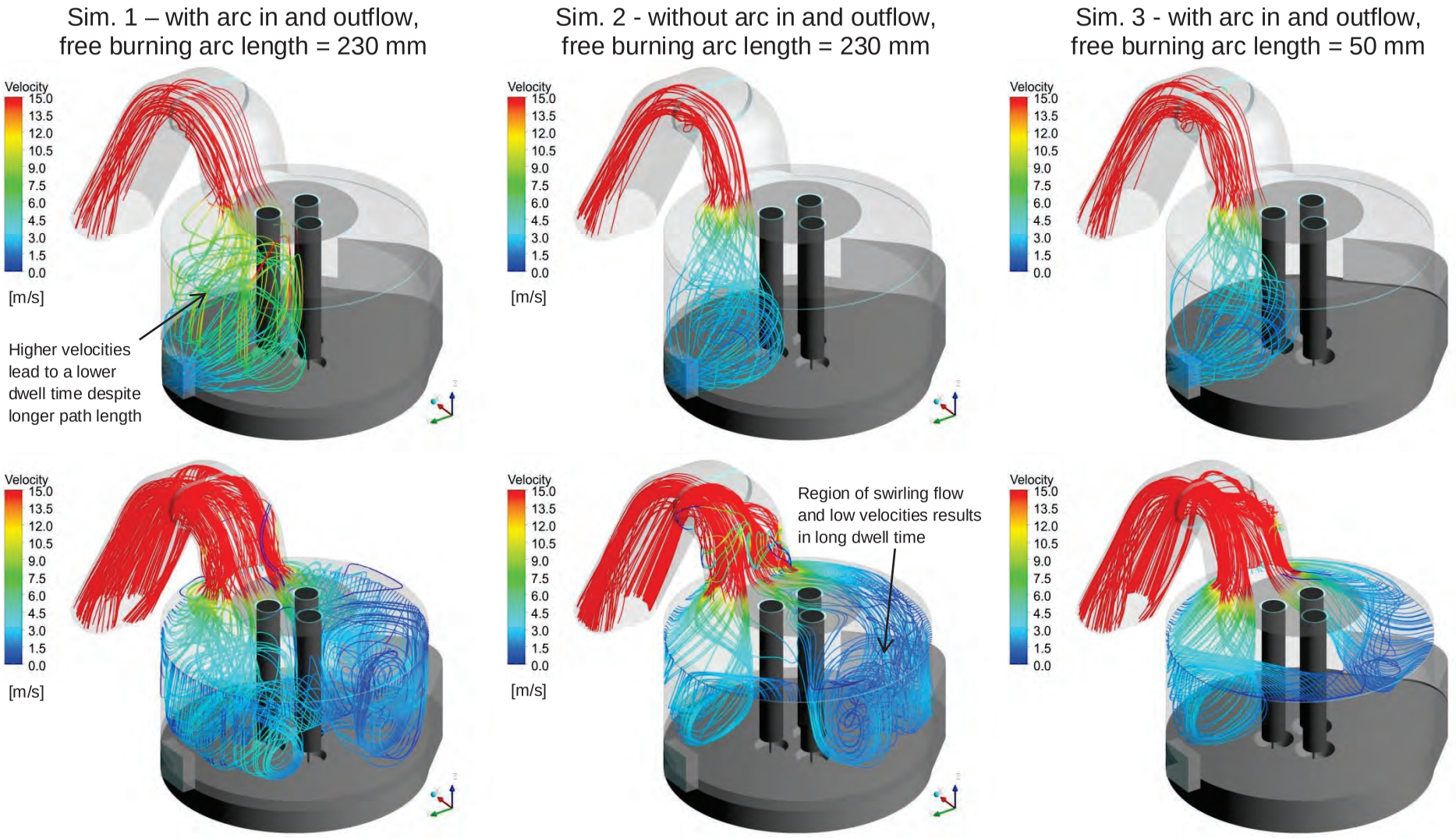

Figure 9-5: Comparison of streamline velocity magnitude

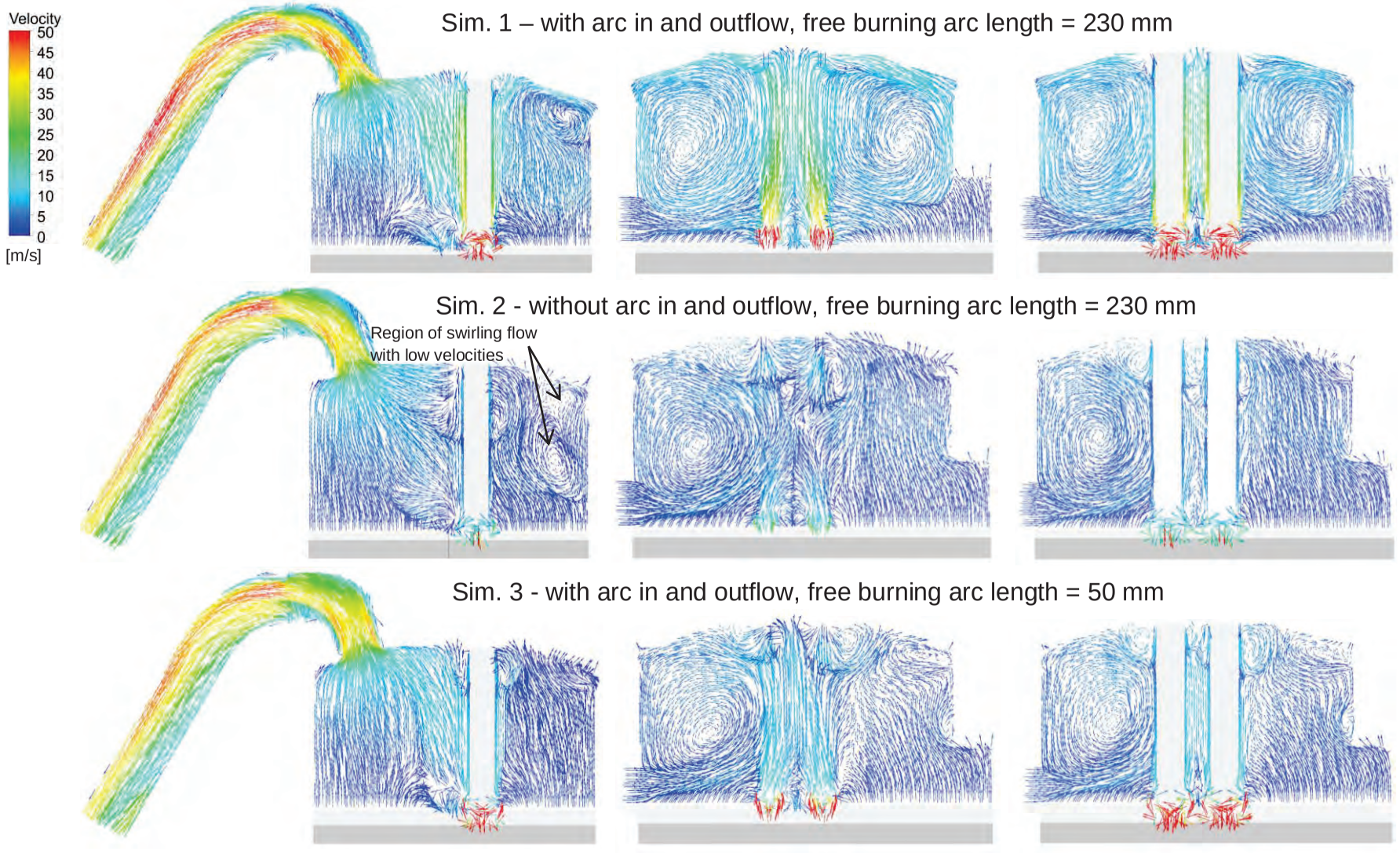

Figure 9-6: Comparison of velocity distributions in vessel (Sim. 1, Sim. 2 and Sim. 3)

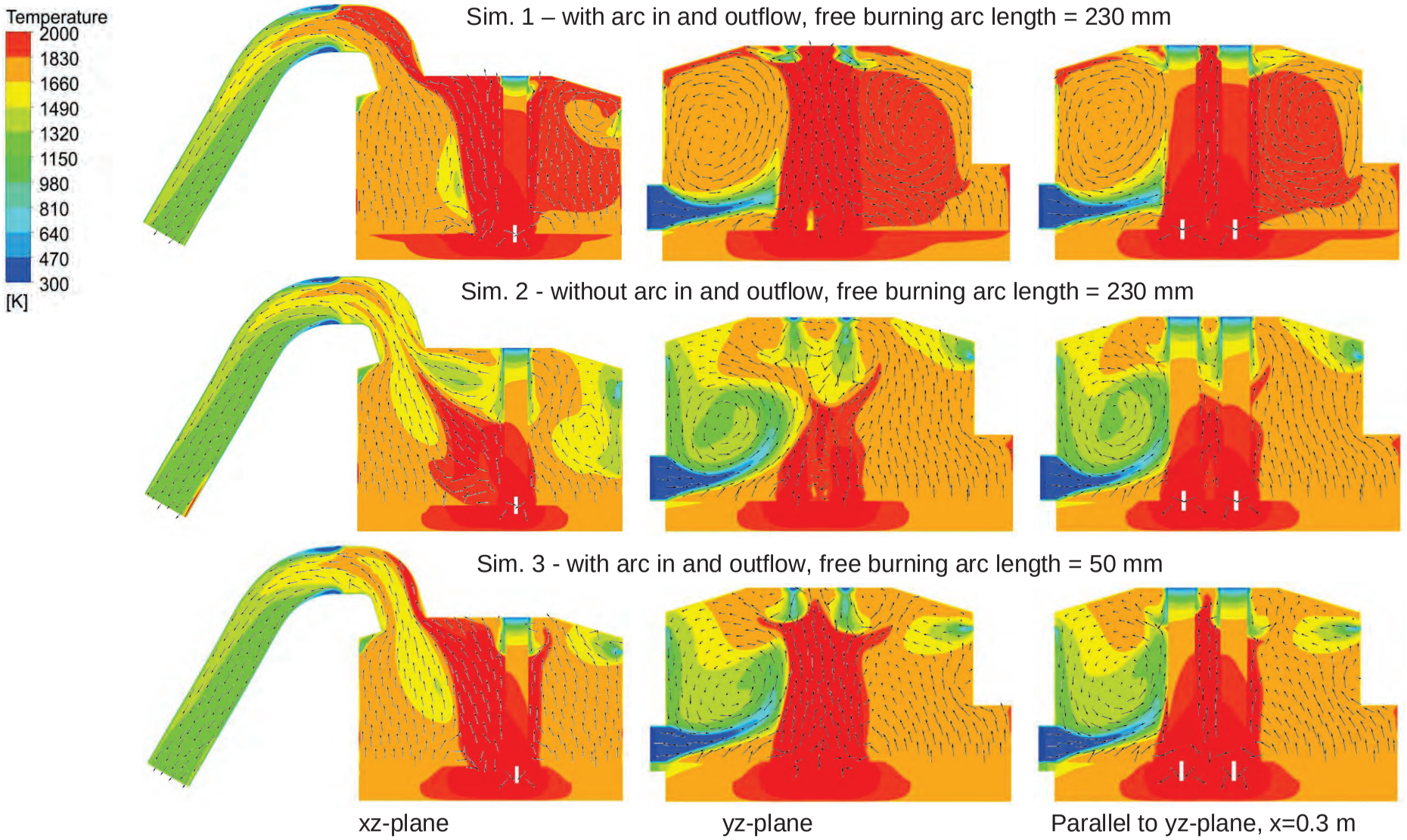

Figure 9-7: Comparison of temperature distribution in vessel (Sim. 1, Sim. 2 and Sim. 3)

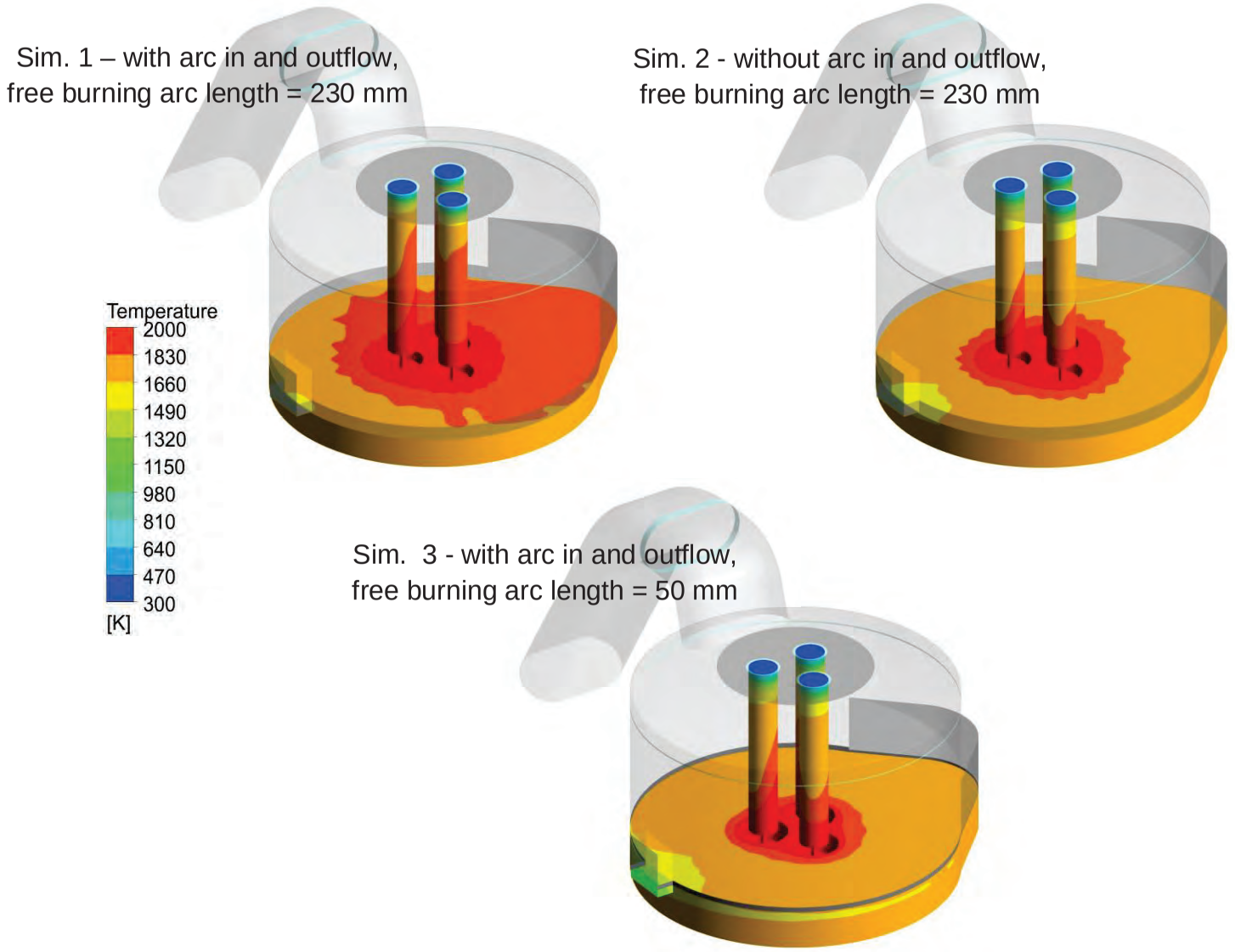

Figure 9-8: Temperature distribution on the outer surfaces of slag and electrodes (Sim. 1, Sim. 2 and Sim. 3)

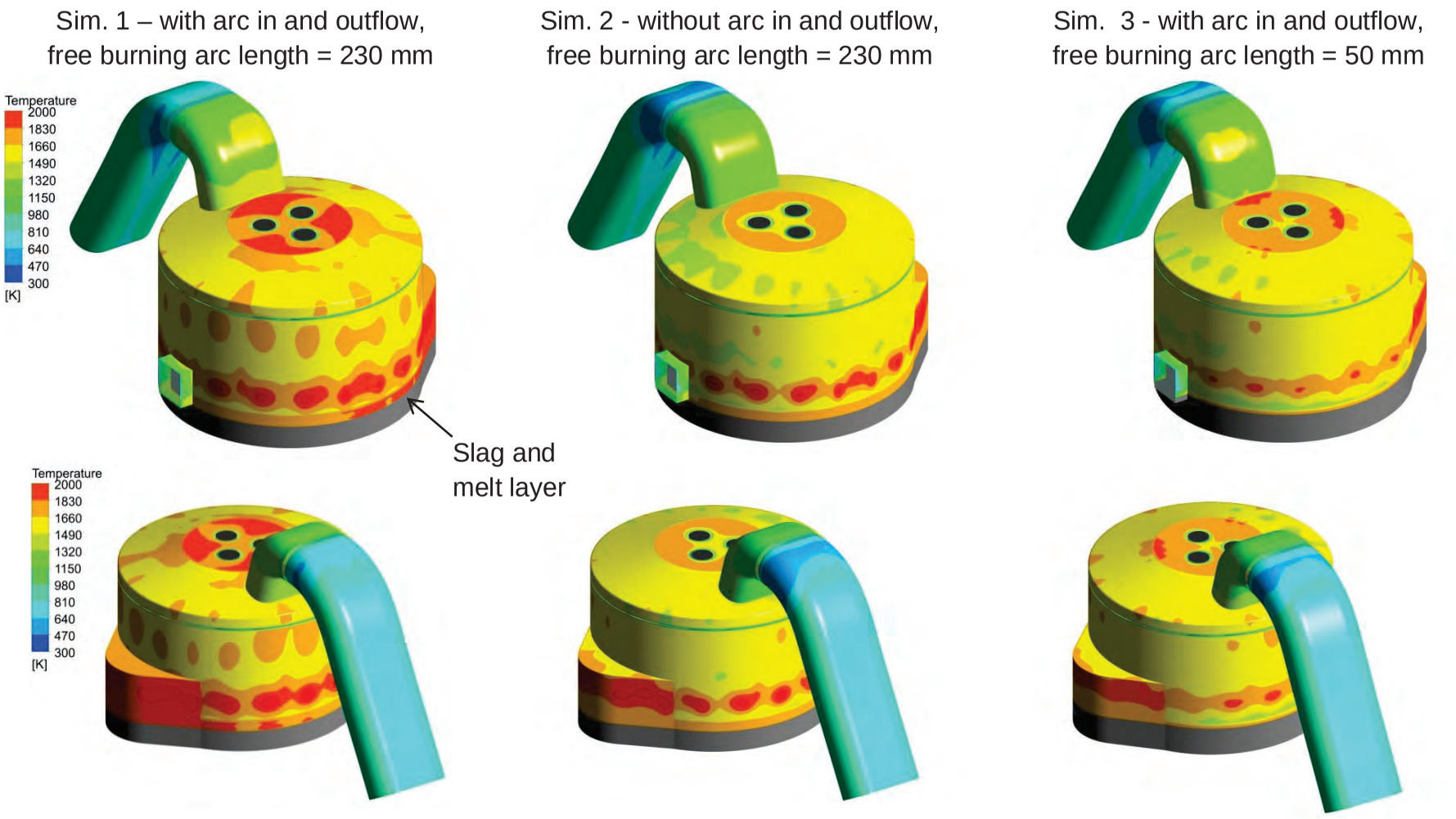

Figure 9-9: Temperature distribution on the inner surfaces of the EAF vessel walls (Sim. 1, Sim. 2 and Sim. 3)

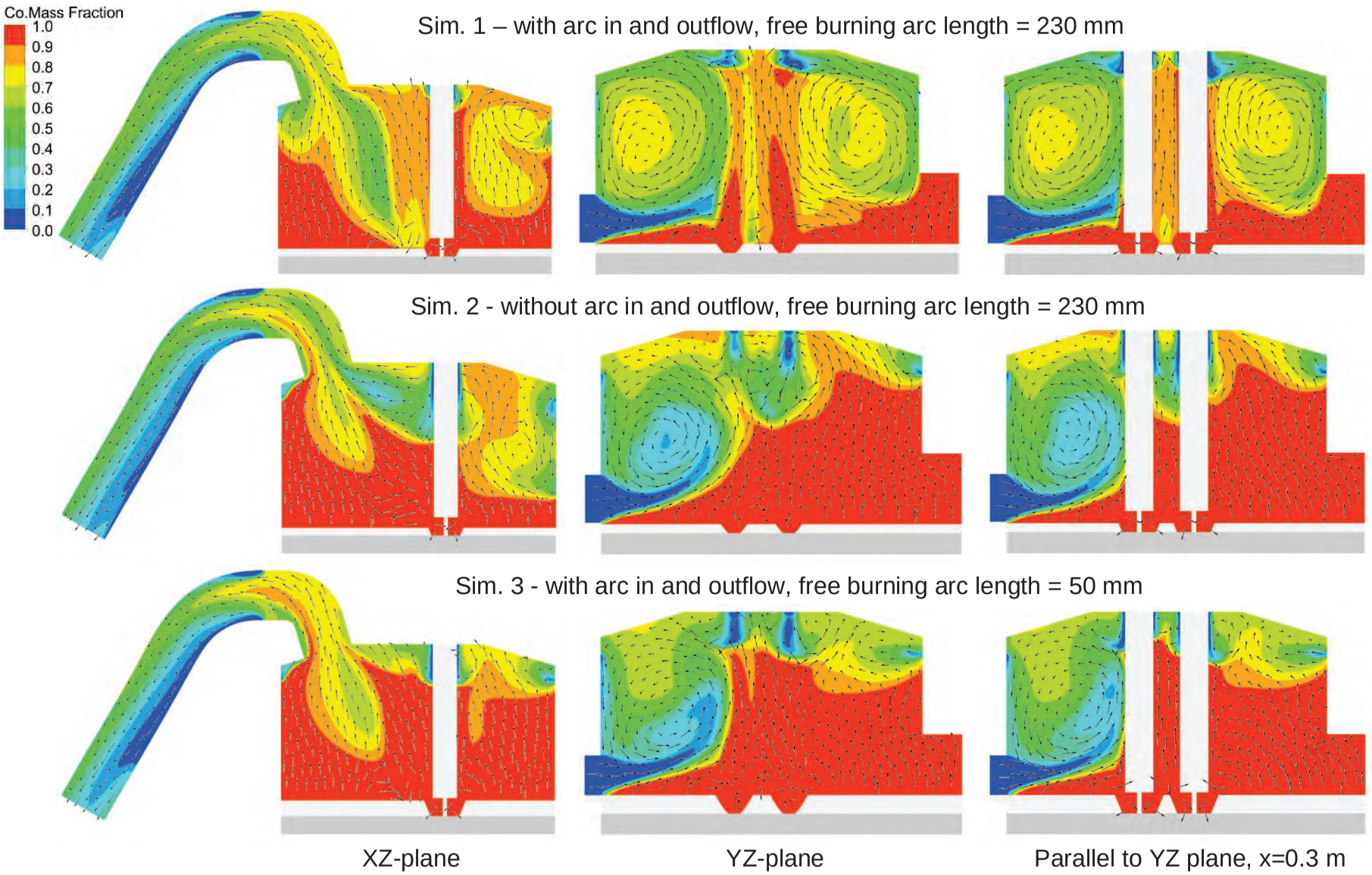

Figure 9-10: Mass fraction distribution of CO (Sim. 1, Sim. 2 and Sim. 3)

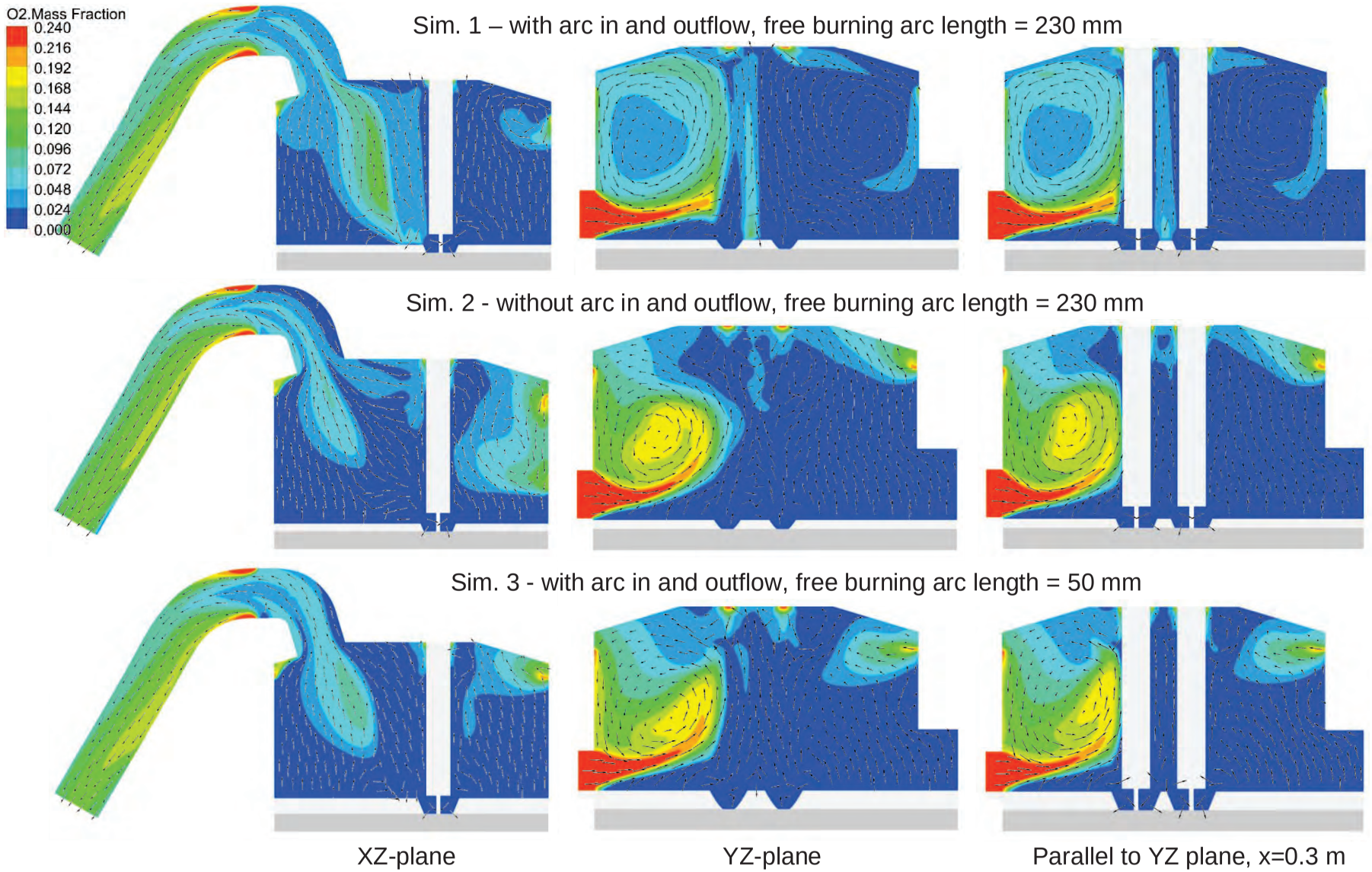

Figure 9-11: Mass fraction distribution of O_2 (Sim. 1, Sim. 2 and Sim. 3)

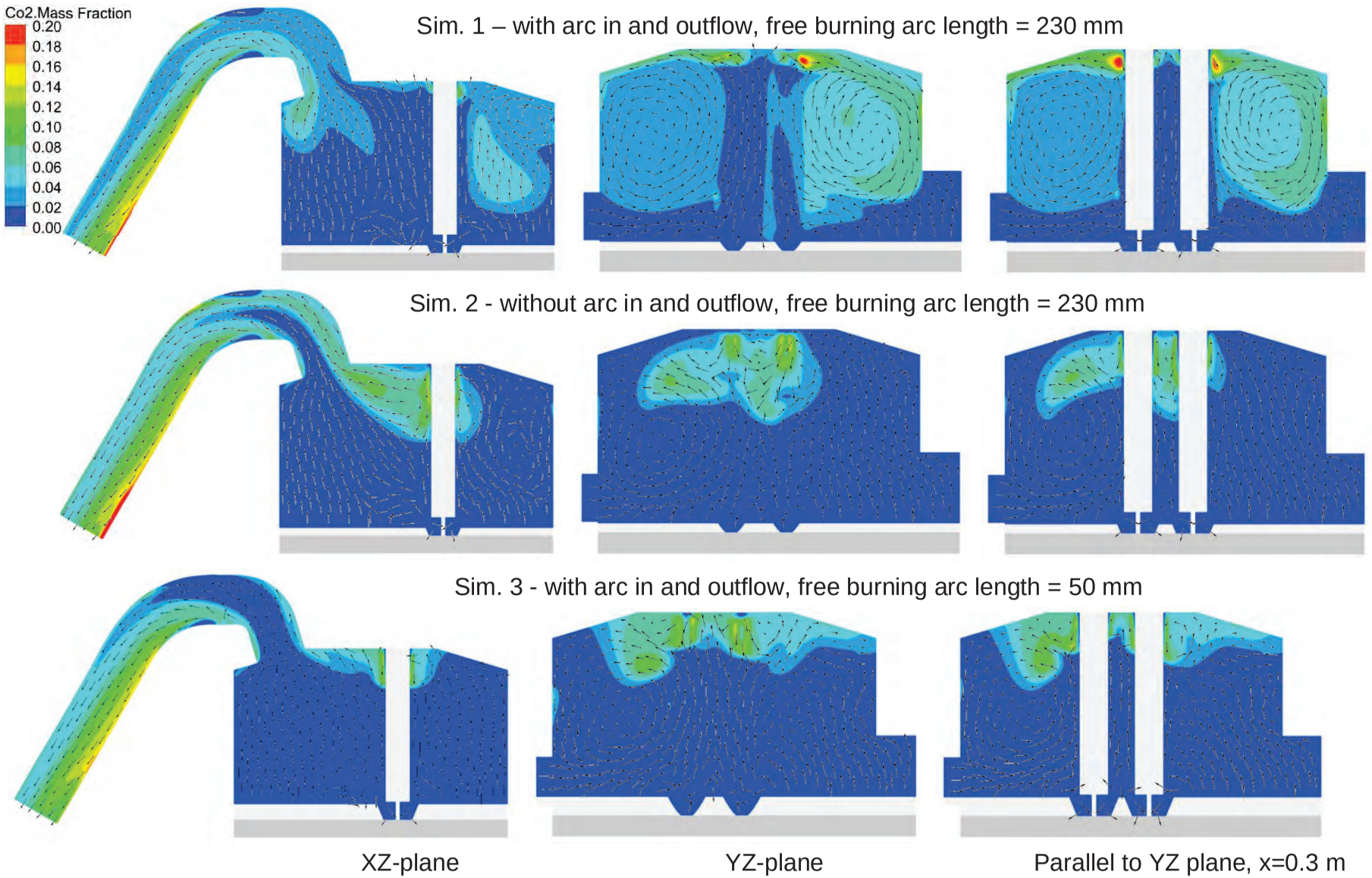

Figure 9-12: Mass fraction distribution of CO_2 (Sim. 1, Sim. 2 and Sim. 3)